The STAR Beam Use Request for Run-23-25

The STAR Collaboration

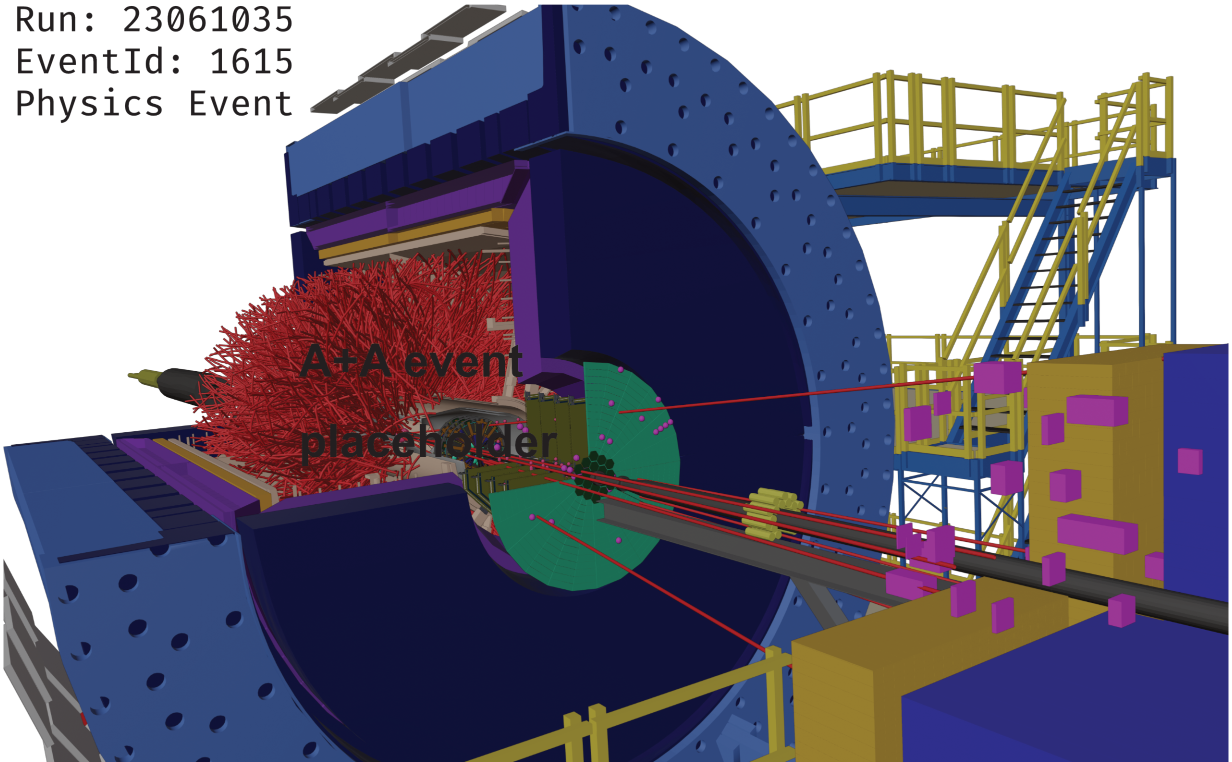

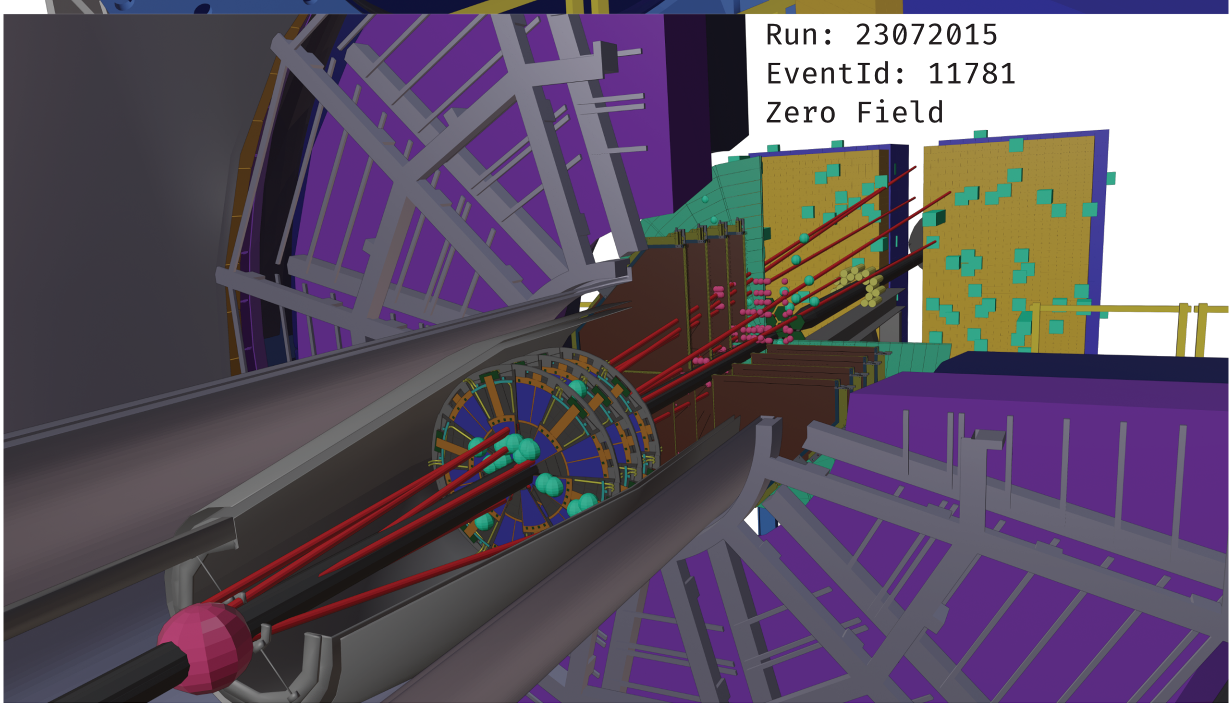

Executive Summary

This Beam Use Request outlines the compelling physics programs proposed by STAR collaboration for data taking in 2023-25.

STAR's **highest scientific priority** is to record a combination of high statistics soft and hard probes data from Au+Au, p+Au, and p+p data at $\sqrt{s_{\rm NN}} = 200$ GeV, during 2023-25 as outlined in Table 1. When fully collected, these datasets will enable the successful completion of RHIC's scientific mission via examination of the microstructure of the Quark Gluon Plasma (QGP) and a continuation of our unique forward physics program.

Table 1: Proposed Run-23 - Run-25 assuming 28 cryo-weeks of running every year, and 6 weeks set-up time to switch species in 2024. For p+p and p+Au sampled luminosities assume a "take all" trigger. For Au+Au we provide the requested event count for our minimum bias trigger, and the requested sampled luminosity from our a high-$p_{\rm T}$ trigger that covers all v_z.

$\sqrt{s_{\rm NN}}$ (GeV)	Species	Number Events/ Sampled Luminosity	Year
200	Au+Au	20B / 40 nb^{-1}	2023+2025
200	p+p	235 pb^{-1}	2024
200	p+Au	1.3 pb^{-1}	2024

STAR's scientific program is enabled by the combination of the detector upgrades for Beam Energy Scan phase II (BES-II) and the Forward Upgrades. In combination they generate STAR's unique capabilities in particle identification (PID) over an extended rapidity acceptance and down to very low transverse momentum ($p_{\rm T}$), while maintaining a low material budget. All these new detectors are now fully commissioned and operated exceptionally well during Run-22.

Significantly increased luminosities, the extended acceptance at mid-rapidity due to the iTPC, improved event plane and triggering capabilities via the EPD, and the ability to probe the previously inaccessible forward region are all exploited in our Hot QCD program, that informs on the microstructure of the QGP, and our Cold QCD program that will utilize transverse polarization setting the stage for related future measurements at the Electron-Ion Collider (EIC).

Combined Au+Au datasets collected in Run-23 and Run-25 will allow STAR to address important questions about the inner workings of the QGP, including the temperature dependence of the shear and bulk viscosities, the 3-D nature of the initial state, how global vorticity is transferred to the spin angular momentum of particles on such short time scales and the chiral properties of the medium.

STAR considers it critical that we collect approximately equal nucleon-nucleon luminosities for p+p and p+Au at 200 GeV during Run-24. This optimizes the statistical precision of several critical observables that require comparisons between results in both p+p and p+Au. We request transversely polarized protons for both datasets. Assuming 28 cryo-weeks in

Run-24 we expect to record samples that represent a factor 4.5 times the luminosity that STAR sampled during the last transversely polarized p+p collisions in Run-15, and 3 times the luminosity sampled during Run-15's transversely polarized p+Au collision period.

As requested, we also considered the scenario that each run is reduced to 24 cryo-weeks. Under this scenario the STAR collaboration continues to request Au+Au, p+Au, and p+p running as outlined in Table 2. In this way we will take the best possible advantage of our recent upgrades. However, this scenario would result in a significant increase in both the statistical and systematic uncertainties of all the data, impacting the excellent precision we aim for with the measurements described in this BUR.

We estimate that 24 as opposed to 28 cryo-weeks will decrease STAR's Au+Au data sample by at least 16%. Measurements of hard probes (jets and quarkonia), thermal di-lepton and photon-induced processes (di-lepton and J/ψ) will be most impacted since they are the most statistically demanding Hot QCD measurements proposed.

There is a much more significant effect on p+p and p+Au running due to both the 6 weeks needed to change beam species, the ramp-up times, and the fact that no low-luminosity running is requested. We estimate at least a 22-25% loss in sampled p+p and p+Au luminosity. There will be an even larger impact on the nuclear PDFs, fragmentation functions, and gluon saturation measurements since these require comparisons of the same observables measured in both p+p and p+Au collisions.

Table 2: Proposed Run-23 - Run-25 assuming 24 cryo-weeks of running every year, and 6 weeks set-up time to switch species in 2024. For p+p and p+Au sampled luminosities assume a "take all" trigger. For Au+Au we provide the requested event count for our minimum bias trigger, and the requested sampled luminosity from our a high-$p_T$trigger that covers all v_z.

$\sqrt{s_{NN}}$ (GeV)	Species	Number Events/ Sampled Luminosity
200	Au+Au	17B / 34 nb^{-1}
200	p+p	176 pb^{-1}
200	p+Au	0.98 pb^{-1}

Finally in Section 5 we propose the collection of two datasets if the opportunity arises after collection of our higher priority datasets outlined above. One proposal enables the imaging of the shape and radial profile of atomic nuclei via collective flow measurements. Such studies are important to improve our understanding of the complex initial conditions and subsequent hydrodynamical response of the medium. Information on these deformation and nuclear skin parameters are also of significant interest to the nuclear structure physics community. Heavy ion collision data have different sensitivities to nuclear structure experiments and are therefore promising complementary tools to probe different aspects of the nucleus' shape and substructure. The other proposal expands our fixed-target program to include other light beam and target combinations. These data will help clarify the role and mechanisms of nucleon stopping. In addition, light nucleus cross sections in the target/projectile regions using beams of 3-50 GeV/n are of great interest to the NASA Space Radiation Protection community.

Contents

1 Highlights from the STAR Program

1.1 Highlights from the Heavy Ion Program

1.1.1 Search for the Chiral Magnetic Effect

Results from the isobar blind analyses A decisive experimental test of the Chiral Magnetic Effect (CME) has become one of the major scientific goals of the heavy-ion physics program at RHIC. Isobars were collided to utilize the fact that the collisions of ruthenium produce larger magnetic fields than those of zirconium by 5–9%, hence a 10–18% larger CME correlation signal because of its B^2 dependence. Therefore, the CME would cause the ratio of CME-sensitive observables in Ru+Ru over Zr+Zr to be greater than one, assuming that backgrounds are the same in the two systems. The isobar run was specially designed to reduce the systematics in this ratio. In order to minimize unconscious and pre-determined biases a blind analysis was performed with pre-defined criteria on what would constitute observation of a CME signal. For example, the double ratio of the primary CME-sensitive correlator $\Delta\gamma$ scaled by ellipticity v_2 in ruthenium over zirconium is expected to be greater than one if there is a non-zero CME fraction.

The measurements of the double ratio of $\Delta\gamma/v_2$ with various kinematic cuts from the isobar blind analysis are shown in Fig. 1. A precision in our measurement down to 0.4% was observed in the measurement of the $\Delta\gamma/v_2$ ratio. However, no predefined signature of CME was observed. The observation that the double ratio of $\Delta\gamma/v_2$ is significantly below unity can be attributed to the multiplicity difference between Ru+Ru and Zr+Zr as shown by the ratio of the inverse of uncorrected tracks $1/N_{\rm trk}^{\rm offline}$ measured within the acceptance of $|\eta| < 0.5$. This ratio being less than one is explainable not by larger charge separation in Zr+Zr compared to Ru+Ru, but rather by larger multiplicity dilution ($\propto 1/N_{\rm trk}^{\rm offline}$) in Ru+Ru. This argument is further demonstrated by the ratio of a similar quantity $r(m_{\rm inv})$, which measures the relative pair multiplicity difference opposite-sign and same-sign pion pairs; in a model in which the background for $\Delta\gamma$ is solely due to flowing clusters, $\Delta\gamma/v_2$ would scale simply as r.

A number of other CME sensitive observables were also measured, such as the factorization coefficients κ_{112}, k_2, the inverse width of the R-variable as shown in Fig. 1. The ratios of these observables in Ru+Ru over Zr+Zr are also found to be less than unity, again not consistent with pre-defined CME signatures. In addition, CME-insensitive charge separation measures using third harmonic event planes such as $\Delta\gamma_{123}/v_3$ and k_3 were also measured to provide data-driven baselines. The utility of these baselines are not affected by multiplicity dilution although their constraining powers are limited by their larger uncertainties as compared to the equivalent observables involving second harmonics.

Non-flow effects on the isobar baseline The overall conclusion from the blind analyses is that no predefined CME signature has been observed in the isobar data. However, to extract a quantiative result utilizing the full sensitivity of the isobar run, careful consideration must be given to the baseline; the baseline of unity is expected to be affected by the

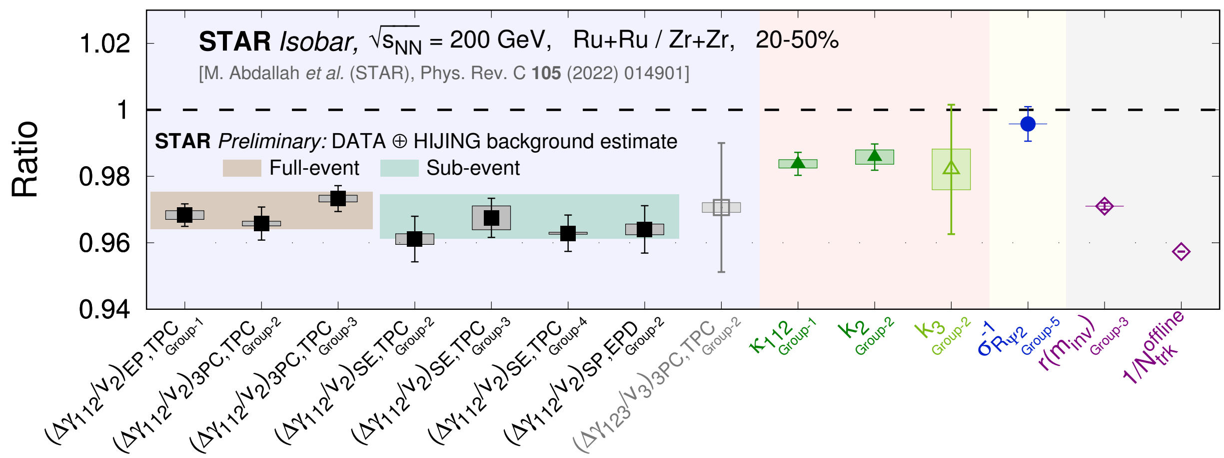

Figure 1: Compilation of results from the blind analysis. Results are shown in terms of the ratio of measures in Ru+Ru collisions divided by Zr+Zr collisions. Solid dark symbols denote CME-sensitive measures whereas open light symbols show counterpart measures that are designed to be insensitive to CME. The vertical lines indicate statistical uncertainties whereas boxes indicate systematic uncertainties. The colors in the background are intended to separate different types of measures. The two data points (open markers) have been added on the right to indicate the ratio of inverse multiplicities ($N_{\rm trk}^{\rm offline}$) and the ratio of relative pair multiplicity difference (r) as explained in the text. The two bands show estimates for background calculated using isobar data and the HIJING model incorporating the multiplicity difference between the two isobars and non-flow effects.

multiplicity difference between the two isobars. At the last quark matter conference (QM 2022), the STAR collaboration presented important progress toward quantifying possible remaining CME signals by incorporating the multiplicity difference between the two isobars and non-flow effects which are also different between the Zr and Ru. As a first step, the estimates are made for the background contribution to the double ratio of the $\Delta\gamma/v_2$ by incorporating: 1) the difference in the multiplicity dilution ($\propto 1/N_{\rm trk}^{\rm offline}$) between the two isobars, 2) data-driven estimates of various sources of two-particle non-flow correlations and, 3) sources of three-particle non-flow correlations estimated using a HIJING simulation. The background estimates for two difference kinematic regions involving full TPC acceptance (Full-event) and TPC acceptance with two sub-events (Sub-event) are shown by bands with different colors in Fig. 1. The conclusion is that the measurements of $\Delta\gamma/v_2$ from isobars are consistent with our preliminary estimate for background expectations.

CME measurement in Au+Au collisions The most recent measurement of charge separation in Au+Au collisions was performed with the spectator plane (SP) and participant plane (PP) using a recently developed method. [1,2] The idea is straightforward: the CME signal is sensitive to the magnetic field which is primarily generated by spectator protons, so the signal is the strongest in the measurement made with respect to SP; on the other hand, flow is strongest along the direction of PP, so is the flow-induced background for

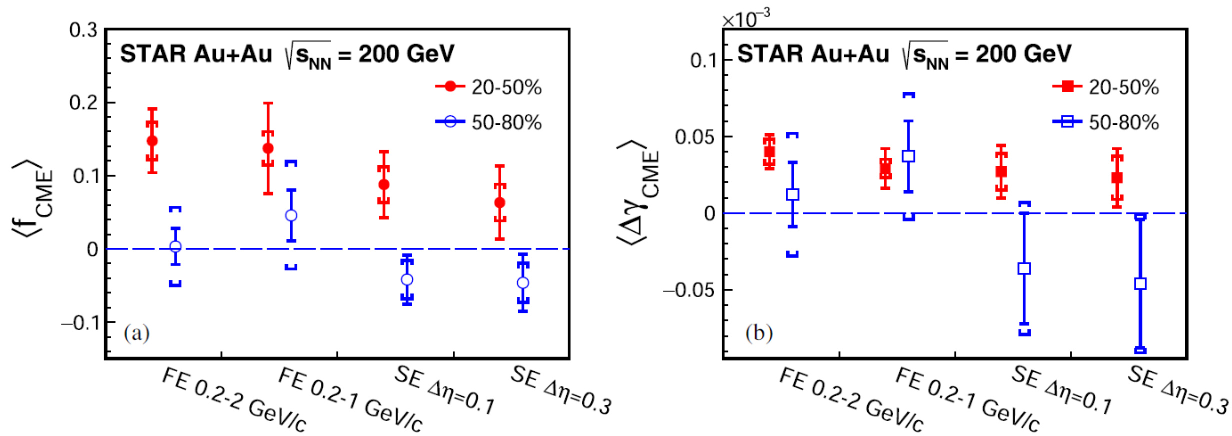

Figure 2: The flow-background removed $f_{\rm CME}$ (a) and $\Delta\gamma_{\rm CME}$ (b) signal in 50%–80% (open markers) and 20%–50% (solid markers) centrality Au+Au collisions at $\sqrt{s_{\rm NN}}$200 GeV, extracted by various analysis methods [full-event (FE), sub-event (SE)] and kinematic cuts. Error bars show statistical uncertainties; the caps indicate the systematic uncertainties.

the CME. From the charge correlation measurements with respect to SP and PP, one can resolve the CME signal and the flow-induced background. Figure 2 shows the CME signal fraction ($f_{\rm CME}$) in the inclusive $\Delta\gamma$ measurement via this SP/PP method. [3] An indication of a positive CME signal is seen in mid-central 20–50% central Au+Au collisions, while the signal is consistent with zero in more peripheral collisions. The significance of the CME signal is on the order of 2σ.

Since the v_2 measurement and the 3-particle correlator measurement with respect to PP are contaminated by non-flow effects, the measured $f_{\rm CME}$ is still affected by non-flow. [3, 4] Unlike isobar collisions where non-flow affects both measurements, non-flow in Au+Au collisions affects only the PP measurements, thus is relatively easier to estimate. Model studies together with non-flow data measurements [5] suggest that non-flow effects on $f_{\rm CME}$ may be small or even negative. [4] This makes the measured positive $f_{\rm CME}$, although with large uncertainties, intriguing. It is noteworthy that the non-observation of the CME in isobar collisions ($\sim$ 4 billion MB events) and a hint of a positive CME signal in Au+Au collisions ($\sim$ 2.4 billion MB events) are not contradictory. It was recently realized, based on mundane physics, that the CME signal to background ratio in isobar collisions can be a factor of 3 smaller than in Au+Au collisions. [6]

CME measurements with the BES-II data One important question regarding the CME is: What happens at lower collision energies? In this context a new idea has emerged. The newly installed event-plane detector (EPD) upgrade provides a new capability at STAR towards the CME search at lower collision energy and for the BES-II program. [7]

The first idea is simple, at lower energies the EPD acceptance ($2.1 < |\eta| < 5.1$) falls in the region of beam rapidity ($Y_{\rm beam}$) and can measure the plane of strong directed flow (Ψ_1) of spectator protons, beam fragments and stopped protons, which is therefore strongly

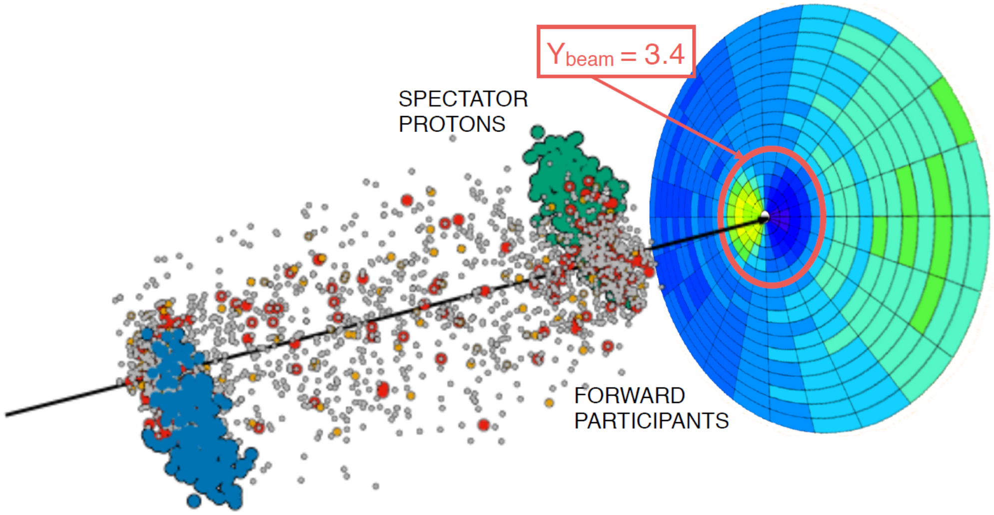

Figure 3: Prospect for the CME search with the BES-II data. (Left) Single simulated UrQMD event and EPD detector acceptance that covers beam rapidity and detects both forward participants and spectators in 27 GeV Au+Au collisions that have large directed flow which changes sign at $\eta = Y_{\text{bean}} = 3.4$. (Right) γ-correlators scaled by v_2 across different event-planes and double ratio of spectator/participant event plane results which would be above unity for finite CME scenario.

correlated to the B-field direction (see Fig. 3). The next step is to measure $\Delta\gamma$ with respect to Ψ_1 and compare it with the measurement of $\Delta\gamma$ along the Ψ_2 planes determined from the outer regions of EPD and the TPC at mid-rapidity that are relatively more weakly correlated to the B-field direction. A test of the CME scenario will be to see if a large difference is observed in the measurements. First preliminary measurements from STAR as shown in Fig. 3 are dominated by uncertainty, but seem to show good prospects for the CME search at lower energies. With the higher statistics data from the BES-II collider data (7.7-19.6 GeV) and fixed target program more precise measurements are possible.

1.1.2 Bulk Correlations

Over the past years, the STAR collaboration has performed a series of correlation measurements directed towards a comprehensive understanding of the QCD phase diagram and the transport properties of the QGP phase. Here we highlight the most recent STAR results on bulk correlations.

Global spin polarization and alignment Non-central heavy ion collisions can generate a large orbital angular momentum (OAM) in the system. Part of OAM is transferred to the system in the form of preferential alignment of the intrinsic angular momentum (spin) of particles along the OAM direction through spin-orbit couplings, a phenomenon called global polarization. [8,9] The global polarization of quarks influences vector mesons such as $\phi(1020)$ and $K^{*0}(892)$. The spin state of a vector meson can be described by a 3×3 spin density matrix with unit trace. [10] The diagonal elements of this matrix, namely, ρ_{11}, ρ_{00} and ρ_{-1-1}, are probabilities for the spin component along a quantization axis to take the values of 1, 0, and -1 respectively. The quantization axis is a chosen axis onto which the projection of angular momentum has well-defined quantum numbers. When the three spin states have equal probability to be occupied, all three elements are 1/3 and there is no spin alignment. If $\rho_{00} \neq 1/3$, the probabilities of the three spin states along the quantization axis are different and there is a spin alignment.

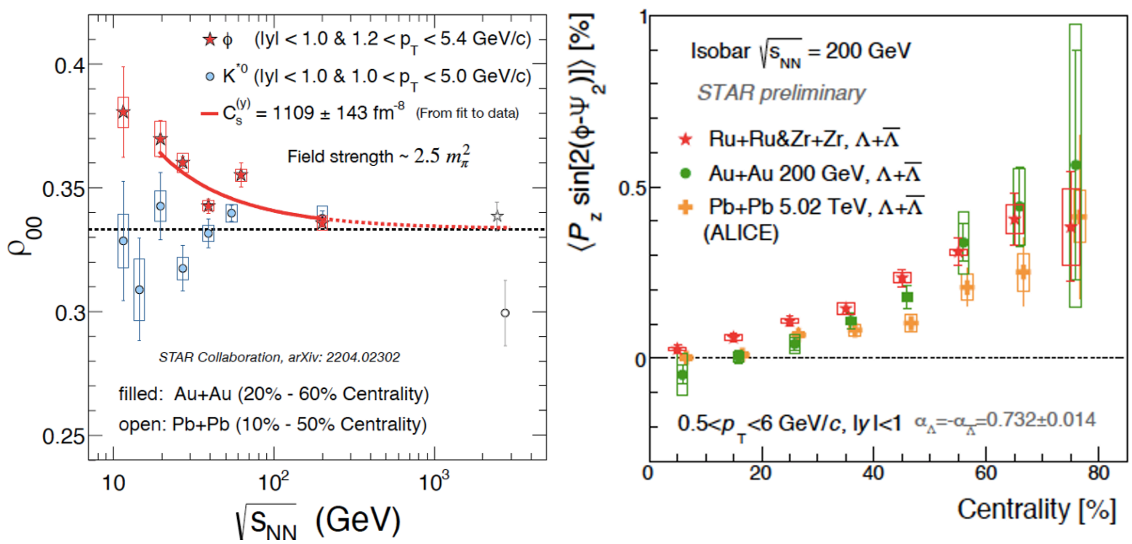

Figure 4: Left panel: Global spin alignment measurement of ϕ and K^{*0} vector mesons in Au+Au (Pb+Pb) collisions. The measured matrix element ρ_{00} is plotted as a function of beam energy for the ϕ and K^{*0} vector mesons within the indicated windows of centrality, transverse momentum p_T, and rapidity y. The two points on the right (Pb+Pb collisions at 2.76 TeV) are integrated over the ALICE collaboration results [?], with a p_T range of 1.0–5.0 GeV/c for ϕ and K^{*0}. The red solid curve is a fit to data in the range of $\sqrt{s_{\mathrm{NN}}}$ = 19.6 to 200 GeV, based on a theoretical calculation with a ϕ-meson field. [11] Right panel: Λ spin polarization along beam direction in isobaric collisions at 200 GeV, Au+Au at 200 GeV, and Pb+Pb at 5.02 TeV.

Hyperons are natural candidates to explore global spin polarization since in the parity violating weak decays of hyperons the momentum vector of the decay baryon is highly correlated with the hyperon spin. The first observation of positive polarization of Λ hyperons in the Beam Energy Scan-I provided evidence for the creation of the most vortical fluid ever observed. [12] In non-central collisions strong anisotropic flow can generate a non-zero vorticity along the beam axis. The vorticity and the corresponding polarization exhibits a quadrupole structure in the transverse plane. This polarization is characterized by the second harmonic sine component in the Fourier decomposition of the polarization along the beam axis (P_z). The P_z for Λ hyperons was measured by STAR and was found to have opposite sign compared to the hydrodynamic and transport model calculations, known as "spin puzzle". The introduction of shear induced polarization can reproduce the sign of P_z

indicating that it is sensitive to the hydrodynamic gradients as well as the dynamics of the spin degrees of freedom.

Figure 4 presents the ρ_{00} for ϕ and K^{*0} vector mesons in Au+Au collisions at beam energies between $\sqrt{s_{\rm NN}} = 11.5$ and 200 GeV. The ϕ-meson results are presented for transverse momentum $1.2 < p_T < 5.4$ GeV/c; ρ_{00} for this species is significantly above 1/3 for collision energies of 62 GeV and below, indicating finite global spin alignment. The ρ_{00} for ϕ mesons, integrated over beam energies of 62 GeV and below, is 0.3541 ± 0.0017 (stat.) ± 0.0018 (sys.); this is a significance of 8.4 σ for the ϕ-meson ρ_{00} to be above 1/3. Figure 4 also presents the beam-energy dependence of ρ_{00} for K^{*0} within $1.0 < p_T < 5.0$ GeV/c. We observe that ρ_{00} for K^{*0} is largely consistent with 1/3, in marked contrast to the case for ϕ. The surprisingly large positive deviation for ϕ meson in mid central collisions is consistent with a model which introduce polarization by a strong force field of vector meson.

Figure 4 right panel shows the Λ polarization along beam direction (P_z) as a function of centrality in isobaric collisions at 200 GeV, Au+Au at 200 GeV, and Pb+Pb at 5.02 TeV. The amplitude of the sine modulation tends to increase from central to peripheral collisions. The results hint at a colliding system size dependence rather than beam energy dependence.

Measurements sensitive to the initial state

Beam-energy dependence of anisotropic flow fluctuations and correlations

The multi-particle flow harmonics $v_n\{k\}$, for k=2, 4, and 6, obtained via multi-particle correlation methods [13,14] can give direct access to the event-by-event flow fluctuations. [15, 16] Also the flow-plane decorrelations (measured by $r_n(\eta)$) that are driven by the eccentricity decorrelations [17,18] are expected to be caused by (i) the effect of the initial state torque [19, 20], and (ii) hydrodynamic fluctuations [21] and expected to give information to the event-by-event flow fluctuations. In addition, correlations between the average transverse radial flow ($[p_T]$) and the v_n coefficients ($\rho(v_n^2, [p_T])$) could encode crucial information on the correlation between the size and the eccentricities in the initial state, and on the correlations of the strength of the hydrodynamic response with the flow coefficients. The ($\rho(v_n^2, [p_T]$) is given by [22–27]

$$\rho(v_n^2, [p_T]) = \frac{\mathrm{cov}(v_n^2, [p_T])}{\sqrt{\mathrm{Var}(v_n^2)}\sqrt{\mathrm{Var}([p_T])}}. \tag{1}$$

Consequently, extensive measurements of $v_n\{k\}$ and $\rho(v_n^2, [p_T])$ for different beam energies could help to disentangle the fluctuation and correlation contributions from their respective sources, as well as establish whether flow fluctuations and correlations depend on the temperature, T, baryon chemical potential, $\mu_{\rm B}$, or both. It could also provide unique supplemental constraints to distinguish between different initial-state models and reduce the fluctuations-related uncertainties associated with the extraction of $\eta/s(T, \mu_{\rm B})$.

Figure 5 provides a summary of the centrality dependence of $v_2\{2\}$ (a), $v_2\{4\}$ (b), $v_2\{6\}$ (c) and the ratio $v_2\{4\}/v_2\{2\}$ (d) for the respective beam energies as indicated. The $v_2\{4\}/v_2\{2\}$ ratios shown in Fig. 5 (d) suggest that within the given uncertainties, the flow

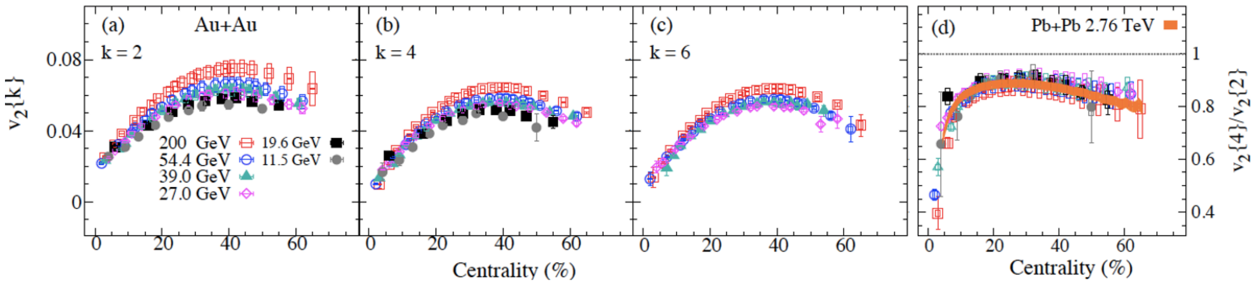

Figure 5: Comparison of the centrality dependence of the charged hadrons $v_2\{2\}$ (a), $v_2\{4\}$ (b), $v_2\{6\}$ (c), and the ratio $v_2\{4\}/v_2\{2\}$ (d), in the p_{T} range $0.2-4.0$ GeV/c for Au+Au collisions at $\sqrt{s_{\mathrm{NN}}}$ = 11.5–200 GeV. The vertical lines and the open boxes indicate the respective statistical and systematic uncertainties. The shaded band in (d) indicates the ratios obtained from the LHC measurements for the p_{T} range $0.2-3.0$ GeV/c for Pb+Pb collisions at $\sqrt{s_{\mathrm{NN}}}$ = 2.76 TeV [28].

.

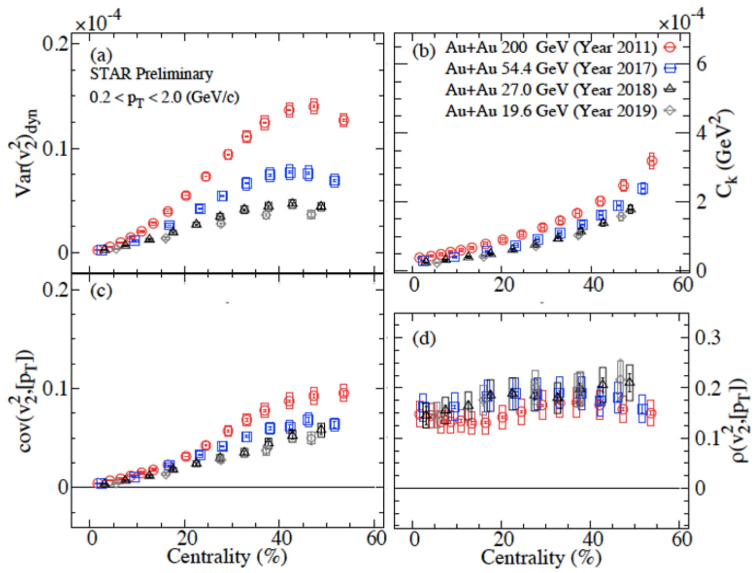

Figure 6: Comparison of the centrality dependence of the values for $\mathrm{Var}(v_n^2)_{dyn}$ (a), c_k (b), $\mathrm{cov}(v_n^2, [p_T])$ (c), and $\rho(v_n^2, [p_T])$ (d), measured for Au+Au collisions at $\sqrt{s_{\mathrm{NN}}}$ = 200, 54.4, 27 and 19.6 GeV.

fluctuations are weakly dependent on the beam energy, if at all, irrespective of the collision centrality. The magnitude and trend of these ratios are also comparable to those for the LHC measurements for Pb+Pb collisions at $\sqrt{s_{\mathrm{NN}}}$ = 2.76 TeV [28] and to the $\varepsilon_2\{4\}/\varepsilon_2\{2\}$ ratios, in central to mid-central collisions, shown in Fig. 5 (b). These results suggest that the flow fluctuations associated with the expansion dynamics do not change substantially over the beam energy range $\sqrt{s_{\mathrm{NN}}}$ = 11.5–2760 GeV.

Figure 6 shows the beam-energy dependence of $\mathrm{Var}(v_2^2)$ (a), c_k (b), $\mathrm{cov}(v_2^2, [p_T])$ (c), and $\rho(v_n^2, [p_T])$ (d). They indicate patterns which depend on beam energy. These results suggest that the beam energy dependence of $\mathrm{Var}(v_2^2)$ and $\mathrm{cov}(v_2^2, [p_T])$ could provide important con-

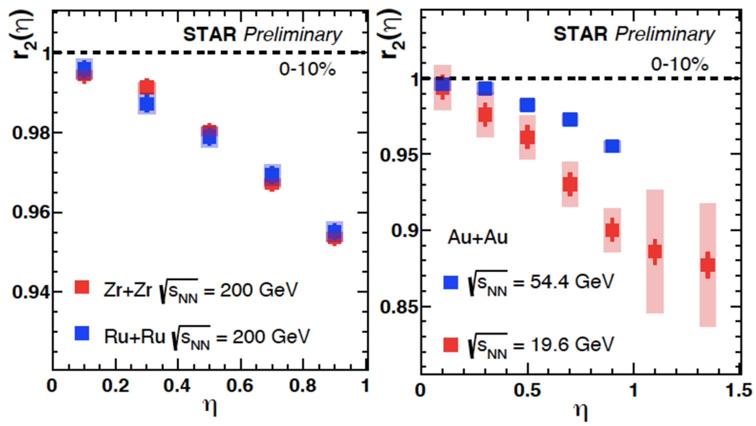

Figure 7: Comparison of the η dependence of the values for $r_n(\eta)$ for Au+Au collisions at $\sqrt{s_{\rm NN}}$ = 54.4 and 19.6 GeV.

straints for η/s while the measurements for $\rho(v_n^2, [p_T])$ provide complimentary constraints for the initial-state eccentricity and its fluctuations.

Figure 7 shows the beam-energy dependence of $r_n(\eta)$. They indicate patterns and values which depend on beam energy.

Nuclear deformation and neutron skin thickness measurements

Nuclear deformation and neutron skin thickness are fundamental properties of atomic nuclei that reflect the correlated nature of the dynamics of nucleons within a quantum many-body system. The majority of atomic nuclei possess an intrinsic deformation, most of which are an axial quadrupole, or ellipsoidal, deformation. Prior relativistic heavy-ion collision measurements from STAR reported strong signatures of nuclear deformation using detailed comparisons between Au+Au collisions and U+U collisions. [29] These measurements suggest that U+U collisions are much more deformed in their ground state. Consequently, we can say that detailed comparisons between different nuclei enabled us to examine the geometry of the colliding ions. [30–32]

Recently we analyzed the Ru+Ru and Zr+Zr collision data and found that they could be used to study the nuclear deformation [33, 34] as well as the neutron skin thickness. [35–37] Figure 8 shows the $N_{\rm trk}^{\rm offline}$, v_2, v_3, and $\langle\delta p_T^2\rangle/\langle p_T\rangle^2$ ratios between the isobar systems. All of them show non-monotonic centrality dependencies similar in shape to the theoretical prediction [33] that include effects of neutron skin as well as deformation parameters β_2 and β_3. Figure 9 shows the centrality dependence of the Ru+Ru/Zr+Zr ratio of $\langle p_T\rangle$ compared to the theoretical expectations. [37] It is shown that this ratio increases with the symmetry energy slope parameter $L(\rho_c)$ because the neutron skin effect, larger in Zr than in Ru, increases with $L(\rho_c)$. Such an effect is non-trivial and can reach as much as 0.5%. The data model comparison should help constrain the symmetry energy slope parameter and the β_2 and β_3 deformation parameters.

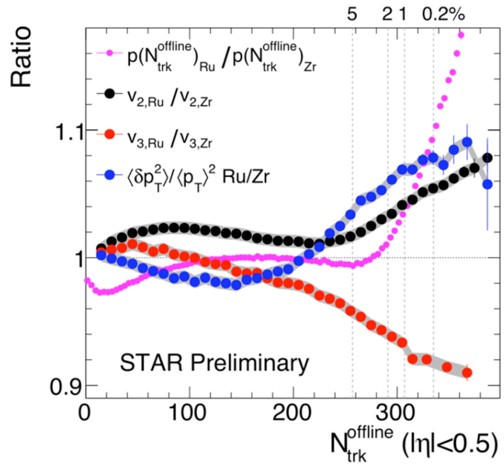

Figure 8: The N_{ch} dependence of the Ru+Ru/Zr+Zr ratio of $N_{trk}^{offline}$, v_2, v_3, and $\langle \delta p_T^2 \rangle / \langle p_T \rangle^2$.

.

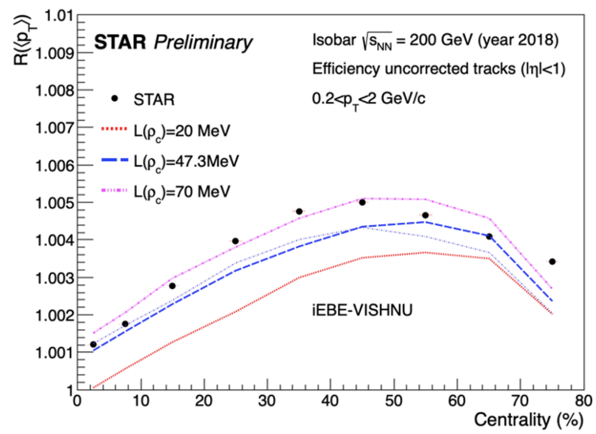

Figure 9: The centrality dependence of the Ru+Ru/Zr+Zr ratio of $\langle p_T \rangle$. The lines represent the theoretical predictions. [37]

.

Azimuthal anisotropy measurements of identified hadrons

Stronger constraints on transport and hydrodynamic model simulations can be achieved via investigating the azimuthal anisotropy of identified particles as a function of transverse momentum and collision centrality. Also, one can understand the initial conditions in heavy-ion collisions via varying the collision system size.

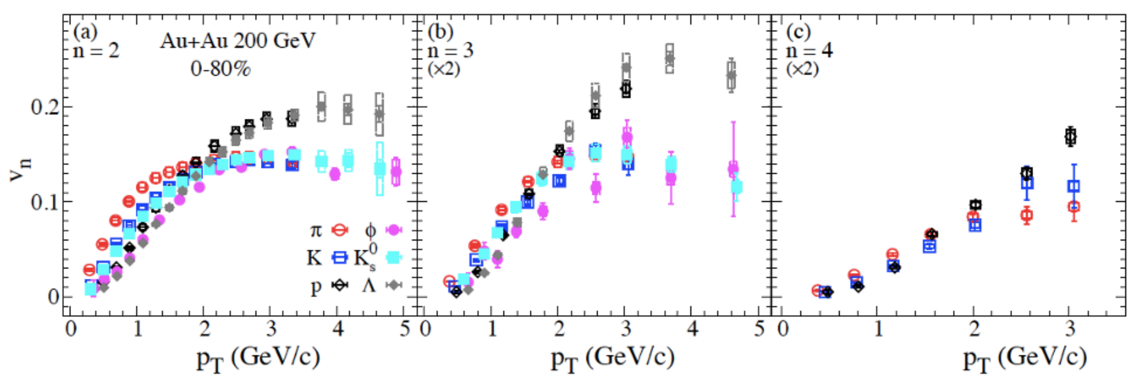

Figure 10: The transverse momentum dependence of the identified particle v_2 (a), v_3 (b), and v_4 (c) for 0—80% central Au+Au collisions at 200 GeV.

.

Recently we reported the results on flow coefficients of v_2 (a) and v_3 (b) of π, K, p, Λ, φ and K_s^0 and v_4 (c) of π, K and p for 0–80% central Au+Au collisions at $\sqrt{s_{\mathrm{NN}}}$ = 200 GeV. The measurements indicate similar increasing then flattening trends as a function of p_{T} in $v_{n=2,3,4}(p_T)$ for all particles shown. Also mass ordering at low p_{T} is observed for v_2, v_3, and v_4. The shapes of the flow harmonics for light and strange mesons are comparable, which suggests similar flow strength for u, d, and s quarks.

Charge dependent directed flow

In non-central heavy-ion collisions, the charged particles in the approaching nuclei can generate a substantial magnetic field. Theoretical calculations predicted that the magnetic field is large ($B \sim 10^{18}$ Gauss) but short lived. As noted above the presence of such a strong magnetic field can lead to novel QCD phenomena such as CME and CMW. To understand the Chiral phenomena, it is of utmost important to understand the initial magnetic field that could drives the charge separation. It was first proposed in [38] that the initial B-field can induce a measurable effect in the form of a charge-odd contribution to the directed flow coefficient (v_1). Experimental attempts have been made by STAR and ALICE by measuring charge dependent Δv_1 for D^0, $\overline{D^0}$ and inclusive charged hadron species, but the statistical significance of those measurements are marginal.

Recently, STAR reported a striking centrality dependence of the v_1 slope difference ($\Delta dv_1/dy$) of protons and anti-protons. The left panel of Fig. 11 presents centrality dependence of $\Delta dv_1/dy$ between proton and anti-proton in 200 GeV Au+Au and isobar collisions. It is observed that the $\Delta dv_1/dy$ changes sign from positive to negative from central to peripheral collisions. While the positive $\Delta dv_1/dy$ is consistent with expectation from transported quarks, the negative sign (with a significance of $\sim 5\sigma$) is qualitatively consistent with expectation from electromagnetic field induced effects, and can be explained by the dominance of the Faraday/Coulomb effect [38].

STAR also followed another novel approach to probe the electromagnetic fields by utilizing the hadrons with constituent quarks ($K^-, \bar{p}, \bar{\Lambda}, \phi, \Xi$ and Ω) that are produced in collisions, which avoids contributions from transported quarks. Under the assumptions of quark coalescence, $\Delta dv_1/dy$ is studied for various pairs of particle combinations corresponding to varying electric charge difference (Δq) and strangeness difference (ΔS). It is observed that the $\Delta dv_1/dy$ increases with Δq and ΔS and the increase is stronger for 27 GeV than for 200 GeV Au+Au collisions. The right panel of Fig. 11 presents $\Delta dv_1/dy$ as function of ΔS for 10–40% Au+Au collisions at 27 and 200 GeV. It is found that the PHSD calculations including electromagnetic fields can describe the charge-dependent splitting within uncertainties.

1.1.3 LFSUPC Highlights

The Light-flavor Spectra and Ultra-peripheral Collisions (LFSUPC) Physics Working Group (PWG) divides its efforts along six different lines of analysis: Light-charged particle (π, K, p) spectra identified through dE/dx and time-of-flight (TOF) information, strange-hadron spectra identified through the secondary vertex decay topology, light-nuclei spectra identified through dE/dx and TOF, hypernuclei identified through decay topology, di-lepton production, and ultra-peripheral collisions. Analysis efforts on the first five topics have focused on newly reconstructed/processed BES-II/FXT datasets (including two articles submitted for publication [], and five talks at Quark Matter 2022 []) and the submitted results be reviewed in section! 1.1.6.

A linearly polarized photon can be quantized from the Lorentz-boosted electromagnetic field of a nucleus traveling at ultra-relativistic speed. By utilizing this source of polarized photons, STAR is experimentally investigating the Breit-Wheeler process through the mea-

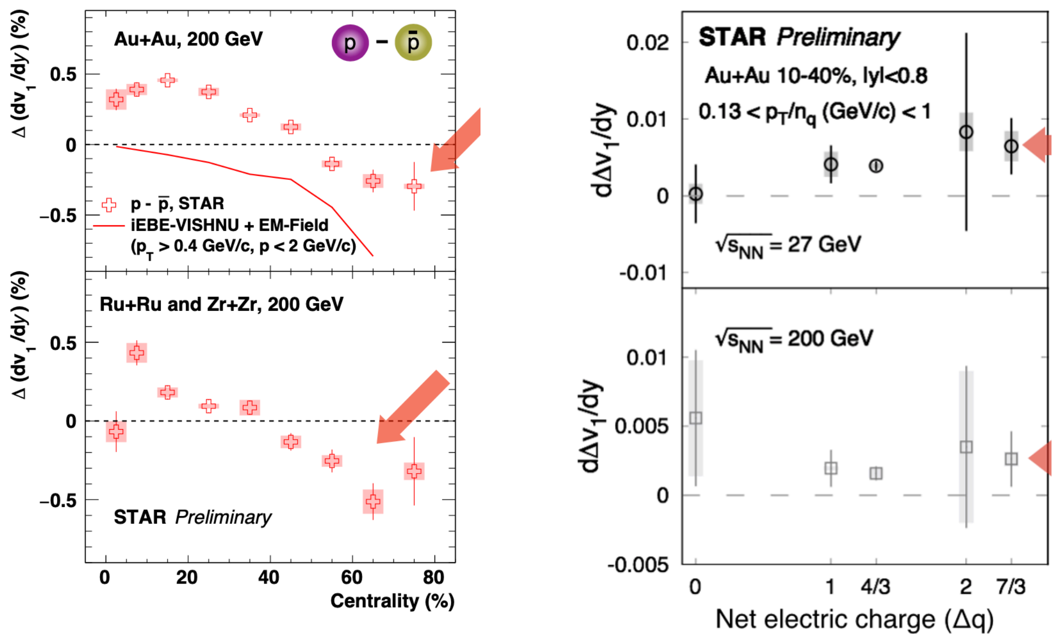

Figure 11: Left: $\Delta dv_1/dy$ as a function of centrality between proton and anti-protons in 200 GeV Au+Au and isobar (Ru+Ru and Zr+Zr) collisions. Right: $\Delta dv_1/dy$ as a function of electric charge difference (Δq) in 10–40% Au+Au collisions at 27 and 200 GeV.

.

surement of electron-positron pairs in ultraperipheral Au+Au collisions at $\sqrt{s_{NN}} = 200$ GeV. [39] The measurements reveal a large fourth-order angular modulation (a $\cos 4\Delta\phi$, as seen in fig. 12) in the angle (ϕ) between the transverse momentum of the pair and the transverse momentum of one of its daughters. The differential cross section as a function of e^+e^- pair transverse momentum $P_\perp$ peaks at low values (~ 30 MeV/c) and displays a significant centrality dependence. These features are consistent with QED calculations for the collision of linearly polarized photons quantized from the extremely strong electromagnetic fields generated by the highly charged Au nuclei at ultrarelativistic speed. The experimental results have implications for vacuum birefringence and for mapping the magnetic field which is important for emergent QCD phenomena.

When two relativistic heavy nuclei pass one another at a distance of a few nuclear radii, the photon from one nucleus may interact through a virtual quark-antiquark pair with gluons from the other nucleus forming a short-lived vector meson (e.g. ρ^0). STAR has studied diffractive photoproduction in Au+Au and U+U ultraperipheral collisions. [40] The polarization was utilized to observe a unique spin interference pattern in the angular distribution of $\rho \longrightarrow \pi^+\pi^-$ decays as seen in fig. 13. The observed interference is a result of an overlap of two wave functions at a distance an order of magnitude larger than the ρ^0 travel distance within its lifetime. The strong-interaction nuclear radii were extracted from these diffractive interactions (fig. 13 right panel), and found to be 6.53 ± 0.06 fm (^{197}Au) and 7.29 ± 0.08 fm

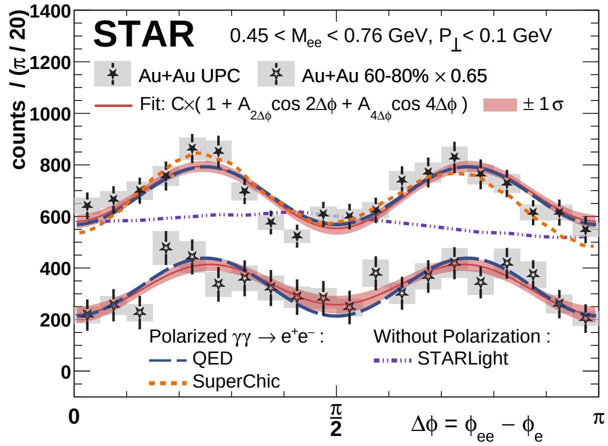

Figure 12: The $\Delta\phi = \phi_{ee} - \phi_e$ distribution from UPCs and 60-80% central collisions for $M_{ee} > 0.45$ GeV with calculations from QED, STARLight, and SuperChic3.

(^{238}U), larger than the nuclear charge radii. The observable is demonstrated to be sensitive to the nuclear geometry and quantum interference of non-identical particles.

Understanding gluon density distributions and their modifications in nuclei are among the most important goals of nuclear physics. Diffractive vector meson production measured in UPCs at heavy-ion colliders has provided a new tool for probing the gluon density. STAR has measured Jψ photoproduction off the deuteron in UPCs at $\sqrt{s_{NN}} = 200$ GeV in d+Au collisions. [41] The differential cross section as a function of momentum transfer $-t$ is shown in fig. 14. In addition, cross section data with a neutron tagged in the deuteron-going Zero-Degree Calorimeter is found to be consistent with the expectation of incoherent diffractive scattering at low momentum transfer. Theoretical predictions based on the Color Glass Condensate (CGC) saturation model and the Leading Twist Approximation (LTA) nuclear shadowing model are compared with the data quantitatively. A better agreement with the saturation model has been observed. With the current measurement, the results are found to be directly sensitive to the gluon density distribution of the deuteron and the deuteron breakup process, which provides insights into the nuclear gluonic structure.

Copious amounts of dielectrons can also be produced by heavy-ion collisions that interact with enough energy to produce a quark-gluon plasma. As this super-heated phase of QCD matter cools, the QGP radiates e^+e^- pairs. Since leptons may travel away from the medium unimpeded by the dense environment of strongly interacting matter, they provide a pristine probe of the temperature of the emitting thermal source. Further, since the dielectrons are not effected by the collective motion of the rapidly expanding fireball, their spectrum is not blue-shifted but instead reveal the true temperature of the medium.

Various phases of the cooling QCD matter may be individually probed by analyzing dielectrons with various invariant masses, with higher invariant mass pairs corresponding to early times, and lower invariant masses corresponding to later times. In the low mass region ($0.2 < M_{ee} < 1.2$ GeV$/c^2$), thermal dielectrons are predicted to originate predominately from radiation of the in-medium ρ^0 meson in the hadronic phase. In this region, the temperature

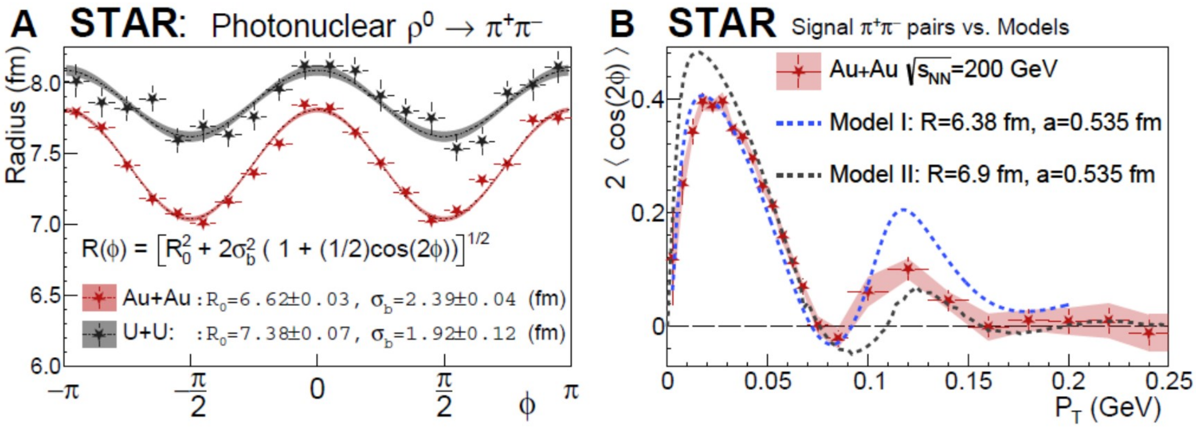

Figure 13: (Left) Radial parameter as a function of the ϕ angle for Au+Au and U+U with an empirical second order modulation fit. (Right) Comparison between the fully corrected Au+Au distribution and theoretical calculations that include the photon's linear polarization and two source interference effects.

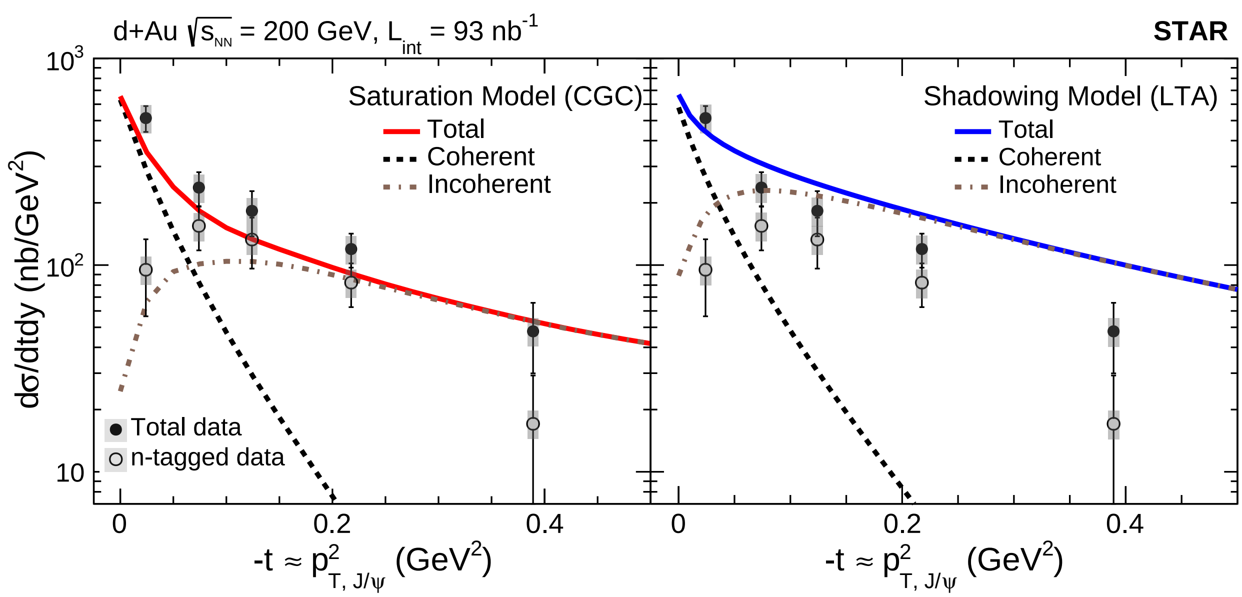

Figure 14: Theoretical predictions of the CGC saturation model (left) and the LTA nuclear shadowing model(right). Coherent and incoherent contributions from the two models are presented separately by the dashed lines.

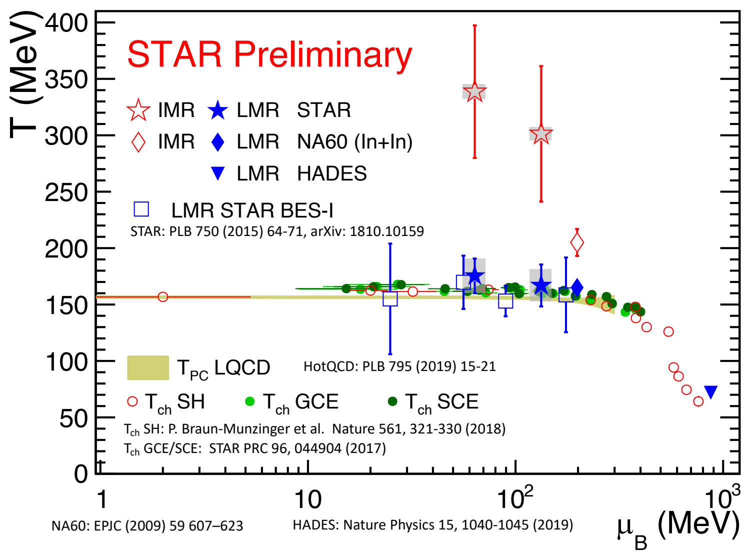

Figure 15: Extracted temperatures vs. baryonic chemical potential (μ_B). Temperatures extracted from the in-medium ρ^0 (blue squares) dominant region and the QGP (open red square) dominant region from STAR data are compared to the temperatures extracted from NA60 data (blue rhombus and open red rhombus) and HADES (blue triangle). Temperatures extracted from the statistical models (GCE, SCE, SH) are shown as solid dots and open circles. The QCD pseudo-critical temperature T_C vs. μ_B at small chemical baryon density predicted by lattice QCD calculations are shown at dotted blue lines.

are extracted to be 167 ± 20 MeV and 174 ± 15 MeV, in $\sqrt{s_{NN}}$ = 27 GeV and 54.4 GeV Au+Au collisions, respectively. These measured temperatures are surprisingly consistent with the temperature (165 ± 4 MeV) extracted from the NA60 data measured in $\sqrt{s_{NN}}$ = 17.3 GeV In+In collisions – a much lower collision energy and a significantly smaller collision system. These temperature measurements provides the first strong evidence that the in-medium ρ^0 mesons are dominantly produced around a constant temperature close to the phase transition boundary temperature (156 ± 1.5 MeV) as predicted by lattice QCD calculations. On the other hand, in the higher mass region ($1.0 < M < 2.9$ GeV/c^2), the temperatures is extracted to be 301 ± 60 MeV and 338 ± 59 MeV, in $\sqrt{s_{NN}}$ = 27 GeV and 54.4 GeV Au+Au collisions, respectively. These temperature values, which are well above the phase transition temperature, indicate that these thermal dielectrons originate predominantly from radiation of the ultra-hot phase of deconfined QCD matter, the quark-gluon plasma.

1.1.4 Heavy-flavor Measurements

Heavy-flavor (HF) quarks are produced predominately via initial hard scatterings of partons in p(A)+p(A) collisions. Kinematic distributions and hadronization probabilities of HF quarks in Å collisions can be different than those in p+p collisions due to interactions of HF quarks with the QGP medium. Understanding these differences allows us to determine properties of the QGP.

STAR has recently published two papers on heavy flavor production: 1) the measurement of cold nuclear matter effects for inclusive J/ψ in p+Au collisions at $\sqrt{s_{\rm NN}}$ = 200 GeV [42] and 2) measurement of inclusive electrons from open heavy-flavor hadron decays in p+p collisions at $\sqrt{s}$ = 200 GeV [43].

J/ψ production has been found to be suppressed in Au+Au collisions at RHIC top energies [44, 45]. Such a suppression can be caused by the color screening of the $c\bar{c}$ potential by the QGP medium, and by cold nuclear matter (CNM) effects from e.g., nuclear parton distribution functions, energy loss or absorption in the nucleus, and interaction with co-moving hadrons. Therefore, in order to precisely determine the suppression due to the color screening effect alone, it is important to quantify the CNM effects. The former paper reports the nuclear modification factor R_{pA} for inclusive J/ψ at mid-rapidity through the dimuon decay channel. At low $p_{\rm T} < 2$ GeV/c, a suppression of approximately 30% is observed indicating that the CNM effects contribute significantly to the J/ψ suppression in heavy-ion collisions in this $p_{\rm T}$ range. On the other hand, higher $p_{\rm T}$ J/ψ (> 3 GeV/c) are observed to be minimally affected by the CNM effects. This provides evidence that the strong J/ψ suppression in Au+Au collisions at higher $p_{\rm T}$ is due to the presence of the QGP. The measurement provides also further constrains on model calculations of the CNM effects for J/ψ. The latter paper provides a high precision reference for measurements of $R_{\rm AA}$ for inclusive electrons from open-charm and -bottom hadron decays in heavy-ion collisions. Compare to the previous measurements, the precision was significantly improved for $p_{\rm T} > 6$ GeV/c, which provides also additional constrains on theoretical pQCD calculations.

In heavy-ion collisions, in addition to the color screening effect that suppresses the J/ψ

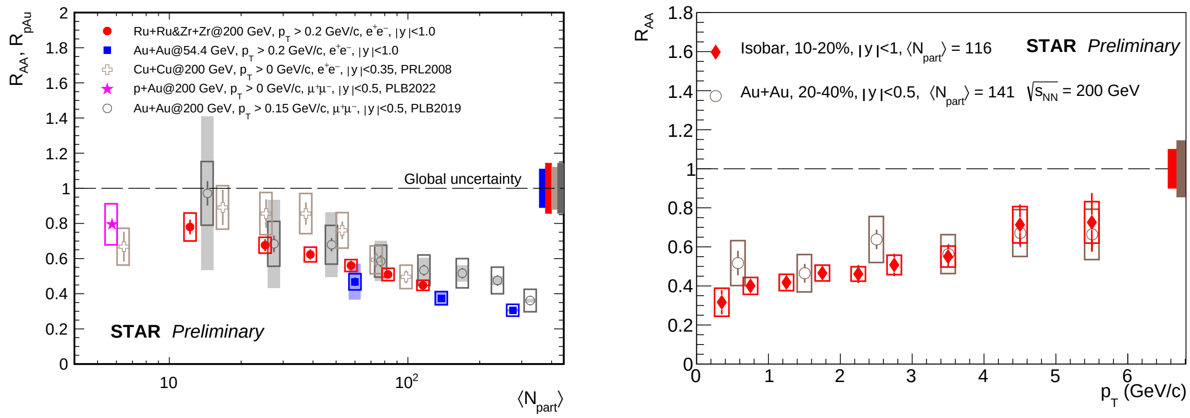

Figure 16: Left: R_{AA} vs. $N_{part.}$ for inclusive J/ψ. Red circles: Ru+Ru and Zr+Zr collisions at $\sqrt{s_{\mathrm{NN}}} = 200$ GeV (this analysis), blue squares: Au+Au collisions at $\sqrt{s_{\mathrm{NN}}} = 54.4$ GeV, open circles: Au+Au collisions at $\sqrt{s_{\mathrm{NN}}} = 200$ GeV [45], open crosses: Cu+Cu collisions at $\sqrt{s_{\mathrm{NN}}} = 200$ GeV [46], magenta star: p+Au collisions at $\sqrt{s_{\mathrm{NN}}} = 200$ GeV [42]. Right: R_{AA} vs. p_{T} for inclusive J/ψ at $\sqrt{s_{\mathrm{NN}}} = 200$ GeV. Red diamonds: Ru+Ru and Zr+Zr for 10–20% centrality, open circles: Au+Au for 20–40% centrality. [45]

production, J/ψ can be produced from recombination of uncorrelated c and $\bar{c}$ in the QGP. STAR has recently reported preliminary result on the nuclear modification factor R_{AA} of inclusive J/ψ in Ru+Ru and Zr+Zr collisions. The result is extracted in the dielectron channel from isobar data at $\sqrt{s_{\mathrm{NN}}} = 200$ GeV collected in 2018. Isobar collisions being smaller (larger) collision systems compare to Au+Au (Cu+Cu) allow us to study the dependence of the hot nuclear matter effects - color screening vs recombination - on the medium size and geometry at the same collisions energy. As can be seen in Fig. 16(left) R_{AA} decreases with N_{part} and no significant species dependence is observed. The result is also consistent with the preliminary R_{AA} in Au+Au collisions at $\sqrt{s_{\mathrm{NN}}} = 54.4$ GeV, confirming the previous observation of no significant energy dependence of the J/ψ suppression at RHIC that suggests a partial cancellation of the J/ψ suppression due to the color screening effect by J/ψ produced from recombination. R_{AA} as a function of p_{T} in isobar collisions shows increasing trend in central and mid-central collisions. When compared to the Au+Au measurement at similar $\langle N_{\mathrm{part}} \rangle$ the two results are in agreement, see Fig. 16(right).

1.1.5 Jet Measurements

Jet is a useful tool to study the properties of QGP. With the help of newly developed techniques and significantly increased statistics in recent RHIC runs, STAR has explored various aspects of jet properties in heavy ion and pp collisions. In this section, we first briefly discuss recent publications of jet measurements in p+p and Au+Au collisions and then highlight new studies with tagged jets, system size dependence of jet quenching and a new data driven way of estimating jet formation time with a study of jet splittings.

Recent published results:

As jets are composite objects built from parton showers and fragmentation, they contain rich substructure information that can be exploited via jet finding algorithms [47]. These algorithms typically employ an iterative clustering procedure that generates a tree-like structure, which upon an inversion, gives access to a jet's substructure at different steps along the cluster tree. The most common toolkit for such measurements is SoftDrop grooming [48] which employs a Cambridge/Aachen (C/A) re-clustering of a jet's constituents and imposes a criterion at each step as we walk backwards in the de-clustered tree. The SoftDrop kinematic variables are,

$$z_g = \frac{\min(\mathrm{p}_{\mathrm{T},1}, \mathrm{p}_{\mathrm{T},2})}{p_{T,1} + p_{T,2}} > z_{\mathrm{cut}} \left(\frac{R_g}{R_{jet}}\right)^{\beta}; R_g = \Delta R(1,2). \quad (2)$$

Where $z_{cut} = 0.1$ is a momentum fraction threshold and β is the angular exponent which in our analysis is set to zero [48]. The subscripts 1 and 2 represent the constituent jet pairs in re-clustered tree with C/A algorithm. These parameters make the SoftDrop observable comparable to theoretical calculations, and at the infinite momentum limit they converge to the DGLAP splitting functions. A recent STAR publication highlighted in PRC presents the differential measurements of jet substructure and partonic energy loss in Au+Au and p+p collisions through substructure observables of SoftDrop z_g, R_g, and subjet momentum fraction (z_{SJ}) and opening angle (Θ_{SJ}) [49]. In these studies, no significant modifications of the subjet observables are found in Au+Au collisions compared to p+p collisions, implying vacuum- like splittings, with a possible interpretation that energy loss in this population of high momentum di-jet pairs is due to soft medium-induced gluon radiation from a single color-charge as it traverses the medium.

STAR also published the groomed and ungroomed jet mass in p+p collisions at $\sqrt{s} = 200$ GeV, together with comparisons to leading-order Monte Carlo event generators predictions [50]. In this study, while STAR-tuned PYTHIA-6 reproduced the data, LHC tunes of PYTHIA-8 and HERWIG-7 failed to do so. The agreement with STAR-tuned PYTHIA-6 and disagreement with LHC tunes were also previously observed in z_g and R_g measurements of jets with a varying resolution parameters of R=0.2-0.6 for a wide transverse momentum range of $15 < p_{\mathrm{T,jet}} < 60 Gev/c$ in p+p collisions at $\sqrt{s} = 200$ GeV [51]. These measurements establish a baseline for future jet mass measurements in heavy-ion collisions at RHIC and compliment LHC measurements at lower kinematic region to provide further tuning inputs to further constrain Monte Carlo simulations.

Preliminary STAR results on system size dependence of inclusive hadron suppression, jet formation time in p+p, flavor dependence of jet shape modification, intra-jet broadening and γ_{dir}+jet (h+jet) acoplanarity measurements are discussed in the following paragraphs.

System size dependence of inclusive charged hadrons suppression: During the recent runs, RHIC facility provided us an opportunity to study system size dependence of jet quenching.

The left panel of Fig. 17 shows the inclusive charged hadron suppression (R_{AA}) as a

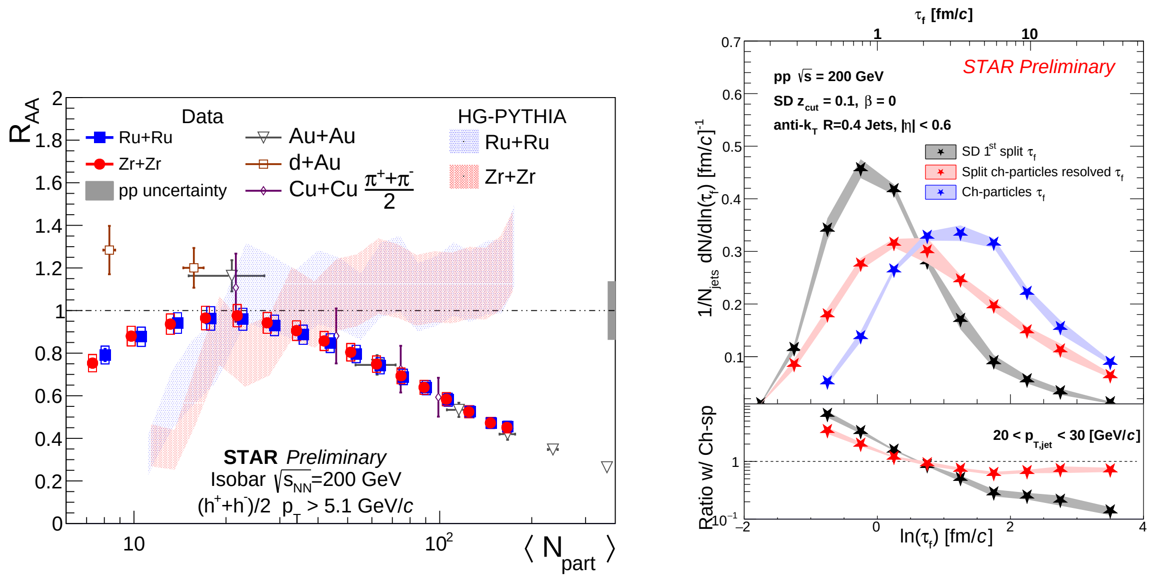

Figure 17: Left: Inclusive charged hadron $R_{\rm AA}$ in different collision systems. Right:Formation time distributions in p+p collisions.

function of $N_{\rm part}$ for Ru+Ru, Zr+Zr, d+Au, Cu+Cu and Au+Au collisions at $\sqrt{s_{\rm NN}} = 200$ GeV. For Isobar (Ru+Ru, Zr+Zr) collisions, the charged hadrons are selected with $p_{\rm T} > 5.1$ GeV/c. It is observed that $R_{\rm AA}$ is independent of collision system for $N_{\rm part} > 20$ with a decreasing trend. For $\rm N_{part} < 20$. The HG-Pythia, that can describe the centrality bias observed at the LHC [52, 53], overpredicts the suppression observed in peripheral Ru+Ru and Zr+Zr collisions. Further studies including high-$p_{\rm T}$ hadron selection bias and differential measurement on path length dependence are ongoing.

Jet formation time and jet substructure: STAR has recently explored the multi-scale nature of jet evolution in p+p collisions. Utilizing the SoftDrop splitting momentum fraction (z) and opening angle (θ), it is possible to define a formation time at a given split as

$$\tau = \frac{1}{z(1-z)\theta^2 E}, \tag{3}$$

where E is the combined energy of the two objects used to calculated the z and θ. The black markers in the right panel of Fig. 17 are the formation times at the first SoftDrop splits for $R = 0.4$ jets with $20 < p_T < 30$ GeV/c. These splits correspond to mostly early times with the most probable value of the distribution being smaller than 1 fm/c. These splittings are expected to be predominantly perturbative in nature , which is supported by the fact that the substructure observables, such as z and θ, are well described by perturbative calculations. The blue markers in the same figure are the formation times calculated using the leading and sub-leading charged particles within the jet. This formation time is independent of the jet clustering history. As seen in the figure, charged-particle formation time shifts significantly towards later times as compared to the first SoftDrop splits. Via the red markers we introduce the resolved splittings which correspond to the formation time calculated from the jet clustering tree wherein the two leading charged-particles are first separated into two individual prongs. The bottom right panel of Fig. 17 shows the ratios of the clustering formation time distributions with respect to that of the charged particles. Comparison of the different splits highlights the transition from pQCD to npQCD. Resolved splits show a similar shape as the charged particle splits at large formation time occurring in the predominantly non-perturbative region. These observables are presented in p+p collisions as an outline for measurements in Au+Au collisions, leading towards a first ever space-time study of jet quenching phenomena.

Flavour dependence of jet shape modification: Jets with heavy quarks are expected to probe the full evolution of the QGP as they are produced early in the collision via hard partonic scatterings. To characterize the jet-medium interactions and distinguish between competing energy loss mechanisms, mass dependence of the energy loss needs to be also studied. Heavy-flavor mesons within a jet is expected to be sensitive to the production mechanism of mesons, energy loss and diffusion of heavy flavor quarks in the QGP.

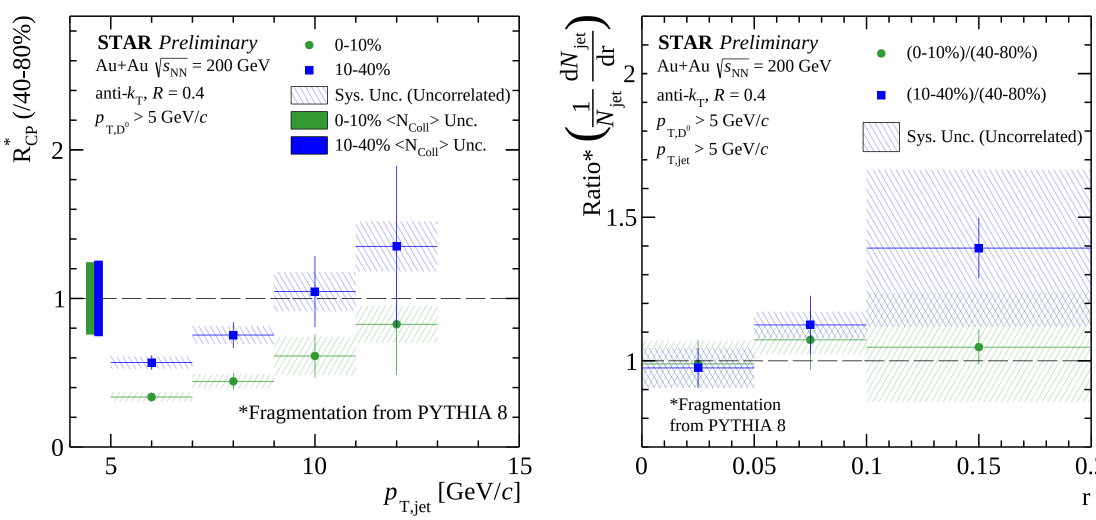

Figure 18: Left: Nuclear modification factor of D^0-tagged jet. Right: Ratio of radial distribution of D^0-tagged jets in central and mid-central collisions to that in peripheral Au+Au collisions.

The nuclear modification factor for jets that include a D^0 meson with $p_\mathrm{T} > 5$ GeV/c is shown in the left panel of Fig. 18. As can be seen in this figure, jets that are formed in the most central collisions appear to be more suppressed than those in mid-central collisions, especially for the lower p_T ranges of $5 < p_\mathrm{T} < 10$ GeV/c. The radial profile, i.e., the distribution of D^0 meson the distance from the jet axis (r), is also studied. As shown in the right panel of Fig. 18, the ratio of the radial distributions in most central collisions to that in most peripheral ones is consistent with unity within uncertainties. Theoretical calculations [54] predict a small amount of diffusion that is also consistent in our measurement.

Jet R dependence of suppression and intra-jet broadening: In STAR, the $\gamma_{\rm dir}/\pi^0$ discrimination method using BEMC and BSMD detectors as well as uncorrelated background jet mitigation procedure using Mixed Event techniques are well calibrated to measure both $\gamma_{\rm dir}$+jet and π^0+jet in p+p and Au+Au collisions.

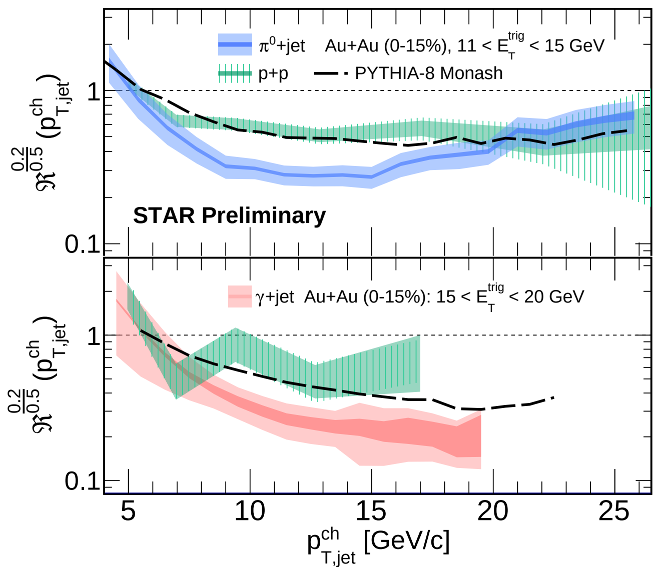

Figure 19: Yield ratio of recoil jets with $R = 0.2$ over $R = 0.5$ as a function of jet $p_{\rm T,jet}^{\rm ch}$. Upper and lower panels are for π^0+ jet and $\gamma_{\rm dir}$+ jet, respectively. Green bands are for p+p collisions.

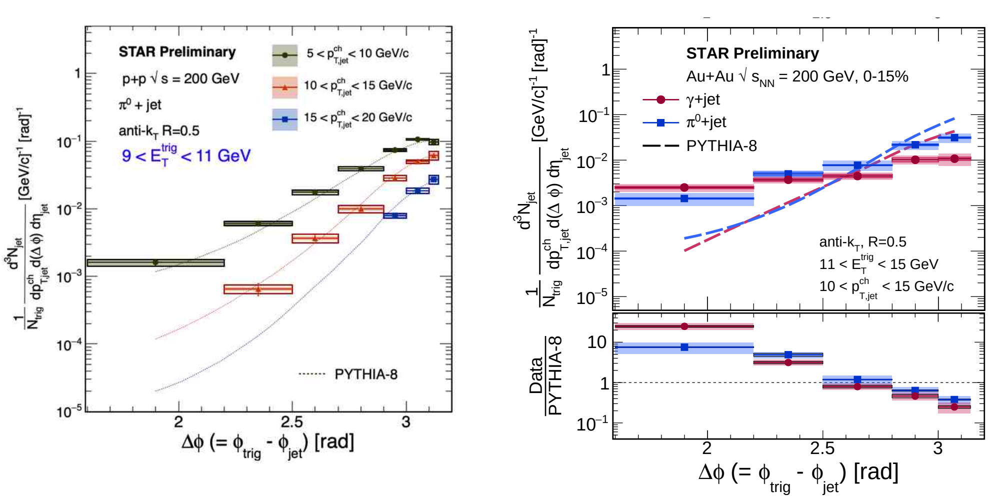

Figure 20: The $\gamma_{\rm dir}$+jet (red) and π^0+jet (blue) acoplanarity measurements in p+p(left) and central Au+Au (right) collisions $\sqrt{s_{\rm NN}} = 200$ GeV. Dashed lines represent PYTHIA-8 predictions.

To investigate the resolution parameter dependence of the suppression of recoil jets, the jet yield ratios of jets that are reconstructed with $R = 0.2$ to those that are reconstructed with $R = 0.5$ as a function of $p_{\rm T,jet}^{\rm ch}$ ($R^{\rm small-R}_{\rm large-R}$) for π^0+jet (upper panel) and $\gamma_{\rm dir}$+jet (bottom panel) shown in Fig. 19. The differences of $R^{\rm small-R}_{\rm large-R}$ in Au+Au to those in p+p implies intra-jet broadening in heavy-ion collisions due to jet quenching.

$\gamma_{\rm dir}$+jet and π^0+jet acoplanarity in p+p and Au+Au collisions: At Born level, dijet or $\gamma_{\rm dir}$+jet productions in p+p collisions are back-to-back in azimuth. However, soft-gluon radiation and NLO effects introduce acoplanarity (decorrelation) between dijet or $\gamma_{\rm dir}$+jet even in vacuum. The acoplanarity measurement in p+p is important studying QCD effects. This also provides a baseline for similar measurement in heavy-ion collisions. Semi-inclusive π^0+jet (alike dijet) $\Delta\phi$ distributions in p+p collisions are reported in the left panel Fig. 20. Here $\Delta\phi$ represents the difference between trigger $\phi^{\rm trig}$ and recoil jet $\phi^{\rm jet}$. The π^0 triggers are selected between $9 < E_{\rm T}^{\rm trig} < 11$ GeV. The $\Delta\phi$ distributions of three different recoil jet $p_{\rm T,jet}^{\rm ch}$ ranges ($5 < p_{\rm T,jet}^{\rm ch} < 10$ GeV/c, $10 < p_{\rm T,jet}^{\rm ch} < 15$ GeV/c, and $15 < p_{\rm T,jet}^{\rm ch} < 20$ GeV/c) are compared with the PYTHIA-8, and a good agreement is seen. Due to limited statistics, this measurement in p+p collisions for $\gamma_{\rm dir}$+jet is not feasible.

In heavy-ion collisions, jet deflection is considered one of the consequences of the jet quenching phenomenon. We report both $\gamma_{\rm dir}$+jet and π^0+jet $\Delta\phi$ measurements with $11 < E_{\rm T}^{\rm trig} < 15$ GeV and $10 < p_{\rm T,jet}^{\rm ch} < 15$ GeV/c for $R = 0.5$ in the right Fig.20. Striking differences in the acoplanarity distributions between PYTHIA-8 and Au+Au collisions are seen. A similar observation is made by ALICE for h+jet measurement in higher kinematic range. Such measurements with extended $E_{\rm T}^{\rm trig}$ and recoil jet $p_{\rm T,jet}$ ranges are important understanding the nature of the acoplanarity of jets produced in p+p and Au+Au collisions.

Aforementioned semi-inclusive jet (like $\gamma_{\rm dir}$+jet and h+jet) measurements and sub-structure observables with extended kinematic coverage need high statistics data for precision and incisive conclusions to understand the inner-working of QGP. Upcoming Run23-25 p+p and heavy-ion collision data taking will be crucial in achieving this goal and a detailed discussion with projections can be found in Section 2.1.

1.1.6 BES-II Results

Data taking for the BES-II/FXT program has completed, with all data acquisition targets being achieved or exceeded. Figure 21 shows a bar chart of the BES-II/FXT data sets recorded and compares the new datasets to the older BES-I data. Also shown in the figure are the energies for which we have overlapping coverage from both the collider and fixed-target programs. The bars are plotted as a function of μ_B, which illustrates the range of μ_B and the step size. For clarity, the collision energies ($\sqrt{s_{\rm NN}}$) are indexed along the top edge of the plot.

Data acquisition is only the first step in the process of data analysis. The calibrations team must carefully perform run-by-run calibrations for all the detector systems prior to 'production', which turns all of the raw information into tracks, time-of-flight, or energy signals (depending on the detector sub-system) which can be used by the analyzers. Following production, run-by-run QA is carried out to exclude runs for which the detector was not performing optimally. It was expected that roughly 5% of the acquired data volume would

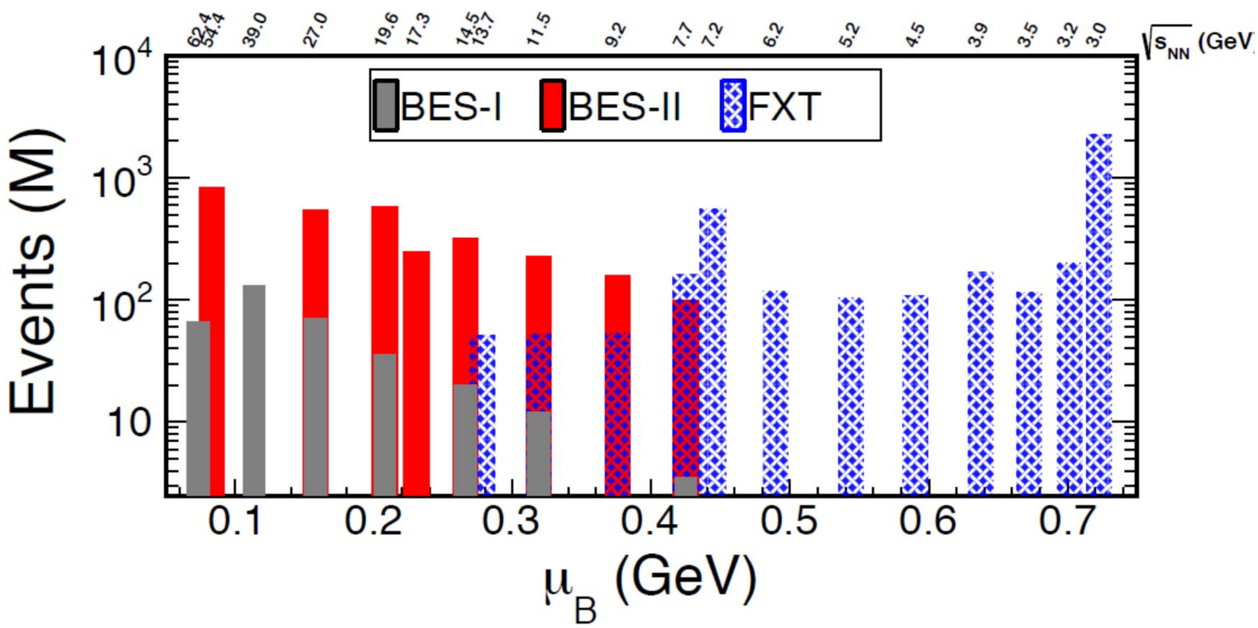

Figure 21: A summary of the good events acquired for the various collision energies (translated to μ_B). The BES-II collider data sets are shown in red bars. The FXT data sets are shown in hashed blue bars. For comparison the BES-I data sets are shown in grey bars. Note that the top FXT energy ($\sqrt{s_{\rm NN}}$= 13.7 GeV) does not quite overlap with the 14.6 GeV collider system; that FXT energy is a single beam energy of 100 GeV, which is the top energy to which RHIC can accelerate Au ions. Also note that the 54.4 GeV "BES-II" does not quite overlap with the 62.4 GeV BES-I system; the 54.4 GeV data were taken in 2017 parasitically with the first year of operation of the CeC program. This system is informally considered to be a part of the BES-II program. Likewise the data for the 7.2 GeV FXT system were parasitically acquired during single beam operations of CeC in 2018-2021.

be rejected in run-by-run QA. For the collider data sets, for which run-by-run QA has been completed, we are indeed finding roughly 5% of the runs to be rejected. The fixed-target data sets from 2019 and 2020 are passing run-by-run QA at a much higher rate, most likely because they were all very short runs, and therefore the chance that a key detector component fails during the run is much smaller. Following run-by-run QA, the centrality team defines the basic event-by-event selection cuts (mostly to eliminate pile-up events) and defines the centrality selections correcting for vertex position and luminosity. Figure 22 shows a table of the energies acquired and status of each data set. This status is indicated with respect to where it stands in the sequence of pre-analysis steps. For the data sets which are available to the analysis teams, those listed as final are data sets for which papers have been published or submitted. Those listed as preliminary are data sets for which preliminary results have been shown at conferences.

The PAC recommended that STAR pay particular attention to analyses which are sensitive to critical behavior. It was recommended "that the STAR collaboration does everything possible to ensure that the analysis of critical observables in the Beam Energy Scan, such

2018	**Start**	**Stop**	**Good**	**Target**	**Status**
27 GeV	May 10th	June 17th	555 M	700 M	Final
3.0 FXT	May 30th	June 4th	258 M	100 M	Final
7.2 FXT	June 11th	June 12th	155 M	none	Final
2019	**Start**	**Stop**	**Good**	**Target**	
19.6 GeV	Feb 25th	April 3rd	478 M	400 M	Preliminary
14.6 GeV	April 4th	June 3rd	324 M	310 M	Post-prod QA
3.9 FXT	June 18th	June 18th	52.7 M	50 M	Produced
3.2 FXT	June 28th	July 2nd	200.6 M	200 M	Post-prod QA
7.7 FXT	July 8th	July 9th	50.6 M	50 M	Produced
200 GeV	July 11th	July 12th	138 M	140 M	Produced
2020	**Start**	**Stop**	**Good**	**Target**	**Status**
11.5 GeV	Dec 10th	Feb 24th	235 M	230 M	*Summer*
7.7 FXT	Jan 28th	Jan 29th	112.5 M	100 M	Produced
4.5 FXT	Jan29th	Feb 1st	108 M	100 M	Produced
6.2 FXT	Feb 1st	Feb 2nd	118 M	100 M	Produced
5.2 FXT	Feb 2nd	Feb 3rd	103 M	100 M	Produced
3.9 FXT	Feb 4th	Feb 5th	117 M	100 M	Produced
3.5 FXT	Feb 13th	Feb 14th	115.6 M	100 M	Produced
9.2 GeV	Feb 24th	Sep 1st	161.8 M	160 M	*Summer*
7.2 FXT	Sep 12th	Sep 14th	317 M	None	*Fall*
2021	**Start**	**Stop**	**Good**	**Target**	**Status**
7.7 GeV	Jan 31st	May 1st	100.9 M	100 M	*May*
3.0 FXT	May 1st	June 28th	2103 M	2.0 B	*Fall*
9.2 FXT	May 6th	May 6th	53.9 M	50 M	*Fall*
11.5 FXT	May 7th	May 7th	51.7 M	50 M	*Fall*
13.7 FXT	May 8th	May 8th	50.7 M	50 M	*Fall*
17.3 GeV	May 25th	June 7th	256.1 M	250 M	*Fall*
7.2 FXT	June 3rd	July 3rd	88.6 M	None	*Fall*

Figure 22: A summary of the BES-II collider and FXT data sets taken from 2018-2021. The Start and Stop columns indicate the periods during which each data set was acquired. The Good and Target columns indicate the number of good events taken and requested. The Status column indicates where a given data set is in the analysis sequence.

as proton number cumulants, are carried out by at least two independent groups within STAR". In addition to independent analyses, STAR has also decided not to release preliminary results from such analyses, similar to the recommendation for the Chiral Magnetic Effect analysis of the Isobar data. STAR has so far identified two lines of analysis that are understood to address critical behavior: the net-proton cumulants, which are sensitive to proton fluctuations, and the light nuclei ratios which are sensitive to neutron fluctuations. Good progress has been made in both of these analysis efforts, although only the net-proton fluctuations observed in the 3 GeV fixed-target data have matured to the point of journal submission. For that analysis, a seminar at BNL was scheduled to coincide with submission of the results to PRL (December 2, 2021). The first presentation of these results at a conference was at the recent QM2022.

The BES-II collider and FXT proposals identified a series of key physics analyses which would have sensitivity to: formation of the QGP, the first order phase transition, the critical point, and chirality. For all of these analyses, the collaboration determined the required event count needed to make a definitive measurement and those events counts were used to set the required number of events at each energy (see the "Target" numbers in Fig. 22). Analysis teams have been identified to address all of these topics. Figure 23 shows the status of all of these various analysis efforts. Significant progress has been made on all topics, with the exception of the Chiral Magnetic Effect (CME). In the case of the expected CME analyses, the teams with the requisite expertise have been fully committed to the analysis of the isobar data and have not yet had a chance to turn their efforts to the new BES-II datasets which are available for physics analyses. For all other expected lines of analysis first results have been either published, submitted for publication, presented at QM2022, or are under review within their respective PWGs. To date, publications have come from the 3 GeV FXT data. Although some preliminary results have been shown for the 27, 19.6, and 14.6 GeV collider datasets, it is expected that publications will wait until all of the collider energies are available for physics analysis, which is expected to be in the Fall (see Fig. 22. The 3 GeV FXT data set was unique enough to justify stand-alone papers. The next wave of papers showing FXT results will cover the energy scan range from 3.0 to 7.7 GeV as those energies are all now available. The three high energy FXT runs and the high statistics 3.0 GeV FXT datasets from 2021 will be the last produced. Those data sets are for specialized analyses which will likely result in another set of papers.

In this highlights section, we will focus on the published or submitted results from the $\sqrt{s_{\rm NN}} = 3$ GeV FXT system. Taken as a group, these results all show a marked change from the behavior seen at collider energies of 7.7 GeV and above. It is not unexpected to see such a significant change as the purpose of the FXT scan was a extend to reach of the energy scan to regions for which QGP formation was likely not to be expected.

The first and second-order azimuthal anisotropy parameters v_1 and v_2 of light nuclei (p, d, t, He^3, and He^4 were studied for 3 GeV Au+Au collisions. [55] The mid-rapidity slopes of the directed flow (v_1) were found to scale with atomic mass number as shown in Fig. 24. The elliptic flow (v_2) behavior is found to be unlike that at higher collision energies. The v_2 values at mid-rapidity for all light nuclei are negative and no scaling is observed with the atomic

Physics Analysis	Status of Analyses
R_{CP} up to p_T = 5 GeV/c	Physics Working Group
Elliptic Flow	Published March 10, 2022
Chiral magnetic Effect	
Directed Flow	Published February 1, 2022
Azimuthal Femtoscopy	Physics Working Group
Net-proton Kurtosis	Submitted December 2, 2021
Di-leptons	QM2022 talk
Lambda Polarization	Published December 21, 2021
Multi-strange Baryons	Submitted December 23, 2021
Hyper-nuclei	Submitted October 18, 2021
Rapidity Dependent Spectra	QM2022 talks (2)

Figure 23: A summary of the key physics analyses which were listed in the BES-II collider and FXT proposals and the status of the efforts on each line of analysis.

mass number. Calculations using the Jet AA Microscopic Transport Model (JAM), with baryonic mean-field plus nucleon coalescence, are in good agreement with the observations, implying baryonic interactions dominate the collective dynamics in 3 GeV Au+Au collisions at RHIC.

The partonic scaling of the elliptic flow (v_2) seen for various mesons and baryons at 200 GeV was seen as a signature of QGP formation and an indication that collective flow was established during the partonic phase of the collisions. It is expected that at lower energies this scaling should break down when one is below that produce a QGP phase. The v_2 results for hadrons are shown in Fig. 25 for $\sqrt{s_{\mathrm{NN}}}$ = 3, 27, and 54.5 GeV Au+Au collisions. While at the two higher energy mid-central collisions the number-of-constituent-quark (NCQ) scaling holds, at 3 GeV the v_2 at mid-rapidity is negative for all hadrons and NCQ scaling is absent. It is not unexpected, or necessarily conclusive, that the v_2 is negative at the 3 GeV energy as this had been seen in previous measurements and has been described as “squeeze-out". What is more telling, and had not been previously measured, is that the scaled v_2 of pions is so different from that of protons and kaons. JAM and UrQMD model calculations with baryonic mean-field potential reproduce the observed negative values of v_2 for protons at 3 GeV. This indicates that partonic interactions no longer dominate and baryonic scatterings take over. This observation is clear evidence that predominantly hadronic matter is created in such low energy collisions.

As a function of collision energy, a rise and then fall of the net-proton C_4/C_2 (or $\kappa|\sigma^2$) has been predicted to indicate the critical behavior expected near the critical point in the QCD phase diagram. Results from BES-I had shown an enhancement at 7.7 GeV and

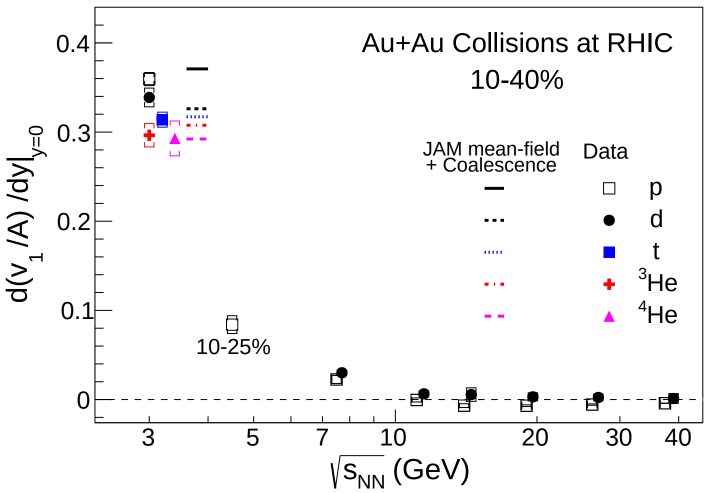

Figure 24: Light nucleus scaled v_1 slopes as a function of collision energy in 10-40% mid-central Au+Au collisions.

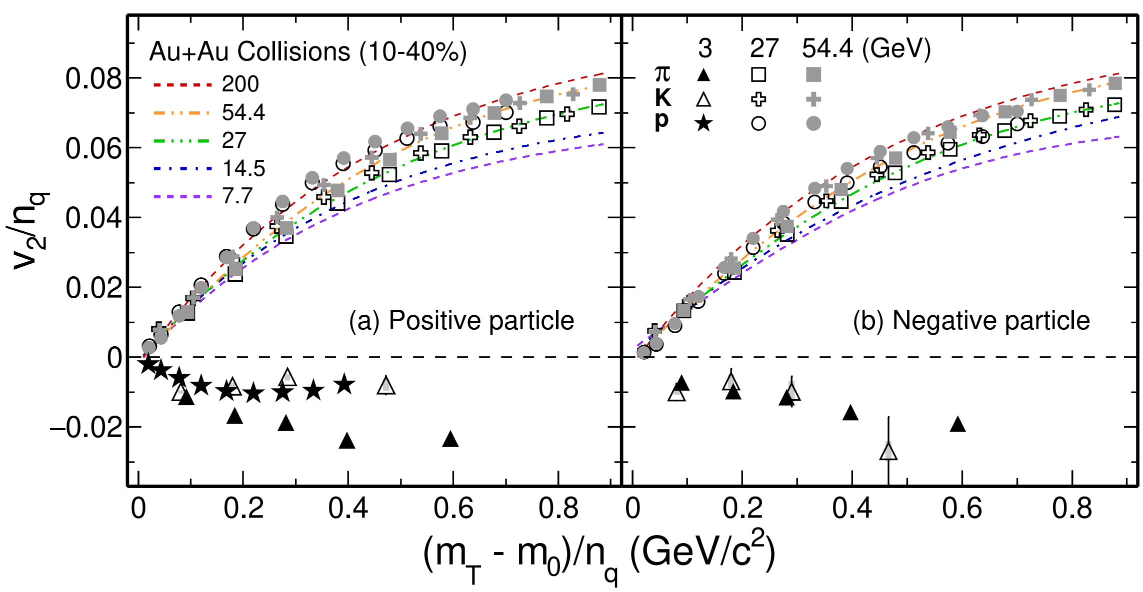

Figure 25: v_2 scaled by the number of constituent quarks, v_2/n_q, as a function of scaled transverse kinetic energy ($(m_T - m_0)/n_q$) for pions, kaons and protons from Au+Au collisions in 10-40% centrality at $\sqrt{s_{\rm NN}} = 3$, 27, and 54.4 GeV for positively charged particles (left panel) and negatively charged particles (right panel).

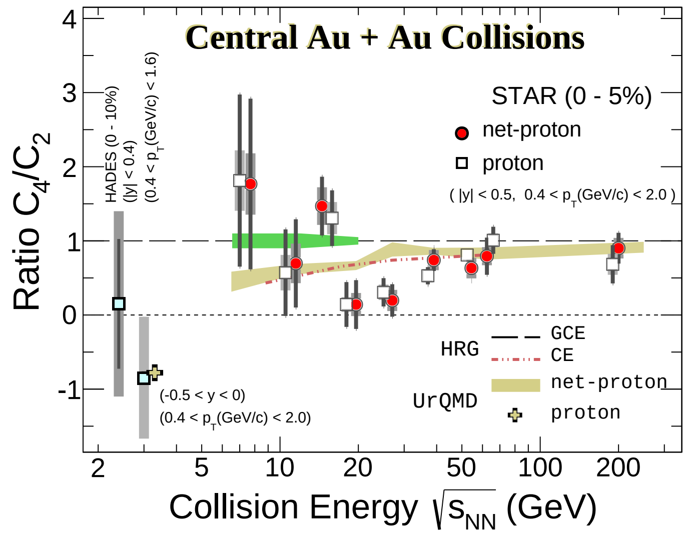

Figure 26: Collision energy dependence of the ratios of cumulants, C_4/C_2, for proton (squares) and net-proton (red circles) from top 0–5% Au+Au collisions at RHIC. The points for protons are shifted horizontally for clarity. The new result for proton from $\sqrt{s_{\rm NN}} = 3.0$ GeV collisions is shown as a filled square. HADES data of $\sqrt{s_{\rm NN}} = 2.4$ GeV 0–10% collisions is also shown. Results from the HRG model and transport model UrQMD are shown.

a subsequent fall around 20 GeV. In order to determine if the value observed above the Poisson baseline is a peak it is necessary both to remeasure that point with high precision and also to carefully measure points at both higher and lower energies. At very low energies, where QGP formation is not expected, the C_4/C_2 signal should be consistent with baseline expectations. HADES has completed a measurement at $\sqrt{s_{\rm NN}} = 2.4$ GeV, and their final result is below the Poisson baseline, albeit with large uncertainty, as shown in Fig. 26. Also shown in this figure is the new STAR result at $\sqrt{s_{\rm NN}} = 3.0$ GeV. [56] The STAR result is well below the Poisson baseline and even negative. By comparing the STAR result to a UrQMD model, which has no phase transition, but does include baryon conservation, we conclude that this energy regime is dominated by hadronic interactions.

Global hyperon polarization, P_H, in Au+Au collisions over a large range of collision energy, $\sqrt{s_{\rm NN}}$ was recently measured and successfully reproduced by hydrodynamic and transport models with intense fluid vorticity of the QGP. While a naive extrapolation of data trends suggests a increasing P_H as the collision energy is reduced, the behavior of P_H at very low energy is unknown. STAR has recently measured the polarization of Λ hyperons along the direction of global angular momentum in Au+Au collisions at $\sqrt{s_{\rm NN}} = 3$ GeV as shown in Fig. 27. [57] The observation of substantial polarization in these collisions may require a reexamination of the viscosity of any fluid created in the collision, of the thermalization timescale of rotational modes, and of hadronic mechanisms to produce global polarization.

Strange hadron yields as well as the ratios in Au+Au collisions at $\sqrt{s_{\rm NN}}\bar{3}$ GeV were mea-

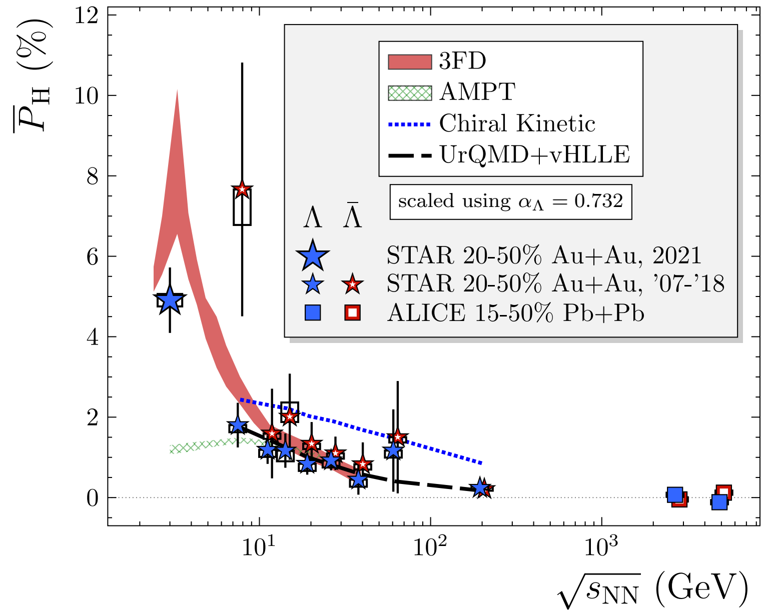

Figure 27: Global Hyperon (Λ) polarization as a function of $\sqrt{s_{\rm NN}}$ in mid-central heavy-ion collisions. The trend of increasing P_H with decreasing $\sqrt{s_{\rm NN}}$ is maintained at the low energy for $\sqrt{s_{\rm NN}} = 3$ GeV.

sured. [58] The 4π yields and ratios are compared to thermal model and hadronic transport model predictions. At this collision energy, as shown in Fig. 28, the thermal model with grand canonical ensemble (GCE) under-predicts the ϕ/K^- and ϕ/Ξ^- ratios while the result of canonical ensemble (CE) calculations reproduce the ratios with correlation lengths r_c of 3-4 fm. Thermal calculations with GCE work well for strangeness production in high energy collisions. The change to CE at 3 GeV implies a different medium property at high baryon density.

In relativistic heavy-ion collisions, hypernuclei form when hyperons (mostly Λs coalesce with neutrons and protons to form nuclei. The study of such exotic nuclei allows one to better understand the hyperon-nucleon interaction and to determine if the lifetime of the hyperon is affected as it is bound into a nucleus. Thermal models have predicted that the maximum yield of hypernuclei should occur in the collision energy range covered by the STAR FXT program. Precision measurements of hypernuclei ${}^3_\Lambda H$ ${}^4_\Lambda H$ were obtained from Au+Au collisions at $\sqrt{s_{\rm NN}} = 3.0$ GeV. [57] Their lifetimes are measured to be 221±15(stat.)±19(syst.) ps for ${}^3_\Lambda H$ and 218±6(stat.)±13(syst.) ps for ${}^4_\Lambda H$. Figure 29 shows the p_T-integrated yields compared to model calculations. The thermal model, using the canonical ensemble for strangeness, describes the ${}^3_\Lambda H$ yield well, while underestimating the ${}^4_\Lambda H$ yield. Transport models, combining baryonic mean-field and coalescence (JAM) or utilizing dynamical cluster formation via baryonic interactions (PHQMD) for light nuclei and hypernuclei production, approximately describe the measured yields. These new measurements provide means to precisely assess the understanding of the fundamental baryonic interactions with strange quarks, which can impact our understanding of more complicated systems involving hyperons, such

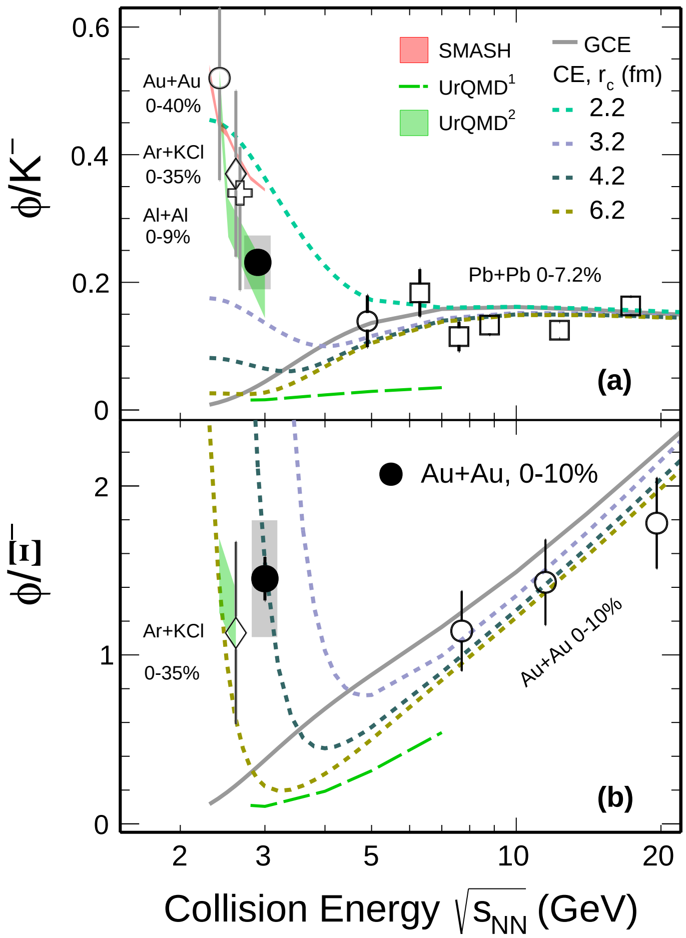

Figure 28: ϕ/K^{-} (top) and ϕ/Ξ^{-} (bottom) ratio as a function of collision energy, $\sqrt{s_{NN}}$. The solid black circles show the new STAR measurements. Data from other energies and/or collision systems are shown with open. The grey solid line represents a THERMUS calculation based on the Grand Canonical Ensemble (GCE) while the dotted lines depict calculations based on the Canonical Ensemble (CE) with different values of the strangeness correlation radius (r_c). The green dashed line, green shaded band and the solid red line show transport model calculations from UrQMD1, UrQMD2, and SMASH.

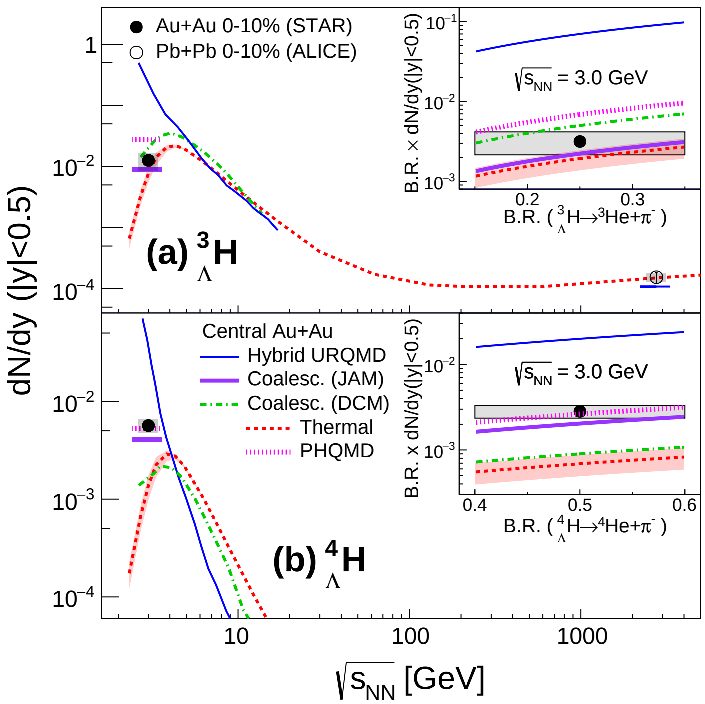

Figure 29: (Top) $^{3}_{\Lambda}H$ and (bottom) $^{4}_{\Lambda}H$ yields at $|y| < 0.5$ as a function of collision energy in central heavy-ion collisions. The solid black circle represent the new STAR measurements while the lines represent theoretical calculations.

as the interior of neutron stars or exotic hypernuclei.

1.2 Highlights from the Spin and Cold QCD Program

Introduction

The goal of the STAR Cold QCD program is to probe the spin and flavor structure of the proton and understand the role of spin in Quantum Chromodynamics, exploiting the unique capability of RHIC to provide longitudinally and transversely polarized $p+p$ collisions at multiple energies. Measurements with longitudinal beam polarizations have given new insights into the helicity structure of the proton, while measurements with transverse polarizations have provided new ways to probe polarized parton distribution functions in the collinear and transverse momentum dependent frameworks. This program is complemented by studies of polarized $p+p$ elastic scattering and central exclusive production, in which a far-forward proton is detected intact.

Since 2009, RHIC STAR has completed several highly successful polarized $p+p$ runs both at $\sqrt{s} = 200$ GeV and $\sqrt{s} = 500/510$ GeV. Moreover, $p+$Au and $p+$Al data sets with a transversely polarized proton beam have been recorded in 2015 at $\sqrt{s} = 200$ to address important physics problems, including the underlying non-perturbative mechanism responsible for large forward transverse single spin asymmetries, the ridge phenomenon and the possible onset of gluon saturation effects. Table 3 summarizes the STAR sampled luminosity and the luminosity averaged beam polarization as measured by the hydrogen jet (H-jet) polarimeter.

Table 3: Summary of polarized p+p and p+A running periods at RHIC since 2009, including center-of-mass energy, STAR's integrated luminosity and the average beam polarization for blue (B) and yellow (Y) beams from the H-jet polarimeter.

Year	System	$\sqrt{s}$ (GeV)	Recorded Lumi. (pb^{-1})	Polarization Orientation	B/Y $\langle P \rangle$ (%)
2009	p+p	200	25	Longitudinal	55/55
2009	p+p	500	10	Longitudinal	39/39
2011	p+p	500	12	Longitudinal	48/48
2011	p+p	500	25	Transverse	48/48
2012	p+p	200	22	Transverse	61/56
2012	p+p	510	82	Longitudinal	50/53
2013	p+p	510	300	Longitudinal	51/52
2015	p+p	200	52	Transverse	53/57
2015	p+p	200	52	Longitudinal	53/57
2015	p+Au	200	0.45	Transverse	60/–
2015	p+Al	200	1	Transverse	54/–
2017	p+p	510	320	Transverse	55/55
2022	p+p	510	400	Transverse	52

Since the last PAC meeting, there are three very mature analyses, which have either been accepted, submitted or are about to be submitted for publication. One analysis on di-jet spin asymmetry which probes the contribution of gluon spin to the proton spin has been accepted to Phys. Rev. D. [59] Another which investigates non-linear gluon effects has been submitted to Phys. Rev. Lett. [60] and is in the second round of journal review. Finally, the analysis of the Collins asymmetry which is sensitive to transversity and the Collins fragmentation function is nearing submission to Phys. Rev. D. Additionally, the Sivers dijet analysis, which is sensitive the the quark Sivers functions have just formed GPC, which will work to have these results published in Phys. Rev. Lett.

Inclusive Jet and Dijet A_{LL}

Studies of the polarized gluon distribution function ($\Delta g(x)$) of the proton to gain deeper insight into its spin structure and dynamics, have been possible due to the unique longitudinally polarized proton-proton collision data provided by RHIC.

The STAR experiment collected several longitudinally polarized p+p collision data sets, mainly dedicated to studying $\Delta g(x)$, which can be accessed by measuring the longitudinal double-spin asymmetry (A_{LL}) of inclusive jet and dijet production. The data were collected at center-of-mass energies of 200 GeV [61–63] and 510 GeV [64] at mid-rapidity, allowing

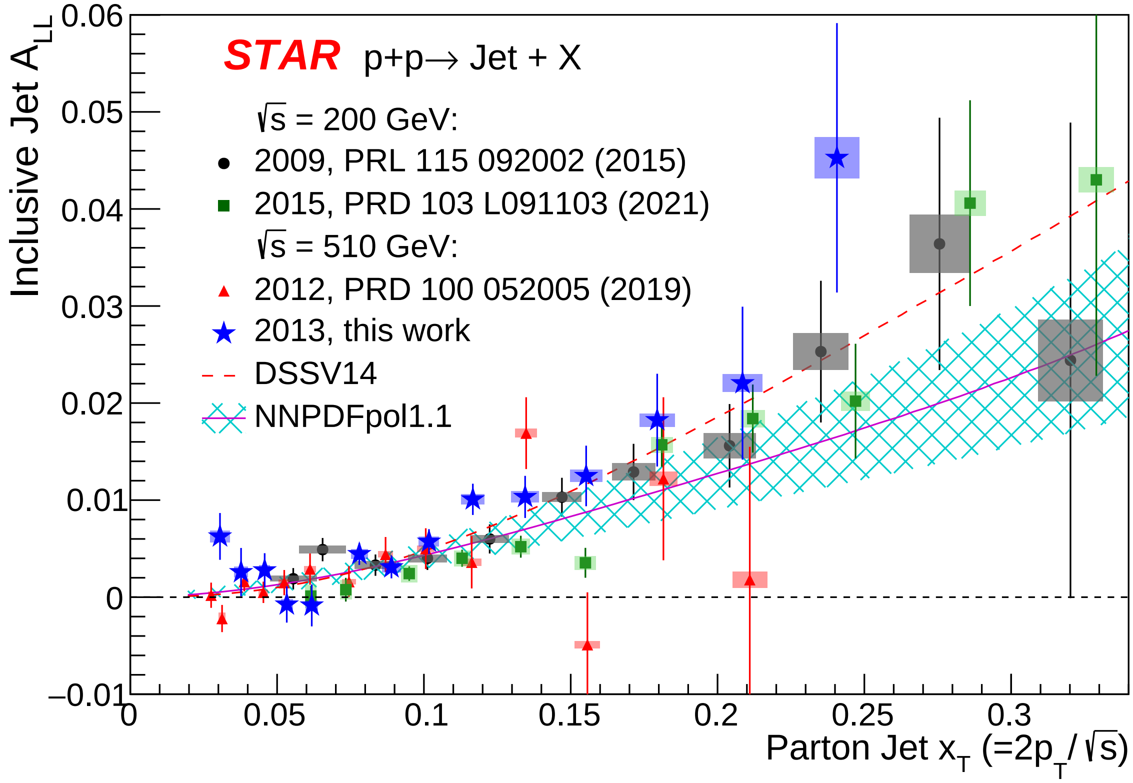

Figure 30: Inclusive jet A_{LL} versus x_T, compared to previous STAR results at $\sqrt{s} = 200$ GeV [61,63] and 510 GeV [64], and evaluations from DSSV14 [65] and NNPDFpol1.1 (with its uncertainty) [66] global analyses. The vertical lines are statistical uncertainties. The boxes show the size of the estimated systematic uncertainties. Scale uncertainties from polarization (not shown) are $\pm 6.5\%$, $\pm 6.6\%$, $\pm 6.4\%$ and $\pm 6.1\%$ from 2009 to 2015, respectively.

to probe a broader kinematic coverage in the partonic momentum fraction x. In 2015, the STAR concluded the collection of longitudinally polarized proton-proton collision data.

The recently published results on longitudinal double-spin asymmetry for inclusive jet and dijet production in polarized proton collisions at $\sqrt{s} = 510$ GeV in Phys. Rev. D [59], provides the last STAR A_{LL} measurements for inclusive jets at mid-rapidity, with data collected in 2013. These measurements complement and improve the precision of previous STAR measurements at the same center-of-mass energy that probe the polarized gluon distribution function at partonic momentum fraction $0.015 < x < 0.25$. The inclusive jet measurements A_{LL}, as shown in Figure 30, are in agreement with previous STAR measurements and with predictions from current next-to-leading-order global analyses. [65, 66]

Additionally, results for dijet production are presented in Fig. 31. These measurements provide a better determination of the functional form of $\Delta g(x)$, compared to inclusive observables, because better constraints on the underlying kinematics. At leading order, the dijet invariant mass is proportional to the square root of the product of the partonic momen-

Table 4: The four dijet topology bins A-D.

Bin	η_3 and η_4 Regions	Physics description
A	$0.3 < \|\eta_{3,4}\| < 0.9$; $\eta_3 \cdot \eta_4 > 0$	Forward-Forward
B	$\|\eta_{3,4}\| < 0.3$; $0.3 < \|\eta_{4,3}\| < 0.9$	Forward-Central
C	$\|\eta_{3,4}\| < 0.3$	Central-Central
D	$0.3 < \|\eta_{3,4}\| < 0.9$; $\eta_3 \cdot \eta_4 < 0$	Forward-Backward

tum fractions, $M_{inv} = \sqrt{sx_1x_2}$, and the pseudorapidity sum of the two jets is proportional to the logarithmic ratio of the x values, $\eta_3 + \eta_4 \propto \log(x_1/x_2)$ [1]. The individual jets in a dijet were separated into three pseudorapidity regions: forward $0.3 < \eta < 0.9$, central $-0.3 < \eta < 0.3$, and backward $-0.9 < \eta < -0.3$. The A_{LL} measurements for dijets are presented in four topology bins A-D (Table 4), as in [64], which allows discrimination between symmetric and asymmetric collisions in terms of the partonic momentum fractions x_1 and x_2. With a redesigned and optimized set of triggers in 2013, we were able to increase the statistics in the low dijet mass region by approximately an order of magnitude, which is critical to enable a controlled extrapolation of the polarized gluon distribution function in this gluon-rich region, with x down to 0.015. Preliminary results of dijet measurements from 2012 [67] and 2013 [68] data at intermediate-pseudorapidity, will probe even lower values of x. These high precision measurements motivate the natural step forward for an Electron Ion Collider in order to study the gluon-rich region of the proton in even greater detail.

Di-Hadron Correlations

The STAR Collaboration recently submitted a paper [60] on measurements of back-to-back azimuthal correlations of di-π^0s in p+p, p+Al, and p+Au collisions at a center-of-mass energy of 200 GeV. The forward π^0s ($2.6 < \eta < 4.0$) were reconstructed from the STAR forward meson spectrometer (FMS), with data recorded in 2015.

The correlation function is defined as $C(\Delta\phi) = \frac{N_{\rm pair}(\Delta\phi)}{N_{\rm trig} \times \Delta\phi_{\rm bin}}$, where $N_{\rm pair}$ is the yield of the correlated trigger and associated π^0 pairs, $N_{\rm trig}$ is the trigger π^0 yield, $\Delta\phi$ is the azimuthal angle difference between the trigger π^0 and associated π^0, and $\Delta\phi_{\rm bin}$ is the bin width of $\Delta\phi$ distribution. After the mixed event correction is applied, the correlation function is fitted with two individual Gaussians at the near- and away-side peak, together with a constant for the pedestal in the whole $\Delta\phi$ range. The area of the away-side peak used to describe the suppression, is defined as the integral of the correlation function from $\Delta\phi = \pi/2$ to $\Delta\phi = 3\pi/2$ after pedestal subtraction. The corresponding width is defined as the σ of the away-side peak according to the fit.

We observe a clear suppression of the correlated yields of back-to-back π^0 pairs in p+Al and p+Au collisions compared to the p+p data at low $p_{\rm T}$, see the top panel of Fig. 32. The suppression disappears at high p_T where x (Q^2) is not sufficiently small to reach the nonlinear regime (bottom panel of Fig. 32). These results are the first measurements of

[1] the kinematics of the initial partons and final jets are denoted by subscripts 1,2 and 3,4, respectively

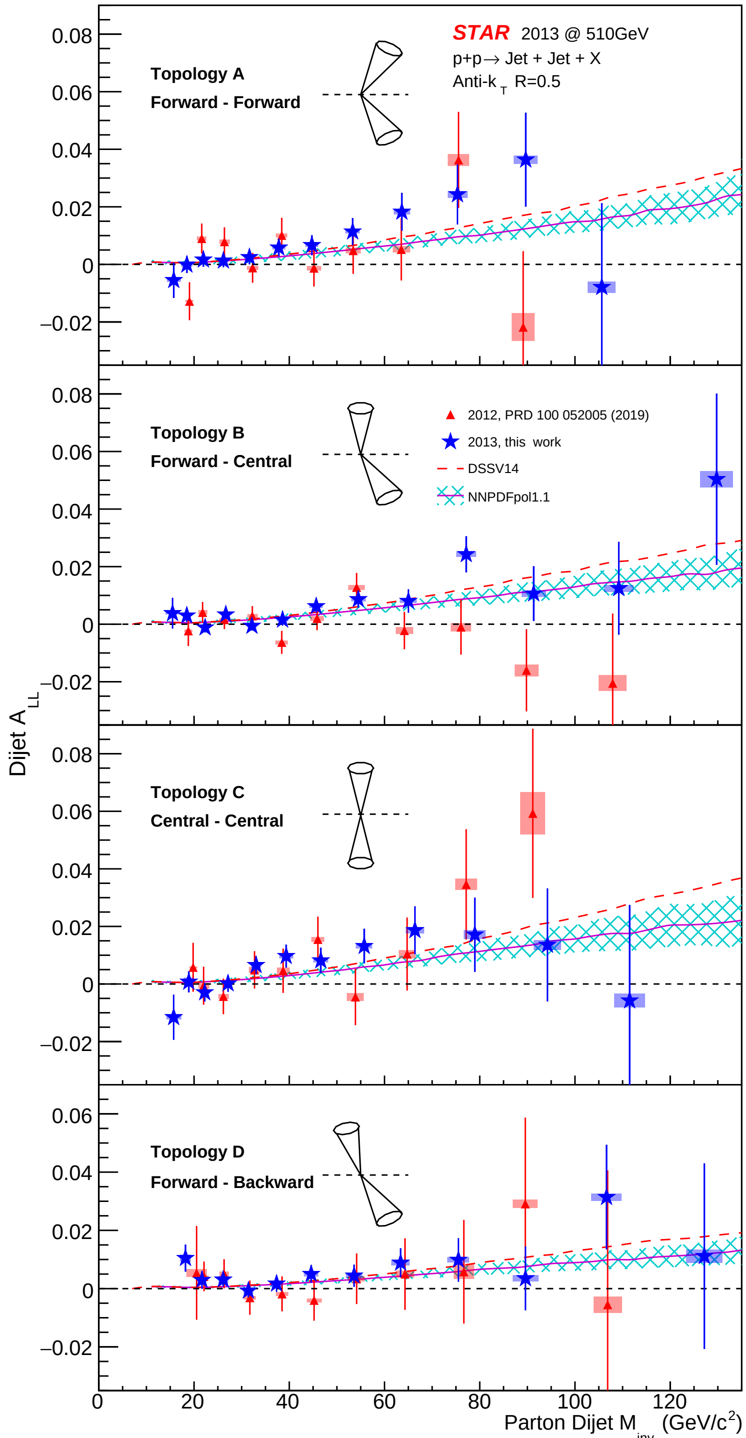

Figure 31: Dijet A_{LL} versus M_{inv} for the A, B, C and D (top to bottom) topological configurations as explained in the text. They are compared to previous STAR results from 2012 data [64] and predictions from DSSV14 [65] and NNPDFpol1.1 (with its uncertainty) [66] global analyses. The vertical lines are statistical uncertainties. The boxes show the size of the estimated systematic uncertainties. Topological configurations are shown for each jet orientation relative to the beam line. Scale uncertainties from polarization (not shown) are $\pm 6.6\%$ and $\pm 6.4\%$ for 2012 and 2013, respectively.

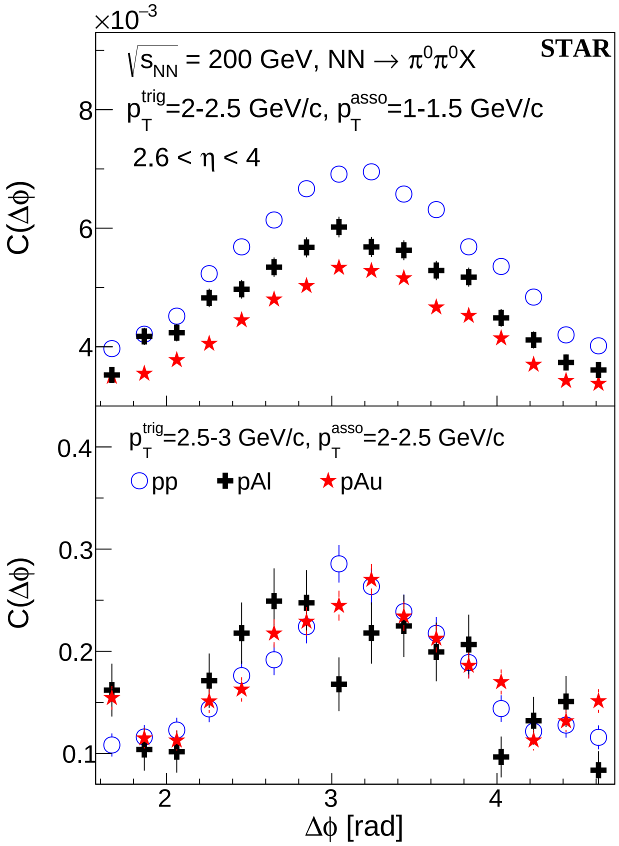

Figure 32: Comparison of the correlation functions (corrected for nonuniform detector efficiency in ϕ; not corrected for the absolute detection efficiency) vs. azimuthal angle difference between forward ($2.6 < \eta < 4.0$) π^0s in p+p, p+Al, and p+Au collisions at $\sqrt{s_{\rm NN}}$=200 GeV. Upper panel: the trigger π^0's $p_{\rm T}$ ($p_T^{\rm trig}$) = 2–2.5 GeV/c and the associated π^0's $p_{\rm T}$ ($p_T^{\rm asso}$) = 1–1.5 GeV/c; Bottom panel: $p_T^{\rm trig}$ = 2.5–3 GeV/c and $p_T^{\rm asso}$ = 2–2.5 GeV/c.

the A-dependence of the cold nuclear effect; the suppression is enhanced with higher A and scales with $A^{1/3}$, see Fig. 33. The suppression is analyzed for various event activities (E.A.) selections and found to be larger with higher E.A. The E.A. describes the degree of violence of the collision and is defined as the energy deposition in the backward (aluminum and gold going direction) inner sectors of the beam beam counter (BBC, $3.3 < -\eta < 5.0$). The measured suppression in high E.A. p+Au collisions is consistent with the predictions calculated from the gluon saturation model [69]. Meanwhile, the broadening predicted in the color glass condensate (CGC) framework in Ref. [70, 71] is not observed. This observation agrees with a similar measurement in d+Au collisions by the PHENIX experiment. [72] The pedestals in p+A and p+p collisions are found to be stable.

The comparison of the correlation function from p+p, p+Au, and d+Au collisions provides opportunities to understand the contributions from multiple parton scatterings [73]. From the preliminary results of d+Au collisions, we found much higher background in d+Au collisions compared to p+p and p+Au collisions reconstructing the π^0 candidates. The generated combinatoric correlation dominates in d+Au collisions, which makes it very challenging to identify the signal correlation. The forward di-π^0 correlation measurement favors for the cleaner p+A collisions rather than d+Au collisions.

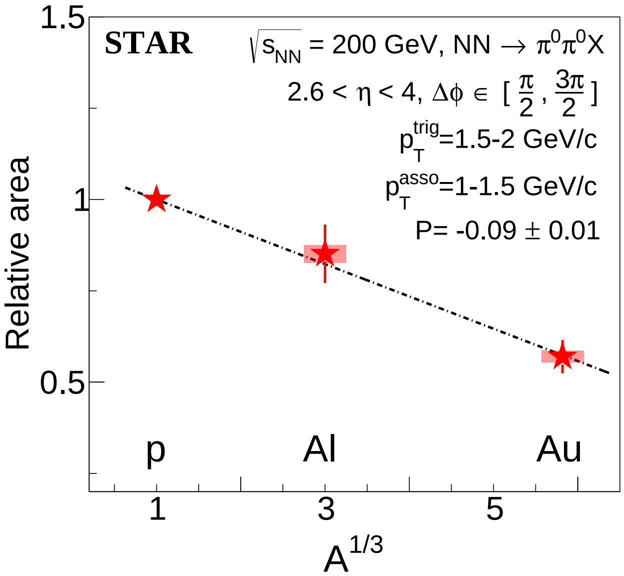

Figure 33: Relative area of back-to-back di-π^0 correlations at forward pseudorapidities ($2.6 < \eta < 4.0$) in p+Au and p+Al relative to $p+p$ collisions for $p_T^{\rm trig} = 1.5$–2 GeV/c and $p_T^{\rm asso} = 1$–1.5 GeV/c. The vertical bars for the Al and Au ratios indicate the statistical uncertainties and the vertical bands indicate the systematic uncertainties. The data points are fitted by a linear function, whose slope (P) is found to be -0.09 ± 0.01.

Collins Asymmetry

Recently, we finalized the measurement of the transverse single-spin asymmetries for charge pions inside a jet at $p+p$ 200 GeV based on the data from 2012 and 2015 running [?]. These observables, so called the Collins asymmetries, combine the quark transversity in the proton with the transverse momentum dependent Collins fragmentation function. Both of them are important topics in the transverse-momentum-dependent (TMD) frameworks.

Figures 34 shows the j_T, momentum transverse to the jet axis, dependence of the Collins asymmetry in six jet-p_T bins, with the average hadron z about 0.22. DMP+2013 model and KPRY model expectations are also presented in the plot. The DMP+2013 model uses the leading order TMD approach, and is based on a fit to transversity and Collins fragmentation function measurements from SIDIS and e^+e^- processes [74]. The KPRY model is also based on the global analysis of SIDIS and e^+e^- data and then treat TMD evolution up to the next-to-leading logarithmic effects using the soft-collinear-effective theory framework [75]. Our results slightly favor the KPRY model, however significant discrepancies exist between the data and both model calculations.

We also presented the first measurement of the Collins asymmetries for charged kaons and protons inside jets at $p+p$ collisions as shown in Fig. 35. These results are plotted with jet-p_T , hadron-z, and hadron-j_T dependence from left to right panels. Due to the limited statistics, they are not further divide into multi-dimensional bins. The asymmetries of K^+ has similar magnitude to those for π^+; while for K^-, proton and anti-proton, the asymmetries are consistent with zero at the one sigma level.

1.3 Run-22 Performance

All RHIC runs are challenging, however Run 22 seemed to have been more challenging than most. Despite the many set backs in the first half of the run, STAR ended up achieving

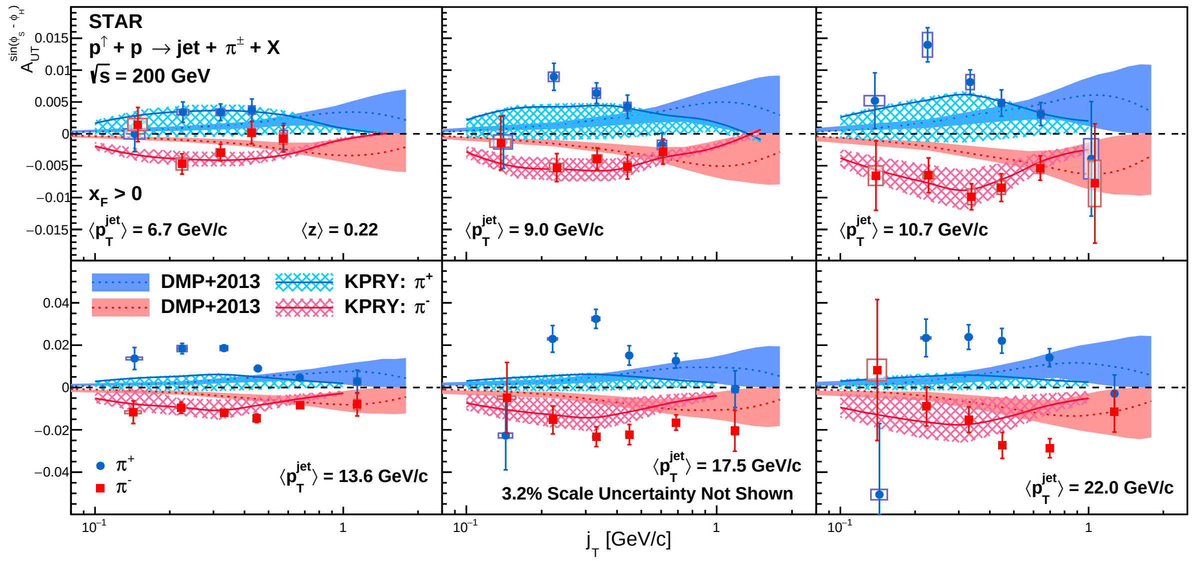

Figure 34: Collins asymmetries, $A_{UT}^{sin(\phi_S-\phi_H)}$, as a function the charged pion's momentum transverse to the jet axis, j_T, for in different jet p_T bins. The bars show the statistical uncertainties, while the size of the boxes represent the systematic uncertainties. The asymmetries are shown in comparison to calculations with the DMP+2013 model from Ref. [74] and the KPRY model from Ref. [75].

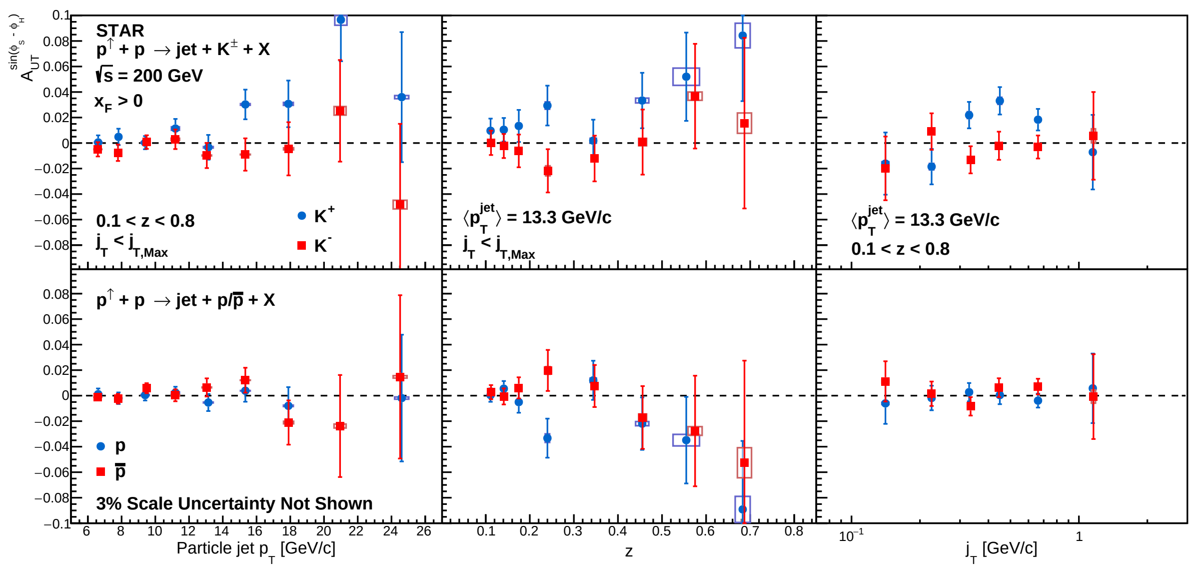

Figure 35: Collins asymmetries, $A_{UT}^{sin(\phi_S-\phi_H)}$, as a function of particle jet-p_T , hadron-z, and hadron-j_T for charged kaons (upper panels) and protons (lower panels) inside jets. In both cases, the p_T dependence is shown integrated over the full ranges of z and j_T, while the z and j_T dependences are shown integrated over detector jet-$p_T > 9.9$ GeV/c. The bars show the statistical uncertainties, while the size of the boxes represent the systematic uncertainties

107% of the forward goal and 98% of the mid-rapidity goal.

Let us start by reviewing the goals and request for Run 22. The run was planned for 20 cyro-weeks. These weeks included time for cool-down and warm-up, sixteen days of CeC running, and the remaining time for the STAR physics program. The specific requests for the STAR physics program were:

- Sampled luminosity of 400 pb^{-1}. This was achieved by April 6th.
- Luminosity leveling for a maximum ZDC rate of 330 kHz. The leveling worked well, especially with the addition of a second beta squeeze to maintain luminosity through the end of the stores.
- A peak luminosity of $135 \times 10^{30} cm^{-2} s^{-1}$. This was achieved in early February.
- A polarization of 55% in both beams. This goal turned out to be extremely challenging due to the loss of two coils in the Siberian Snake and the loss of the Siemans Motor Generator from January 12th to March 8th. Despite these challenges, polarizations close to 55% were achieved for the final six weeks of the run.
- Spin pattern and abort gaps similar to those for Run 17.
- Commissioning of the Forward Upgrade Detectors. This was expected to take place in the initial two weeks of the run with beam, however the start-up of operations was delayed due to the cyro-system upgrades. STAR was able to complete the commissioning using cosmics during this initial period when beams were not available.
- A few special runs were required with low luminosity and a small number of bunches for calibrations. These runs were completed early in the run, before RHIC achieved peak luminosities.
- Optimized time sharing with CeC. This was efficiently planned and executed to minimize the impacts on the STAR physics program.

From the STAR operation point of view, the run started on schedule. The Forward Upgrade Detector systems were all installed on schedule and ready for the start of the run. The STAR magnet power supply heat runs were conducted from November 5th to 9th, verifying that the STAR magnet was ready for operations. STAR started two-person shift crews in November 9th when gas was introduced to the TPC. Initial cosmic ray data taking to test the detector systems was started on November 11th. The full four-person (plus trainees) were in place on November 16th and STAR was ready to take data. Much credit should go to the shift coordination as STAR in still operating under COVID precautions and many international institutions were unable to travel to the US.

Unfortunately, beam operations did not start as expected due to a delay caused by the RHIC cyro-systems upgrade. STAR made use of this period of time without beam to commission the Forward Upgrade Detectors using cosmic rays. Although commissioning with cosmics was less efficient than commissioning with beam there was ample time to complete the process. Beams were first injected into the blue ring on December 3rd and into the yellow ring on December 7th.

The start of RHIC operations was further effected by two significant power dips. The first on December 3rd and the second on December 12th. After the first power dip, which was an 86 second long site-wide power dip, a superconducting helical coil in the blue Siberian Snake was found to be damaged. The second power dip damaged a second coil in the snake. The snakes are essential for maintaining the polarization of the beams. Credit must go to the CAD experts who were able to determine how to operate the damaged snake, which allowed the run to go forward, however initially the polarizations were achievable were only 45% in both rings, and as the figure of meter is polarization squared times integrated luminosity, the reduction in polarization significantly impacted the ability to achieve the physics goals. On December 18th, physics running started. This was almost one month behind the expectation.

Another major set-back occurred on January 12th when the Siemans Motor Generator failed. CAD was able to quickly switch to the Westinghouse, however polarizations dropped to 40%. At the end of January, STAR was projecting to only reach 30% on our goals.

In early February, due to improvements in injection and optimization, RHIC was able to achieve the luminosity goals, however the polarization was still low. This improved on March 8th when the repaired Siemans Motor generator was out back online. With the return of the Siemans and much optimization, the polarizations in both beams finally reached 55% and remained at that level for the remained of the run.

On March 8th, the run was extended by an additional two weeks. The new end date for beam operations was scheduled for April 18th. The sampled luminosity goal of 400 pb^{-1} was achieved on April 6th. However due to the reduced polarizations at the start of the run, the figure of merit polaziation squared times sampled luminosity goal was delayed. At the end of beam operations, STAR had achieved 98% of the figure of merit goal (as is shown in Fig. 36, which is quite remarkable considering the challenges which needed to be overcome.

Throughout the run period, STAR operations achieved the expected up-time of twelve hours per day of data taking.

Tremendous credit must go to CAD for overcoming the series of challenges. These challenges caused an inital delay of almost a month and reduced polarizations for the first half of the run. STAR was able to commission the Forward Upgrades with cosmics which allowed us to start taking data as soon as beams were available. The two week extension to the run was essential. By April, everything was running extremely well.

1.3.1 Forward Upgrade

The forward upgrade consists of four major new subsystems an electromagnetic and hadronic calorimeter and a tracking system, including a silicon and a small-strip Thin Gap Chambers tracking detector. The calorimeter subsystems were fully installed, instrumented, and commissioned during the 2021 RHIC running period. The tracking detectors were installed in summer and fall 2021, on schedule and ready for the start of Run 22. All the systems were further commissioned at the beginning of the run. They performed well and took data smoothly throughout Run 22.

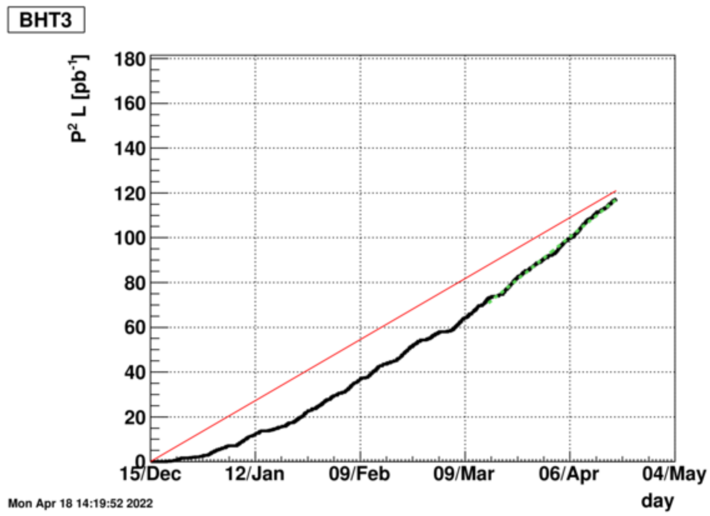

Figure 36: The figure of merit polarization squared times integrated luminosity as a function of date. The red line represents the rate necessary to achieve the physics goals. The black line displays the actual accumulation of the data. The trigger which is displayed uses a 3 GeV signal in a single barrel calorimeter tower (BHT3).

FCS Run-22 Summary Forward Calorimeter System (FCS) consists of Electro-Magnetic Calorimeter (Ecal) owith 1486 towers, and Hadronic Calorimeters (HCal) with 520 towers. Ecal was installed in 2019 and Hcal was installed in 2020, both on the west platform at STAR. All SiPM sensors, front-end electronics boards and readout & triggering boards called DEP were installed, commissioned and calibrated during Run-21. Signal splitter boards for west EPD detector were installed before Run-22 and West EPD was used as pre-shower detector in electron triggers. FPGA code for FCS triggers was developed in fall 2021, and total of 29 triggers, including triggers for di-electron (J/Ψ and DY), jets, hadrons, and photons were commissioned and verified within few days after RICH started delivering stable pp collisions and then used for data taking throughout Run-22 successfully. Calibration of Ecal was quickly done with reconstructing π^0, and calibration of Hcal was done by MIP peak from $<1\%$ of hadrons from pp collisions which did not start hadronic shower in Hcal, together with cosmic muon signals with Hcal module oriented vertically outside STAR. FCS operation during Run-22 was successful and smooth, besides 3 LVPS modules needed to be replaced, and occasional power cycling of electronics were needed due to beam related radiation upsets in the electronics. All 1486 channels of Ecal were working without any bad channels, and Hcal had only a couple of dead channels. Radiation damage to the SiPM sensors due to beam was within the expectation. There was unexpected loss of signal amplitudes of 20% per week in Ecal near beam, which turned out to be radiation damage in the front-end electronics boards. The loss of signal was compensated during Run-22 by changing gain factor on DEP boards, attenuator setting in the front-end electronics, and raising voltage settings tower by tower based on LED signals. Details on the radiation damage on the front-end electronics are currently under investigation.

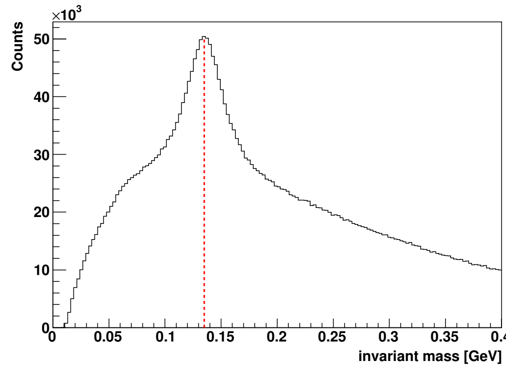

Figure 37: Invariant mass distribution and π^0 peak reconstructed with Ecal from pp collision data taken during Run-22.

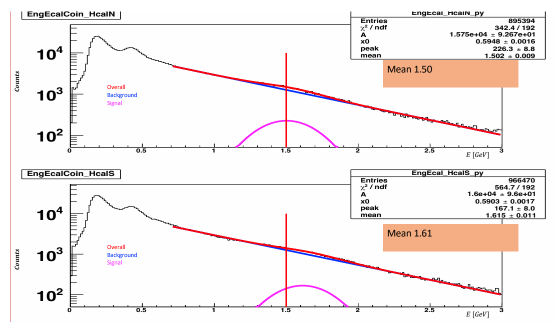

Figure 38: MIP peak in Hcal from $< 1\%$ of charged hadrons which did not start hadronic shower in Hcal from pp collision data taken during Run-22

sTGC Run-22 Summary The sTGC has four identical planes, each plane has four identical pentagonal shaped gas chambers. These gas chambers are made of double-sided and diagonal strips that give x,y,u in each plane. Sixteen chambers and about 5 spare chambers are built at Shandong University in China. Custom designed and fabricated aluminum frame allowed to fit the detector inside the pole-tip of the STAR magnet and around the beam-pipe on the west side of the STAR.

The sTGC chambers are operated with a quenching gas mixture of n-Pentane and CO_2 at a ratio of 45%:55% by volume at a typical high voltage of 2900 V. This gas mixture allowed the chambers to operate at high amplification mode. This mixture forms a flammable gas and the n-Pentane is liquid at normal atmospheric pressure and temperature. This made building the gas mixing systems extremely challenging. The supply chain issue caused by the pandemic added another layer of difficulty in completing the gas system. Allowable maximum pressure tolerance for the sTGC chambers are about 4 mBar above the atmospheric pressure and gas flow rate is extremely low, about 50 cc/min per chamber. In house, a newly designed

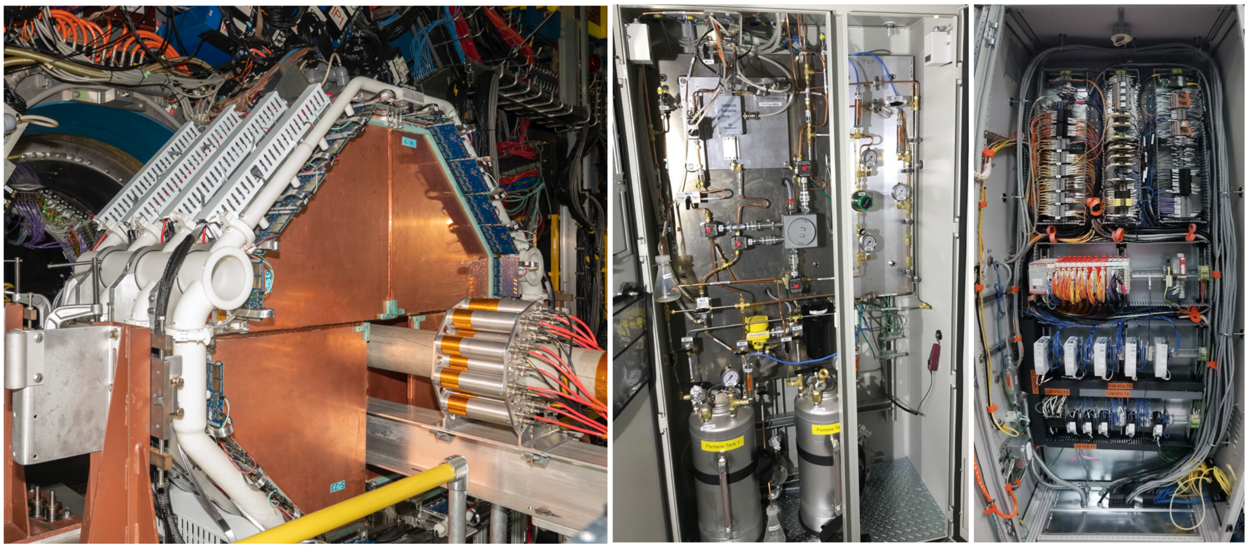

Figure 39: Left:sTGC detector module on a temporary platform prior to insertion into the pole-tip, middle: sTGC gas mixing system cabinet, right: sTGC interlock system cabinet.

and built gas system for mixing, and supplying the gas along a long-heated path to deliver to the chambers, met above requirements, and performed exceptionally well during the Run-22. Specially with many storms and power outages during the run, these systems performed uninterrupted. Added independent binary gas analyser during Run22 ensures that the gas mixture is at the right ratio. Since the gas mixture is flammable and liquefaction is possible inside the gas tubing, an independent redundant interlock system was designed and developed according to the industry standards. This system places the gas system in a safe state during any unforeseen situation such as flammable gas leak, fire, pentane liquefaction or over pressure occurs inside the chambers. Left panel of Fig. 39 shows the sTGC detector module on a temporary platform built prior to insertion into the pole-tip. Middle and right pictures show the gas mixing system and the interlock system respectively.

The sTGC readout is based on ATLAS VMM chips designed for ATLAS sTGCs. FEE cards were directly mounted on the edge of the sTGC chambers. This location is subjected to high radiation and magnetic field but the FEE cards performed exceptionally well during the operation. The sTGC was fully installed prior to the start of Run-22, and the detector was fully commissioned during the first few weeks of the run. Operating point of the high voltage was scanned for optimum efficiency. Gas chambers were stable at the desired operational high voltage and at the high luminosity, also the leakage current is well within the operational limits. sTGC has exceeded designed hit efficiency of 97% with the VMM chip gain set 3 mV/pC and the high voltage 2900V. During the running four chambers were lost, the reason for losing the chambers are still known. But, during initial training of the chambers, these four chambers performed poorly compared to the rest. These chambers will get replaced for the next run.

FST Run-22 Summary Forward Silicon Tracker (FST) consists three identical disks and each disk contains 12 modules. Each module has 3 single-sided double-metal Silicon mini-strips sensors and readout by 8 APV chips. The installation of FST was completed on August 13th, 2021 and the first collision p+p 510 GeV collision data recorded on December 15, 2021. The FST has been running smoothly through the whole run22 and the detector operation via slow control software remains minimum to the shift crew.

To find the optimal operation high voltage, a voltage scan was performed with low luminosity runs on December 17th, 2021. The operation high voltage decided to be 140V and 160V for inner and outer silicon sensors separately. The FST was running with 9 time bins initially for the detector commissioning and tuned to 3 time bins on December 21st, 2021 to increase the maximum DAQ rates of FST to 4.5kHz.

The noise level of FST silicon sensors is 10 to 20 ADC depending on position of the silicon strip and the average signal to noise ratio is about 25. Due to irradiation damage, the leakage current of silicon sensors increased from 2 uA to around 10uA (inner silicon sensor) and 15uA (outer silicon sensor) after 4 months of p+p 510 GeV data taking. This increase is consistent with expectation. There are 2 inner sectors and 2 outer sectors were operating at a lower high voltage value due to abnormal bias current behavior. Those modules will be investigated during the shutdown.

The FST readout chips are kept at room temperature by the cooling crate (same crate also used by Intermediate Silicon Tracker) running 3M NOVEC. The leak rate of the whole cooling system increased from 0.6% per day to 0.9% per day at the end of run22. The coolant tank were refilled every 6 weeks by expert.

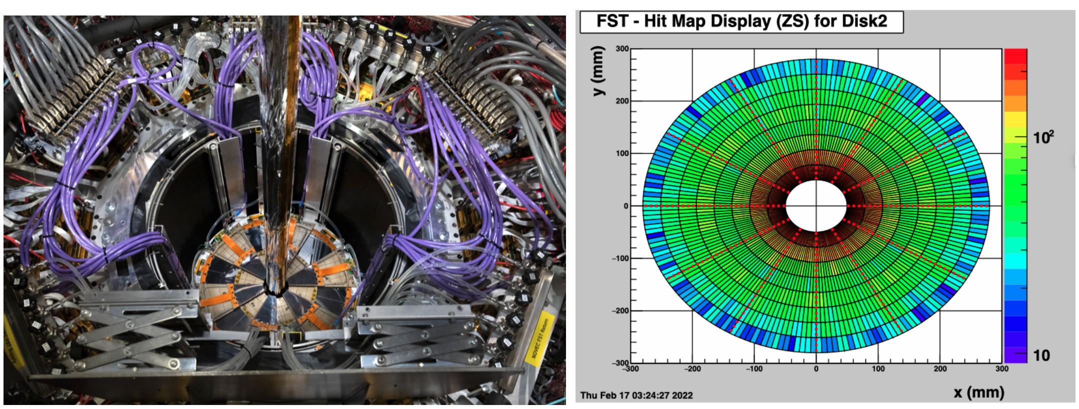

Figure 40: Left: FST after installation; Right: event display for p+p 510 GeV collisions.

Software and Tracking

2 Run-23 and Run-25 Requests for Au+Au Collisions at 200 GeV

2.1 Explore the Microstructure of the QGP

The completion of RHIC's scientific mission involves the two central goals: (i) mapping out the phase diagram of the QCD, and (ii) understanding the inner workings of the QGP by resolving its properties at varying length scales [76]. The former goal is addressed by the BES-II/FXT program. For the latter goal, the complementarity of the RHIC and LHC facilities is scientifically as essential as is having more than one experiment independently study the microstructure of the QGP at RHIC. With several years of operating the iTPC upgrade and commissioning and operation of the forward detectors in Run 22, the STAR collaboration is in an excellent position to take advantage of its vastly improved detection capabilities. Combining this with the prospect of a substantial increase in beam luminosities, RHIC will be uniquely positioned to fully engage in a detailed exploration of the QGP's microstructure.

Through careful discussions in its physics working groups, the STAR collaboration has identified a number of topics that together with the expected sPHENIX results in 23-25 make up a comprehensive study of the QGP microstructure, and successfully complete RHIC's scientific mission. In this section, we present a selection of those topics that will take full advantage of both STAR and RHIC's unique capabilities and address the following important questions about the inner workings of the QGP. We enumerate questions below that follow the chronology of an event; from questions addressing the QCD vacuum and the initial conditions, to the formation, temperature, and properties of the QGP, to the quenching of jets in said QGP, to its phase transition back to hadronic matter, and finally to the interactions of those final state hadrons.

1. **What is the nature of the 3-dimensional initial state at RHIC energies?** How does a twist of the event shape break longitudinal boost invariance and decorrelate the direction of an event plane? Can the v_1 of the J/ψ tell us about the initial tilt angle of the source? Can the Wigner distributions of photon tell us about the magnetic field effects in the initial state?

2. **What is the precise temperature dependence of the shear η/s, and bulk ζ/s viscosity?** Can combining precision flow results with those from other energies can help determine the temperature dependence of the viscosity.

3. **What can we learn about confinement from charmonium measurements?** Can the elliptic flow of J/ψ tell us the charmed quarks are deconfined?

4. **What is the temperature of the medium?** Do the Υ and $\psi(2s)$ melt at RHIC energies, and if so can their suppression be used to determine the temperature of the QGP? The thermally produced di-leptons are also produced in the plasma. Does their temperature agree with that found via quarkonium suppression?

5. **What are the electrical, magnetic, and chiral properties of the medium?** How is global vorticity transferred to the spin angular momentum of particles on such short time scales? And, how can the global polarization of hyperons be reconciled with the spin alignment of vector mesons? Can dilepton production in the low mass region tell us about the electrical conductivity of the plasma? Can clear observation of the ρ^0-a_1 mixing tell us about the degrees of freedom therefore the chirality of the plasma? Is there local parity violation and chiral magnetic effect?

6. **What are the underlying mechanisms of jet quenching at RHIC energies?** What do jet probes tell us about the microscopic structure of the QGP as a function of resolution scale?

7. **What is the precise nature of the transition near $\mu_B = 0$?** Where does the sign-change of the susceptibility ratio χ_6^B/χ_2^B take place?

8. **What can we learn about the strong interaction?** Can correlation functions between baryons emitted at the surface of the fireball tell us how they interact in free space.

The event statistics projections that are used in this section will rely on the CAD's 2023E and 2025E Au+Au luminosities [77] and the improved iTPC readout speed, and are listed in Table 5. For each year we presume 24 weeks of physics data taking, and based on past run operations an overall average of 85% × 60% (STAR×RHIC) uptime, respectively.

It was realized that it will be possible to improve the readout speed of the iTPC detector as deployed in BES-II, to a substantial higher rate for the runs 23-25 program. The upgrade is primarily firmware and software development. It consists of the following components:

- Rewrite the FPGA firmware for FEEs and RDOs. The FPGAs are different for the outer sectors (TPX) and inner sectors (iTPC)
- Rewrite DAQ online software for TPC in framework as for FCS
- Redo and evaluate cluster finder
- Improve network connectivity
- Add some DAQ PC and event builders to handle increased data volume.
- The original gating grid driver that had a limit of 2.2 kHz was replaced for Run 22 and can now easily handle more than 5 kHz.

The expectation is that data rate can be approximately doubled with nominal deadtime. Thus:

- Minimum Bias data taken at low luminosity should be able to record 5 kHz with 30% deadtime.

- High luminosity data for rare triggers should be able to be recorded at 3 kHz at 20% deadtime.

The coding has already begun and is being developed and tested on the actual hardware using one of the TPC sectors. Performance is being evaluated using actual Au+Au low luminosity data from Run 19. Progress is good and expect that the development and system testing will be completed by end of the year.

In order to achieve a balance between those physics observables which are acquired with a minimum bias trigger (and negatively impacted by excess tracks in the TPC) and the rare probes which require specialized triggers (high tower (HT), dimuon) and the highest luminosity which can be accommodated with the TPC, the collaboration will optimize the interaction rates at STAR by allocating high and low luminosity periods within fills. CAD can offset the beam to independently control the maximum luminosity in each IR. Such periods, in which low interaction rates (specialized triggers) are sampled in the early part of a fill and high interaction rates (min bias trigger) typically in the later part, will allow us to collect clean, low pile-up, minimum bias events, while at the same time not burn beam luminosities that could affect interaction rates for sPHENIX. Clean minimum bias events will improve tracking efficiencies which in turn are expected to benefit many of the proposed correlation analyses. Optimization of the available bandwidth for rare triggers would allow us to push for lower p_T thresholds, thus further reducing biases. The impact of such an optimization will lead to some reduction in the projected rates, while still enabling a significant improvement in the precision and kinematic reach of current STAR measurements, and making important measurements that are yet more differential possible.

year	minimum bias [$\times 10^9$ events]	high-p_T int. luminosity [nb^{-1}]		
		all vz	$\lvert vz \rvert <$70cm	$\lvert vz \rvert <$30cm
2014 2016	2	27	19	16
2023 2025	20	40	36	24

Table 5: STAR minimum bias event statistics and high-p_T luminosity projections for the 2023 and 2025 Au+Au runs. For comparison the 2014/2016 event statistics and luminosities are listed as well.

It is possible to build detectors that can span from mid-rapidity to beam rapidity – with the BES-II upgrades and the recent Forward upgrade STAR is able to achieve this unique capability. STAR's BES-II upgrade sub-systems comprised of the inner Time Projection Chamber (iTPC, $1.0 < |\eta| < 1.5$) , endcap Time Of Flight (eTOF, $1 < \eta < 1.5$) and Event Plane Detectors (EPDs, $2.1 < |\eta| < 5.1$), that are all fully operational since the beginning of 2019 [7,78,79]. The STAR Collaboration has commissioned and operated a forward rapidity ($2.5 < \eta < 4$) upgrade that includes charged particle tracking and electromagnetic/hadronic calorimetry [80]. Charged particle tracking is achieved using a combination of silicon detectors and small strip thin gap chamber detectors. The combination of these two tracking detectors is referred to as the forward tracking system (FTS). The FTS is capable of discriminating the hadron charge sign. It can measure p_T of charged particles in the range of $0.2 < p_{\mathrm{T}} < 2$ GeV/c with $20 - 30\%$ momentum resolution.

In what follows, we will refer to the combination of the existing TPC ($|\eta| < 1$) and the iTPC upgrade as iTPC ($|\eta| < 1.5$) for simplicity.

The impetus for running STAR during runs 23 and 25 in Au+Au 200 GeV collisions comes from gains via: i) extended acceptance, ii) enhanced statistics, and iii) low material budget. The extended acceptance is important for analyses that probe the η dependencies and especially so for those that require correlations between particles (CME, $v_2(\eta)$, $r_n(\eta)$, and $P_H(\eta)$). The enhanced statistics through longer running time and higher luminosities is especially important for the rare probes (jets, J/ψ, CME, net-p C_6). In the previous 200 GeV runs in 2014-2016 STAR included inner silicon detectors (the Heavy Flavor Tracker). This has since been removed and by comparison in run 23-25 STAR will have a reduced material budget between the beam and the iTPC, and will be uniquely positioned to perform dielectron measurements. With these measurements, we propose to study the initial conditions (Wigner functions, photoproduction of J/ψ), the degrees of freedom of the medium (excess yield), and its transport properties (temperature through slope in the IMR).

A synopsis of the proposed analyses, which questions they address, whether they will be part of the minimum bias (low luminosity) or specialized trigger (high luminosity) program, which coverage is essential, and the required trigger is shown in Fig. 41.

The following subsections will address the specific analyses which are proposed to answer the questions outlined previously in the section. The questions sequentially step through the chronology of an event.

What is the nature of the 3D initial state?

Pseudorapidity-dependent Azimuthal Correlations to Constrain the Longitudinal Structure of the Initial State ($v_n(\eta)$)

Initial-state longitudinal fluctuations and the fluid dynamical response of the medium formed in heavy ion collisions can lead to de-correlations of the direction of the reaction planes Ψ_n (which determines the orientation of the harmonic anisotropies) with pseudorapidity (see Fig. 42). Such effects are often referred to as a torque or twist of the event shape [19, 81, 82] that eventually leads to a breaking of longitudinal/boost/rapidity invariance. The magnitude of the de-correlation is determined by the details of the dynamics of initial state, and the distribution of nucleons and partons inside the colliding nuclei.

Several promising observables have been proposed to study this effect, Fig. 42 shows one which can be expressed as $r_n(\eta_a, \eta_b) = V_{n\Delta}(-\eta_a, \eta_b)/V_{n\Delta}(\eta_a, \eta_b)$, where $V_{n\Delta}$ is the Fourier coefficient calculated with pairs of particles taken from three different pseudorapidity regions $-\eta_a$, η_a and η_b. The observable $r_n(\eta_a, \eta_b)$ was originally introduced and measured by CMS collaboration in Ref. [84] and also been measured by the ATLAS collaboration in [85]. An observable using three-particle correlations that is sensitive to this effect is the relative pseudorapidity dependence of the three-particle correlator $C_{m,n,m+n}(\eta_a, \eta_b, \eta_c) = \langle \cos(m\phi_1(\eta_a) + n\phi_2(\eta_b) - (m+n)\phi_3(\eta_c)\rangle$ [86]. Another, very similar to r_n in terms of design

Observable	Question	PWG	MB/H$\mathcal{L}$	Coverage	Trigger
$v_2(\eta)$ Twist	1) Initial State	FCV	Min bias	iTPC, TOF, EPD, FTS	VPDMB
$r_n(\eta_a,\eta_b)$	1) Initial State	FCV	Min Bias	iTPC, TOF, EPD, FTS	VPDMB
J/ψ v_1	1) Initial State	HF	Luminosity	iTPC, TOF, EPD	Dimuon
Photon WF	1) Initial State	LFSUPC	Min Bias	iTPC, TOF	VPDMB
$v_2(\eta)$	2) Viscosity	FCV	Min bias	iTPC , TOF, EPD, FTS	VPDMB
J/ψ v_2	3) Deconfinement	HF	Luminosity	iTPC, TOF, EPD	Dimuon
Υ suppression	4) Temperature	HF	Luminosity	iTPC, TOF	Dimuon
ψ(2s) suppress.	4) Temperature	HF	Luminosity	iTPC, TOF	Dimuon
Di-elec IMR	4) Temperature	LFSUPC	Min bias	iTPC, TOF	VPDMB
$P_H(\eta)$	5) Properties	FCV	Min Bias	iTPC, TOF, FTS	VPDMB
P_H of J/ψ	5) Properties	FCV	Luminosity	iTPC, TOF	dimuon
ρ^0 a_1 mixing	5) Properties	LFSUPC	Min Bias	iTPC, TOF	VPDMB
Di-elec LMR	5) Properties	LFSUPC	Min Bias	iTPC, TOF	VPDMB
CME	5) Properties	FCV	Min Bias	iTPC, TOF	VPDMB
γ_{Dir} + jet I_{AA}	6) Jet quenching	Jet Corr	Luminosity	Bcal, Ecal, Fcal	BHT3
γ_{Dir} + jet acopl.	6) Jet quenching	Jet Corr	Luminosity	Bcal, Ecal, Fcal	BHT3
Jet substruct.	6) Jet quenching	Jet Corr	Luminosity	Bcal, Ecal, Fcal	BHT3
Net-p C_6	7) Phase Transition	CF	Min Bias	iTPC, TOF	VPDMB
Baryon CF	8) Strong Interact.	CF	Min Bias	iTPC, TOF	VPDMB

Figure 41: A tabulation of the proposed analysis. The columns indicate which of the nine questions a given analysis addresses, which physics working group will lead the analysis effort, whether the analysis will be part of the low or high luminosity program, which detector systems are essential, and the required trigger for that analysis.

but involving four-particle correlations, is: $R_{n,n|n,n}(\eta_a, \eta_b)$ [17]. As shown in Fig. 42, CMS measurements of r_n show strong de-correlation ($\sim$ 16% for n=3, $\sim$ 8% for n=2) in central events within the range of their acceptance. In the 3D-Glasma model of initial state, the breaking of boost invariance is determined by the QCD equations which predict the evolution of gluons in the saturation regime with Bjorken-x. At the LHC such models predict weaker de-correlation as compared to when the initial state is described by wounded nucleon models. The 3D-Glasma model does a good job in explaining the r_2 data from CMS [18] but over-predicts the r_3 results. One expects the nature of the initial state to change from LHC to RHIC, in particular the region of Bjorken-x probed is very different. It is therefore extremely important to utilize the enhanced acceptance of the STAR detector with a Au+Au 200 GeV run to study this effect. In Fig. 42 STAR's projections using preliminary Run-19 results to estimate the uncertainties for 10 B events are shown for the measurement of r_n within the acceptance $|\eta| < 1.5$. The colored regions show that the current and future capabilities at STAR (with iTPC+EPD+FTS) can extend such measurements using observ-

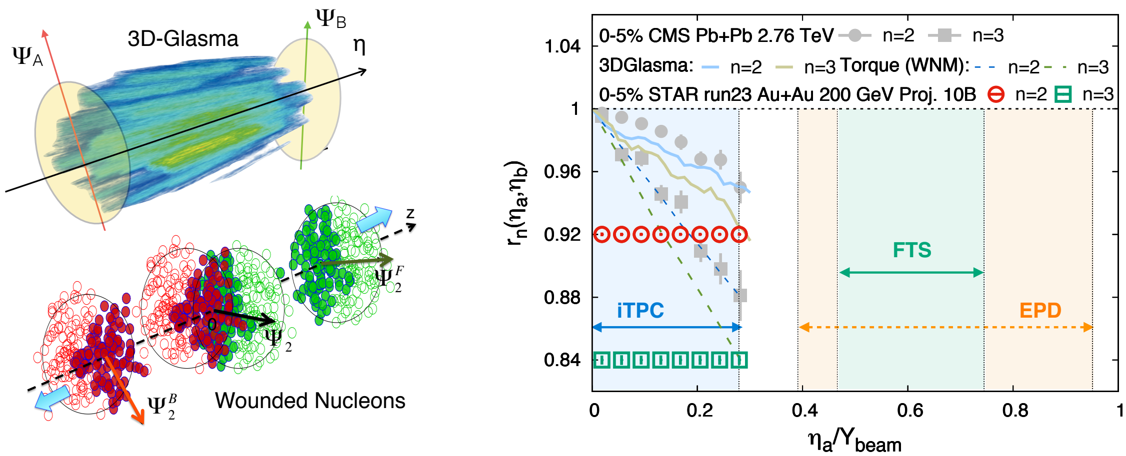

Figure 42: (Left) Cartoon to demonstrate the de-correlation of event planes in the longitudinal direction of a collision from a gluon saturation based 3D-Glasma model [18] and a wounded nucleon model (WNM) [19, 83]. (Right) The longitudinal de-correlation of the elliptic anisotropy plane as a function of pseudorapidity in units of beam rapidity. CMS results are compared to predictions from two models in the left with STAR projection for Run 23 (using preliminary Run 19 results) from an anticipated 10 B min-bias events. The colored regions show that the current and future capabilities at STAR (with iTPC+EPD+FTS) can extend such measurements with good precision by covering a large fraction of the beam rapidity at 200 GeV – this demonstrates the unique strength of STAR to study the physics of 3D initial state.

ables $r_n, C_{m,n,m+n}, R_{n,n|n,n}$ with good precision by covering either an equal (iTPC only) or larger (iTPC+FTS+EPDs) fraction of the beam rapidity at 200 GeV compared to the LHC measurements. This unique measurement capability will help pin down the nature of the 3-D initial state of heavy ion collisions. It will also help constrain different models of QCD that predict the rapidity (or Bjorken-x) dependence of valance quark and gluon distributions inside colliding nuclei as has been demonstrated by theoretical calculations in Ref. [18, 20].

$J\psi$ v_1 to Study the Initial Tilt

Studies of the directed flow, v_1, as a function of rapidity provide crucial information to understand the initial tilt of the medium produced in heavy-ion collision [87, 88]. Heavy quarks are produced in the early stage of a heavy-ion collision and thus are of particular interest for the medium initial asymmetry studies. STAR recently reported the first measurement of D-meson v_1 in Au+Au collisions at 200 GeV where the magnitude of the heavy-flavor meson v_1 is about 25 times larger than the v_1 for charged kaons. With the runs 23 and 25 data, STAR would have a unique opportunity to study the v_1 of a bound $c\bar{c}$ state, the J/ψ mesons, for which even larger directed flow can be expected [89]. In addition to STAR's excellent capability to reconstruct low-p_{T} J/ψ, the iTPC will improve the momentum resolution and extend the pseudorapidity coverage. This will provide better precision for the slope extraction of the v_1 vs y measurement, that quantifies the strength of directed flow. The expected precision of a J/ψ v_1 measurement vs p_{T} at STAR in runs 23 and 25, assuming 20 B MB events and 40 nb^{-1} of HT trigger sampled luminosity, in 0-80% central Au+Au collisions at 200 GeV is shown in Fig. 43.

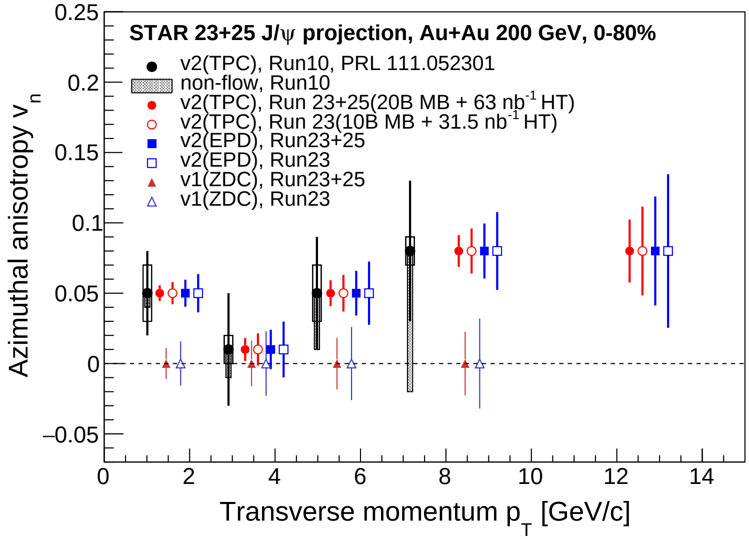

Figure 43: Projections for the J/ψ ($J/\psi \rightarrow e^+e^-$) directed ($v_1$) and elliptic ($v_2$) flow vs J/$\psi$ p_{T} in 0-80% Au+Au collisions at 200 GeV, assuming 20 B MB events and 40 nb^{-1} of HT trigger sampled luminosity.

Studying the Photon Wigner Function and Final-state Magnetic Fields in the QGP (photon WF)

The unsuccessful description of STAR data by the STARLight model led to the attribution of the broadening to the possible residual magnetic field trapped in an electrically conducting QGP [90]; which is key information to the study of the chiral magnetic effect.

Similarly, ATLAS quantified the effect via the acoplanarity of lepton pairs in contrast to the measurements in UPC and explained the additional broadening by multiple electromagnetic scatterings in the hot and dense medium [91], which is analogous to the medium $P_\perp$-broadening effects for jet quenching.

These descriptions of the broadening in hadronic collisions are based on the assumption that there is no impact parameter dependence of the p_T distribution for the electromagnetic production. Recent lowest-order QED calculations, in which the impact parameter dependence is recovered, could reasonably describe the broadening observed by STAR and ATLAS without any in-medium effect. To solve the puzzle, we propose to precisely study the initial $P_\perp$-broadening for the dilepton pair in ultra-peripheral collisions. Different neutron emission tags serve as the centrality definition, and will allow us to explore the broadening baseline variation with impact parameter. Furthermore, the differential spectrum as a function of pair $P_\perp$, rapidity, and mass enable us to study the Wigner function of the initial electromagnetic field, which provide the information to extract the momentum and space correlation of EM field.

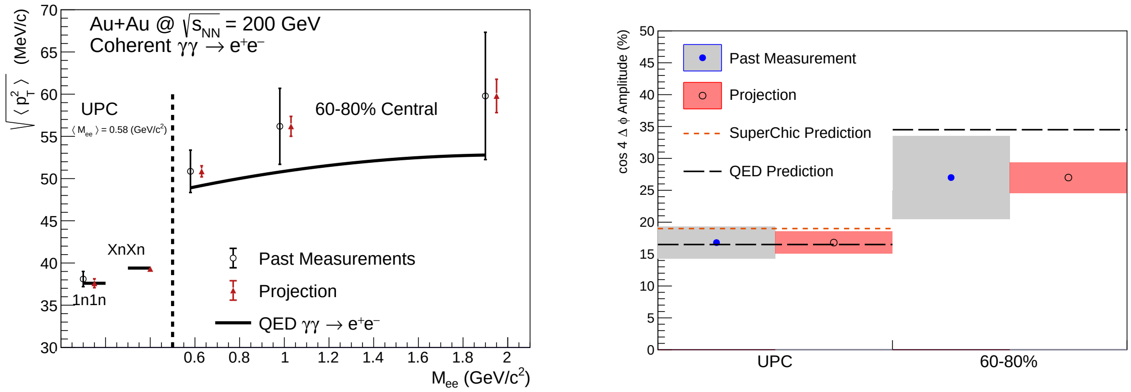

Figure 44: Projections for measurements of the $\gamma\gamma \to e^+e^-$ process in peripheral and ultra-peripheral collisions. Left: The $\sqrt{\langle p_T^2 \rangle}$ of di-electron pairs within the fiducial acceptance as a function of pair mass, M_{ee}, for 60–80% central and ultra-peripheral Au+Au collisions at $\sqrt{s_{\rm NN}} =$ 200 GeV. Right: The projection of the $\cos 4\Delta\phi$ measurement for both peripheral (60–80%) and ultra-peripheral collisions.

As shown in Fig. 44, comparing with the latest QED calculation, there still exists additional broadening in peripheral collisions, although the significance is only about 1σ, which still leave room for the medium effect. In Runs 23 and 25, as projected in the figure, we could judge the existence of additional broadening with much higher precision and further constrain the strength of final-state magnetic field in the QGP.

Precision measurement of the amplitude of the recently observed $\cos 4\Delta\phi$ modulation of the $\gamma\gamma \to e^+e^-$ process will allow precision mapping of the photon Wigner function and provide additional constraints on possible final-state effects, thereby complementing the $P_\perp$ broadening measurement. Figure 44 right panel shows the projected precision for a measurement of the $\cos 4\Delta\phi$ modulation in Runs 23 and 25. The modulation is a direct result of the mismatch in initial and final spin configuration of the $\gamma\gamma \to e^+e^-$ process. Any final-state effect that modifies the $P_\perp$ will necessarily reduce the amplitude of the modulation. Assuming the same central value as previously measured, evidence for suppression of the $\cos 4\Delta\phi$ modulation will be visible at the $> 3\sigma$ level (stat. & syst. uncertainty). Precision measurement of the $\cos 4\Delta\phi$ modulation in Runs 23 and 25 may also allow a first direct experimental measurement of the impact parameter dependence of this new observable (by comparing UPC and 60–80%). Assuming the same central values as previously measured, the improved precision will provide evidence for impact parameter dependence at the $> 3\sigma$ level (stat. & syst. uncertainty). Assuming the central value predicted by QED would lead to a $> 5\sigma$ difference between the UPC case and the 60–80% case.

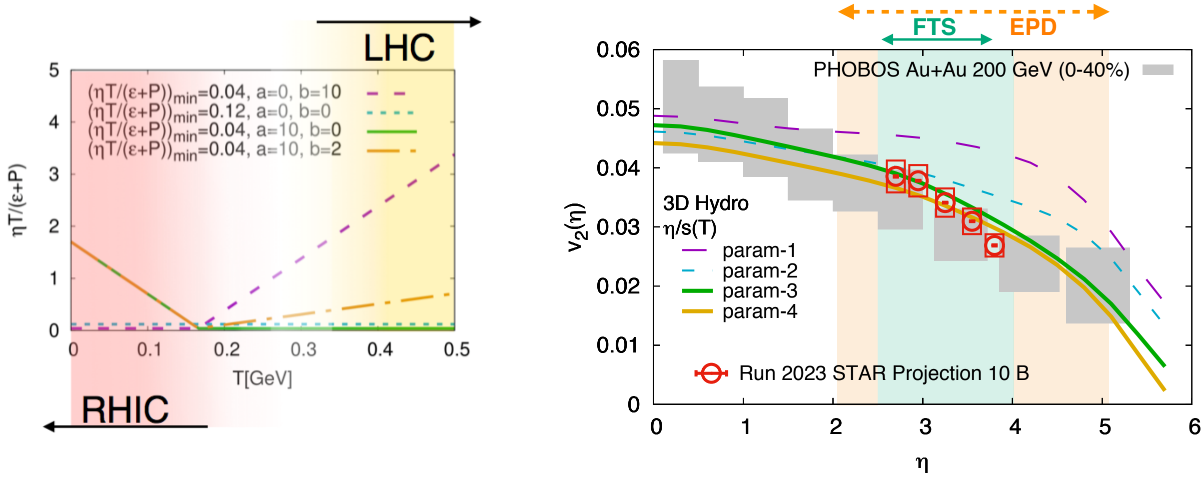

Figure 45: (Left) Different parameterizations of the temperature dependence of the shear viscosity to entropy η/s (T) (at $\mu_B = 0$) used in the hydrodynamical simulation of Ref. [95]. It has been demonstrated in Ref. [96] that the region of lowest η/s is the one that can be probed at RHIC. (Right) Effects on the elliptic flow co-efficient v_2 due to different parameterizations of the viscosity parameter, indicating better constraints on η/s (T) can only be performed by measurements at forward rapidities at RHIC. The interpretation of the existing PHOBOS data is limited by the large uncertainties. Projections for STAR measurements are shown on the same plot.

What is the precise temperature dependence of viscosity?

The idea of tightly constraining the temperature dependent viscosity of the QGP was envisioned in the 2015 Long Range Plan for Nuclear Science [76]. The QCD matter formed at RHIC shows nearly perfect fluidity characterized by the smallest viscosity to entropy ratio η/s known in nature. One major aim is to perform precision measurements to constrain the temperature dependence of the shear η/s (T) and bulk ζ/s (T) viscosities. Recent state-of-the-art Bayesian analyses of flow and spectra data within sophisticated event-by-event hydrodynamics models has show strong evidence for temperature dependence of η/s and ζ/s [92–94], but the uncertainties are still quite large. On the other hand, hydrodynamic simulations have demonstrated that since the temperature of the produced fireball varies with rapidity, the measurement of the rapidity dependence of flow harmonics can provide additional constraints on the η/s (T) and ζ/s (T) [95]. For this, RHIC measurements have an advantage over the LHC since the smaller beam rapidity at RHIC provides stronger variations of the temperature with rapidity. The beam energy scan at RHIC provides an additional handle on temperature to map η/s (T), and ζ/s (T) over a wide range of temperatures. Indeed, the hydrodynamic simulation of Ref. [95] indicates that η/s (T) at lower temperatures, near its possible minimum ($T = T_c$), can be better constrained by RHIC measurements. Results from such simulations are shown in Fig. 45. In this simulation, a number of QCD-motivated parameterizations of the temperature dependence of the shear viscosity were assumed, as shown in Fig. 45 (left).

Existing data from the PHOBOS collaboration suffer from large uncertainties, therefore only limited constraints on the temperature dependence of the transport parameters can be achieved. The BES-II upgrades and the FTS will provide precise estimations of different azimuthal correlation observables: $v_n(\eta)$ and other higher-order ($n > 2$) flow coefficients $v_n(\eta)$, its fluctuations $\sigma(v_n)/v_n$ that have never been measured at forward rapidity, are essential in terms of constraining η/s (T) near its possible minimum. These quantities previously measured at mid-rapidity are not enough for discriminating different parameterizations of η/s (T) as shown in the hydrodynamic simulation of Ref. [95]. While p_T integrated quantities at forward rapidity can constrain the shear viscosity, measurement of the p_{T} of particles at forward rapidity (i.e. FTS) is essential to constrain the bulk ζ/s – in particular the information of $\langle p_T \rangle$ is needed to constrain ζ/s(T). With the FTS it will be possible to measure the p_{T} dependence of v_n in Au+Au collisions in runs 23 and 25.

What can charmonium tell us about deconfinement?

The strong collectivity of the QGP is studied by measuring the azimuthal anisotropy of the produced particles in heavy-ion collisions. A positive elliptic flow coefficient (v_2) of the light flavor hadrons, and also D-mesons and electrons from heavy-flavor hadron decays are observed in Au+Au collisions at $\sqrt{s_{\mathrm{NN}}}$= 54.4 and 200 GeV at RHIC. This corroborates that, like light-flavor, the charm quarks are (partially) thermalized and show collectivity in the QGP. On the other hand, the v_2 of heavier J/ψ reported by STAR based on the 2010 Au+Au 200 GeV data sample was found to be consistent with zero, albeit within large statistical uncertainties and systematic uncertainties due to non-flow effects. The precision of the measurement was also not enough to distinguish between theoretical model calculations that assume only primordial J/ψ production and ones that include additional J/ψ production via recombination. This calls for a larger sample of heavy-ion data at 200 GeV, as will be provided by RHIC in runs 23 and 25, in order to observe a possible non-zero J/ψ v_2 at RHIC energies and put more constraints on the J/ψ production models especially regarding its regeneration. Particularly important for these studies is STAR's potential to measure low p_T J/ψ with a very good precision. This excellent low-p_{T} performance at STAR can be achieved thanks to its low material budget and great particle identification capabilities.

The second order event plane will be reconstructed using the EPDs which will significantly decrease the contribution from the non-flow effects and consequently the measurement's systematic uncertainties. Also, an inverse of the EP resolution enters directly the J/ψ v_2 uncertainty calculation. Due to the use of the EPD, the resolution of the EP at forward rapidity for the J/ψ v_2 measurement at STAR will improve. Figure 43 presents statistical projections for the J/ψ v_2 measurement in 0-80% central Au+Au collisions assuming 20 B MB events and 40 nb^{-1} of HT trigger sampled luminosity. Both cases of the second order EP reconstruction, using the forward EPD and mid-rapidity TPC, are considered and shown. A significant improvement in the precision of the J/ψ v_2 can be seen across the experimentally accessible J/ψ p_{T} coverage. In addition, the larger dataset would allow to extend the measured p_{T} range beyond 10 GeV/c.

What is the temperature of the medium?

Υ Suppression

In the QGP, the confining potential of a heavy quark-antiquark pair is predicted to be screened by the surrounding partons leading to the quarkonium dissociation. Within this static picture, a quarkonium state dissociates if its size is larger than the Debye screening length of the medium that is inversely proportional to the medium temperature. Consequently, different quarkonium states, depending on their sizes, are expected to dissociate at different temperatures, which is usually referred to as the quarkonium sequential suppression. Quarkonia are therefore considered excellent probes of the medium thermodynamic properties. In particular, differences in the dissociation temperatures between Υ(1S), Υ(2S) and Υ(3S) states are larger compared to the charmonium states, providing a longer lever arm. In addition, the regeneration contribution for bottomonia is expected to be negligibly small at RHIC energies. Figure 46 presents statistical projections for Υ(1S) and Υ(2S) R_{AA} as a function of p_{T} and N_{part} (centrality), compared to STAR's latest results from the 2011, 2014 and 2016 datasets. The projections are done combining the di-electron and di-muon Υ decay channels and for an integrated luminosity of 40 nb^{-1} that corresponds to the runs 23 and 25 data samples. One can see a clear improvement of the statistical precision for both Υ states. Due to the larger suppression of the Υ(3S) state, only an upper limit on the R_{AA}, 0.29 at 99% confidence level, was obtained so far. With an integrated luminosity of 40 nb^{-1} we expect a precision of about 30% for Υ(3S) that may allow us to extract the Υ(3S) signal if the meson is not fully dissociated in the medium or significantly improve precision of our upper limit. The requested luminosity is therefore crucial to obtain a full picture of the bottomonium family suppression at the RHIC top energy.

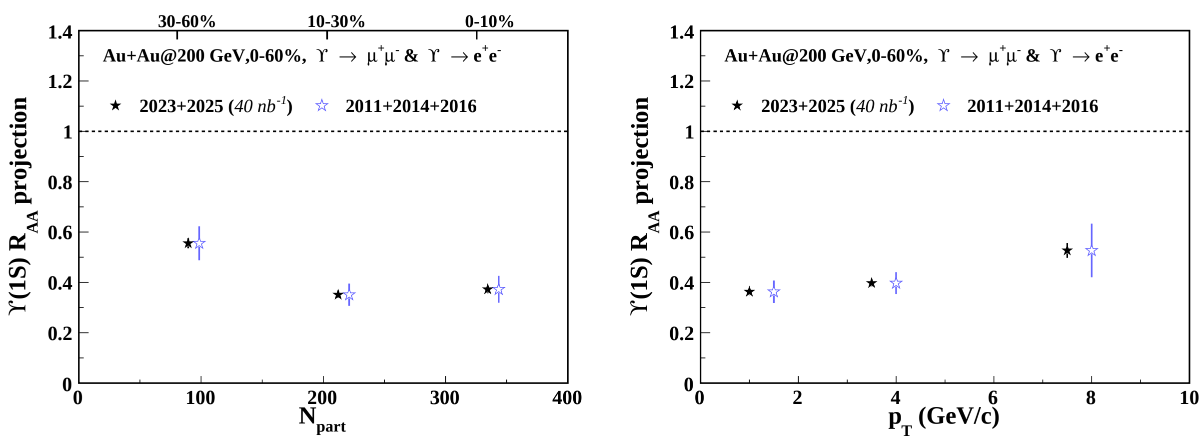

Figure 46: Statistical projections for the Υ(1S) and Υ(2S) R_{AA} as a function of N_{part} (left) and p_{T} (right) in 0-60% Au+Au collisions at 200 GeV, assuming 40 nb^{-1} of HT triggered events. The projections are done combining the di-electron and di-muon decay channels and are compared to the STAR results from 2011, 2014 and 2016 datasets. Υ(2S) to be added

ψ(2s) Suppression

ψ(2S) is the most loosely bounded quarkonium state currently accessible to heavy-ion collision experiments. Its dissociation temperature is predicted to be around, or below, the critical temperature, and is much less than that of J/ψ and Υ states. It is therefore more likely to be dissociated in the early stage and in the core of the fireball, and those ψ(2S) that are measured may have significant contributions from regeneration at a later stage in the evolution of the fireball. The relative suppression of ψ(2S) and J/ψ is sensitive to the temperature profile of the fireball produced in heavy-ion collisions and its space-time evolution. It is also argued that the charmonium formation process from a $c\bar{c}$ pair may be affected by both the QGP and the initial strong external magnetic field, altering the relative yields among different charmonium states [97, 98]. The measurement of ψ(2S) is much more difficult than that of J/ψ due to a much smaller production cross-section and dilepton decay branching ratio, resulting in a very low signal-to-background ratio. The ALICE Collaboration successfully measured the relative suppression of ψ(2S) and J/ψ in Pb+Pb collisions at forward rapidity [99], and the ATLAS and CMS Collaborations published the relative suppression in Pb+Pb collisions at mid-rapidity and high p_T [100, 101]. Attempts to measure ψ(2S) suppression in heavy-ion collisions at RHIC have not been successful to date. The low material budget and excellent particle identification capability of STAR together with the combined large data sample in runs 23 and 25 will provide a unique opportunity to measure the suppression of ψ(2S) at low p_T and mid-rapidity in heavy-ion collisions. Figure 47 shows the projections of ψ(2S) signal and the yield ratio of ψ(2S) and J/ψ from 20 B MB events in Au+Au collisions. Here the $\psi(2S)/J/\psi$ ratio is assumed to be 0.02, and the performance of detectors from existing data before STAR iTPC upgrade is used for the projection. As shown in the figure, the ψ(2S) signal significance will be around 3σ level in the 0-20% centrality bin. This significance could become even smaller depending on the level of further suppression for ψ(2S) compared to J/ψ. Despite the improvement of momentum and dE/dx resolution thanks to the STAR iTPC upgrade, it is crucial to have both the runs 23 and 25 data for a significant ψ(2S) measurement.

QGP Temperature from Di-lepton in the IMR

The dilepton mass spectrum has many contributions. A cocktail of known processes is subtracted to find the excess radiation. To gain a deeper understanding of the microscopic origin of the excess radiation, we will

- separate early from later time radiation by measuring dilepton elliptic flow (v_2) as a function of dilepton mass;
- identify the source of dilepton radiation by studying dilepton polarization versus invariant mass (helicity angle);
- measure precisely the lifetime of the interacting fireball. As an observable we will use integrated low-mass yield but also compare explicit model calculations with various $\tau_{fireball}$;

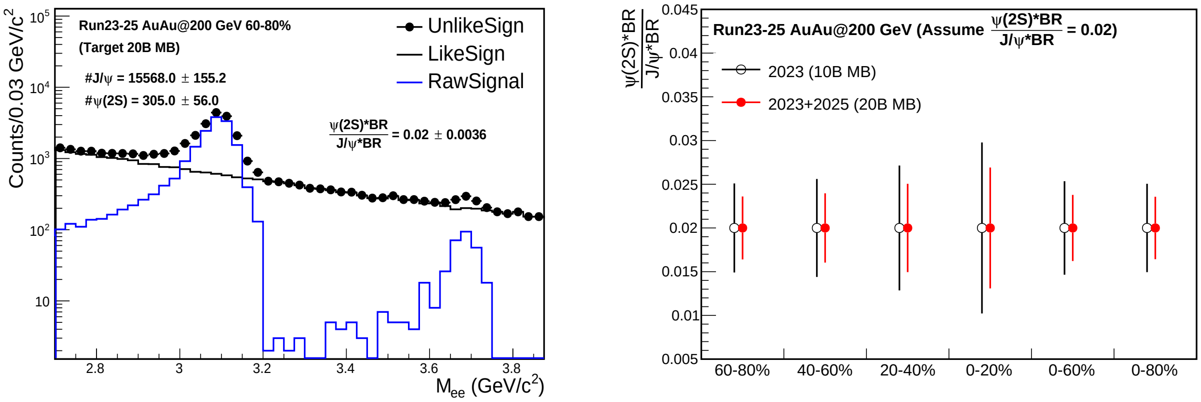

Figure 47: Projections for the J/ψ and ψ(2S) signals in 60-80% Au+Au collisions at 200 GeV and the yield ratio in various centrality bins.

- extract an average radiating source temperature from the fit of a Boltzmann distribution to the invariant mass slope in the range 1.1 - 2.5 GeV/c^2 spectrum. The higher the invariant mass, the stronger the QGP contribution to the spectrum, the higher the chance to measure temperature of the QGP.

The di-lepton intermediate mass region, between the peaks from the decays of the ϕ and $J\psi$, is dominated by thermal emission from the QGP. The slope of the spectrum in this region can be used as a blue-shift free measurement of the temperature at the time of di-lepton emission. As was shown in the Highlight section, di-lepton IMR temperatures of 301 ± 60 and 338 ± 59 were found for the $\sqrt{s_{NN}}$ = 27 and 54.4 GeV systems respectively. Extraction of a di-lepton temperature at $\sqrt{s_{NN}}$ = 200 GeV will be directly comparable to the temperatures suggested by the Υ and ψ (2s).

Last, but not least, concerning direct-photon emission, the existing difference, on the order of a factor of two, between the low momentum spectra from PHENIX and STAR in 200 GeV Au+Au collisions, has to be resolved. In order to clarify the direct photon puzzle we will measure with precision the direct virtual photon yield as well as its elliptic flow coefficient. We will particularly focus on low p_T η measurement which might be instrumental in clarifying this long standing question.

What are the electrical, magnetic, and chiral properties of the medium?

The QGP medium which is created during the collision of two heavy ions has significant electric fields, magnetic fields, vorticity, and chirality.

Pseudorapidity Dependence of Global Hyperon polarization ($P_H(\eta)$)

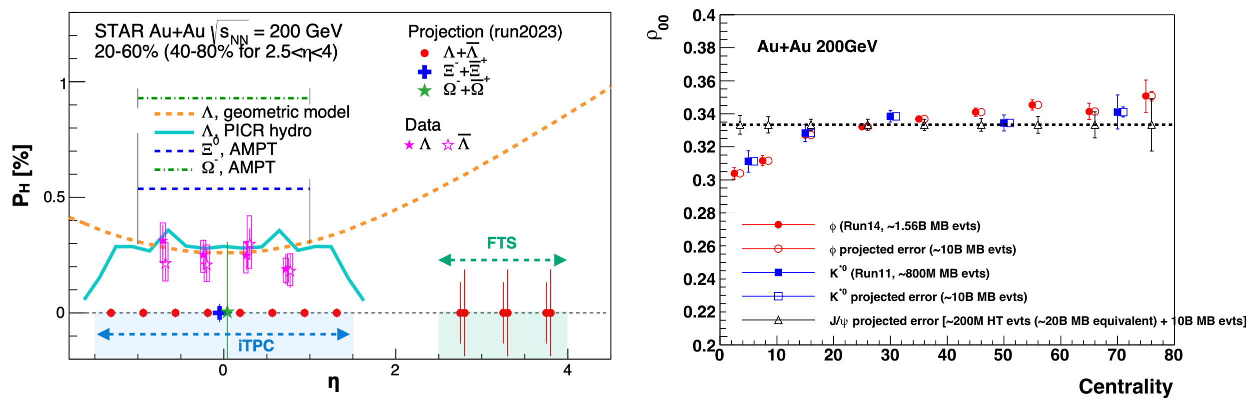

Figure 48: (Left) Projections (along with preliminary data) for differential measurements of $\Lambda(\bar{\Lambda}$ polarization over the extend range of pseudorapidity with the iTPC and FTS detectors of STAR that will help resolve tension between different theoretical model predictions (shown by curves) of polarization with η. In addition, projections for the measurements of spin-1/2 Ξ and spin-3/2 Ω particles are also shown. (Right) Spin alignment co-efficient ρ_{00} as a function of centrality, with projected errors. The enhanced statistics from run 23 and 25, combined with the excellent dilepton capabilities of STAR, will enable us to measure J/ψ alignment along with increasing the significance of the ϕ and K^{*0} measurements.

The global polarization of hyperons produced in Au+Au collisions has been observed by STAR [102]. The origin of such a phenomenon has hitherto been not fully understood. Several outstanding questions remain. How exactly is the global vorticity, and its associated strong magnetic fields, generated by the two incident heavy ions dynamically transferred to the fluid-like medium on the rapid time scales of a collision? Then, how does the local thermal vorticity of the fluid gets transferred to the spin angular momentum (magnetic moment) of the produced particles during the process of hadronization and decay? In order to address these questions one may consider measurement of the polarization of different particles that are produced in different spatial parts of the system, or at different times. A concrete proposal is to: 1) measure the $\Lambda(\bar{\Lambda})$ polarization as a function of pseudorapidity and 2) measure it for different particles such as Ω and Ξ. Both are limited by the current acceptance and statistics available as recently published by STAR [103]. However, as shown in Fig. 48 with the addition of the iTPC and FTS, and with high statistics data from runs 23 and 25 it will be possible to perform such measurements with a reasonable significance. iTPC (+TPC) has excellent PID capability to measure all these hyperons. Although the

FTS has no PID capability we can do combinatorial reconstruction of $\Lambda(\bar{\Lambda}$ candidates via displaced vertices. A similar analysis was performed and published by STAR using the previous FTPC [104]. In order to make a conservative projection we assume similar momentum resolution of $10-20\%$ for single charged tracks, similar overall tracking efficiency, charge state identification capability for the FTS and FTPC. We also assume the FTS, with it's novel-tracking framework, will be able to measure a minimum separation of 20 cm between the all pairs of one positive and one negative track (a possible decay vertex) from the main vertex of the event. This will give rise to about 5% efficiency of $\Lambda(\bar{\Lambda})$ reconstruction with about $15-20\%$ background contribution from $K_S^0 \rightarrow \pi^+ + \pi^-$ [104]. With this we can make projections for a polarization measurement in Au+Au 200 GeV $40-80\%$ as shown in Fig. 48. The two different error bars correspond to lower and upper limits considering current uncertainties on the efficiency of charged track reconstruction and the final efficiency of Λ reconstruction. Currently theoretical models predict contradictory trends for the pseudorapidity dependence of Λ polarization. If the initial local orbital angular momentum driven by collision geometry [105] plays a dominant role it will lead to increases of polarization with pseudorapidity. On the other hand if the local thermal vorticity and hydrodynamic evolution [106] play a dominant role it will predict decreasing trend or weak dependence with pseudorapidity. Such tensions can be easily resolved with the future proposed measurement during runs 23 and 25.

Global Spin Alignment of J/ψ

Surprisingly large signals of global spin alignment of vector mesons such as $\phi(1020)$ and $K^{*0}(892)$ have been measured via the angular distribution of one of their decay products. These experimental observations of vector meson spin alignment have yet to be interpreted satisfactorily by theory calculations. It has been realized that the mechanism driving the global polarization of hyperons can have its imprint on vector meson spin alignments albeit the observed strength of signals for the two measurements cannot be reconciled. In fact the large quantitative difference between the measurements of $\phi(1020)$ and $K^{*0}(892)$ spin alignment as shown in Fig 4 cannot be simultaneously explained by conventional mechanisms of spin-orbit coupling, driven by angular momentum, without invoking strong force fields. It is argued that the strong force field makes a dominant contribution to the spin-alignment coefficient ρ_{00} of ϕ, while for K^{*0}, the contribution is diminished due to the mixing of quark flavors (averaging-out of different meson fields) [11,107]. Therefore, the current experimental data from STAR [108] supports the role of strong force field as a key mechanism that leads to global spin alignment. An extended test of such a prediction can be performed by measuring the spin alignment of J/ψ. This is because similar arguments apply for both and J/ψ, i.e. like s and $\bar{s}$, the strong field component also couples to c and $\bar{c}$ quarks leading to large ρ_{00} for J/ψ. ALICE recently reported $\rho_{00} \approx 0.37$ for J/ψ at forward rapidity $(2.5 < y < 4)$ with a 3.9σ significance, seemingly supporting this argument. STAR can definitely contribute to this study by measuring J/ψ global spin alignment at mid rapidity with large data set taken during runs 23 and 25.

In Fig 48 we present the projected uncertainties for ρ_{00} of J/ψ estimated for various

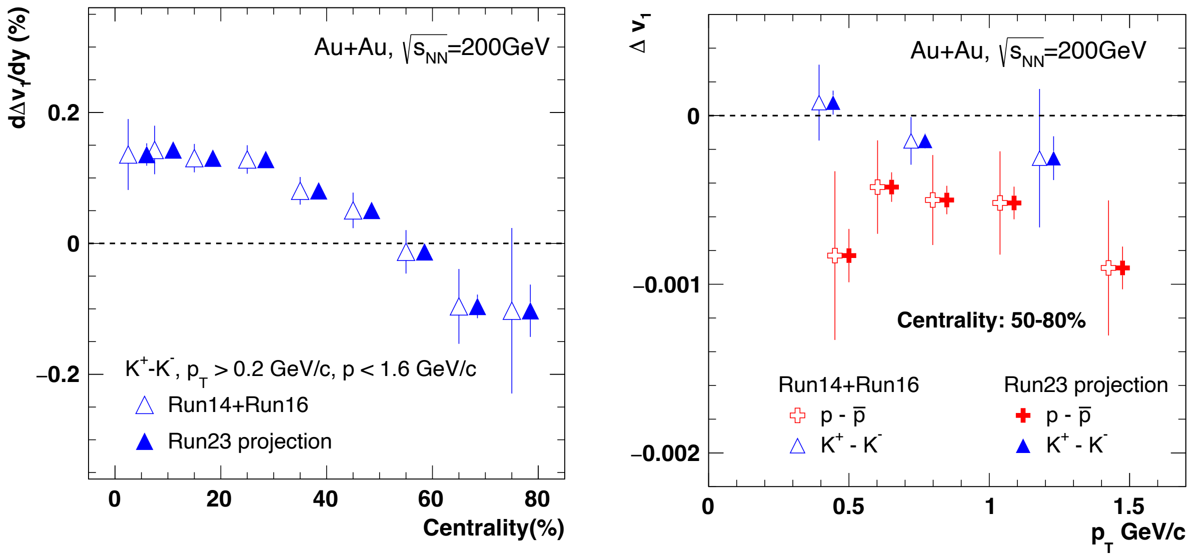

Figure 49: (Left) Plot shows the $\Delta dv_1/dy$ between K^+ and K^- as a function of centrality Au+Au collisions at $\sqrt{s_{NN}} = 200$ GeV. Open markers indicate the projection for Run 23. (Right) The $\Delta dv_1/dy$ of proton and kaon as a function of p_T in $50 - 80\%$ Au+Au collisions at 200 GeV.

centralities assuming: 1) 10 B min-bias events for low p_T J/ψmeasurements and, 2) 200 M events implementing High Tower (BHT3) triggers with the Barrel Electromagnetic Calorimeter for the high p_T J/ψ. Both assume 24 weeks running anticipated in Run 23. It is worth to mention that apart from J/ψ spin alignment, such a large statistics dataset will also allow addition differential study of global spin alignment of ϕ and K^{*0} and help to further elucidate the mechanism behind vector meson spin alignment.

Probing Electromagnetic Effect via Charge-dependent Directed Flow

One of the features in high energy heavy-ion collisions is the generation of an ultra-strong magnetic field, which is predicted to have the strength of 10^{18} Gauss [109–113]. The interplay between magnetic field and QGP may induce many interesting phenomena, such like the CME and CMW. Recent studies suggest that the charge dependent directed flow can be the probe to search for it in experiment [38, 114]. It predicts a negative $\Delta dv_1/dy$ between positively and negatively charged particles due to the influence of electromagnetic field. Some experimental efforts have been made for searching this effect, such as the charge dependent v_1 measurements presented by LHC-ALICE collaboration [115], and the directed flow of D^0 and $\overline{D^0}$ in RHIC-STAR experiment [116]. Results of light flavors in Pb+Pb collisions at $\sqrt{s_{NN}} = 5.02$ TeV show large discrepancy to theoretical calculations, which gives an order of magnitude larger and positive Δv_1 slope. Similar results have been obtained in Au+Au collisions at several energies at RHIC, which measured positive Δv_1 slope between proton and anti-proton in semi-central collisions owning to the transported quark contributions.

Recent analysis in Au+Au collisions at $\sqrt{s_{NN}} = 200$ GeV and isobar collisions shows striking centrality dependence of this Δv_1 slope. It was found that the $\Delta dv_1/dy$ between proton and anti-proton changes from positive to negative as centrality going from central to peripheral. The negative value in peripheral collisions, with the significance of 5σ, qualitatively agree with theoretical calculations. However, the $\Delta dv_1/dy$ between K^+ and K^-, π^+ and π^- are less significant because of the limitation of statistics. If 20 B events in Au+Au collisions at 200 GeV could be collected, the $\Delta dv_1/dy$ between K^+ and K^- will have the significance $> 5\sigma$, as illustrated in left panel of Fig. 49. Moreover, the EM-field prediction shows nontrivial p_T dependence, but this measurements are limited by current statistics. As illustrated in right panel of Fig.49, with the data accumulated in Runs 23 and 25, we will be able to measure the p_T dependence of $\Delta dv_1/dy$ with higher precision.

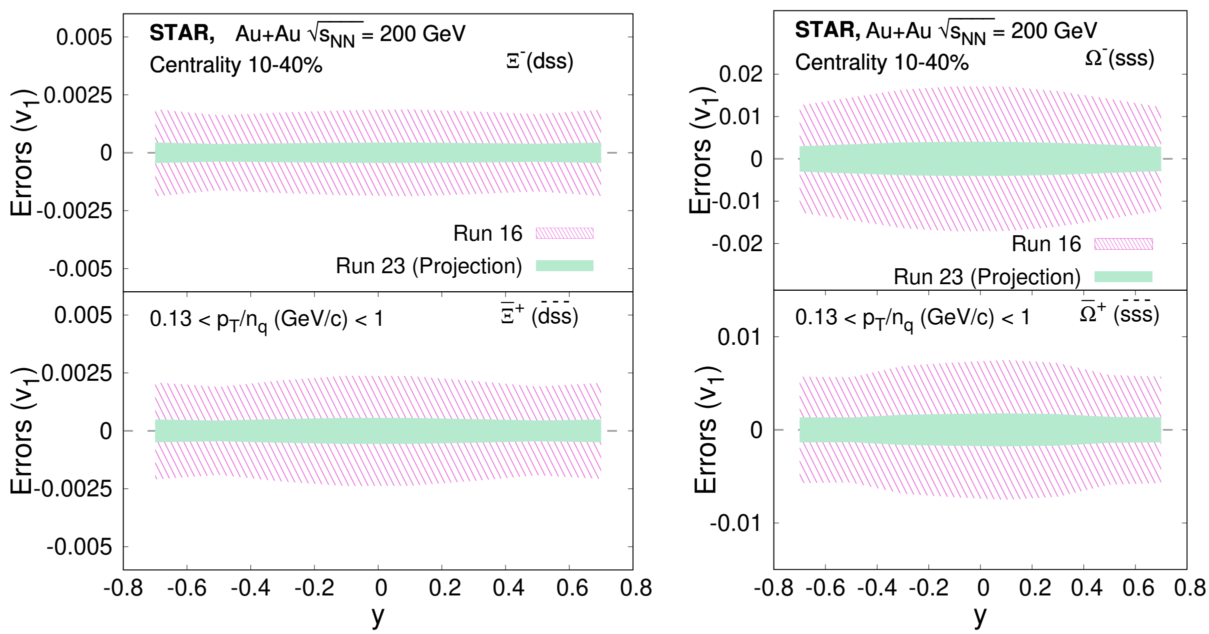

Figure 50: Projection of directed flow (v_1) of Ξ^-, $\overline{\Xi}^+$, Ω^- and $\overline{\Omega}^+$ as a function of rapidity (y) for 10%-40% centrality in Au+Au collisions at $\sqrt{s_{NN}} = 200$ GeV. The projections are made by assuming 20B events will be collected in runs 23 and 25.

The existing measurements of v_1 for Ξ and Ω in Au+Au collisions at $\sqrt{s_{NN}} = 200$ GeV have large uncertainties. There is a hint of a large v_1 for Ω baryons from recent measurements, however, as shown in Fig.50, the statistical uncertainties of the current STAR measurements are large. There are also measurements for electric charge and strangeness dependent splitting in Au+Au collisions at $\sqrt{s_{NN}} = 200$ GeV. These measurements also suffer from insufficient statistics. The EM field is expected to lead to increasing splitting with increasing electric charge difference. Recent STAR measurements using data from Run 16 were presented at the Quark Matter 2022 conference. Statistical uncertainties from such

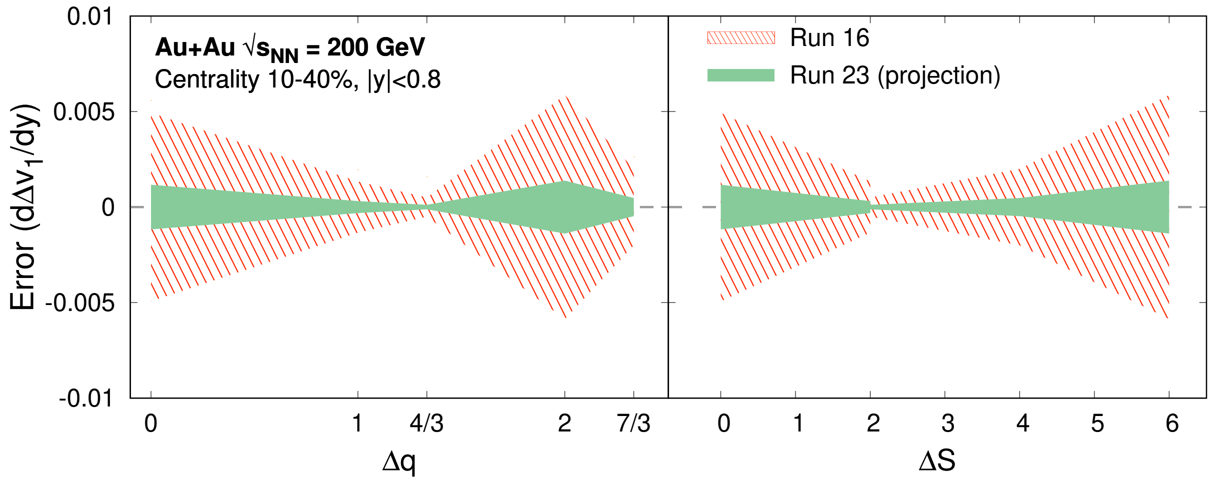

Figure 51: Δv_1 slope ($d\Delta v_1/dy$) at midrapidity as a function of electric charge difference (Δq) and strangeness difference (ΔS) for 10-40% centrality in Au+Au collisions at $\sqrt{s_{\mathrm{NN}}}$= 200 GeV. The projections are made by assuming 20 B events will be collected in runs 23 and 25.

measurements, as are shown in Fig.51, are limited by statistics. A large dataset (20B) from the upcoming Au+Au Runs 23 and 25 at $\sqrt{s_{NN}}$ = 200 GeV will definitely help improve the precision of these measurements. The projection plots, obtained by assuming that 20B events will be collected in the future runs (runs 23 and 25), are shown in Figs. 50 and 51.

Chiral Properties: ρ-a_1 Mixing

At $\mu_B \sim 0$ Lattice QCD works and can be directly tested against experimental results. In case the measured in-medium spectral function merges into the QGP description this would indicate a transition from hadrons into a structure-less quark-antiquark continuum, thus providing the manifestation of chiral symmetry restoration. We will continue to search for a direct signature of chiral symmetry restoration via chiral ρ-a_1 mixing. The signal is predicted to be detectable in the dilepton intermediate mass range. Difficulties are related to the fact that correlated charm-anticharm and QGP saturate the invariant mass region of 1.1 — 1.3 GeV/c^2. Therefore an accurate measurement of the excess dilepton yield, i.e. dilepton yield after subtraction of the cocktail of contributions from final-state decays, Drell-Yan and those from correlated heavy-flavor decays, up to invariant mass of 2.5 GeV/c^2 is required. The challenging analysis on charmed-decayed dielectron is ongoing from the datasets taken with the Heavy Flavor Tracker at STAR [117]. Thus deeper understanding of origin of thermal radiation in Au+Au collisions at $\sqrt{s_{\mathrm{NN}}}$ = 200 GeV from ∼zero mass up to 2.5 GeV/c^2 will become possible with rigorous theoretical efforts and improved dielectron measurements. Figure 52 shows the expected statistical and systematic uncertainties of the dielectron excess mass spectrum with all the detector upgrades and for the anticipated total Runs 23 and 25 statistics of 20 B events.

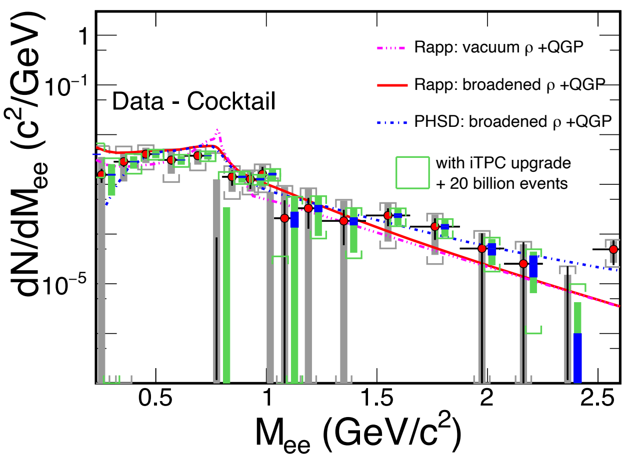

Figure 52: The expected statistical and systematic uncertainties on the dielectron excess mass spectrum with the iTPC upgrade compared to the current TPC case. The data are from our measurements in $\sqrt{s_{\rm NN}} = 200$ GeV Au+Au collisions [118]. Model comparisons are also shown. The boxes represent systematic uncertainties from data and the brackets represent the total systematic uncertainties including those from cocktails. The grey ones are for the current case while the green ones are for the Runs 23 and 25 case. The blue bands represent statistical uncertainties from 20 B min-bias events with the iTPC upgrade.

Electrical Conductivity (Dielectron LMR)

Another application of dielectrons is to use them to measure transport coefficients. The electrical conductivity can be directly obtained as the low-energy limit of the EM spectral function. We aim to extract such information by studying excess dielectron yields at the low-energy regime of the dilepton spectra and the conductivity peak at small invariant masses, i.e. at low invariant mass and low p_T^{ee}. Measurement of Drell-Yan in p+A collisions at low p_T would provide an important reference to constrain the dilepton cocktail.

Local Parity Violation and the Chiral Magnetic Effect A decisive experimental test of the Chiral Magnetic Effect (CME) has become one of the major scientific goals of the heavy-ion physics program at RHIC. The existence of CME would be a leap towards an understanding of the QCD vacuum, establishing a picture of the formation of a deconfined medium in which chiral symmetry is restored, and it would also provide unique evidence that the strongest known electromagnetic fields are created in relativistic heavy-ion collisions [119, 120]. The impact of such a discovery would go beyond the community of heavy-ion collisions and will possibly be a milestone in physics. The remaining few years of RHIC running and analyses of previously-collected data will likely provide the only chance for CME searches in heavy-ion collisions in the foreseeable future.

The isobar collisions provided an unique opportunity to search for the CME because of the $\sim 15\%$ difference in B^2 and hence the CME correlation signals between Ru+Ru and Zr+Zr collisions. No CME signal has been observed in isobar data even with an improved understanding of background baseline. The signal/background ratio is expected on general

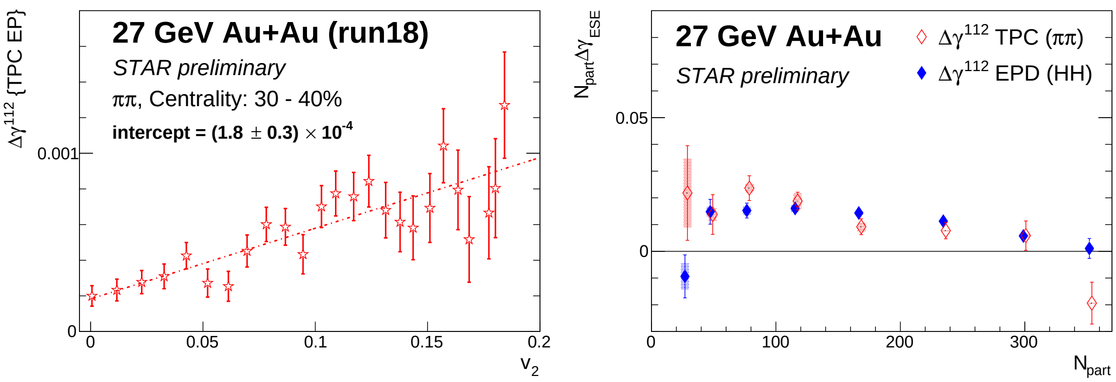

Figure 53: (Left) $\Delta\gamma_{112}$ for π-π vs v_2 measured with the TPC event plane in 30–40% Au+Au collisions at 27 GeV. (Right) $\Delta\gamma_{112,\mathrm{ESE}}$ scaled by N_{part} as a function of N_{part} for π-π using the TPC event plane, and for hadron-hadron using the EPD event plane in Au+Au collisions at 27 GeV.

ground to be smaller in isobar collisions than in Au+Au collisions by an approximately factor of 3 [6]. This would be in line with the Au+Au data which indicate a positive CME signal of $\sim 8\%$ with $\sim 2\sigma$ significance using the spectator/participant plane method [3].

The current Au+Au data statistics are total 2.4 B events from Runs 2011, 2014 and 2016 [3]. In order to achieve 5σ significance with the same analysis one needs to have 15 B events. Therefore, with the proposed 20 B events that can be collected by STAR during runs 23 and 25, one can achieve more than 5σ significance provided the possible CME signal remains at 8%. A stringent upper limit will be possible on the CME.

This estimate does not account for two important facts that can lead to higher significance. The first is that the iTPC upgrade enhances the charge particle multiplicity by 50% and therefore triplet($\sim dN/d\eta^3$) (pair $\sim dN/d\eta^2$) statistics by a factor of 3.4 (2.3). The second one is the addition of the EPD detector which will significantly reduce nonflow contaminations in the measurements with respect to the participant plane. Our estimate assumes that the systematic uncertainty can be controlled to be smaller than the statistical uncertainty, i.e. below 1%.

Running STAR in runs 23 and 25, concurrently with sPHENIX, would be essential to perform precision measurements to further investigate and characterize the CME phenomenon. Such a program will have a strong discovery potential.

The dominant background in the CME-sensitive $\Delta\gamma_{112}$ correlator is caused by the coupling of elliptic flow and other mechanisms such as resonance decays and local charge conservation. Accordingly, the event-shape engineering (ESE) method aims to project $\Delta\gamma_{112}$ to a class of events with minimal flow to suppress the v_2-related background. We adopt an ESE technique [121] that uses the flow vector ($q_{2,x} = \frac{1}{\sqrt{N}}\sum_i^N \cos(2\phi_i)$, $q_{2,y} = \frac{1}{\sqrt{N}}\sum_i^N \sin(2\phi_i)$) to select spherical sub-events with almost zero v_2. Observables like v_2 and γ_{112} are measured as a function of q_2^2 from the particles of interest (POIs), and then $\Delta\gamma_{112}$ is plotted against v_2 in the same q_2^2 interval to yield a reliable projection to the zero-flow mode.

Figure 53 (left) demonstrates the application of the ESE approach to the STAR data of 30–40% Au+Au collisions at 27 GeV (run 2018), and the decrease of $\Delta\gamma_{112}$ for π-π with decreased v_2 illustrates how the v_2-related background is suppressed. Figure 53 (right) shows the centrality dependence of $N_{\rm part}\ \Delta\gamma_{112\rm ESE}$ for π-π using the TPC event plane, and for hadron-hadron using the EPD event plane in Au+Au collisions at 27 GeV.

The ESE method will be applied to the 200 GeV Au+Au data from Run-23 and Run-25. With the large data set of anticipated 20 B events, we are able to perform more differential measurements and involve identified particles such as kaons and protons.

Event-by-event correlations between CME charge separation and other parity-odd features of the event will be studied. One such analysis is motivated by the idea that the local parity violation (characterized in each event by a net topological charge Q) that is expected to work with the spectator-produced magnetic field to give the CME should also cause a net helicity of $\Lambda(\bar{\Lambda})$ in the event. Importantly, even though both of these parity-odd signatures switch handedness event-by-event, in any given event they should have the same handedness as one another and so can be compared with one another in a correlation analysis. To do this, the charge separation with respect to the first-order reaction plane must be determined in each event.

We are looking for evidence of an event-by-event correlation between these two parity-odd effects. A measured event-by-event correlation between Δa_1 and ΔN would be strong evidence for the CME and underlying local parity violation, and would extend the measurement into other parity-odd effects. Note also that the flow-related backgrounds that plague charge-separation measurements are not expected to affect ΔN and so should not be a background for this correlation measurement.

We use a similar toy model to that used in [122] to estimate the number of events required to see non-zero correlations between Δa_1 and ΔN with different CME signal fraction in the $\Delta\gamma$ measurement (see Fig. 54). The chief unknown in this estimate is the extent to which strange quarks may be counted as light quarks and so will have a net handedness imparted by the parity-odd domain. Recent theoretical work [123] makes a direct connection between the net lambda helicity and the axial chemical potential developed from local parity violation. Such work holds promise of leading to an improved estimate of the expected signal size, but it is likely that this will remain a speculative measurement in which a non-observation will be difficult to interpret quantitatively but a positive observation would be a very significant result.

Figure 54 suggests that this will be a topic requiring the large datasets of runs 23 and 25. To explore this correlation, we have analyzed the Run-18 Au+Au collision data at $\sqrt{s_{NN}}$ = 27 GeV. The $\Lambda(\bar{\Lambda})$ baryons are reconstructed by their decay daughter tracks and identified by the `KFParticle` package. Each Λ handedness is estimated by decay kinematics. After a purity correction, $N_{\rm L}$ and $N_{\rm R}$ are calculated for both Λ and $\bar{\Lambda}$ in each event, and then Δn (normalized ΔN, $\Delta n = \frac{N_{\rm L}-N_{\rm R}}{\langle N_{\rm L}+N_{\rm R}\rangle}$) is calculated. The observable Δa_1 can be calculated from primordial particles' azimuthal angles w.r.t. the first-order EP measured by the EPD. The covariance between Δn and Δa_1 is then calculated for the event sample. In this exploratory measurement, the covariance is consistent with zero, and so no significant correlations have been observed (see Fig. 55). However, this event-by-event correlation method

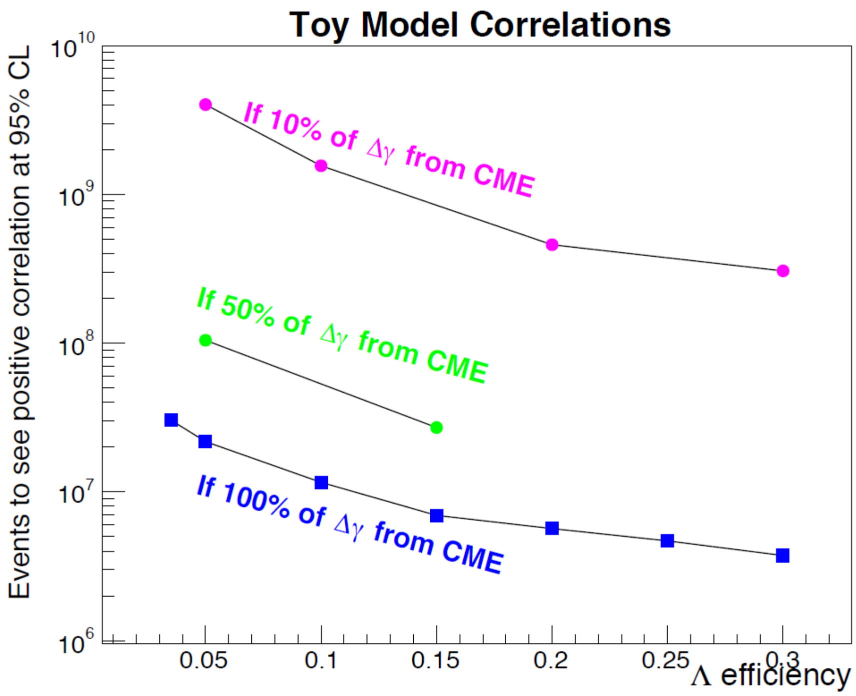

Figure 54: Estimation of the number of events required to see positive correlation between net Λ helicity with out-of-plane charge separation sensitive to local parity violation at 95% confidence level, plotted against the efficiency of $\Lambda(\bar{\Lambda})$ reconstruction (see Ref. [122] for details).

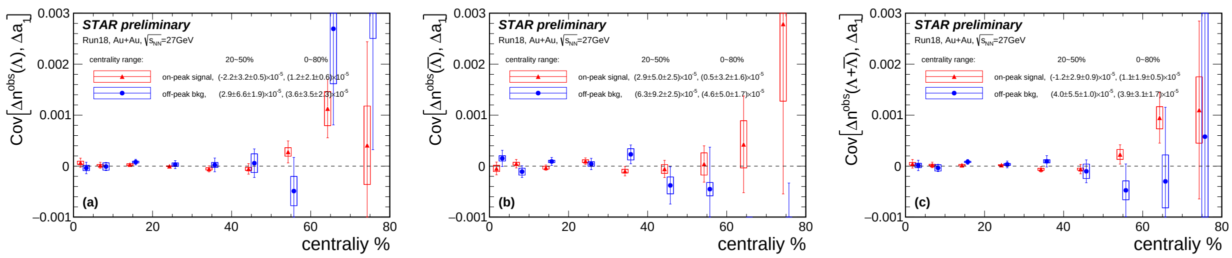

Figure 55: The covariance between Δa_1 and measured Δn for Λ (Left), $\bar{\Lambda}$ (Middle), and the sum of them (Right) as functions of centrality. The red markers come from the $\Lambda(\bar{\Lambda})$ mass peak region with purity correction and blue markers come from the side bands for pure background.

holds great potential with future high statistics data from Runs 23 and 25 by a qualitatively new technique different from all existing analyses.

What are the underlying mechanisms of jet quenching?

The dependence of jet energy loss on the jet p_{T} and/or resolution or angular scale tagged by jet substructure observables are key tools in discriminating various jet quenching mechanisms [124–127]. In addition, the measurement of jet acoplanarity is a sensitive probe of p_T broadening and medium-induced radiative effects [128], particularly for jets at low p_{T} which are accessible at STAR by selecting a given momentum transfer via a photon trigger. Such a measurement is also affected by background arising from vacuum Sudakov radiation at RHIC energies [129, 130], potentially enabling a precise extraction of in-medium jet scattering.

STAR's unique geometry allows collection of events over a wide range of vertex positions along the beam direction (vz) for jet analyses, thereby efficiently sampling the provided RHIC luminosity. Optimization of the vz range used in the various analyses involves a balance between statistical precision and complexity of corrections, with the latter predominantly contributing to the systematic uncertainties of the measurement. Recent STAR jet measurements in Au+Au collisions have employed two classes of vz cuts: the inclusive charged-particle jet analysis [131] utilizes $|\mathrm{vz}| < 30$ cm, whereas the $\gamma_{\mathrm{dir}}+$jet analysis utilizes $|\mathrm{vz}| < 70$ cm. With the $\gamma_{\mathrm{dir}}+$jet measurement successfully utilizing the broad vz range with controlled systematic precision, we are exploring similar event selections maximizing the available statistics for future jet measurements, including the inclusive/differential jet analyses. In the following discussions, we assume an integrated luminosity of 40 nb^{-1}, which is roughly a factor 4 increase in trigger statistics relative to the current analyses based on Run 14 data.

To quantify the effect of the marked increase in integrated luminosity, we utilize two mature jet measurements and discuss their expected improvements. These analyses are the semi-inclusive distribution of charged-particle jets recoiling from a high-E_{T} direct-photon trigger ($\gamma_{\mathrm{dir}}+$jet); and the differential measurement of energy loss for jet populations selected by varying a substructure metric. Since these analyses are mature, their analysis methodologies and correction schemes are optimized, so that their projections based on increased statistics are meaningful.

Semi-inclusive $\gamma_{\rm dir}+$jet measurements (I_{AA})

Figure 56 shows $I_{\rm AA}$ for fully-corrected semi-inclusive distributions of charged-particle jets (anti-$k_{\rm T}$, $R=0.5$) recoiling from a direct-photon trigger with $15 < E_{\rm T} < 20$ GeV in central Au+Au collisions at $\sqrt{s_{\rm NN}} = 200$ GeV, for the current analysis based on 10 nb^{-1} [132] within $|{\rm vz}| < 70$ cm. The projected uncertainties, including the previous years and runs 23 and 25, are shown in green bands. Significant reduction in the uncertainty band is seen resulting from the increase in integrated luminosity, together with a significant increase in kinematic reach as indicated by the extended green band along the x-axis.

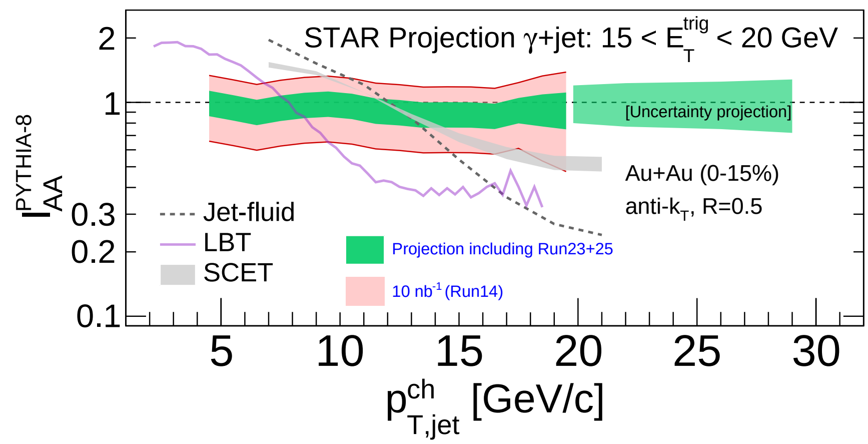

Figure 56: Projections of the $I_{\rm AA}$ for semi-inclusive anti-$k_{\rm T}$, $R=0.5$ jets recoiling from a direct-photon trigger with $15 < E_{\rm T} < 20$ GeV for central (0-15%) Au+Au collisions at $\sqrt{s_{\rm NN}} = 200$ GeV. The colored bands show the cumulative uncertainties for the current analysis and projections for future analysis with the higher statistics datasets.

The luminosity projection of 40 nb^{-1} is expected to reduce the systematic uncertainty band by a factor of 2 from the current measurement since systematic uncertainty of this measurement, dominated by the unfolding procedure, is correlated with the statistical precision. Due to this correlation, the improvement shown in Fig. 56 should be regarded as a conservative estimate of the improvement in precision of this measurement with the projected integrated luminosity increase.

Jet acoplanarity

The $p_{\rm T}$ broadening due to medium effects not only modifies the shape but also introduces a decorrelation between the di-jet angular distributions. The vacuum QCD process (Sudakov radiation) makes such measurements challenging in heavy-ion collisions, but at RHIC the Sudakov effect is smaller than at the LHC as it depends on the virtuality Q^2 [129, 130]. A detailed study is needed to understand both effects (medium-induced and vacuum radiation) in a wide range of jet $p_{\rm T,jet}$ both at RHIC and the LHC energies. Such measurements are crucial to probe $\hat{q}$ and/or quest for the predicted large-angle jet scattering off of quasi-particles in the QGP [133].

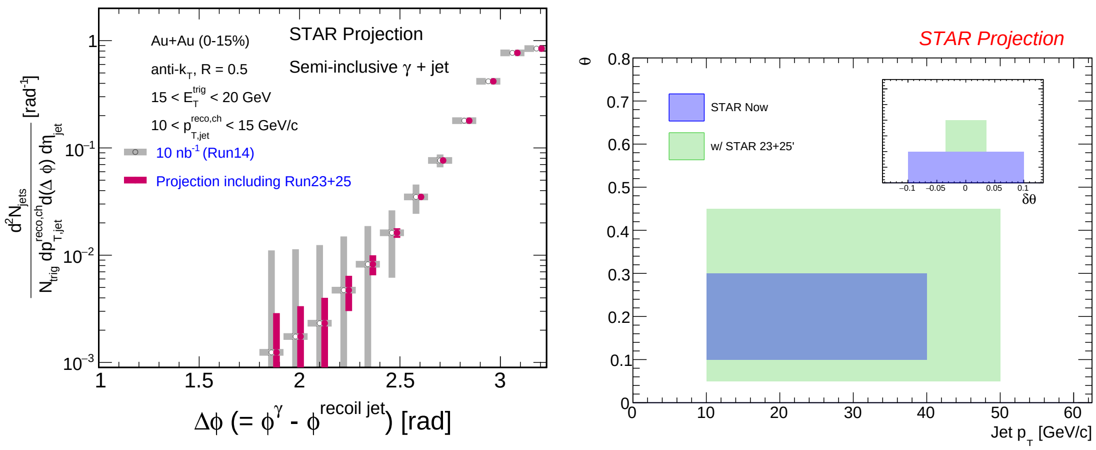

Figure 57: Left: Projections of the acoplanarity for semi-inclusive anti-k_T, $R = 0.5$ jets recoiling from a direct-photon trigger with $15 < E_\mathrm{T} < 20$ GeV and $10 < p^\mathrm{ch}_\mathrm{T,jet} < 15$ GeV/c for central (0-15%) Au+Au collisions at $\sqrt{s_\mathrm{NN}} = 200$ GeV. The colored bands show the cumulative uncertainties for the current analysis and projections for future analysis with the higher statistics datasets. Right: The subjet opening angle as a function of jet $p_\mathrm{T,jet}$ in 0-20% central Au+Au collisions. The inset is the corresponding resolution of θ. Blue and green represent current (10 nb^{-1}) and future (including runs 23 and 25) analyses, respectively.

In this direction, the STAR experiment reports the first signature of medium-induced acoplanarity in the central Au+Au collisions as discussed in section 1.1.5 Fig. 20 (right figure). This measurement is performed for both γ_dir and π^0 triggers with $11 < E_\mathrm{T} < 15$ GeV and charged-particle jets (anti-k_T, $R = 0.2$ and 0.5) with $10 < p^\mathrm{ch}_\mathrm{T,jet} < 15$ GeV/c. To have a better understanding of the nature of this acoplanarity, we plan to extend both $E^\mathrm{trig}_\mathrm{T}$ and recoil jet $p_\mathrm{T,jet}$ kinematic ranges which demands high statistics datasets. On the other hand, the STAR experiment also reports the same measurements in p+p collisions to study the shape of this acoplanarity in vacuum. In this direction, both γ_dir+jet and π^0+jet measurements would be crucial to study trigger dependence of $\Delta\phi$ decorrelation between the trigger and recoil jets in p+p collisions and sets a baseline for Au+Au collisions. However, due to limited statistics we only report π^0+jet measurement in p+p collisions as shown in Fig. 20 left. Furthermore, this measurement could exploit forward triggering using forward calorimeter to explore a relatively small x region, compared to mid-rapidity measurement, in p+p collisions. This is important to study various pQCD effects like NLO corrections, ISR/FSR, and MPI effects. Upcoming Run-24 p+p collision data-taking is very important in this direction.

The left plot of Fig. 57 shows the semi-inclusive distribution of the azimuthal separation between a direct-photon trigger with $15 < E_\mathrm{T} < 20$ GeV and a charged-particle jet (anti-k_T, $R = 0.5$) with $10 < p^\mathrm{ch}_\mathrm{T,jet} < 15$ GeV/c, in central Au+Au collisions at $\sqrt{s_\mathrm{NN}} = 200$ GeV with only statistical uncertainties. The azimuthal smearing of this observable due to uncorrelated background is small, and such acoplanarity measurements are therefore strongly statistics-limited [134,135]. The grey vertical bars represent the statistical uncertainty with the current preliminary measurement based on 10 nb^{-1}, whereas the red vertical bars correspond to including Run-23+25.

Differential Measurement of Energy Loss Tagged with a Substructure Metric Systematic exploration of parton energy loss controlled for variations in the jet shower forms an integral part of the jet program at STAR. Since parton showers are inherently probabilistic, a jet population contains patterns of radiation varying in both angle and momentum scales which can be extracted via jet substructure measurements defined based on jet constituents' angle and/or momentum via algorithms or correlations. By selecting jets based on their substructure, STAR can differentially measure jet-medium interactions for various types of energy loss e.g. color coherence, dead cone, etc. In other words, the STAR jet program for Run-23+25 will focus on jet substructure as a jet-tagger.

Theory calculations show significant differences between energy loss signatures for jets perceived by the medium as a single or multiple color charges [126]. The integrated luminosity from the Runs 23 and 25 datasets not only provide a substantial increase in statistics in the current measurements of jet substructure, they also increase the available phase space for rare processes such as wide angle emissions from high-p_{T} jets. This enables STAR to extend our current measurements of differential energy loss from a resolution of $\delta\theta = 0.1$ to finer resolution $\delta\theta \approx 0.025$ in the jet opening angle as shown in Fig. 57 (right), and also extend to jets of higher momenta. By extending to high energy splittings within jets at varied opening angles, we can probe earlier formation times whereby vacuum-like emissions and medium induced radiations are expected to occur.

Given the unique nature of jet-medium interactions at RHIC, with the jet and sub-jet scales sufficiently closer to the medium scale than the LHC, the aforementioned measurements bolster the importance of the STAR jet program with the goal of extracting the microscopic properties of the QGP as outlined in the 2015 LRP.

What is the nature of the phase transition near $\mu_B = 0$?

LQCD calculations [136, 137] predict a sign change of the susceptibility ratio χ_6^B/χ_2^B with temperature (T at $\mu_B = 0$) taking place in the range of 145-165 MeV. The observation of this ratio going from positive to negative values is considered to be a signature of a crossover transition. Interestingly, as shown in Section **??**, values of net-proton C_6/C_2 are found to be negative systematically from peripheral to central Au+Au 200 GeV collisions within large statistical uncertainties. The observation of negative C_6/C_2 is intriguing and so far only hinted at in the 200 GeV data, the current result has less than 2.3σ significance for 30-40% centrality in terms of statistical uncertainties. The current systematic uncertainty is of similar order as the statistical uncertainty and if based off of combining datasets from Run-10 and Run-11. As shown in the projection plot of Fig. 58 it is possible to establish definitive

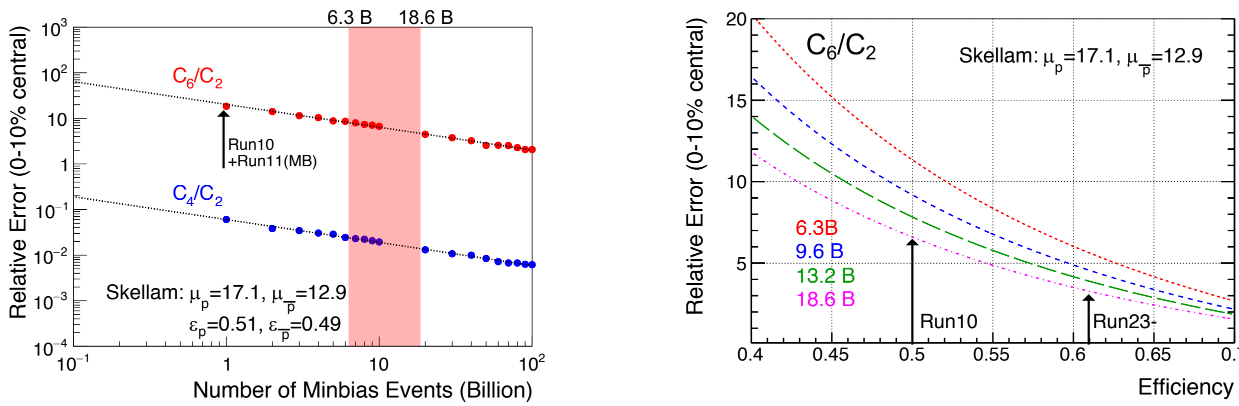

Figure 58: Projection for measurement of ratio of sixth order over second order cumulants of net-proton distribution.

observation of negative C_6/C_2 at 200 GeV the 20 B minimum-bias events to be collected during the run 23 and 25 with 15% increase in the reconstruction efficiency and enhanced acceptance of the iTPC detector upgrade. A similar measurement can be performed at the LHC for vanishing baryon chemical potential, while only STAR measurements can explore the finite $\mu_{\rm B}$ region. Our measurement at $\sqrt{s_{\rm NN}}$ =200 GeV has the potential to establish the first experimental observation of QCD chiral crossover transition at $\mu_{\rm B} \approx 20$ MeV.

What can we learn about the strong interaction?

The strong interaction between baryons leads to a residual force; the most common example is NY. The same force is responsible for binding n-p into d. So far, understanding the strong interaction has been limited to the effective theories related to nucleons and the scattering experiments, which are very challenging due to the short lifetime of those baryons (a few cm decay length). One of the current challenges is to evaluate the strong interaction between hyperons, as experimentally still very little is known about NY and YY interactions. Hypernuclei (a hyperon bound inside an atomic nucleus) are proof of a positive, attractive interaction of NY. Measurements of NN and NY interactions have crucial implications for the possible formations of bound states. Studies of the strong interaction potential via two-particle correlations in momentum space measured in relativistic heavy-ion and elementary collisions have proven to be useful to gain access to the interactions between exotic and rare particles. Possible combinations can be: $p\Lambda$, $p\Sigma$, $p\Omega$, $p\Xi$, $\Lambda\Lambda$, $\Xi\Xi$. In contrast to $p\Lambda$, the nature of $p\Sigma$, $p\Omega$, $\Lambda\Lambda$ still need experimental verification. Even if scattering experiments are available, they are not very conclusive.

Figure 59 shows the preliminary $p\Xi$ correlations function. All available statistics, 3 B events accumulated over all previous runs, were used for the $p\Xi$ and $p\Omega$ cases. Combining such datasets leads to the run-to-run variations resulting in larger total systematic uncertainties in the detector responses. A long run with similar detector settings during the runs 23 and 25 will avoid such issues. Statistical uncertainties of the current measurements re-

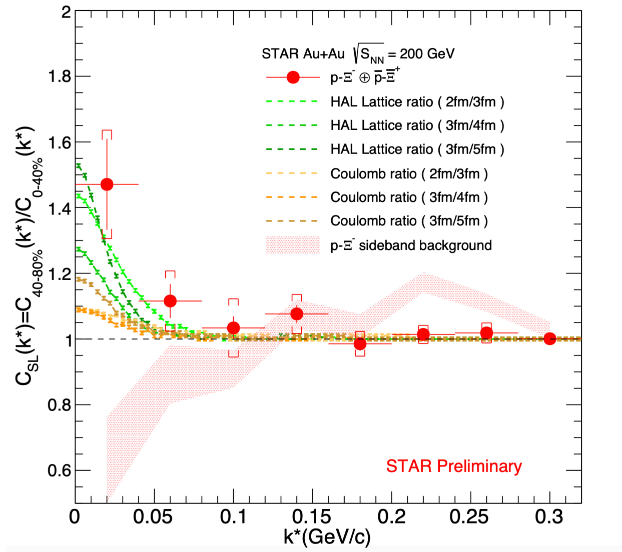

Figure 59: Solid circles represent the ratio (R) of the small system (40-80% collisions) to the large system (0-40% collisions) for proton–Ξ and $\bar{p}$–Ξ correlations. The bars correspond to the statistical uncertainties. The shaded area represents R for background candidates from the side-band of the Ξ invariant mass. Coulomb-induced R are shown in yellow and orange colors. HAL Lattice predictions of R are shown in green.

main high, and the number of points that build the correlation function is minimal. This means that the current results are not conclusive enough to study in detail the parameters of the strong interaction. The collection of 10 B events from run 23 will make possible the construction of correlation functions of the $p\Xi$ case with double the number of points and smaller statistical uncertainties than the current measurement.

The $p\Omega$ system is more statistics hungry, and will require 20 B events, from combining runs 23 and 25. Previous STAR measurements of $p\Omega$ correlations show that the parameters of the strong interaction can be studied. However, with higher data collections, more precise and detailed studies would be possible.

The description of the $\Lambda\Lambda$ interaction is still an open issue. Such a description is fundamental since it plays a decisive role in understanding the nature of hyperons that appear in neutron stars. If many hyperons appear close to each other and their fraction becomes significant, the YY interactions are expected to play an essential role in describing the equation of state of the dense system. An alternative way to study hypernuclei is two-particle momentum correlations of $\Lambda\Lambda$ pairs produced in hadron-hadron collisions thanks to femtoscopy. Figure 60 shows primary $\Lambda\Lambda$ (left) and $\Xi\Xi$ (right) correlation functions. For current $\Lambda\Lambda$ and $\Xi\Xi$ systems also data from all previous runs were combined. Due to differences between individual runs, a significant source of systematic uncertainties exist now, and it will disappear with all events collected during run 23 for the $\Lambda\Lambda$ case. More critical seems to be the increased statistics for the $\Xi\Xi$ case, and having 20 B events from runs 23 25 enables the reduction of

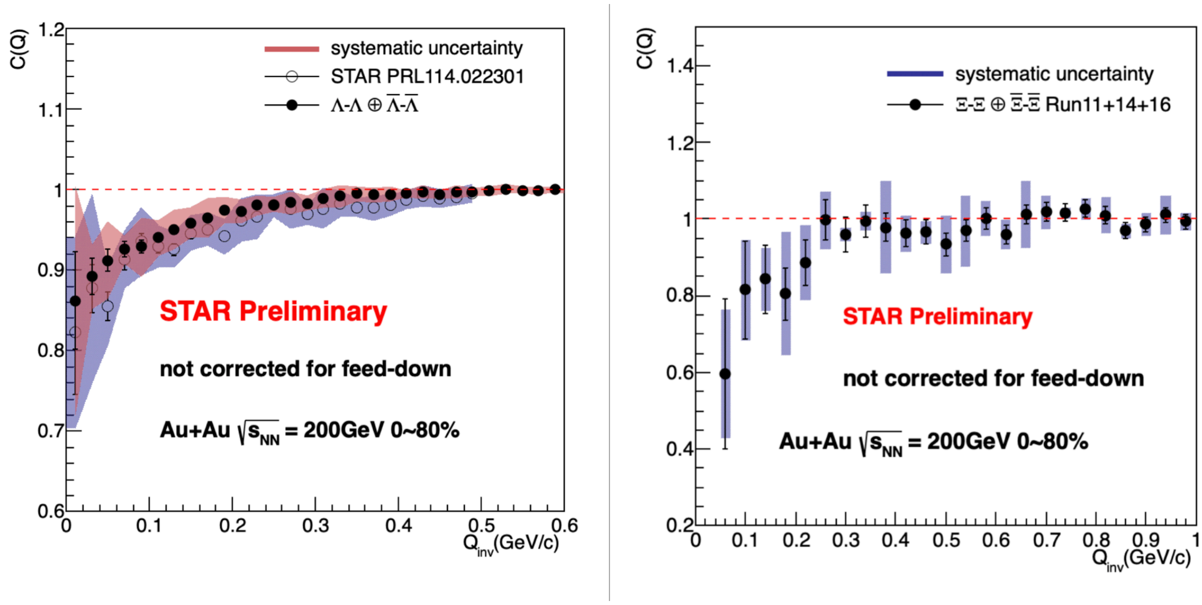

Figure 60: Left: combined ΛΛ and $\bar{\Lambda}\bar{\Lambda}$ preliminary correlation functions with systematic uncertainties compared with already published previous STAR results. Right: combined ΞΞ and $\bar{\Xi}\bar{\Xi}$ correlation functions with systematic uncertainties.

statistical uncertainties significantly and makes it possible to determine parameters of the strong interaction with higher precision. Having combined data from the runs 23 and 25 will also allow the hypotheses about possible bound states to be verified.

2.2 Ultra-Peripheral Collisions

One of the most important scientific goals in high-energy nuclear physics is to understand the nuclear structure under extreme conditions. Thanks to ultra-relativistic heavy-ion collider facilities, e.g., the Relativistic Heavy-Ion Collider, one direction is to create a system that has an extremely high temperature of partons, and study its deconfined properties of strongly interacting quarks and gluons. However, the other direction is to reveal the property of nucleons and nuclei before such violent collision happens, where the initial-state dynamics inside these particles may provide ultimate understanding of the Quantum Chromodynamics (QCD) in generating the visible matter. These two aspects are usually known as the heavy-ion hot Quark-Gluon-Plasma (QGP) physics and cold QCD physics, respectively. Both of them are indispensable building blocks of our fundamental understanding of nuclear physics. In this section, we will focus on the initial-state physics program via the ultra-peripheral collision in nucleus-nucleus (AA) interactions.

In relativistic heavy-ion collisions, a large fraction of the total cross section or interaction between the two colliding nucleus is provided by photon-induced reactions. Most of these events are removed by the requirement of inelastic collisions, because the hot quark-gluon-plasma (QGP) can be more likely, if not only, to be produced in such high parton density system. However, these events are difficult to understand if one wants to separate effects related to the initial state, e.g., nuclear parton distribution functions (nPDFs), from final-state interactions, such as fragmentation, medium-induced collective effects, etc. One way to overcome this difficulty is to "turn off" the QGP and use a simple and clean probe to examine the nuclear target - photon-nucleus collisions, which is also known as the "ultra-peripheral collisions" (UPC).

Typically, the UPC takes places when the impact parameter between the two colliding nucleus is greater than the sum of their radii. The interaction is initiated by one or multiple photons emitted from the moving charged ions, where the photon interacts with the other nucleus. Due to the large mass of the heavy nucleus, the emitted photons have very small virtualities or very small p_T. This process is regarded as *photoproduction*. For example, diffractive Vector Meson (VM) photoproduction has been extensively studied at the RHIC and at the LHC, where the gluon density distribution of the nucleon and nucleus target can be directly probed. In recent analyses carried out by the LHC collaborations [138–145], photoproduction of the J/ψ meson has been measured in UPCs of heavy ions. The resulting cross sections were found to be significantly suppressed with respect to that of a free proton [138,139,143,144]. Leading Twist Approximation (LTA) calculations strongly suggest that the suppression is caused by the gluon shadowing effect [146–148], while other models, e.g., the Color Dipole Model with gluon saturation and nucleon shape fluctuations [149], can also describe the UPC data qualitatively. The mechanism of gluon density modification in the nuclear environment remains unknown.

However, there are other processes of photoproduction that are sensitive to the nPDFs. For example, inclusive and diffractive back-to-back jets (dijets) in nuclei are sensitive to both quark and gluon distribution, and it is theoretically easier to be used in the global PDF analysis. Recent studies from Refs. [150–152] have shown the uncertainty of nPDFs can be reduced by a factor of 2 by having these experimental measurements. In addition, the incoming low-virtuality photons can have properties of a point-like particle (direct process) or a hadron with partonic substructure (resolved process). The dijets photoproduction process can be extremely useful in constraining the photon structure, which still remains poorly known to-date. Finally, the diffractive dijets contribution is a sensitive experimental observable to understand the QCD factorisation breaking and the diffractive nPDFs.

Last but not least, inclusive particle photoproduction at high energy provides important insights to the *soft physics* of photon-nucleus interactions, where cold nuclear matter and Intra-Nuclear Cascade can be studied via fragmentation in both current and target fragmentation regions. One recent study led by Chang et al [153] has shown the difficulty of describing the charged particle production in nuclei of existing E665 experimental data. Although the experimental data is with higher photon virtualities, not many data exists at high energy at all for photoproduction. Furthermore, inclusive charged particle photoproduction can be a baseline for comparison to the diffractive VM production, where different theoretical models have drastically different prediction, e.g., gluon saturation model [149] verse nuclear shadowing model [146–148]. Together with the VM production and with different level arm of photon virtualities, this measurement is one of the most important scientific goals at the upcoming US-based Electron-Ion Collider (EIC).

Hereby, we propose to utilize the unique capability of the RHIC experimental program in the upcoming 2023-2025 runs with the STAR detector and its recent forward upgrades, to study photoproduction processes in details. The major advantage is that the top RHIC energy can access a kinematic regime that is hardly, if not at all, accessible by the LHC experiments, and provide a seamless transition to the physics at the EIC.

Photoproduction of Vector-Meson

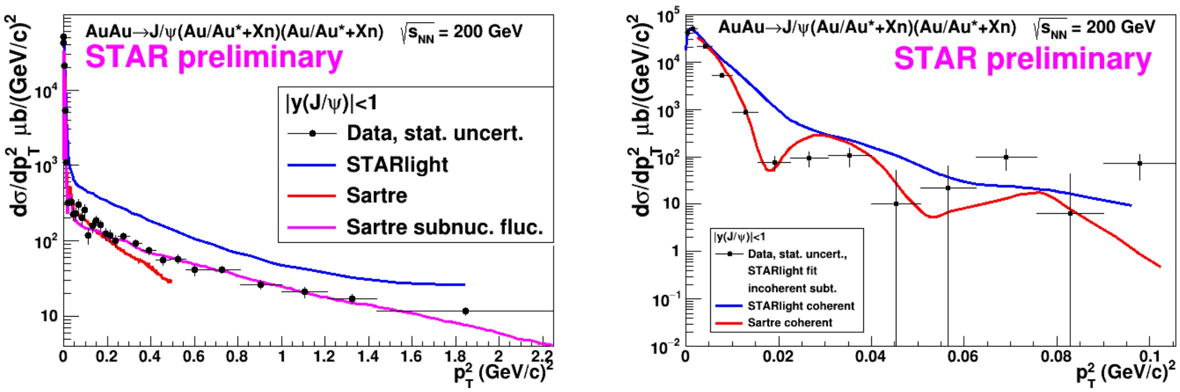

Figure 61: Left: differential cross section $d\sigma/dp_T^2$ of J/ψ photoproduction as a function of p_T^2 in Au+Au UPC at 200 GeV. Right: the same cross section but with incoherent contribution subtracted.

One of the most important and direct measurements of the gluon density in the initial-state of nuclei is the photoproduction of Vector-Meson, e.g., ρ^0, ϕ, and J/ψ. The process can be generally considered in a color dipole picture, where the quasi-real photon emitted from the heavy nucleus fluctuates into a quark and anti-quark pair (leading order). The quark and anti-quark pair scatters off the nucleus with a Pomeron exchange and becomes a Vector-Meson; the cross section of this process is directly sensitive to the gluon density and its spatial distribution.

In previous STAR publications, there has been studies on ρ^0 meson, e.g., the most recent analysis in Ref. [140] for coherent photoproduction. Although the measurement has provided important insights to the structure of the gold nucleus, e.g., the impact parameter distribution from a Fourier transform of the momentum transfer $-t$ distribution, the general theoretical concern is that the process lacks of a hard scale because the mass of ρ^0 is rather small. Therefore, perturbative calculations of QCD are difficult to be carried out. In addition, the scale dependence of the photoproduction process is also of great interest, which can be only achieved by varying the mass of the Vector-Meson in photoproduction. Therefore, heavier vector-mesons, e.g., ϕ and J/ψ, are important to be measured.

In Fig. 61, the STAR preliminary results on J/ψ photoproduction are shown in Au+Au UPC at 200 GeV. The differential cross section of $d\sigma/dp_T^2$ as a function of p_T^2 is presented,

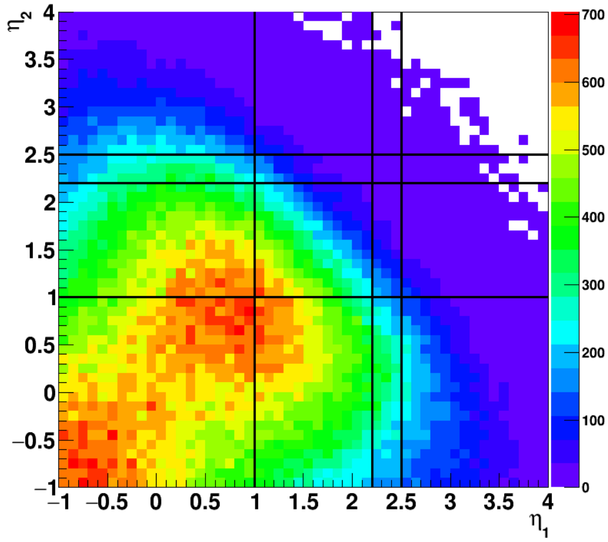

Figure 62: Pseudorapidity distribution of daughter electrons from the J/ψ decay using STARLight MC simulations. Lines are boundary acceptance of Barrel, Endcap, and Forward upgrade detectors.

with the total contribution (left) and coherent contribution only (right). The data has been compared with leading Monte Carlo models STARlight and Sartre, where a much better description by Sartre is found. This is the first differential measurement of J/ψ photoproduction off gold nucleus at the center-of-mass energy between photon and nucleon (proton or neutron), $W \sim 25$ GeV, which provides important constraints to the gluon density and its spatial distribution at this kinematic region, $x_g \sim 0.01$. The observed suppression of the gluon density from this data, compared to the Impulse Approximation, is found to be 15-20%.

Since the data presented above was taken in 2016, the acceptance of J/ψ is limited to rapidity $y < 1$ due to the η acceptance of the daughter electrons. However, this can be significantly improved in Run 2023 and 2025 Au+Au at 200 GeV with the endcap EMC, inner TPC, and forward upgrade detectors. The extension of acceptance in rapidity to $1 < y < 1.5$ can lead to a lower x down to 4×10^{-3}, which overlaps with the LHC kinematics, as well as going to higher x up to 0.05. With the forward upgrades, $y > 2.5$, the kinematic coverage will be even wider, where STAR can cover a regime that is complementary to the LHC, e.g., the anti-shadowing region $x_g \sim 0.1$.

In Fig. 62, it shows the pseudorapidity distribution of both daughter electrons from the J/ψ decay, simulated by the STARLight MC model. The lines are boundaries of the barrel, endcap, and forward detector acceptances. By extending to the endcap and forward, there is a significant improvement in the J/ψ acceptance. Based on the established UPC J/ψ trigger using both barrel and endcap, a high statistics event sample can be collected.

When extending the acceptance of J/ψ to higher rapidity, there is a long standing issue of photon energy ambiguity. At a J/ψ rapidity that $y \neq 0$, the photon energy can be

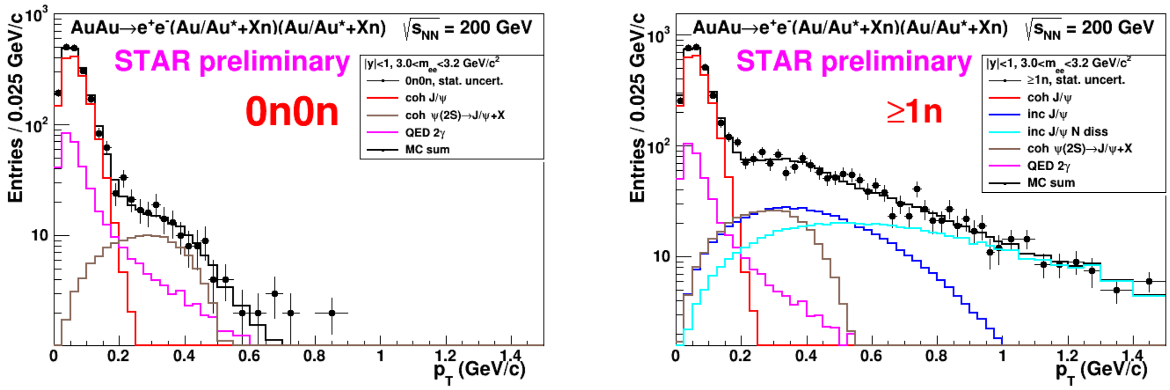

Figure 63: Uncorrected p_T of J/ψ mesons fitted with different contributions in Au+Au UPC at 200 GeV with no neutron on either side (left) and at least 1 neutron on either side (right).

$(M_J/2)e^{\pm y}$, which corresponds to a higher and lower photon energy, respectively. However, thanks to the neutron tagging in the ZDCs, this ambiguity can be resolved by considering different neutron multiplicities and their theoretical expected photon fluxes [154]. The STAR analysis using this method has just begun. In order to qualitatively see the difference by introducing different neutron tagging classes, see Fig. 63. For details of this method, see Ref. [154].

Finally, for the STAR upcoming Run 2023 and 2025, there is an opportunity for measuring the photoproduction of ϕ meson for the first time. The experimental challenge of this measurement is that ϕ is usually reconstructed via the kaon channel. However, for photoproduction process, the momentum of the kaon daughters are very soft, $\sim$ 100 MeV/c, such that reconstructing the daughter tracks has been impossible with only the TPC. However, for the upcoming runs, the inner TPC could push the low momentum tracking down to $\sim$ 100 MeV/c. There are two ways to achieve a statistical significant event sample of UPC ϕ meson.

The first one is to use ZDC coincidence trigger with no TOF requirement at the full magnetic field in STAR, while the second one is to use the standard TOF-base UPC Vector-Meson trigger at half-field. At full field, although the inner TPC can reconstruct tracks down to $\sim$ 100 MeV/c, it would not reach TOF for triggers due to the small bending radius. Therefore, events can be collected without a dedicated UPC ϕ trigger. This requires a large integrated luminosity to reach a few thousand raw ϕ events, based on the recent study using 2019 Au+Au data. However, if STAR can be run at half field, the TOF-base trigger might be applicable. See Fig. 64 for illustration of the TOF-based trigger acceptance in kaon p_T. Detail simulations will be followed up for the half-field running.

With all three Vector-Meson (ρ^0, ϕ, and J/ψ) measured at STAR in Au+Au UPC, they will provide an unprecedented understanding of the diffractive process off the gold nucleus in photoproduction, laying the foundation for such physics at the EIC.

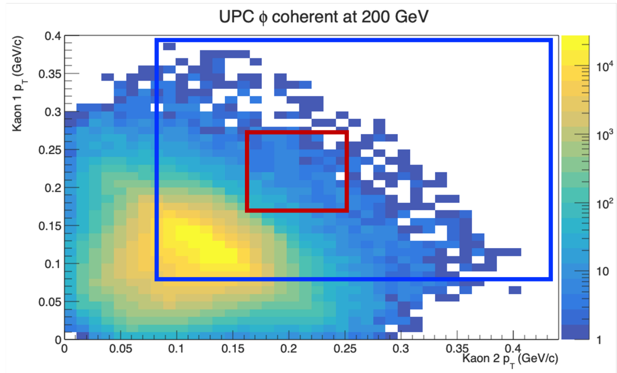

Figure 64: UPC ϕ meson decay p_{T} distributions of daughter 1 vs 2. The red box is the acceptance in p_{T} if requiring track to reach the location of TOF at STAR's full magnetic field; blue box is showing the same but with STAR at the half-field running.

Vetor-Meson decay: probing gluon distribution inside the nucleus

STAR recently observed a significant $\cos 2\Delta\phi$ azimuthal modulation in $\pi^+\pi^-$ pairs from photonuclear ρ^0 and continuum production. The structure of the observed modulation as a function of the $\pi^+\pi^-$ pair $P_\perp$, appears related to the diffractive pattern. Recent theoretical calculations [155], which implemented linearly polarized photons interacting with the saturated gluons inside a nucleus, have successfully described the qualitative features of the observed modulation (see Fig. 65), and indicate that the detailed structure of the $\cos 2\Delta\phi$ modulation vs. $P_\perp$ is sensitive to the nuclear geometry and gluon distribution. Data from Run-23 and Run-25 would allow the additional statistical reach needed to perform multi-differential analysis, providing stronger theoretical constraints. Specifically, multi-differential analysis of the $\cos 2\Delta\phi$ modulation with respect to pair rapidity and pair mass are needed. Multi-differential analysis with respect to pair mass is needed to separate the ρ^0 production from the continuum Drell-Soding production. Multi-differential analysis with respect to the pair rapidity is needed to quantitatively investigate how the double-slit interference mechanism effects the structure of the observed azimuthal modulation. Additional statistical precision is also needed for measurement of the higher harmonics. Similar measurements with $J/\Psi \to e^+e^-$ can be performed and such measurements at higher mass provide better comparison with more reliable QCD calculation.

Ultraperipheral AA collisions, where photons generated by the Lorentz-boosted electromagnetic field of one nucleus interact with the gluons inside the other nucleus, can provide certain 3D gluonic tomography measurements of heavy ions, even before the operation of the future EIC. STAR has performed experimental measurements of the photoproduction of J/ψ at low p_T in non-UPC heavy-ion collisions [156], accompanying the violent hadronic collisions. A detailed study with p_T distributions has shown that the $|t|$ distribution in peripheral collisions is more consistent with the coherent diffractive process than the incoherent process. Although models [157, 158] incorporating different partial coherent photon and nuclear interactions could explain the yields, it remains unclear how the coherent process

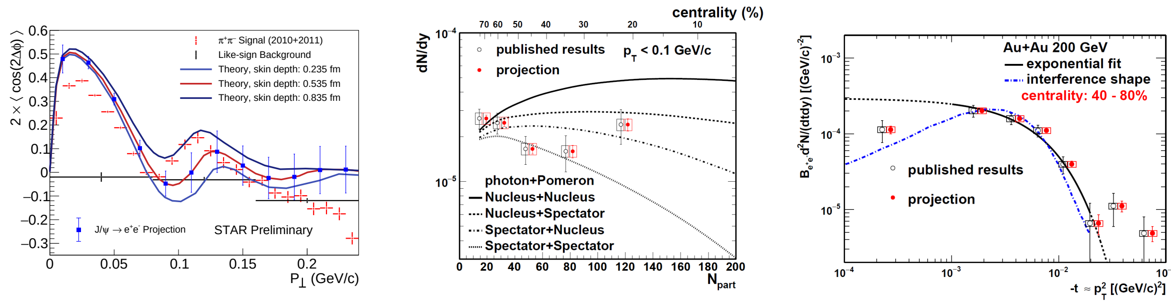

Figure 65: Left: Measurement of the $\cos 2\Delta\phi$ modulation of $\pi^+\pi^-$ pairs from photonuclear ρ^0 and continuum production compared to theoretical predictions [155]. Projections are shown for a similar measurement of the azimuthal modulation of e^+e^- pairs from photonuclear production of the J/ψ. Center: Projection of the dN/dy of photoproduced J/ψ in non-UPC events vs. the event centrality ($\mathrm{N_{part}}$) compared to various theoretical production scenarios. Right: Projection of the t spectra of photoproduced J/ψ in $40 - 80\%$ central collisions.

happens and whether final-state effects play any role [159]. Resolving this puzzle with high statistical data and detailed $|t|$ distributions at different centralities at RHIC as projected for Run-23+25 in Fig. 65 may be important for understanding what defines the coherentness of the photoproduction, how vector mesons are formed in the process and how exclusive the similar process has to be in future EIC experiments with forward neutron veto/tagging.

Photoproduction of dijets

In addition to photoproduction of Vector-Meson, photoproduction of back-to-back jets has been increasingly interested in the context of nuclear PDF. The process is a two-to-two hard scattering between a direct or resolved photon from the projectile (photon from UPC) and the quarks or gluons from the nucleus target. The final-state is a pair of back-to-back jet, which is directly sensitive to the photon and nuclear structure in terms of parton distribution functions. At the LHC, this process corresponds to the kinematic region $x_A \sim 10^{-3}$, which is the gluon dominated regime. Here we propose to measure the photoproduction dijets at STAR, where kinematic regions, e.g., the anti-shadowing and the EMC region, can be reached. This measurement has never been done at RHIC and will provide a significant constraints to the nPDFs of heavy nucleus at this kinematics for photoproduction.

The pseudo-data from eA collisions used here is generated by BeAGLE (**B**enchmark **eA** **G**enerator for **LE**ptoproduction) [153], based on the lepton and gold beam energy of $18\times$ 100 GeV, where the input PDF for the the exchanged photon is the CTEQ 5 from the LHAPDF library [160] and EPS09 for the nuclear PDF.

Jets are reconstructed by FastJet [161] with the anti-k_T algorithm, which is based on the energy distribution of final state particles in the angular space. All the stable and visible particles produced in the collisions with $p_T > 250$ MeV/c and $-1.5 < \eta < 1.5$ and $2.5 < \eta < 4.0$ in the laboratory system are taken as input. The jet cone radius parameter has been set to $R_{\text{jet}} = 1$ in the jet finding algorithm. To obtain the events in Au+Au UPC collisions at $\sqrt{s_{\rm NN}} = 200$ GeV from simulations of eAu at 18×100 GeV, an event-by-event weight is applied according to the photon flux difference between eA and Au+Au UPC collisions.

After reweighing we obtain the dijet events with the pesudorapidity of jets ($\eta^{\rm jet}$) from -1.5 to 1.5 in middle rapidity region and $2.5 < \eta^{\rm jet} < 4.0$ in the forward region. In each event, the jet with the highest p_T is called the trigger jet, the jet with the second highest p_T is called the associate jet. Events are selected with the requirement that the trigger jet has $p_T^{\rm trig} > 5$ GeV/c and the associated one has $p_T^{\rm asso} > 4.5$ GeV/c. 100 M event are generated, after all cuts applied, we found ~ 5600 dijet events corresponding to the integrated luminosity $L = 9$ nb^{-1}. Therefore, with STAR Run 2023 and 2025 Au+Au collisions, an event sample of dijets of 50-60k is expected.

In 200 GeV AuAu UPC collisions, the distributions of jets' pesudorapidity and p_T can be found in Fig. 66. Jets dominate at $\eta \sim 0.5$ with the maximum $p_T \sim 20$ GeV/c.

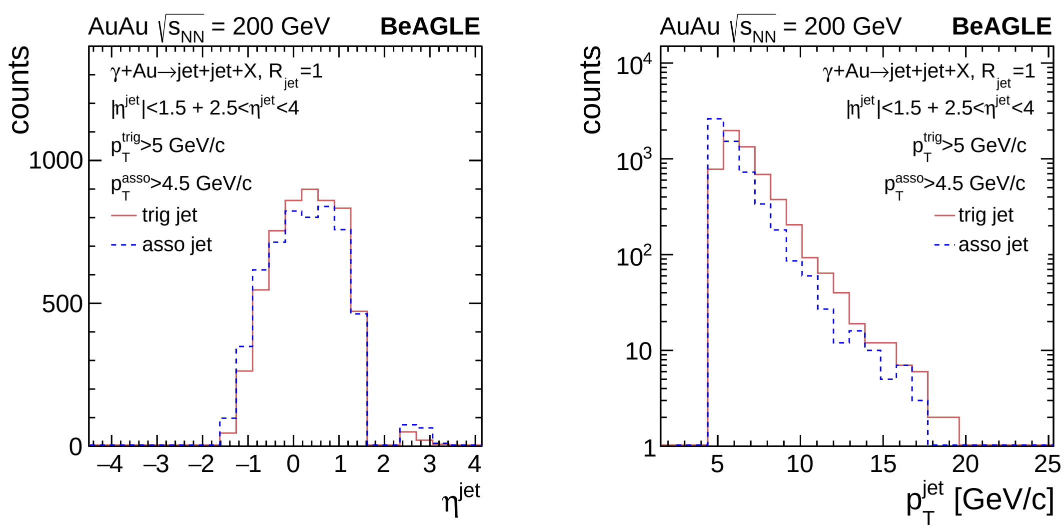

Figure 66: In Au+Au UPC collisions at $\sqrt{s_{\rm NN}} = 200$ GeV, the dijet events are selected with $|\eta^{\rm jet}| < 1.5 + 2.5 < \eta^{\rm jet} < 4.0$. For the trigger jet: $p_T^{\rm trig} > 5$ GeV/c, associate jet: $p_T^{\rm asso} > 4.5$ GeV/c. Left: the pesudorapidity distributions of the trigger and associated jets; right: the p_T distributions of the trigger and associated jets.

In BeAGLE, depending on the wave function components for the incoming virtual photon, the major hard processes are divided into three classes: the direct processes, the soft VMD processes and the resolved processes (hard VMD and anomalous). The direct photon interacts as a point-like particle with the partons of the nucleon, major subprocesses in direct category: LO DIS, Photon-Gluon Fusion (PGF) and QCD Compton (QCDC). While the VMD and anomalous components interact through their hadronic structure. Resolved photon processes play a significant part in the production of hard high-p_T processes at $Q^2 \approx 0$. The following hard subprocesses are grouped in the resolved processes category:

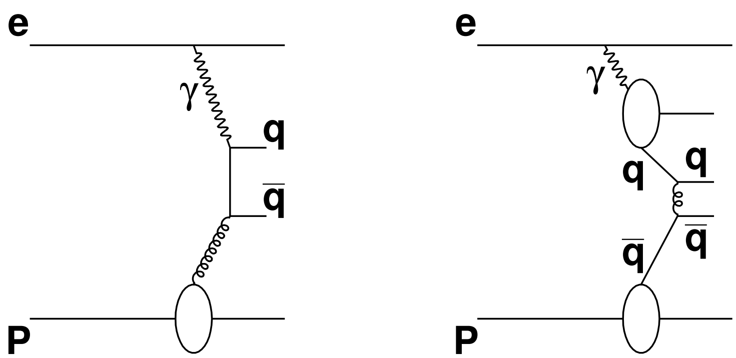

Figure 67: Examples of diagrams for direct (left) and resolved (right) processes in electron-proton scattering. In UPC, the photon emitter is replaced with the Au nucleus.

$qq \to qq$, $q\bar{q} \to q\bar{q}$, $q\bar{q} \to gg$, $qg \to qg$, $gg \to q\bar{q}, gg \to gg$. The examples of Feynman diagrams of resolved and direct processes are shown in FIG. 67.

The momentum fraction of the parton from the exchanged photon (x_γ) and the momentum fraction of the parton from the gold beam (x_{Au}) can be reconstructed knowing the momentum and angles of dijets as

$$x_\gamma = \frac{1}{2E_\gamma}(p_T^{\mathrm{tirg}} e^{-\eta_{\mathrm{trig}}} + p_T^{\mathrm{asso}} e^{-\eta_{\mathrm{asso}}}) \quad (4)$$

$$x_{\mathrm{Au}} = \frac{1}{2E_{\mathrm{Au}}}(p_T^{\mathrm{tirg}} e^{\eta_{\mathrm{trig}}} + p_T^{\mathrm{asso}} e^{\eta_{\mathrm{asso}}}) \quad (5)$$

where E_γ is the photon energy which can be determined from the hadronic final-state, see later for details. Eq. 4 and Eq. 5 are valid in the lab frame in LO.

The reconstructed x_γ and x_{Au} in AuAu UPC dijet events can be seen from Fig. 68. The reconstructed x_γ covers a wide range from 0.2 to 0.9 in resolved process, and dominates at high x in direct process. The reconstructed x_{Au} distributions contain two peaks as there are two pseudorapidity regions. The forward pseudorapidity ($2.5 < \eta^{\mathrm{jet}} < 4.0$) leads to the peak at high $x_{\mathrm{Au}} \sim 0.5$, while middle rapidity jets ($|\eta^{\mathrm{jet}}| < 1.5$) contribute the peak at x_{Au} $<\sim 0.2$. With the Run 2023 and 2025 data of Au+Au and Run 2024 $\mathrm{p}^\uparrow$+Au at STAR, this will become the first measurement at this kinematic region at RHIC with good statistical precision.

Taking one step further, the exclusive or diffractive dijets can also be measured in $p^\uparrow p^\uparrow$, $\mathrm{p}^\uparrow$+Au, and Au+Au at $\sqrt{s_{\mathrm{NN}}} = 200$ GeV. The process is diffractive such that there are only two jets in the event, where the target nucleon or nucleus stay intact. Similar to exclusive Vector-Meson production discussed earlier, the exclusive dijets can provide a large impact in understanding the nucleon and nuclear structure over a wide range of kinematics. In addition, with the unique target polarization at RHIC, the exclusive dijets can be sensitive to Generalized Parton Distributions and p_T Dependent PDFs. This process is expected to

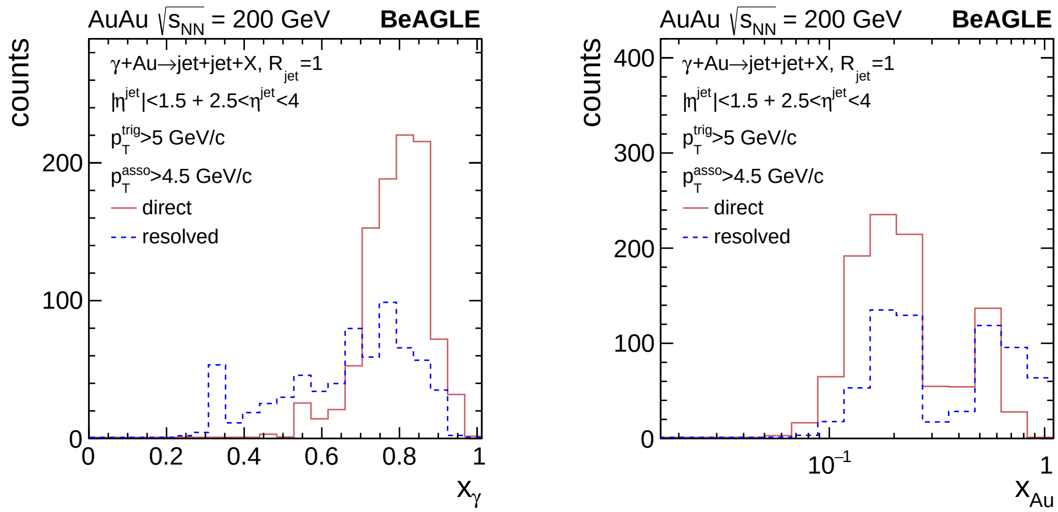

Figure 68: In AuAu UPC collisions at $\sqrt{s_{\rm NN}} = 200$ GeV, the dijet events are selected with $|\eta^{\rm jet}| < 1.5 + 2.5 < \eta^{\rm jet} < 4.0$. For the trigger jet: $p_T^{\rm trig} > 5$ GeV/c, associate jet: $p_T^{\rm asso} > 4.5$ GeV/c. Left: the x_γ distributions in resolved and direct processes; right: he $x_{\rm Au}$ distributions in resolved and direct processes.

be complementary to the process discussed in Sec. 3.1. In Fig. 69, the diffractive dijets photoproduction in p+Au UPCs are shown, with the transverse energy ($E_{\rm T}$) on the left panel and the dijet η separation distribution on the right panel. For a first look, the STAR Upcoming run 2024 would have enough luminosity to achieve reasonable statistics of this measurement; the same measurement can be done in $p+p$ and Au+Au collisions.

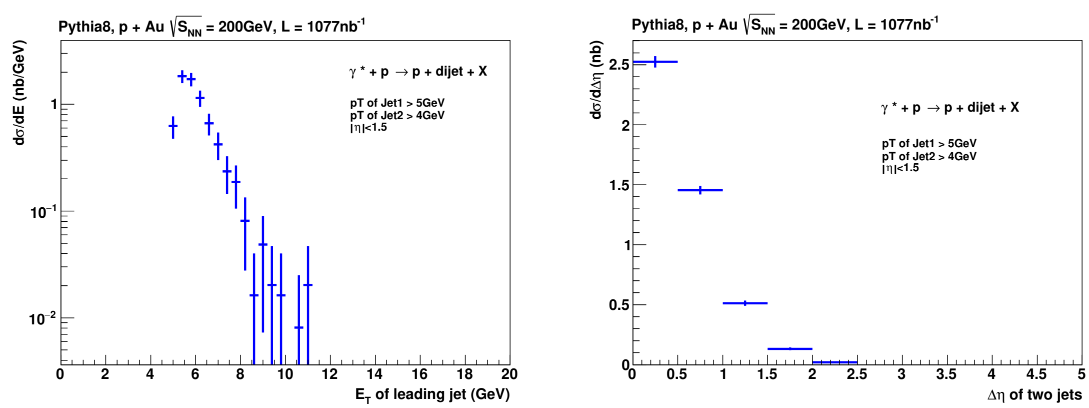

Figure 69: In p+Au UPC collisions at $\sqrt{s_{\rm NN}} = 200$ GeV, the diffractive dijet events are selected with the trigger jet: $p_T^{\rm trig} > 5$ GeV/c and associate jet: $p_T^{\rm asso} > 4.0$ GeV/c. The $E_{\rm T}$ distributions of the leading jet (left) and $\Delta\eta$ of the dijets distributions (right) are shown with $\sim 1\ \mu b^{-1}$ integrated luminosity.

Additional opportunities are available for STAR Run 2023-2025 based on UPC jets, e.g., measurement of diffractive dijets off polarized proton target, and azimuthal correlation of the dijets, which will be sensitive to nPDFs, diffractive nPDFs, QCD factorisation breaking, and spin structure of the proton. Here we do not elaborate them in details but defer the readers to Refs. [151, 152, 162–165] for both UPCs and at the EIC.

Photoproduction of inclusive charged particles and cross sections

Inclusive photoproduction processes in high-energy *ep* collisions have been extensively studied at HERA, e.g., charged particle productions, inclusive cross section, heavy-flavor production, etc. Recently, there have been efforts re-analyzing the HERA data in photoproduction and deep inelastic scattering to look for collectivity in terms of azimuthal correlations [166], inspired by the outstanding flow phenomena in heavy-ion collisions. At the LHC, experiments have just begun using the UPCs to look at collisions between photons and heavy nuclei in photoproduction, primarily to search for the collective phenomena. However, inclusive photoproduction processes in nuclei at high energy remains largely unexplored.

Inclusive photoproduction process is generally challenging for the UPC in heavy-ion experiments. At HERA, photoproduction in *ep* scattering can be unambiguously identified by the small angle electron taggers, where event kinematics can be reconstructed. However, in heavy-ion UPCs, the photon emitting nucleus is invisible to the experiment, leaving the kinematics, e.g., W, largely unconstrained. In a recent study using general-purpose eA MC model BeAGLE, it is found that the event kinematic reconstruction in UPC can be approached based on the hadronic final-state (HFS).

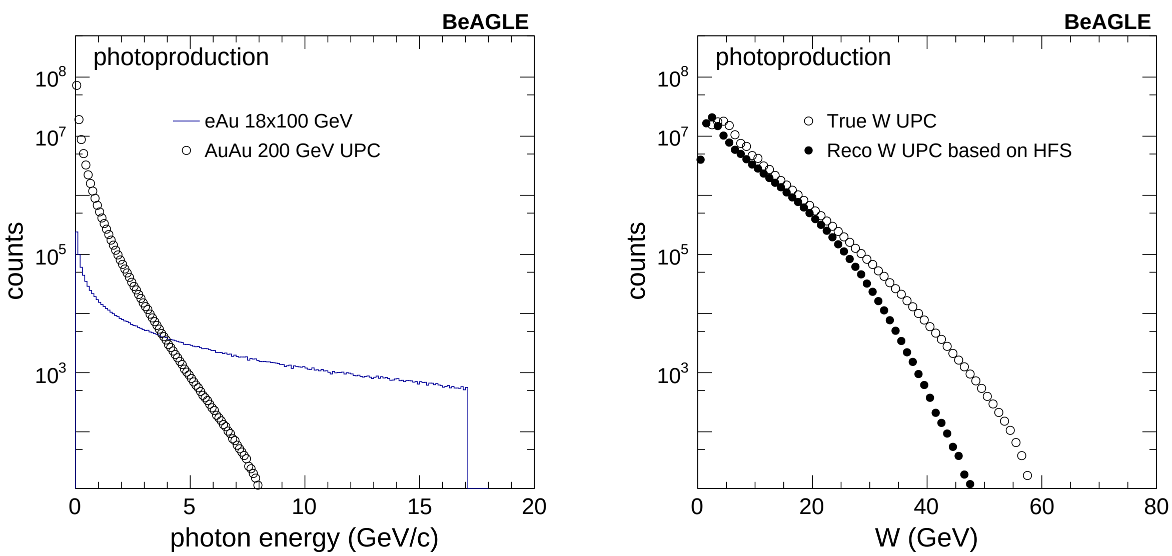

Figure 70: Left: photon energy distribution in eA and Au+Au UPC. Right: The truth level W in Au+Au UPC and the corresponding reconstructed level based on the HFS method.

In Fig. 70 left, it shows the photon energy distribution based on MC simulation of BeAGLE of eAu 18×100 GeV. In addition, by using the photon flux generated by the UPC at 200 GeV Au+Au collisions, the photon energy spectra is reweighted and shown as the open circle. The low photon energy is greatly enhanced due to the large flux generated by the heavy nucleus, while the spectra is much steeper than in the eAu collisions. In Fig. 70 right, the HFS method has been adopted to reconstruct the kinematic variable W, based on the STAR acceptance including the forward upgrade detectors. The smearing from truth to reconstructed W is visible and stronger at large W. However, by selecting on the reconstructed W, the event kinematics can be better controlled than using the average only. Unfolding technique can be used here for correcting the bin migration in W as well. Note that there is no detector simulations shown here.

In the upcoming RHIC Run 2023 and Run 2025, the inclusive photoproduction is of great interest. The cross section of such events is generally large, while a different trigger is required comparing to the standard minimum-bias hadronic collision trigger. The baseline trigger has been developed during the Au+Au 200 GeV data taken in 2019, where only a ZDC coincidence was required. For Run 2023 and 2025, asymmetry BBC response could be added to more efficiently select the inclusive photoproduction process.

Search for Collectivity in Photo-nuclear (γ+Au) Processes

Until the EIC is built, high-energy photoproduction processes (low virtuality limit of the deep inelastic scattering) can be studied using ultra-peripheral ion collisions (UPCs) that occur when two heavy ions interact at large impact parameters. Such collisions can be considered as γ+Au processes but unlike at the EIC, the photons involved in UPCs are quasi-real. For UPCs at top RHIC energies one expects the energy of the quasi-real photon to be approximately $E_\gamma \approx 3$ GeV. The typical range of the center of mass energy of the photon-nucleon system will therefore be $W_{\gamma N} \approx 40$ GeV. Therefore, Au+Au collisions at $\sqrt{s_{_{NN}}} = 200$ GeV will provide access to the γ+Au process at 40 GeV center of mass energy. Our specific interest is high activity inclusive γ+Au process to search for collectively and improve our understanding of the mechanism of baryon stopping.

A satisfactory microscopic explanation of how collectivity originates from the basic processes of QCD and evolves with collision system size is a topic of broad interest in the community of high energy nuclear physics. The formation of a quark-gluon plasma medium and its fluid-dynamic expansion explain the origin of collectivity in Au+Au collisions. Results from RHIC small system scan indicate fluid-dynamic expansion are essential to drive collectivity in ^{3}He/d/p+Au collisions [167]. A search for collectivity in γ+Au interactions at RHIC will be a natural continuation of the recent system size scan [167], extending it at the small end to complete the hierarchy: Au+Au $>$ ^{3}He+Au $>$ d+Au $>$ p+Au $>$ γ+Au. This will help better address how collectivity originates and evolves with system size. If collectivity is observed in γ+Au processes it can provide a way to explore the creation of a many-body system exhibiting fluid behavior in photon-induced processes [168]. A recent calculations in Ref [168] assumes γ+A processes are equivalent to collisions of vector meson with ions (ρ+A collisions) and describe first measurements of harmonic coefficients v_n in photonuclear processes measured by the ATLAS collaboration [169]. The hypothesis of γ+A process as ρ+A collisions and the formation of a fluid-dynamic medium can be tested at RHIC in a data-driven way. This can be done by comparing measurements in γ+Au processes at $W_{\gamma N}$ ≈40 GeV and in d+Au collisions at $\sqrt{s_{_{NN}}}$ = 39 GeV. The former will be possible if a high statistics data set is collected for Au+Au collisions at $\sqrt{s_{_{NN}}}$ = 200 during the Run 23 and 25 and the later can be performed with the existing RHIC data on tape. It is known from RHIC measurements, argument based on initial geometry and, fluid dynamic calculations that elliptic anisotropy coefficient follow a hierarchy of v_2(d+Au) > v_2(p+Au) at a fixed collision energy and multiplicity [167, 170]. Following a similar argument one expects v_2(d+Au) > v_2(ρ+Au). In the fluid dynamic picture of Ref [168] the elliptic anisotropy coefficient will show the following hierarchy: v_2(d+Au) > v_2(γ+Au). A similar test by comparing v_2(p+Pb) and v_2(γ+Pb) at the LHC is difficult since the center of mass energy differs by a factor of six between p+Pb and γ+Pb collisions.

Photonuclear processes can also be used to study the origin of baryon stopping and baryon structure in general. One proposed mechanism for explaining the baryon stopping is the baryon junction: a nonperturbative Y-shaped configuration gluons which is attached to all three valence quarks. In this picture it is the baryon junction that carries the baryon number rather than the valence quarks. The existence of baryon junctions and their interaction with the incoming target or projectile are theorized to be an effective mechanism for substantial baryon stopping in pp and AA [171], but this has yet to be confirmed experimentally. Photonuclear processes allow us to study baryon stopping in the simplest possible process. The vast majority of these collisions occur through what is called the resolved process where the quasi-real photon fluctuates into a quark-antiquark pair which then collides with the other ion [?]. If the baryon number were carried by the three valence quarks, then this quark-antiquark pair would not be able to stop the baryons, but it is possible for the quark-antiquark pair to interact with the junction and produce a midrapidity baryon. An added benefit is that photonuclear processes are highly asymmetric and baryons only enter from one side of the collision. The baryon-junction stopping mechanism is predicted to cause an exponential damping of the cross section with rapidity $\sim \exp\big(-\alpha_0^J(y - Y_{\rm beam})\big)$, where $\alpha_0^J \simeq 1/2$ is the Regge intercept of the baryon junction [171]. In a symmetric hadronic collision, baryons are traveling from either direction so the stopping of both the target ($\sim \exp\big(-\alpha_0^J(y-Y_{\rm beam})\big)$) and the projectile ($\sim \exp\big(\alpha_0^J(y-Y_{\rm beam})\big)$) will likely compensate for each other, leading to a nearly symmetric distribution. But in an asymmetric system like a photonuclear collision, this exponential shape should be visible.

A handful of data sets exist on the disk with the appropriate event trigger selection for studying photonuclear processes at RHIC. In Fig.71 we present preliminary results on γ+Au-rich interactions using Au+Au 54 GeV data from STAR shown at the Quark Matter 2022 conference. By identifying the single neutron peak for individual ZDCs, we require the cuts equivalent to 1nXn. We apply an asymmetric cut on east and west BBCs to improve the purity. We also make sure the position of the primary vertex along collision direction V_z from TPC and VPD detectors differs by about 10 cm. After applying such cuts on Au+Au

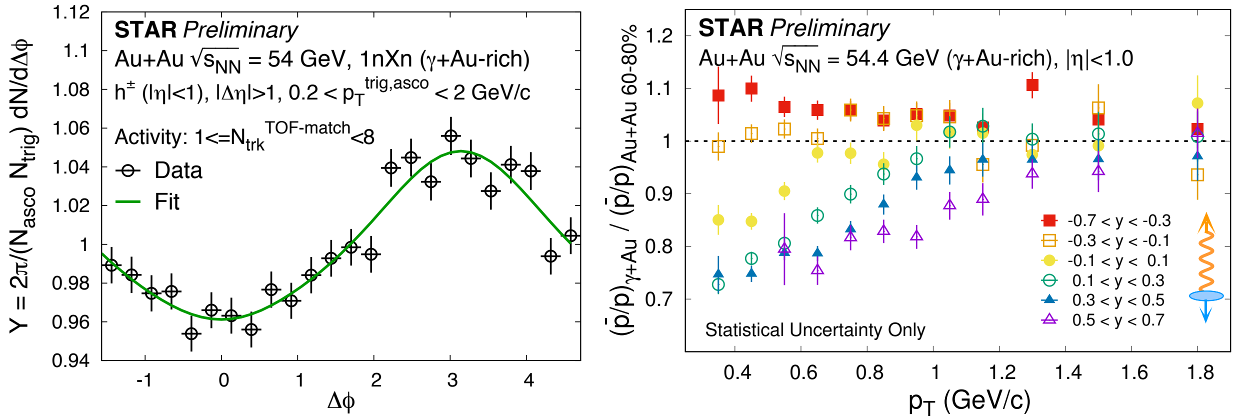

Figure 71: (Left) STAR preliminary data on normalized yield of long range di-hadron correlations in γ+Au-rich events with a relative pseudoapidity gap of $|\Delta\eta| > 1$ between two hadrons. The events are selected by applying asymmetric cuts on the energy deposition of neutrons in ZDCs (1nXn) and on TPC tracks matched with TOF $N_{\rm trk}^{\rm TOF-match}$ in the window of $1 <= N_{\rm trk}^{\rm TOF-match} < 8$. The green curve represents a fit to data using a function: $1 + 2\sum a_n \cos(n\Delta\phi)$. No signatures of collectivity associated with enhancement of correlation near relative azimuthal angle $\Delta\phi \sim 0$ is observed. (Right) The double ratio of antiprotons to protons in γ++Au-rich events compared to peripheral Au+Au events, indicating significant enhancement of protons at low p_T and at mid-rapidity. The enhancement shows a strong rapidity dependence while going from the photon to ion direction.

54 GeV data we perform measurements in γ+Au+Aurich events.

Fig. 71 (left) shows the normalized yield, differential in relative azimuthal angle of the trigger and associated particles $Y(\Delta\phi) = 1/N_{\rm trig}/N_{\rm asco} d^2N^{\rm pair}/d\Delta\phi$ integrated over a relative pseudorapidity window of $|\Delta\eta| > 1$. For this analysis, the p_T of trigger and associated particles is chosen to be within $0.2 < p_T^{\rm trig,asco} < 2$ GeV/c. The distribution $Y(\Delta\phi)$ is shown for two different bins of activity characterized by the number of TPC tracks matched with the TOF $1 <= N_{\rm trk}^{\rm TOF} < 8$ (low activity). The distribution is fitted using a Fourier function of the form $(1 + 2\sum a_n \cos(n\Delta\phi))$ (green curve). No ridge-like component associated with a significant enhancement of $Y(\Delta\phi)$ near $\Delta\phi = 0$ that is related to the signature of collectivity is seen.

Fig. 71 (right) shows the measurement of the yield of anti-protons-to-protons ($\bar{p}/p$) with p_T. The quantity plotted is a double ratio of $\bar{p}/p$ for the measurements in γ+Au-rich events over the same in 60-80% peripheral Au+Au events. We see a suppression of the $\bar{p}/p$ yield in γ+Au events at low $p_T < 0.6$ GeV/c and for the symmetric window of $-0.1 < y < 0.1$ around mid-rapidity. The suppression of $\bar{p}/p$ yield gets stronger while going from the photon to the ion direction, with the double ratio dropping by a factor 0.75 at low p_T. We have checked that this trend is not seen for π^-/π^+, K^-/K^+ and not explained by PYTHIA 6 model. This important observation provides the necessary impetus for further exploration using various available data sets. In particular, we would like to test if this strong rapidity dependence of the $\bar{p}/p$ yield is consistent with the picture of baryon junction that predicts an exponential dependence of stopping with rapidity of form $\exp(-\alpha(y - Y_{\rm beam}))$ with α =0.5.

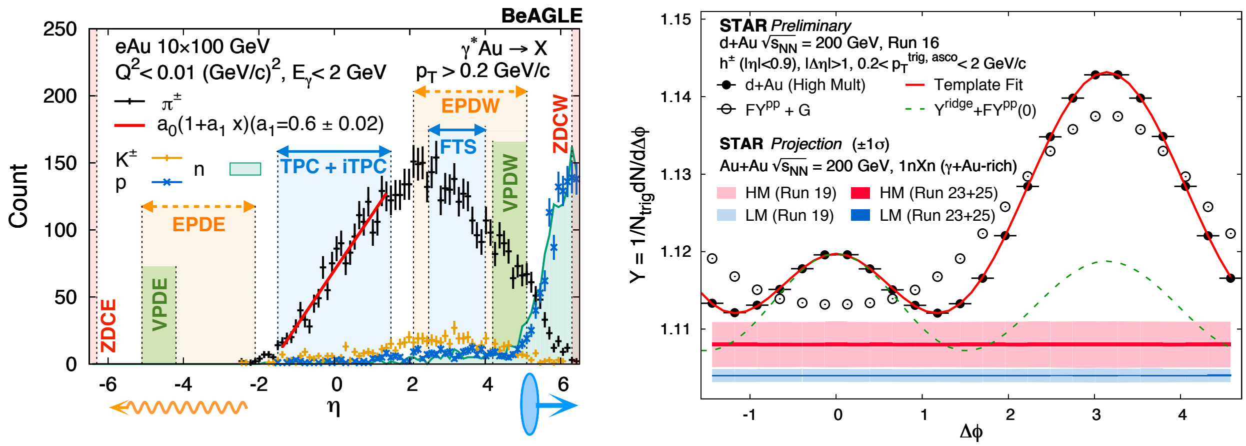

Figure 72: (Left) Pseudorapidity distribution of different particles using the state-of-the-art BeAGLE [172,173] event generator for the EIC in e+Au events. By restricting the virtuality and energy of the photon (γ^*) we try to mimic the kinematics of a $\gamma + Au$ (Au+Au UPC) event. The purpose of this plot is to demonstrate how different STAR detectors will be used to identify such UPC processes. (Right) STAR preliminary data on per-trigger yield estimated using di-hadron correlations in d+Au (hadornic) 200 GeV collisions. The correlation function in pp collisions (open circle) is used as a template to fit the same in relatively high multiplicity d+Au collisions (solid circle) and to extract the long-range ridge-like component. The red and blue band show projections for $\gamma + Au$ enriched events for two different multiplicity bins. The aim is to use the correlation function from the low multiplicity $\gamma + Au$ to perform template fit in the high multiplicity bin.

Our aim will be extend these measurements with high statistics γ+Au-rich event samples using Run 2023 and 2025 data on Au+Au collisions at $\sqrt{s_{NN}}$ = 200 GeV. Fig.72(Left) shows the pseudorapidity (η) distribution of identified particles with $p_T > 0.2$ GeV/c in inclusive e+Au DIS (γ^*+Au, where γ^* refers to a virtual photon) processes simulated using the EIC Monte Carlo BeAGLE event generator [172,173] with electron and ion beam energy of 10 and 100 GeV, respectively. The virtuality of the exchanged photon is restricted to be $Q^2 < 0.01$ GeV/c^2 and photon energy is restricted to be $E_\gamma < 2$ GeV to mimic γ+Au interactions in Au+Au UPCs at $\sqrt{s_{NN}}$=200 GeV. This figure demonstrates how the combination of the inner Time Projection Chamber (iTPC), the new highly granular Event-Plane Detectors (EPD) and forward tracking system (FTS) and the Zero-Degree Calorimeters (ZDC) can be used to isolate γ+Au events from peripheral Au+Au events (symmetric in η with no gaps). In terms of triggering the γ+Au interactions, the most stringent selection criterion is that the ZDCE detector should be restricted to have a single neutron hit (1n), while no restriction (Xn) should be placed on the ZDCW to trigger on γ+Au candidates with east-going photons, and vice versa. We perform a feasibility study using Run 19 data on min-bias Au+Au collisions using about 130 M events. Fig.72 shows STAR preliminary data on the per-trigger yield in di-hadron correlations in d+Au events where a clear ridge can be seen after template fitting. On the same plot we show projections of uncertainties for the di-hadron correlations in possible γ+Au-rich events using Au+Au 200 GeV data from Run 19 (130 M events) and using Au+Au 200 GeV data from anticipated Run 23 and

Run 25 (20 B events). Projections are shown for high activity (HM) and low activity (LM) event classes determined by the uncorrected track multiplicity in TPC matched with TOF of $15 <= N_{\rm trk}^{\rm TOF} < 25$ and $1 <= N_{\rm trk}^{\rm TOF} < 8$, respectively. Even without any dedicated trigger, 20 B minbias Au+Au events can already give us enough $\gamma+Au$ candidates to significantly reduce the uncertainties shown by the red and blue projection bands in Fig.72. This will enable us to perform differential measurements of di-hadron correlations with different combinations of triggers and associated p_T and perform a search for collectivity and in addition to testing the baryon-junction conjecture.

Other inclusive photoproduction measurements

Besides the search for collectivity in photon-nucleus collisions, there are many other inclusive photoproduction processes are of great interest. In the upcoming Run 2023-2025, inclusive photoproduction processes only require a large sample of “minimum-bias" photo-nucleus collision events, instead of special triggered events.

For example, one measurement that will have a large impact is the inclusive J/ψ photoproduction. Note that STAR has results on exclusive J/ψ photoproduction, the complementary inclusive measurement (together with exclusive measurements) can be sensitive to the saturation or non-linear gluon dynamics. The observable is as follows,

$$\frac{\sigma_{\rm J/\psi}^{\rm exclusive}/\sigma_{\rm J/\psi}^{\rm inclusive}|_{\rm Au}}{\sigma_{\rm J/\psi}^{\rm exclusive}/\sigma_{\rm J/\psi}^{\rm inclusive}|_{\rm p}}. \tag{6}$$

The J/ψ in the inclusive photoproduction provides a hard scale that theoretical calculations, e.g., dipole model, can be performed. Qualitatively, the nuclear shadowing model (Leading Twist Approximation [146–148]) predicts this double ratio to be below unity, while saturation models predict above unity [174]. This is one of the very few observables that qualitatively separates these two long standing models. In the upcoming STAR runs of Au+Au and p+Au collisions, this measurement will play an important role in understanding the saturation phenomena before the EIC. For the EIC measurement, see Fig. 73 for details. The reason we can do this similar measurement in UPCs is because we can replace the inclusive DIS measurement (finite Q^2) with inclusive photoproduction of J/ψ, where the charm quark mass provides the hard scale.

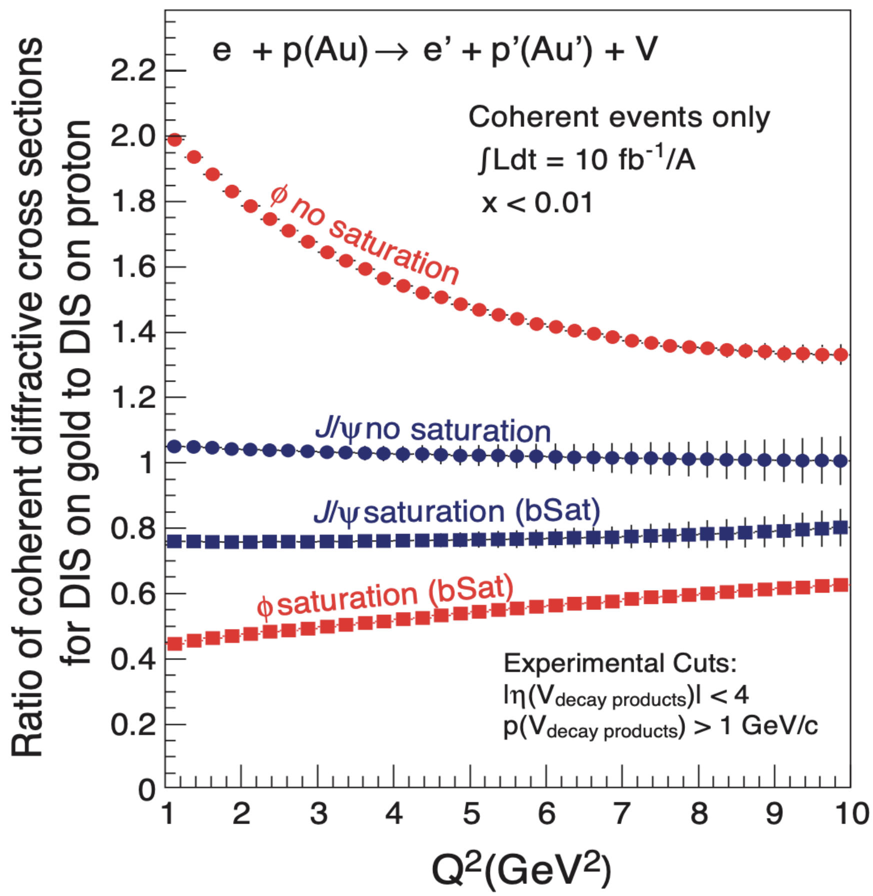

Figure 73: Figure from the EIC White Paper - Fig 1.6 [174]. The ratio of the coherent diffractive cross-section in e+Au to e+p collisions normalized by $A^{4/3}$ and plotted as a function of Q^2 for both saturation and non-saturation models. The $1/Q$ is effectively the initial size of the quark-antiquark systems (ϕ and J/ψ) produced in the medium.

3 Run-24 Request for Polarized pp and p+A Collisions at 200 GeV

The exploration of the fundamental structure of strongly interacting matter has always thrived on the complementarity of lepton scattering and purely hadronic probes. As the community eagerly anticipates the future Electron Ion Collider (EIC), an outstanding scientific opportunity remains to complete "must-do" measurements in p+p and p+A physics during the final years of RHIC. These measurements will be essential if we are to fully realize the scientific promise of the EIC, by providing a comprehensive set of measurements in hadronic collisions that, when combined with future data from the EIC, will establish the validity and limits of factorization and universality. Much of the Run-24 physics program outlined here is, on the one hand, unique to proton-proton and proton-nucleus collisions and offers discovery potential on its own. On the other hand, these studies will lay the groundwork for the EIC, both scientifically and in terms of refining the experimental requirements of the physics program, and thus are the natural next steps on the path to the EIC. When combined with data from the EIC these STAR results will provide a broad foundation to a deeper understanding of fundamental QCD.

The separation between the intrinsic properties of hadrons and interaction-dependent dynamics, formalized by the concept of factorization, is a cornerstone of QCD and largely responsible for the predictive power of the theory in many contexts. While this concept and the associated notion of universality of the quantities that describe hadron structure have been successfully tested for unpolarized and, to a lesser extent, longitudinally polarized parton densities, its experimental validation remains an unfinished task for much of what the EIC is designed to study – the three-dimensional structure of the proton and the physics of dense partonic systems in heavy nuclei. To establish the validity and limits of factorization and universality, it is essential to have data from *both* lepton-ion and proton-ion collisions, with experimental accuracy that makes quantitative comparisons meaningful.

Run-24, with polarized p+p and p+Au collisions at $\sqrt{s_{\rm NN}} = 200$ GeV, will likely be the last RHIC spin/cold QCD run. This run will provide STAR with the unique opportunity to investigate these 200 GeV collision systems with the Forward Upgrade providing full tracking and calorimetry coverage over the region $2.5 < \eta < 4$ and the iTPC providing enhanced particle identification and expanded pseudorapidity coverage at mid-rapidity. These powerful detection capabilities, when combined with substantially increased sampled luminosity compared to Run-15, will enable critical measurements to probe universality and factorization in transverse spin phenomena and nuclear PDFs and fragmentation functions, as well as low-x non-linear gluon dynamics characteristic of the onset of saturation. This will provide unique insights into fundamental QCD questions in the near term, and essential baseline information for precision universality tests when combined with measurements from the EIC in the future.

We therefore request at least 11 weeks of polarized p+p data-taking at $\sqrt{s} = 200$ GeV and 11 weeks of polarized p+Au data-taking at $\sqrt{s_{\rm NN}} = 200$ GeV during Run-24. Effectively, we request approximately equal nucleon-nucleon luminosities for p+p and p+Au which is essential to optimize several critical measurements that require comparisons of the same observable in (polarized or unpolarized) $p+p$ and $p+$Au collisions described in the following sections.

All of the running will involve vertically polarized protons. Based on recent C-AD guidance, we expect to sample at least 208 pb^{-1} of $p+p$ collisions and 1.2 pb^{-1} of $p+$Au collisions. These totals represent 4 times the luminosity that STAR sampled during transversely polarized $p+p$ collisions in Run-15 and 2.7 times the luminosity that STAR sampled during transversely polarized $p+$Au collisions in Run-15.

The reduction in cyo-weeks from 28 to 24 is projected to have a significant impact on the sampled luminosity, reducing the statistics quoted above by about a factor of 1.3.

3.1 Spin Physics with Polarized pp and $p+$A Collisions at 200 GeV

Run-24 will enable STAR to probe the physics questions that can be assessed in the transversely polarized $p+p$ and $p+$A collisions, including those described in highlights section 1.2 and recent STAR publications [175, 176], but with a far more capable detector and much larger datasets than were available during Run-15. With the overlapping kinematic coverage for both $p+p$ and $p+$A data, this program is critical to set the stage for related future measurements at the EIC. Here we give brief descriptions of several of the opportunities presented by Run-24.

Forward Transverse Spin Asymmetries

The experimental study of spin phenomena in nuclear and particle physics has a long history of producing important, and often surprising, results. Attempts to understand such data have pushed the field forward, forcing the development of both new theoretical frameworks and new experimental techniques. Recent detector upgrades at STAR, at mid- and forward-rapidity, coupled with the versatility of RHIC, will allow us to gain new insights into long-standing puzzles, and to probe more deeply the complexities of emergent behavior in QCD.

Results from PHENIX and STAR have shown that large transverse single-spin asymmetries (TSSA) for inclusive hadron production, first seen in $p+p$ collisions at fixed-target energies and modest p_{T}, extend to the highest RHIC center-of-mass energies, $\sqrt{s} = 510$ GeV, and surprisingly large p_{T}. Figure 74 summarizes the world data for the inclusive neutral pion asymmetries A_N as a function of Feynman-x. The asymmetries are seen to be nearly independent of $\sqrt{s}$ over the very wide range of roughly 19 to 500 GeV.

To understand the observed TSSAs, one needs to go beyond the conventional leading-twist (twist-2) collinear parton picture for the hard-scattering processes. Two theoretical formalisms have been developed to try to explain these sizable asymmetries in the QCD framework: transverse-momentum-dependent (TMD) parton distribution and fragmentation functions, such as the Sivers and Collins functions; and transverse-momentum-integrated (collinear) quark-gluon-quark correlations, which are twist-3 distributions in the initial state

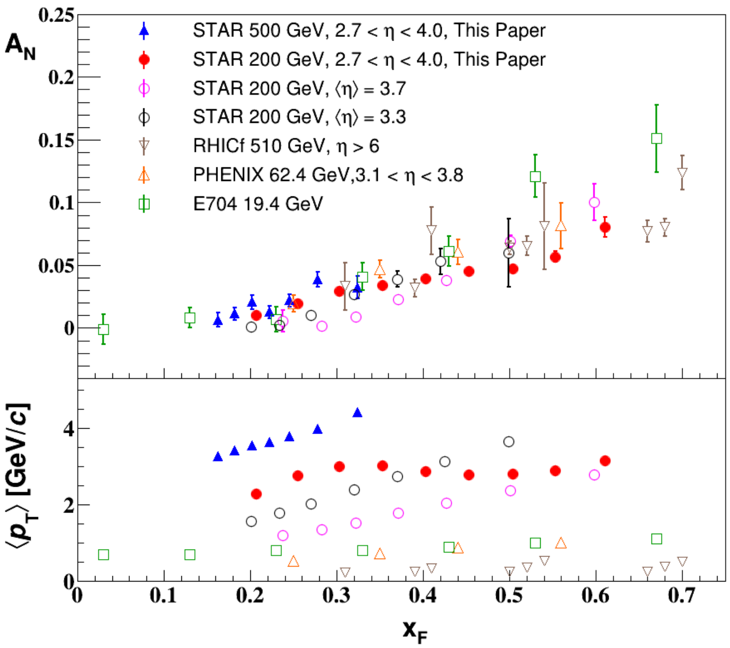

Figure 74: Transverse single-spin asymmetry A_N measurements for neutral pion in p+p collisions at different center-of-mass energies as a function of Feynman-x [175].

proton or in the fragmentation process. For many of the experimentally accessible spin asymmetries, several of these functions can contribute, and need to be disentangled in order to understand the experimental data in detail, in particular the observed p_T dependence. These functions manifest their spin dependence either in the initial state–for example, the Sivers distribution and its twist-3 analog, the Efremov-Teryaev-Qiu-Sterman (ETQS) function [177]–or in the final state via the fragmentation of polarized quarks, such as in the Collins function and related twist-3 function $\hat{H}_{FU}(z, z_z)$.

Incorporating the fragmentation term within the collinear twist-3 approach demonstrated the ability of this formalism to describe the large values of A_N for π^0 production observed at RHIC [178]. In this work, the relevant (non-pole) 3-parton collinear fragmentation function $\hat{H}_{FU}(z, z_z)$ was fit to the RHIC data. The so-called soft-gluon pole term, involving the ETQS function $T_{q,F}(x_1, x_2)$, was also included by fixing $T_{q,F}$ through its well-known relation to the TMD Sivers function $f_{1T}^{\perp}$. The authors obtained a very good description of the data due to the inclusion of the non-pole fragmentation function and based on this work they were able to make predictions for π^+ and π^- production asymmetries A_N at the forward rapidities covered by the STAR upgrades, $2.5 < \eta < 4$. The results are shown in Fig. 75 for $\sqrt{s}$= 200 and 500 GeV for two rapidity ranges, $2 < \eta < 3$ and $3 < \eta < 4$.

STAR recently published in a pair of papers discussing forward transverse spin asymmetries in p+p, p+Al, and p+Au collisions measured with the Forward Meson Spectrometer (FMS). One paper focuses on the dynamics that underlie the large asymmetries that have been seen to date [175]. The data show that A_N for forward π^0 production in p+p collisions

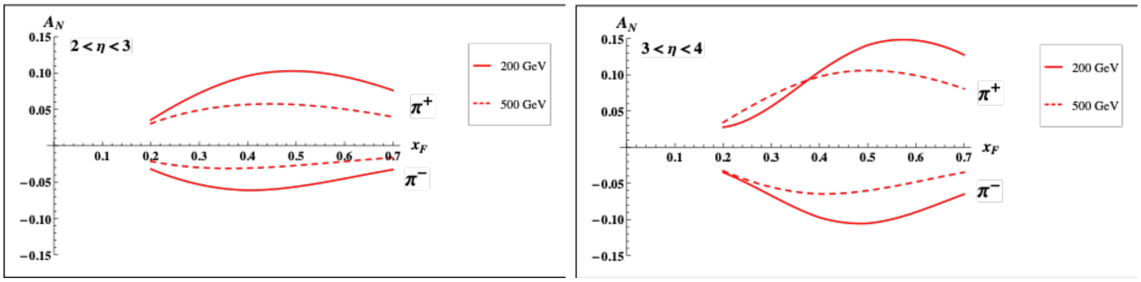

Figure 75: Predictions for A_N for π^+ and π^- production over the ranges $2 < \eta < 3$ (left) and $3 < \eta < 4$ (right) at $\sqrt{s} = 200$ GeV (solid lines) and 500 GeV (dashed lines).

at 200 and 500 GeV is substantially larger when the π^0 is isolated than when it is accompanied by additional nearby photons. The same analysis also shows that A_N for inclusive electromagnetic jets (EM-jets) in 200 and 500 GeV collisions is substantially larger than that for EM-jets that contain three or more photons and that the Collins asymmetry for π^0 in EM-jets is very small. The other paper focuses on the nuclear dependence of A_N for π^0 in $\sqrt{s_{NN}} = 200$ GeV collisions [176]. It presents a detailed mapping of A_N as functions of x_F and p_T for all three collision systems. It is shown that the observed nuclear dependence is very weak. The same analysis shows that isolated *vs.* non-isolated π^0 behave similarly in p+Al and p+Au collisions as they do in p+p collisions.

These two papers provide a wealth of new data to inform the ongoing discussion regarding the origin of the large inclusive hadron transverse spin asymmetries that have been seen in p+p collisions at forward rapidity over a very broad range of collision energies. Nonetheless, the STAR Forward Upgrade will be a game changer for such investigations. It will enable measurements of A_N for $h^{+/-}$, in addition to π^0. It will enable isolation criteria to be applied to the $h^{+/-}$ and π^0 that account for nearby charged, as well as neutral, fragments. It will enable full jet asymmetry and Collins effect measurements, again for $h^{+/-}$ in addition to π^0, rather than just EM-jet measurements. It will permit all of these measurements to be performed at both 510 GeV (measured during Run 22), and at 200 GeV (to be measured in Run 24).

In addition, all of these observables can be tagged by requiring rapidity gaps to identify the diffractive component of the observed transverse spin asymmetries. For p+p there will be considerable overlap between the kinematics at the two energies, but the 510 GeV measurements will access higher p_T, while the 200 GeV measurements will access higher x_F. Moreover, at 200 GeV we will also perform the full suite of measurements in p+Au to identify any nuclear effects. Furthermore, it is important to stress that the 200 GeV running with the Forward Upgrade will give the unique opportunity for jet reconstruction studies at the exact same rapidity that is critical for the future EIC. The data will provide an extraordinary possibility to exercise new reconstruction techniques incorporating AI/ML methods and train the next generation of scientists.

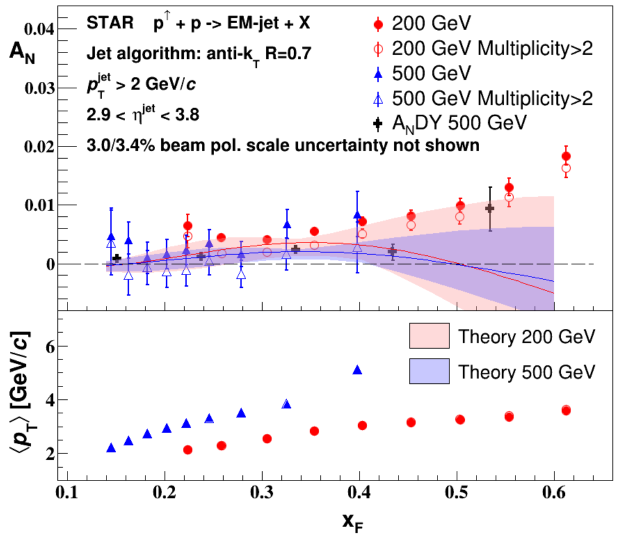

Figure 76: Recent STAR results on inclusive electromagnetic jets TSSA in pp collisions at both 200 and 500 GeV [175].The results that require more than two photons observed inside a jet are shown as open symbols. Theory curves [182] for TSSA of full jets at rapidity $\langle y \rangle = 3.25$ for 200 GeV (red) and $\langle y \rangle = 3.57$ for 500 GeV (blue) are also shown. The average p_{T} of the jet for each x_{F} bin is shown in the lower panel.

Sivers and Efremov-Teryaev-Qiu-Sterman Functions

There is great theoretical interest in testing the relation between the ETQS correlation functions and the Sivers function. As discussed above, both the Sivers and the ETQS functions encapsulate partonic spin correlations within the proton, but they are formally defined in different frameworks. While the Sivers function is a TMD quantity that depends explicitly on spin-dependent transverse partonic motion k_T, the ETQS function is a twist-3 collinear distribution, in which SSAs are generated through soft collinear gluon radiation.

Measurements of forward jet production from the ANDY collaboration [179] indicated rather small asymmetries. This was argued to be consistent with the idea that the twist-3 parton correlation functions for up and down valence quarks should cancel, because their behavior reflects the Sivers functions extracted from fits to the SIDIS data that demonstrate opposite sign, but equal magnitude, up and down quark Sivers functions. STAR results on charge-tagged dijets at mid-rapidity [180] (see Fig. 79) support this interpretation, with the caveat that the measured observable (a spin-dependent $\langle k_T \rangle$) is defined in the TMD, and not the twist-3, framework. Moreover, recently published STAR results for forward inclusive electromagnetic jets [175] also show small TSSA as seen in Fig. 76. The results have been analyzed with the generalized parton model approach [181], and when incorporated in the reweighing procedure of the quark Sivers functions extracted from SIDIS data they significantly improved its uncertainty at larger momentum fraction x (see Fig. 77).

To better test quantitatively the relation between the two regimes, one can measure spin asymmetries for jets which are *intentionally* biased towards up or down quark jets via detection of a high-z charged hadron within the jet. Higher-twist calculations of jet asymmetries based on the Sivers function predict sizeable effects for these flavor-enhanced jets. With the suite of new forward detectors installed at STAR, full jet reconstruction, along with identification of a high-z hadron of known charge sign is be possible at high pseudorapidity. Using

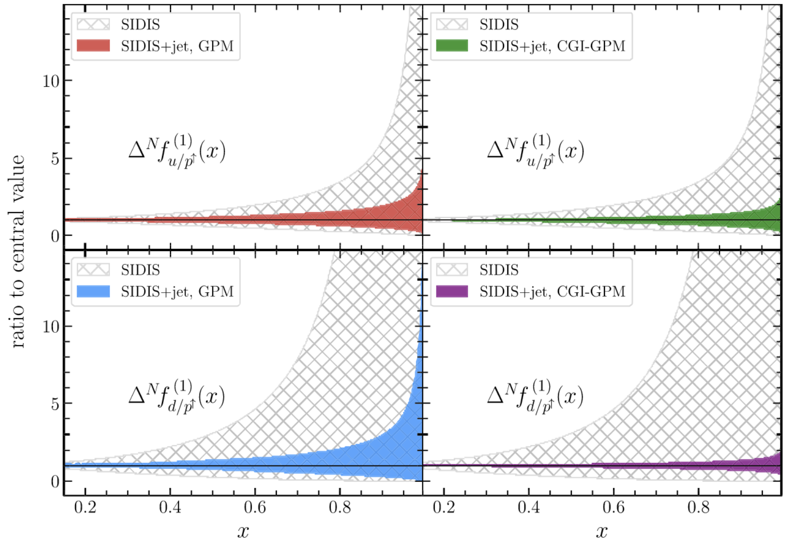

Figure 77: Comparison between the Sivers function first moments normalized to the corresponding central value from SIDIS data and their reweighted counterparts that incorporate new STAR results on electromagnetic jets [175] extracted in [181] in the generalized parton model (left panels) and color gauge invariant generalized parton model (right panels) framework. In both plots, results for u (upper panels) and d (lower panels) quarks are shown.

realistic jet smearing in a forward calorimeter and tracking system, and requiring a charged hadron with $z > 0.5$, the asymmetries can be separated and compared to the predictions for the Sivers function based on current SIDIS data. The expected uncertainties, plotted at the predicted values, can be seen in Fig. 78. Dilutions by underlying event and beam remnants were taken into account. The simulations have assumed only an integrated luminosity of 100 pb^{-1} at $\sqrt{s} = 200$ GeV, which is significantly lower than what is currently expected for the Run-24 200 GeV polarized p+p run.

In a TMD framework, the Sivers effect manifests itself as a correlation (a triple product) between the transverse momentum of a parton ($\overrightarrow{k}_T$) with momentum fraction x, and the transverse spin ($\overrightarrow{S}$) of a polarized proton moving in the longitudinal ($\overrightarrow{p}$) direction. Thus, for transversely polarized protons, the Sivers effect probes whether the k_T of the constituent quarks is preferentially oriented in a direction perpendicular to both the proton momentum and its spin. Momentum conservation then implies that the two jets in the final state will not emerge back-to-back on average, but instead will 'tilt' in the direction of the summed k_T of the initial state partons. Moreover, the (average) tilt of interest will reverse direction under a 'flip' of the proton spin; a spin-dependent $\langle k_T \rangle$ can then be extracted by associating the azimuthal opening angle of the jet pair with this tilt.

STAR carried out an earlier measurement of this transverse single-spin asymmetry using a dijet dataset with ∼1 pb^{-1} of integrated luminosity [183], and found it to be consistent with zero within 2σ. Figure 79 shows the first ever observation of the Sivers effect in dijet

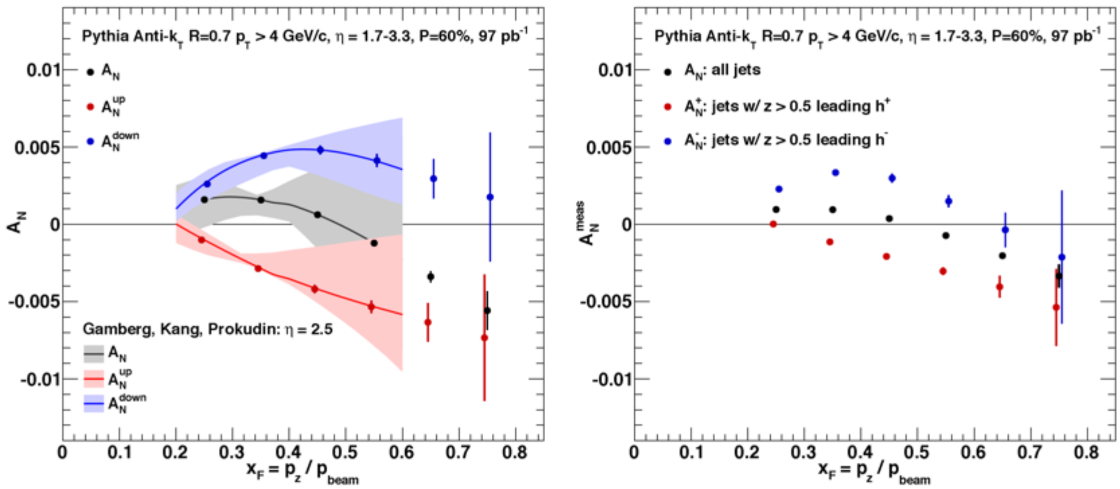

Figure 78: Left: up quark (red points), down quark (blue points) and all jet (black points) single spin asymmetries as a function of x_F as calculated by the ETQS based on the SIDIS Sivers functions. Right: Expected experimental sensitivities for jet asymmetries tagging in addition a positive hadron with z above 0.5 (red points), a negative hadron with z above 0.5 (blue points) or all jets (black) as a function of x_F. Note: these figures are for 200 GeV center-of-mass energy proton collisions.

production, which just entered GPC for publication. The jets were sorted according to their net charge Q, calculated by summing the signed momentum of all particle tracks with $p >$ 0.8 GeV, to minimize underlying event contributions, yielding jet samples with enhanced contributions from u quarks (positive Q) and d quarks (negative Q), with a large set near $Q = 0$ dominated by gluons. Simple kinematics allow for conversion from the spin-dependent 'tilt' of the dijet pair to a value of k_T on an event-by-event basis; these are then sorted by the Q of the jet and binned by the summed pseudorapidities of the outgoing jets, $\eta^{\text{total}} \equiv \eta_3 + \eta_4$. Because the contributions of different partons (u, d, all else) to $\langle k_T \rangle$ vary with both Q and also η^{total}, in a way that can be estimated robustly using simulation, the data can be inverted to yield values of $\langle k_T \rangle$ for the individual partons, though with coarser binning in η^{total}.

Such measurements are crucial to explore questions regarding factorization of the Sivers function in dijet hadroproduction [184–187]. Those results were derived from 200 GeV transverse spin data that STAR recorded in Run-12 and Run-15 (total sampled luminosity ~ 75 pb^{-1} for the two years combined). Nonetheless, the uncertainties remain large, as can be seen in Fig. 79. Run-24 data will reduce the uncertainties for $|\eta_3 + \eta_4| < 1$ by about a factor of two. The increased acceptance from the iTPC will reduce the uncertainties at $|\eta_3 + \eta_4| \approx 2.5$ by a much larger factor, while the Forward Upgrade will enable the measurements to be extended to even larger values of $|\eta_3 + \eta_4|$. When combined with the 510 GeV data from Run-17 and Run-22, the results will provide a detailed mapping *vs.* x for comparison to results for Sivers functions extracted from SIDIS, Drell-Yan, and vector boson production.

Transversity and Related Quantities

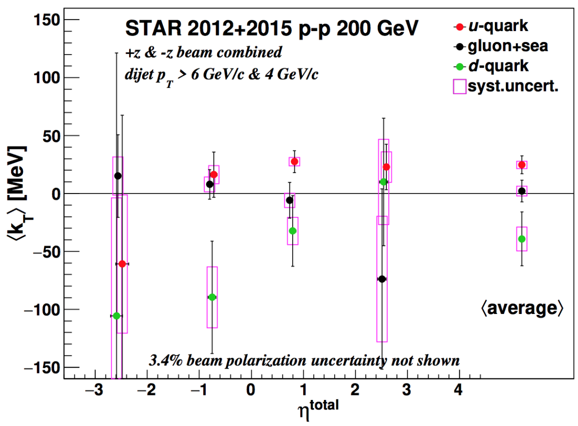

Figure 79: The $\langle k_T \rangle$ for individual partons, inverted using parton fractions from simulation and tagged $\langle k_T \rangle$ in data, is plotted as a function of $\eta_{\text{total}} \sim \log(x_1/x_2)$). The rightmost points represent the average of all the η_{total} bins. The systematic uncertainty in η_{total} is set to be non-zero to improve the visibility of the error bars.

A complete picture of nucleon spin structure at leading twist must include contributions from the unpolarized and helicity distributions, as well as those involving transverse polarization, such as the transversity distribution [188–190]. The transversity distribution can be interpreted as the net transverse polarization of quarks within a transversely polarized proton. The difference between the helicity and transversity distributions for quarks and antiquarks provides a direct, x-dependent connection to nonzero orbital angular momentum components in the wave function of the proton [191]. Recently, the first lattice QCD calculation of the transversity distribution has been performed [192]. In addition, the measurement of transversity has received substantial interest as a means to access the tensor charge of the nucleon, defined as the integral over the valence quark transversity: $\delta q^a = \int_0^1 [\delta q^a(x) - \delta \overline{q}^a(x)]\, dx$ [189, 193]. Measuring the tensor charge is very important for several reasons. First, it is an essential and fundamental quantity to our understanding of the spin structure of the nucleon. Also, the tensor charge can be calculated on the lattice with comparatively high precision, due to the valence nature of transversity, and hence is one of the few quantities that allow us to compare experimental results on the spin structure of the nucleon directly to *ab initio* QCD calculations. Finally, the tensor charge describes the sensitivity of observables in low-energy hadronic reactions to beyond the standard model physics processes with tensor couplings to hadrons. Examples are experiments with ultracold neutrons and nuclei.

Transversity is difficult to access due to its chiral-odd nature, requiring the coupling of this distribution to another chiral-odd distribution. Semi-inclusive deep-inelastic scattering (SIDIS) experiments have successfully probed transversity through two channels: asymmetric distributions of single pions, convoluting the TMD transversity distribution with the TMD Collins fragmentation function, and azimuthally asymmetric distributions of dihadrons, coupling transversity to the so-called "interference fragmentation function" (IFF) in the framework of collinear factorization. Yet in spite of a wealth of lepton-scattering data, the kinematic reach of existing SIDIS experiments limits the precision with which the proton's transversity can be extracted, as the range of Bjorken-x values that can be accessed does not extend above $x \sim 0.3$.

In hadronic collisions, the k_T integrated quark transversity distribution may be accessed mainly via two channels. The first is the single spin asymmetry of the azimuthal distribution of hadrons in high energy jets [194]. In the jet+hadron channel, the collinear transversity distribution couples to the TMD Collins function [194, 195]. This makes $p+p$ collisions a more direct probe of the Collins fragmentation function than Collins asymmetries in SIDIS [194], where a convolution with the TMD transversity distribution enters. This also makes the Collins asymmetry in $p+p$ collisions an ideal tool to explore the fundamental QCD questions of TMD factorization, universality, and evolution. The second channel is the single spin asymmetry of pion pairs, where transversity couples to the collinear interference fragmentation function [196]. STAR mid-rapidity IFF data [197] have been included in the first extraction of transversity from SIDIS and proton-proton IFF asymmetries [198]. In addition, transverse spin transfer, D_{TT}, of Λ hyperons in $p+p$ collisions is also expected to be able to provide sensitivity for the strange quark transversity through the polarized fragmentation functions. The strange quark transversity is not constrained at all currently. The first D_{TT} measurement of Λ and $\bar{\Lambda}$ hyperons at $\sqrt{s} = 200$ GeV has been performed with the Run-12 $p+p$ dataset [199] and preliminary results based on Run-15 have been released [200]. Current results didn't indicate a sizable spin transfer yet. The iTPC upgrade will help to reach near-forward pseudo-rapidity $\eta < 1.5$ for the spin transfer measurements.

The universality of TMD PDFs and fragmentation functions in $p+p$ collisions has been an open question. General arguments [184, 185] have shown that factorization can be violated in hadron-hadron collisions for TMD PDFs like the Sivers function, though very recent calculations indicate the violations might be quite small [186, 187]. In contrast, while there is no general proof that the Collins effect in $p+p$ collisions is universal to all orders, explicit calculations [194, 195, 201, 202] have shown that diagrams like those that violate factorization of the Sivers function make no contribution to the Collins effect at the one- or two-gluon exchange level, thereby preserving its universality at least to that level.

Comparisons of the transversity distributions extracted from the Collins and IFF channels will allow STAR to study the size and nature of any factorization breaking effects for TMD observables in hadronic collisions. Likewise, comparisons with the transversity, Collins and IFF distributions extracted from SIDIS collisions will shed light on universality and constrain evolution effects. The measurement of evolution effects in TMD distributions is particularly important because, unlike the collinear case, TMD evolution contains a non-perturbative component that cannot be calculated directly.

Data from 200 GeV $p+p$ collisions will play an essential role toward answering these questions. Figure 80 shows that 200 GeV $p+p$ collisions interpolate between the coverage that we will achieve with collected Run-22 data at high-x with the Forward Upgrade and at low-x with the STAR mid-rapidity detectors. They will also provide a significant overlapping region of x coverage, but at Q^2 values that differ by a factor of 6. This will provide valuable information about evolution effects, as well as cross-checks between the two measurements. Furthermore, for most of the overlapping x region, 200 GeV $p+p$ collisions will also provide the greatest statistical precision (see for example Fig. 81), thereby establishing the most precise benchmark for future comparisons to ep data from the EIC. It is important to also recognize that the hadron-in-jet measurements with the STAR Forward Upgrade will provide very valuable experience detecting jets close to beam rapidity that will inform the planning for future jet measurements in similar kinematics at the EIC.

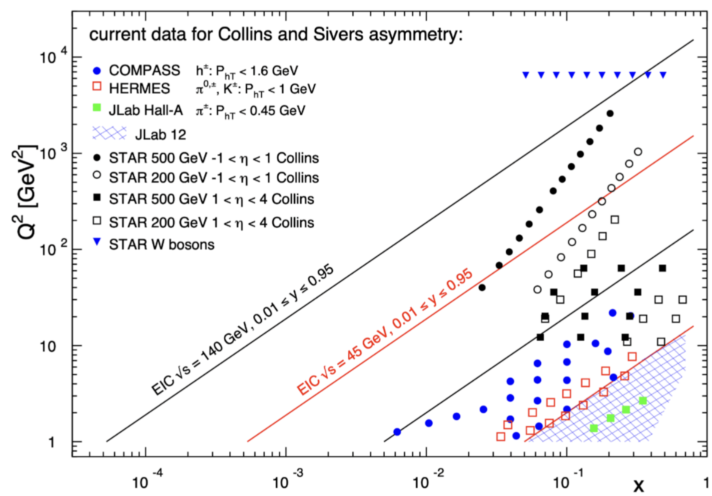

Figure 80: $x - Q^2$ coverage of RHIC measurements compared to existing Collins and Sivers effect measurements in SIDIS and the future coverage of the EIC.

The high statistical precision of the Run-24 data will enable detailed multi-dimensional binning for the Collins asymmetry results. This is particularly valuable because, as emphasized in [194, 195], hadron-in-jet measurements in $p+p$ collisions provide a direct probe of the Collins fragmentation function since they combine it with the *collinear* transversity dis-

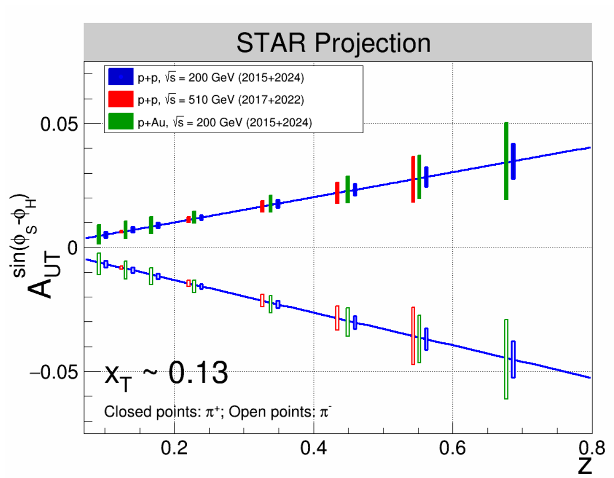

Figure 81: Projected statistical uncertainties for STAR Collins asymmetry measurements at $0 < \eta < 0.9$ in $p+p$ at $\sqrt{s} = 200$ and 510 GeV and p–Au at $\sqrt{s_{\rm NN}} = 200$ GeV. The points have arbitrarily been drawn on the solid lines, which represent simple linear fits to the STAR preliminary 200 GeV $p+p$ Collins asymmetry measurements from 2015. (Note that only one bin is shown spanning $0.1 < z < 0.2$ for 510 GeV $p+p$ whereas three bins are shown covering the same z range for the 200 GeV measurements).

tribution. In general, the observed asymmetries are functions of jet (p_T, η), hadron (z, j_T), and Q^2. However, the physics interpretations associated with these variables separate, with p_T and η primarily coupling to the incident quark x and the polarization transfer in the hard scattering, while z and j_T characterize the fragmentation kinematics. Thus, A_{UT} *vs.* p_T provides information about the transversity distribution, while the (z, j_T) dependence provides a detailed look at the Collins fragmentation function. Recently finalized results based on Run-12 and Run-15 datasets, discussed in Sec 1.2, finds the maximum value of A_{UT} shift to higher j_T as p_T increases (see Fig. 34) which is not seen in the current theory evaluations [203]. The statistical uncertainties in Fig. 34 will be reduced by a factor of about 2.5 when Run-12, Run-15 and Run-24 data are combined together.

The Run-15 Collins analysis has also, for the first time, measured the Collins effect for charged kaons and protons/anti-protons in p+p collisions, as shown in Fig. 35. The asymmetries for K^+, which like π^+ have a contribution from favored fragmentation of u quarks, are similar in magnitude to the π^+ asymmetries, while those for K^-, which can only come from unfavored fragmentation, are consistent with zero at the 1-sigma level. These trends are similar to those found in SIDIS by HERMES [204] and COMPASS [205], and provide additional insight into the Collins fragmentation function. This same analysis with Run-24 data will yield statistical uncertainties about a factor of 3 smaller than those in Fig. 35. This is a much greater improvement than would be expected from the increase in sampled luminosity thanks to the improved dE/dx resolution provided by the iTPC. In addition, the iTPC will enable the measurements in Figs. 34 and 35 to be extended to an additional higher η bin $(0.9 < \eta < 1.3)$.

RHIC has the unique opportunity to extend the Collins effect measurements to nuclei. This will provide an alternative look at the universality of the Collins effect in hadron-production by dramatically increasing the color flow options of the sort that have been predicted to break factorization for TMD PDFs like the Sivers effect [184, 185]. This will also explore the spin dependence of the hadronization process in cold nuclear matter. STAR collected a proof-of-principle dataset during the 2015 p+Au run that is currently under analysis. Those data will provide a first estimate of medium-induced effects. However, the small nuclear effects seen by STAR for forward inclusive π^0 A_N [176] indicate that greater precision will likely be needed. Figure 81 shows the projected Run-15 and Run-24 statistical uncertainties for the p+Au Collins asymmetry measurement at $\sqrt{s_{\rm NN}} = 200$ GeV, compared to those for the p+p at the same energy.

Ultra-peripheral Collisions

The formalism of generalized parton distributions (GPDs) provides a theoretical framework which addresses some of the above questions [206–209]. Constraints on GPDs have mainly been provided by exclusive reactions in DIS, e.g. deeply virtual Compton scattering. RHIC, with its unique capability to collide transversely polarized protons at high energies, has the opportunity to measure A_N for exclusive J/ψ production in ultra-peripheral collisions (UPCs) [210]. In such a UPC process, a photon emitted by the opposing beam particle (p or A) collides with the polarized proton. The measurement is at a fixed $Q^2 \sim M^2_{J/\psi} \approx 10$ GeV^2

and $10^{-4} < x < 10^{-1}$. A nonzero asymmetry would be the first signature of a nonzero GPD E_g for gluons, which is sensitive to spin-orbit correlations and is intimately connected with the orbital angular momentum carried by partons in the nucleon and thus with the proton spin puzzle.

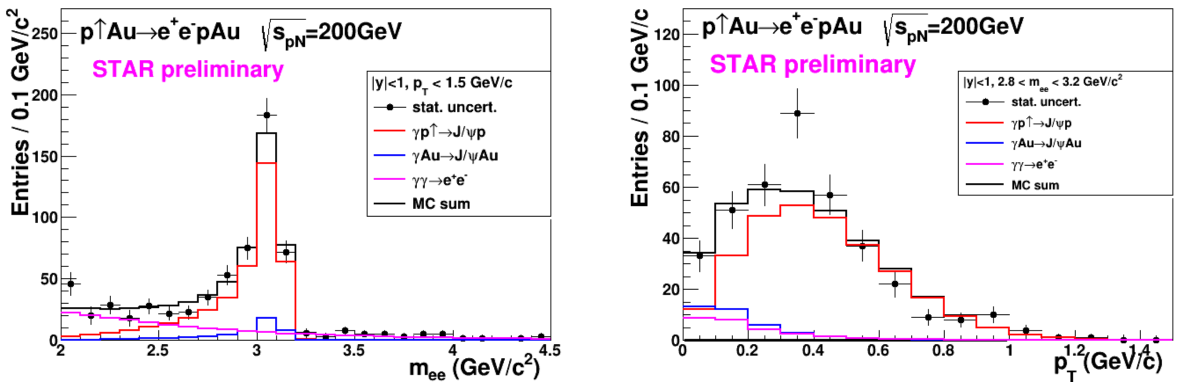

Figure 82: Mass distribution of selected e^+e^- pairs (left), and p_T distribution of the J/ψ mass peak (right). The colored histograms are the indicated processes modelled by STARlight and the sum fit to the data.

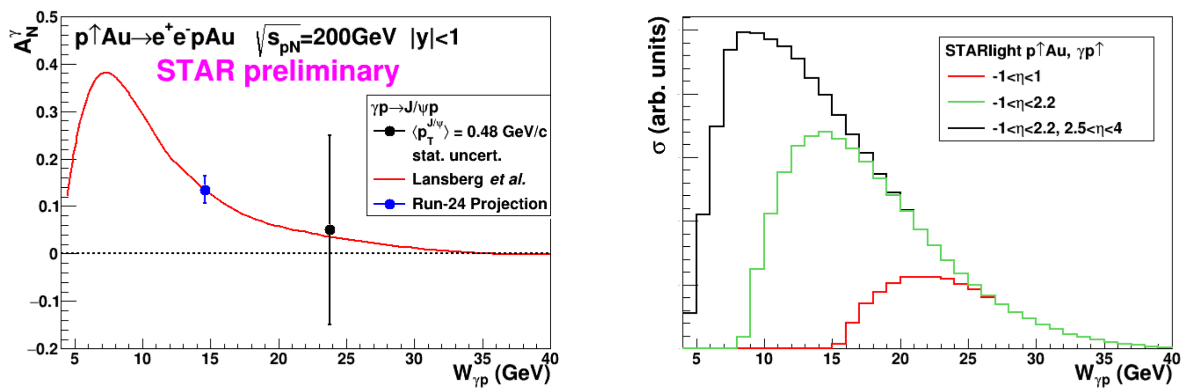

Figure 83: Left: The measured J/ψ transverse asymmetry A_N^γ and a prediction based on a parameterization of E_g. Right: The accepted cross section for γ+p$^\uparrow \to J/\psi$ for various detector pseudorapidity η ranges; the black curve shows the result for the full STAR detector with the Forward Upgrade and the iTPC.

The Run-15 p$^\uparrow$+Au data allowed a proof-of-principle of such a measurement. A trigger requiring back-to-back energy deposits in the Barrel Electromagnetic Calorimeter selected J/ψ candidates. The e^+e^- mass distribution after selection cuts is shown in the left of Fig. 82, and the pair p_T distribution of the J/ψ mass peak is shown on the right of that figure. The data are well described by the STARlight model [211] (colored histograms in the figure), including the dominant γ+p$^\uparrow \to J/\psi$ signal process and the γ+Au$\to J/\psi$ and

γ+γ→e^+e^- background processes. The left of Fig. 83 shows the STAR preliminary measurement (solid circle marker) of the transverse asymmetry A_N^γ for the J/ψ signal, which has a mean photon-proton center-of-mass energy $W_{\gamma p} \approx 24$ GeV. The result is consistent with zero. Also shown is a prediction based on a parameterization of E_g [212]; the present data provide no discrimination of this prediction.

This measurement can be greatly improved with a high statistics transversely polarized p$^\uparrow$+Au Run-24. The integrated luminosity for the Run-15 measurement was 140 nb^{-1}; the Run-24 will provide about 1.2 pb^{-1}, allowing a sizeable reduction of statistical uncertainty in the same $W_{\gamma p}$ range. However, the Forward Upgrade and iTPC will also provide a significant extension of the $W_{\gamma p}$ range of the measurement. The right panel of Fig. 83 shows the accepted cross section for γ+p$^\uparrow$ → J/ψ for various detector pseudorapidity ranges. With the full detector, the sensitive cross section is a factor of five times the central barrel alone and the expected asymmetry is substantially larger. The projected statistical uncertainty on A_N^γ as shown in the left of Fig. 83 (blue square marker) offering a powerful test of a non-vanishing E_g. Also, the accepted region has a lower mean $W_{\gamma p} \approx 14$ GeV. Predictions based on E_g parameterizations such as shown in the figure have a larger asymmetry at lower $W_{\gamma p}$, with increased possibility of a nonzero result. Alternatively, the increased statistics will allow a measurement of A_N^γ in bins of $W_{\gamma p}$.

The UPC cross section scales with Z^2 of the the nucleus emitting the photon; for protons this is $1/79^2$ relative to Au nuclei, which makes analogous measurements in p+p collisions extremely luminosity-hungry. Therefore, the p+Au run is important for this measurement.

In addition to the J/ψ measurements, the exclusive dijet studies, described in Sec. 2.2, can be also sensitive to Generalized Parton Distributions.

3.2 Physics Opportunities with Unpolarized proton-Nucleus Collisions

Our quest to understand QCD processes in Cold Nuclear Matter (CNM) centers on the following fundamental questions:

- Can we experimentally find evidence of a novel universal regime of non-linear QCD dynamics in nuclei?
- What is the role of saturated strong gluon fields, and what are the degrees of freedom in this high gluon density regime?
- What is the fundamental quark-gluon structure of light and heavy nuclei?
- Can a nucleus, serving as a color filter, provide novel insight into the propagation, attenuation and hadronization of colored quarks and gluons?

Various aspects of these questions have been addressed by numerous experiments and facilities around the world, most of them at significantly lower center-of-mass energies and kinematic reach than RHIC. Deep inelastic scattering on nuclei addresses some of these questions with results from, for instance, HERMES at DESY [213–215], CLAS at JLab [216], and in the future from the JLab 12 GeV. This program is complemented by hadron-nucleus reactions in fixed target p+A at Fermilab (E772, E886, and E906) [217] and at the CERN-SPS.

In the following we propose a measurement program unique to RHIC to constrain the initial state effects in strong interactions in the nuclear environment. We also highlight the complementarity to the LHC p+Pb program and stress why RHIC data are essential and unique in the quest to further our understanding of nuclei. The uniqueness of the RHIC program is based on the flexibility of the RHIC accelerator to run collisions of different particle species at very different center-of-mass energies. This in combination with the enhanced STAR detector capabilities in Run-24 allows to disentangle nuclear effects in the initial and final state as well as leading twist shadowing from saturation effects in a kinematic regime where all these effects are predicted to be large. Most of the discussed measurements critically rely on the Forward Upgrade.

The Initial State of Nuclear Collisions

Nuclear parton distribution functions: A main emphasis of the Run-15 and later p+A runs is to determine the initial conditions of the heavy ion nucleus before the collision to support the theoretical understanding of the A–A program both at RHIC and the LHC. In the following, the current status of nPDFs will be discussed, including where the unique contributions of RHIC lie, in comparison to the LHC and the future EIC.

Our current understanding of nuclear parton distribution functions (nPDFs) is still very limited, in particular, when compared with the rather precise knowledge of PDFs for free protons collected over the past 30 years. Figure 84 shows an extraction of nPDFs from available data, along with estimates of uncertainties. All results are shown in terms of the nuclear modification ratios, i.e., scaled by the respective PDF of the free proton. The kinematic coverage of the data used in the EPPS21 fits [218] are shown in Fig. 85. Clearly, high precision data at small x and for various different values of Q^2 are needed to better constrain the magnitude of suppression in the x region where non-linear effects in the scale evolution are expected. In addition, such data are needed for several different nuclei, as the A-dependence of nPDFs cannot be predicted from first principles in pQCD and, again, currently relies on assumptions. The PHENIX midrapidity $\pi^0 R_{dAu}$ data [219], are the only data which can probe the gluon in the nucleus directly, but these data also suffer from unknown nuclear effects in the final state (see [220]). Therefore, it is critical to have high precision data only sensitive to nuclear modification in the initial state over a wide range in x and intermediate values of Q^2 (away from the saturation regime) to establish the nuclear modification of gluons in this kinematic range.

It is important to realize that the measurements from RHIC are compelling and essential even when compared to what can be achieved in p–Pb collisions at the LHC. Due to the higher center-of-mass system energy most of the LHC data have very high Q^2, where the nuclear effects are already reduced significantly by evolution and are therefore very difficult

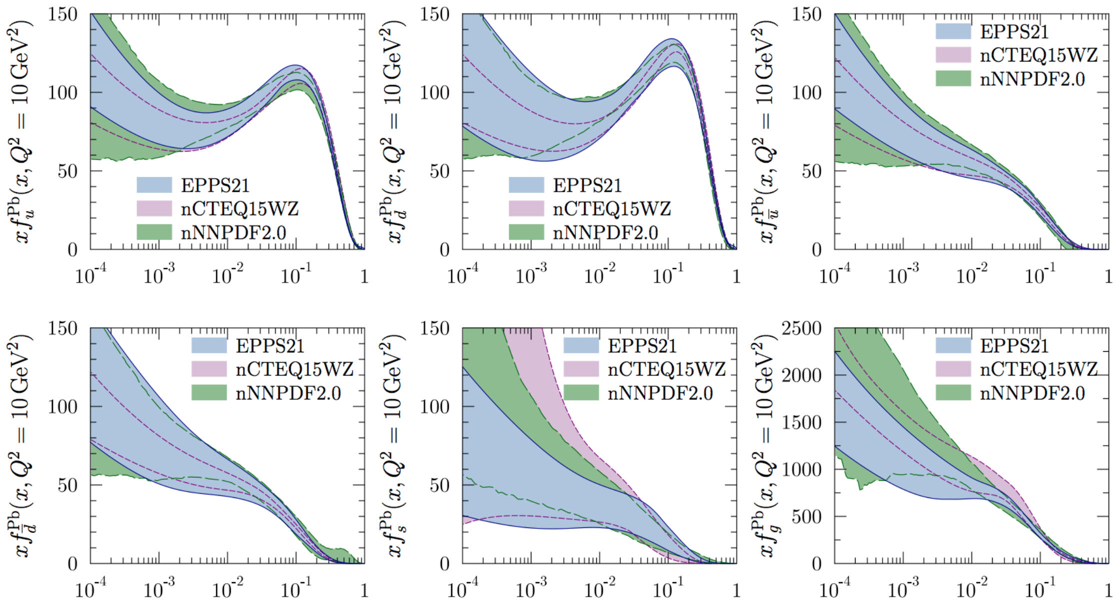

Figure 84: Summary of the most recent sets of nPDFs at 90% confidence-level [218].

to constrain.

RHIC has the *unique* capability to provide data in a kinematic regime (moderate Q^2 and medium-to-low x) where the nuclear modification of the sea quark and the gluon is expected to be sizable. In addition, and unlike the LHC, RHIC has the potential to vary the nucleus in p+A collisions and as such also constrain the A-dependence of nPDFs.

Extraction of this information is less ambiguous if one uses processes in which strong (QCD) final-state interactions can be neglected or reduced. Such golden channels would include a measurement of R_{pA} for Drell-Yan production at forward pseudo-rapidities with respect to the proton direction ($2.5 < \eta < 4$) to constrain the nuclear modifications of sea-quarks. Moreover, the R_{pA} for direct photon production in the same kinematic regime will help constrain the nuclear gluon distribution. Data for the first measurement of R_{pA} for direct photon production have already been taken during the p+Au and p+Al Run-15, with recorded luminosities by STAR of $L_{pAu} = 0.45$ pb^{-1} and $L_{pAl} = 1$ pb^{-1}, respectively. Like all other inclusive probes in p+p and p+A collisions, e.g., jets, no access to the exact parton kinematics can be provided event-by-event but global QCD analyses easily account for that. After the p+Au Run-24, the statistical precision of the prompt photon data will be sufficient to contribute to a stringent test of the universality of nuclear PDFs when combined with the expected data from the EIC (see Figure 2.22 and 2.23 in Ref [221]). The Forward Upgrade with its tracking at forward rapidities will also provide the possibility to measure R_{pA} for positive and negatively charged hadrons. Approximately equal nucleon-nucleon luminosities for p+p and p+Au are important for the optimization of R_{pA} measurements as they directly compare the same observable—yields—in both collision systems.

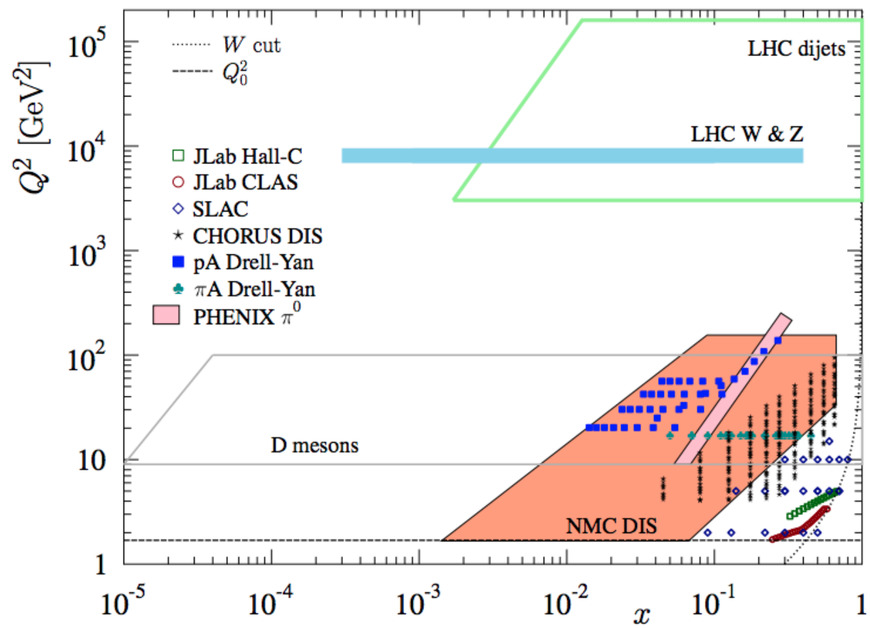

Figure 85: The kinematic x and Q^2 coverage of data used in the EPPS21 nPDF fits [218].

Figure 86 shows the kinematic coverage in x–Q^2 of past, present, and future experiments capable of constraining nuclear parton distribution functions. The shown experiments provide measurements that access the initial state parton kinematics on an event-by event basis (in a leading order approximation) while remaining insensitive to any nuclear effects in the final state. Some of the LHC experiments cover the same x-range as DY at forward pseudorapidities at RHIC but at a much higher scale Q^2, where nuclear modifications are already significantly reduced [222–224]. At intermediate Q^2, DY at STAR will extend the low-x reach by nearly one decade compared to EIC.

The biggest challenge of a DY measurement is to suppress the overwhelming hadronic background: the total DY cross-section is about 10^{-5} to 10^{-6} smaller than the corresponding hadron production cross-sections. Therefore, the probability of misidentifying a hadron track as a lepton has to be suppressed to the order of 0.1% while maintaining reasonable electron detection efficiencies. To that end, we have studied the combined electron/hadron discriminating power of the Forward Upgrade. It was found that by applying multivariate analysis techniques to the features of EM/hadronic shower development and momentum measurements we can achieve hadron rejection powers of 200 to 2000 for hadrons of 15 GeV to 50 GeV with 80% electron detection efficiency.

The potential impact of the DY R_{pA} data for the EPPS-19 sets of nPDFs was studied through a re-weighting procedure [225]. We expect a significant impact on the uncertainties of R_{pA} DY upon including the projected and properly randomized data. Clearly, the DY data from RHIC will be instrumental in reducing present uncertainties in nuclear modifications of sea quarks. Again, these data will prove to be essential in testing the fundamental

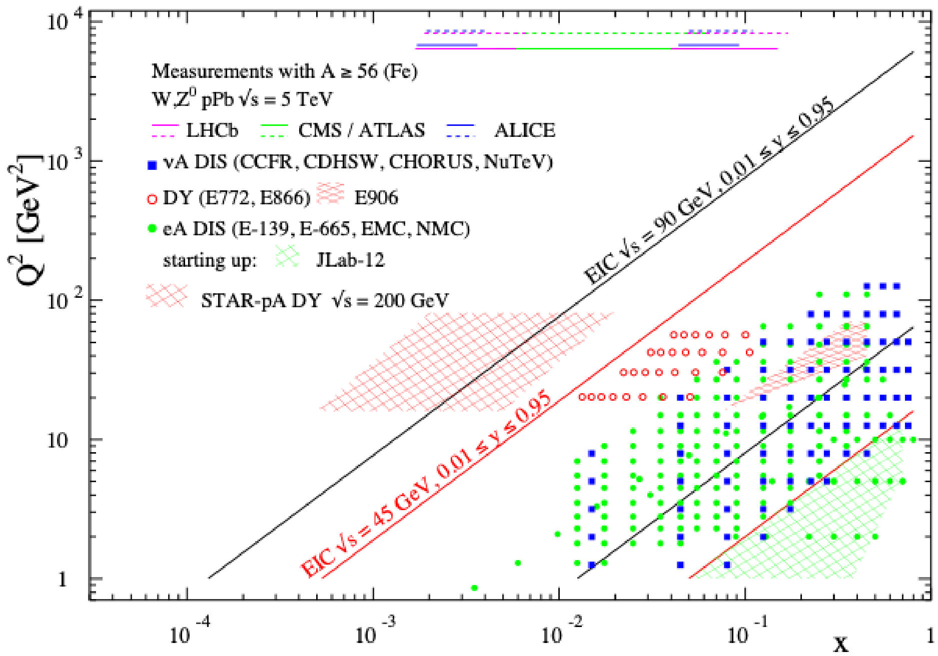

Figure 86: The kinematic coverage in $x - Q^2$ of past, present and future experiments constraining nPDFs with access to the exact parton kinematics event-by-event and no fragmentation in the final state.

universality property of nPDFs in the future when EIC data become available.

STAR's unique detector capabilities provide data on J/Ψ-production in ultra-peripheral collisions. This measurements can provide access to the spatial gluon distribution by measuring the t-dependence of $d\sigma/dt$. To study the gluon distribution in the gold nucleus, events need to be tagged where the photon is emitted from the proton (γ+Au$\rightarrow$ J/ψ). However, with the signal-to-background ratio in p+Au collisions (see, e.g., Fig. 82), we expect much better sensitivity to the gluon distributions in the Au+Au program. In addition to J/Ψ photoproduction in UPC for exclusive reaction, photoproduction back-to-back jets is also sensitive the PDFs (nPDFs in Au+Au UPC). This measurement has never been performed at RHIC experiments, where the kinematic coverage can go to moderate to high-x. The anti-shadowing region in nuclei, for example, is of great interest by comparing to this measurement in proton. Furthermore, we can possibly extend the measurement from inclusive photoproduction dijets to diffractive dijets in $p+p$ and p+Au collisions, which will be sensitive to the QCD factorisation breaking [151]. For details, see Sec. 2.2 for discussion in UPCs.

Gluon Saturation: Our understanding of the proton structure and of the nuclear interactions at high energy would be advanced significantly with the definitive discovery of the saturation regime [226–232]. Saturation physics would provide an infrared cutoff for perturbative calculations, the saturation scale Q_s, which grows with the atomic number of the nucleus A and with decreasing value of x. If Q_s is large it makes the strong coupling constant small, $\alpha_s(Q_s^2) << 1$ allowing for perturbative QCD calculations to be under theoretical control.

It is well known that PDFs grow at small-x. If one imagines how such a high number of

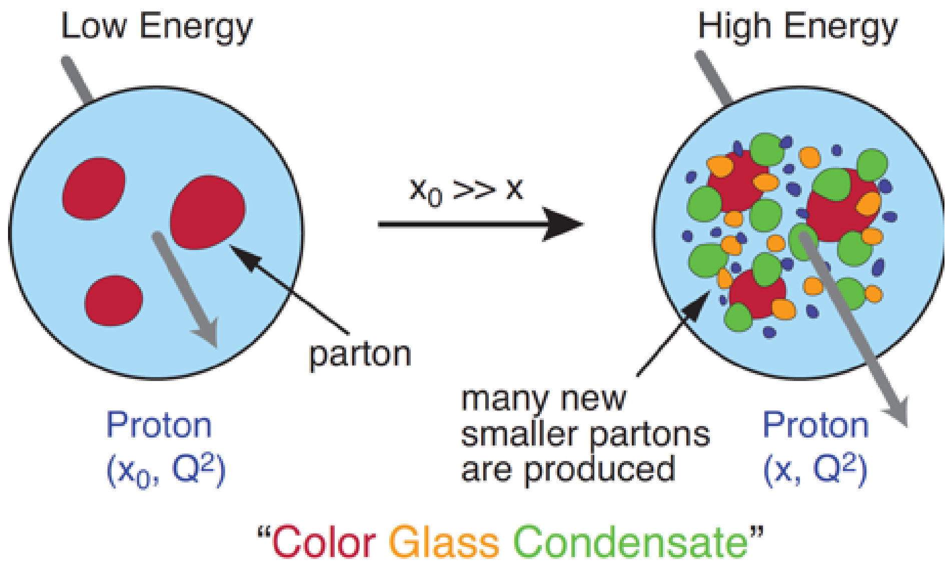

Figure 87: Proton wave function evolution towards small-x.

small-x partons would fit in the (almost) unchanged proton radius, one arrives at the picture presented in Fig. 87: the gluons and quarks are packed very tightly in the transverse plane. The typical distance between the partons decreases as the number of partons increases, and can get small at low-x (or for a large nucleus instead of the proton). One can define the saturation scale as the inverse of this typical transverse inter-parton distance. Hence Q_s indeed grows with A and decreasing x.

The actual calculations in saturation physics start with the classical gluon fields (as gluons dominate quarks at small-x) [233–239], which are then evolved using the nonlinear small-x BK/JIMWLK evolution equations [240, 241, 241–249]. The saturation region can be well-approximated by the following formula: $Q_s^2 \sim (A/x)^{1/3}$. Note again that at small enough x the saturation scale provides an IR cutoff, justifying the use of perturbative calculations. This is important beyond saturation physics, and may help us better understand small-x evolution of the TMDs.

While the evidence in favor of saturation physics has been gleaned from the data collected at HERA, RHIC and the LHC, the case for saturation is not sealed and alternative explanations of these data exist. The EIC is slated to provide more definitive evidence for saturation physics [174]. To help the EIC complete the case for saturation, it is mandatory to generate higher-precision measurements in p+Au collisions at RHIC. These higher-precision measurements would significantly enhance the discovery potential of the EIC as they would enable a stringent test of universality of the CGC. We stress again that a lot of theoretical predictions and results in the earlier Sections of this document would greatly benefit from saturation physics: the small-x evolution of TMDs in a longitudinally or transversely polarized proton, or in an unpolarized proton, can all be derived in the saturation framework [250] in a theoretically better-controlled way due to the presence of Q_s. Hence saturation physics may help us understand both the quark and gluon helicity PDFs as well as the Sivers and

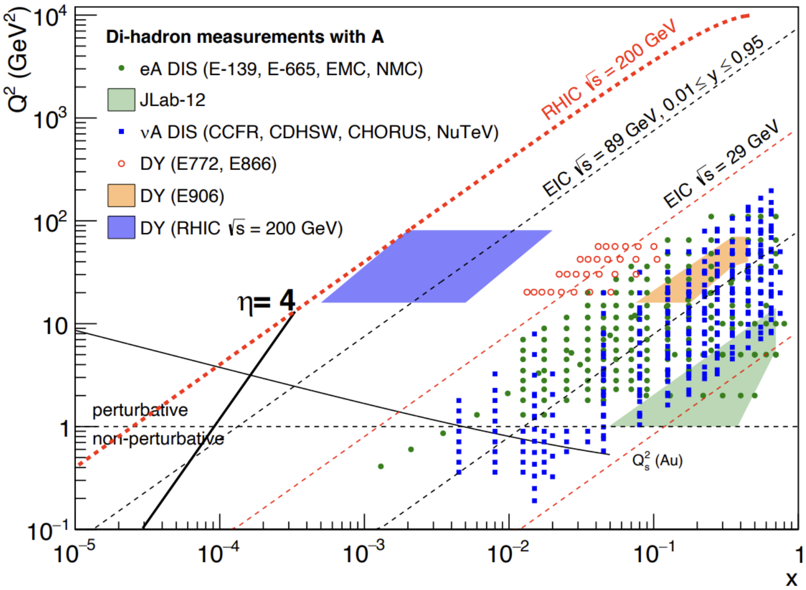

Figure 88: Kinematic coverage in the $x - Q^2$ plane for p+A collisions at RHIC, along with previous e+A measurements, the kinematic reach of an electron-ion collider, and estimates for the saturation scale Q_s in Au nuclus and the line illustrating the range in x and Q^2 covered with hadrons at rapidity $\eta = 4$.

Boer-Mulders functions.

The saturation momentum is predicted to grow approximately like a power of energy, $Q_s^2 \sim E^{\lambda/2}$ with $\lambda \sim 0.2 - 0.3$, as phase space for small-x (quantum) evolution opens up. The saturation scale is also expected to grow in proportion to the valence charge density at the onset of small-x quantum evolution. Hence, the saturation scale of a large nucleus should exceed that of a nucleon by a factor of $A^{1/3} \sim 5$ (on average over impact parameters). RHIC is capable of running p+A collisions for different nuclei to check this dependence on the mass number. This avoids potential issues with dividing say p–Pb collisions in N$_{part}$ classes [251]. Figure 88 shows the kinematic coverage in the $x - Q^2$ plane for p+A collisions at RHIC, along with previous e+A measurements and the kinematic reach of an EIC. The saturation scale for a Au nucleus is also shown. To access at RHIC a kinematic regime sensitive to saturation with $Q^2 > 1$ GeV^2 requires measurements at forward rapidities. For these kinematics the saturation scale is moderate, on the order of a few GeV^2, so measurements sensitive to the saturation scale are by necessity limited to semi-hard processes.

Until today the golden channel at RHIC to observe strong hints of saturation has been the angular dependence of two-particle correlations, because it is an essential tool for testing the underlying QCD dynamics [251]. In forward-forward correlations facing the $p(d)$ beam direction one selects a large-x parton in the $p(d)$ interacting with a low-x parton in the nucleus. For $x < 0.01$ the low-x parton will be back-scattered in the direction of the large-x parton. Due to the abundance of gluons at small x, the backwards-scattered partons are dominantly gluons, while the large-x partons from the $p(d)$ are dominantly quarks. The measurements of di-hadron correlations by STAR and PHENIX [72,252], have been compared with theoretical expectations using the CGC framework based on a fixed saturation scale Q_s and considering valence quarks in the deuteron scattering off low-x gluons in the nucleus with impact parameter $b = 0$ [71, 253]. Alternative calculations [254] based on both initial and

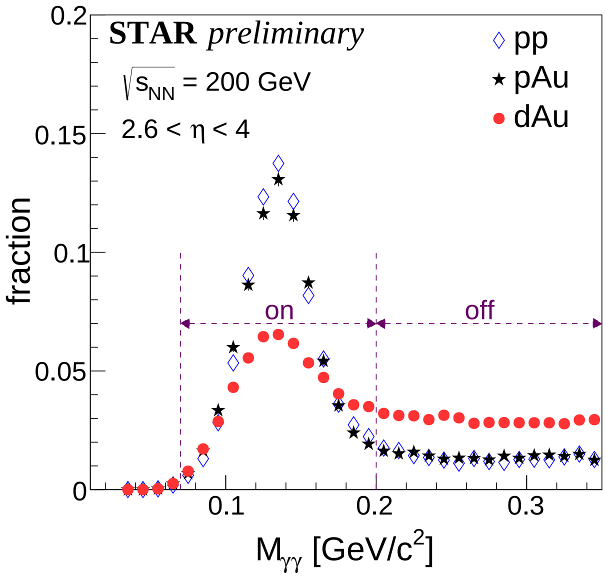

Figure 89: The invariant mass spectra for di-photon in p+p p+Au and d+Au. The on mass range is chosen as 0.07-0.2 GeV/c^2, the off mass range is 0.2-0.35 GeV/c^2.

final state multiple scattering, which determine the strength of this transverse momentum imbalance, in which the suppression of the cross-section in d+Au collisions arises from cold nuclear matter energy loss and coherent power corrections have also been very successful to describe the data.

The p+A Run-15 at RHIC has provided unique opportunities to study this channel in more detail at STAR. The high delivered integrated luminosities allow one to vary the trigger and associated particle p_T from low to high values and thus crossing the saturation boundary as shown in Fig. 88 and reinstate the correlations for central p+A collisions for forward-forward π^0's. Studying di-hadron correlations in p+A collisions instead of d+A collisions has a further advantage. In reference [73], the authors point out that the contributions from double-parton interactions to the cross-sections for $dA \rightarrow \pi^0\pi^0X$ are not negligible. They find that such contributions become important at large forward rapidities, and especially in the case of d+A scattering. Figure 33 shows the relative area of back-to-back di-π^0 correlations in p+Al and p+Au collisions relative to p+p collisions. The results show suppression with increasing A, and an enhanced suppression that scales as $A^{1/3}$. This behavior is consistent with different calculations based on the CGC formalism and is a clear hint of non-linear effects. A comparison between p+p (Run-15), p+Au (Run-15), and d+Au (Run-16) collisions can help provide insight into the contributions from multiple parton scattering [73]. Figure 89 shows the invariant mass spectra for final p+p and p+Au results and the preliminary d+Au. It is clear from the comparison that there is significantly more background in the the d+Au data than the p+p and p+Au data, which makes isolating the signal correlation more difficult. The generated combinatoric correlation dominates in d+Au collisions, which makes it very challenging to identify the signal correlation. The forward di-π^0 correlation measurement favors for the cleaner p+A collisions rather than d+A collisions. Run-24 will be able to measure di-hadron correlations taking advantage of the cleaner p+Au collisions and the extended pseudorapidity reach of the Forward upgrade detectors.

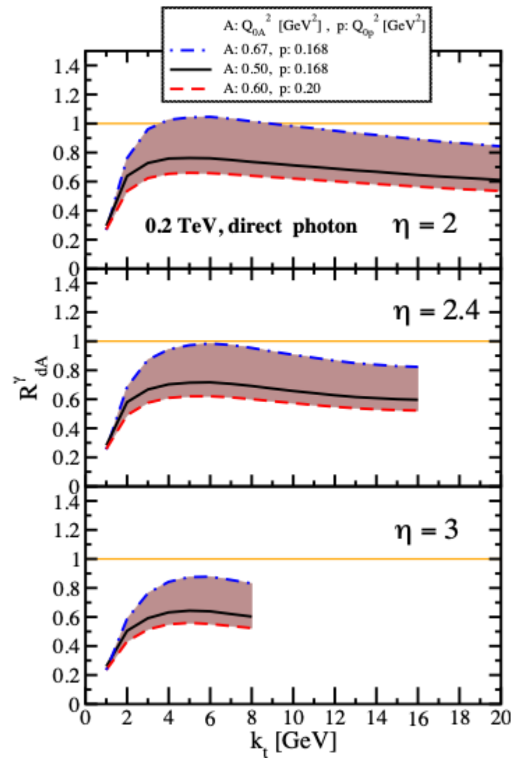

Figure 90: Nuclear modification factor for direct photon production in $p(d)$+A collisions at various rapidities at RHIC $\sqrt{s}$ = 200 GeV. The curves are the results obtained from Eq. (12) in Ref. [255] and the solution to rcBK equation using different initial saturation scales for a proton Q_{op} and a nucleus Q_{oA}. The band shows our theoretical uncertainties arising from allowing a variation of the initial saturation scale of the nucleus in a range consistent with previous studies of DIS structure functions as well as particle production in minimum-bias p+p, p+A and A+A collisions in the CGC formalism, see Ref. [255] for details.

It is important to note that for the measurements to date in $p(d)$+A collisions both initial and final states interact strongly, leading to severe complications in the theoretical treatment (see [256, 257], and references therein). As described in detail in the Section above in p+A collisions, these complications can be ameliorated by removing the strong interaction from the final state, by using photons and Drell-Yan electrons. The Run-15 p+A run will for the first time provide data on R_{pA} for direct photons and therefore allow one to test CGC based predictions on this observable as depicted in Fig. 90 (taken from Ref. [255]). The higher delivered integrated luminosity for the upcoming p+Au Run-24 together with the Forward Upgrade will enable one to study more luminosity hungry processes and/or complementary probes to the di-π^0 correlations, i.e. di-hadron correlations for charged hadrons, photon-jet, photon-hadron and di-jet correlations, which will allow a rigorous test of the calculation in the CGC formalism. It is important to stress that the comparison of these correlation probes in p+p and p+Au requires approximately equal nucleon-nucleon luminosities for these two collision systems for optimal measurements. It is noted that these results are crucial for the equivalent measurements at an EIC, which are planned at close to identical kinematics, because only if non-linear effects are seen with different complementary probes, i.e., *ep* and p+A one can claim a discovery of saturation effects and their universality.

We use direct photon plus jet (direct γ+jet) events as an example channel to indicate what can be done in Run-24. These events are dominantly produced through the gluon Compton scattering process, g+q $\rightarrow$ γ+q, and are sensitive to the gluon densities of the nucleon and nuclei in p+p and p+A collisions. Through measurements of the azimuthal correlations in p+A collisions for direct γ+jet production, one can study gluon saturation phenomena at small-x. Unlike di-jet production that is governed by both the Weizsäcker-Williams and dipole gluon densities, direct γ+jet production only accesses the dipole gluon density, which is better understood theoretically [255, 258]. On the other hand, direct γ+jet production is experimentally more challenging due to its small cross-section and large background contribution from di-jet events in which photons from fragmentation or hadron decay could be misidentified as direct photons. The feasibility to perform direct γ+jet measurements with the Forward Upgrade in unpolarized p+p and p+Au collisions at $\sqrt{s_{\rm NN}} = 200$ GeV has been studied. PYTHIA-8.189 [259] was used to produce direct γ+jet and di-jet events. In order to suppress the di-jet background, the leading photon and jet are required to be balanced in transverse momentum, $|\phi^{\gamma} - \phi^{jet}| > 2\pi/3$ and $0.5 < p_T^{\gamma}/p_T^{jet} < 2$. Both the photon and jet have to be in the forward acceptance $1.3 < \eta < 4.0$ with $p_T > 3.2$ GeV/c in 200 GeV p+p collisions. The photon needs to be isolated from other particle activities by requiring the fraction of electromagnetic energy deposition in the cone of $\Delta R = 0.1$ around the photon is more than 95% of that in the cone of $\Delta R = 0.5$. Jets are reconstructed by an anti-k_T algorithm with $\Delta R = 0.5$. After applying these selection cuts, the signal-to-background ratio is around 3:1 [260]. The expected number of selected direct γ+jet events is around 0.9M at $\sqrt{s_{\rm NN}} = 200$ GeV in p+Au collisions for the proposed Run-24. We conclude that a measurement of direct photon-jet correlation from p+Au collisions is feasible, which is sensitive to the gluon density in $0.001 < x < 0.005$ in the Au nucleus where parton saturation is expected.

Saturation with Ultra-Peripheral Collisions. There are other potential opportunities with the upcoming p+Au and $p + p$ runs for studying the gluon saturation phenomena using the ultra-peripheral collisions (UPC). For example, one of the most powerful measurements proposed at the EIC for discovery of gluon saturation is to look at double ratio between heavy nucleus and proton in terms of diffractive processes, see details in Sec. 2.2. With the STAR Run-2024, the p+Au UPC (also applies to $p + p$ UPC) may provide two important measurements, e.g., exclusive and inclusive J/ψ production off the proton target. The same measurement will be performed in Au+Au UPC with Run-2023 and 2025, and together with different system comparison, the STAR data may provide strong evidences for saturation.

The Final State

Fragmentation Functions: In spite of the remarkable phenomenological successes of QCD, a quantitative understanding of the hadronization process is still one of the great challenges for the theory. Hadronization describes the transition of a quark or gluon into a final state hadron. It is a poorly understood process even in elementary collisions. RHIC's unique versatility will make it possible to study hadronization in vacuum and in the nuclear medium, and additionally with polarized beams (see Sect. 3.1 for the latter).

It has long been recognized that the hadron distributions within jets produced in p+p collisions are closely related to the fragmentation functions that have typically been measured in e^+e^- collisions and SIDIS. The key feature of this type of observable is the possibility to determine the relevant momentum fraction z experimentally as the ratio of the hadron to the jet transverse momentum. Recently [261] a quantitative relationship has been derived in a form that enables measurements of identified hadrons in jets in p+p collisions to be included in fragmentation function fits on an equal footing with e^+e^- and SIDIS data. Furthermore, hadrons in p+p jets provide unique access to the gluon fragmentation function, which is poorly determined in current fits [262], in part due to some tension found in the inclusive high p_T pion yields measured by the PHENIX and ALICE collaborations. Here, the proposed measurements can provide valuable new insight into the nature of this discrepancy.

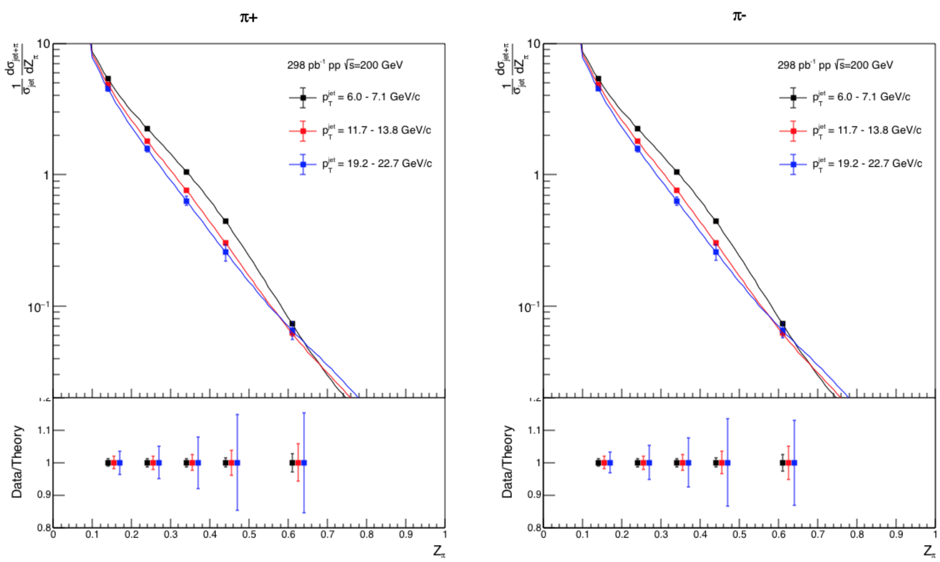

Figure 91: Anticipated precision for identified π^+(left) and π^-(right) within jets at $|\eta| < 0.4$ in 200 GeV p+p collisions for three representative jet p_T bins. The data points are plotted on theoretical predictions based on the DSSV14 pion fragmentation functions [261, 262]. Kaons and (anti)protons will also be measured, over the range from $z < 0.5$ at low jet p_T to $z < 0.2$ at high jet p_T, with uncertainties a factor of $\sim$3 larger than those for pions.

This development motivated STAR to initiate a program of identified particle fragmentation function measurements using p+p jet data at 200 and 500 GeV from Run-11, Run-12, and Run-15. Figure 91 shows the precision that is anticipated for identified π^+ and π^- in 200 GeV p+p collisions for three representative jet p_T bins after the existing data from Run-12 and Run-15 are combined with future 200 GeV p+p data from Run-24. Identified kaon and (anti)proton yields will also be obtained, with somewhat less precision, over a more limited range of hadron z. Once the Run-17 data are fully analyzed, the uncertainties for 510 GeV p+p collisions will be comparable to that shown in Fig. 91 at high jet p_T, and a factor of $\sim$ 2 larger than shown in Fig. 91 at low jet p_T. Identified hadron yields will also be measured multi-dimensionally vs. j_T, z, and jet p_T, which will provide important input for unpolarized TMD fits.

Data from the HERMES experiment [213, 215, 263] have shown that production rates of identified hadrons in semi-inclusive deep inelastic e–A scattering differ from those in ep

scattering. These differences cannot be explained by nuclear PDFs, as nuclear effects of strong interactions in the initial state should cancel in this observable. Only the inclusion of nuclear effects in the hadronization process allows theory to reproduce all of the dependencies (z, x, and Q^2) of R_{eA} seen in SIDIS, as shown in Fig. 92.

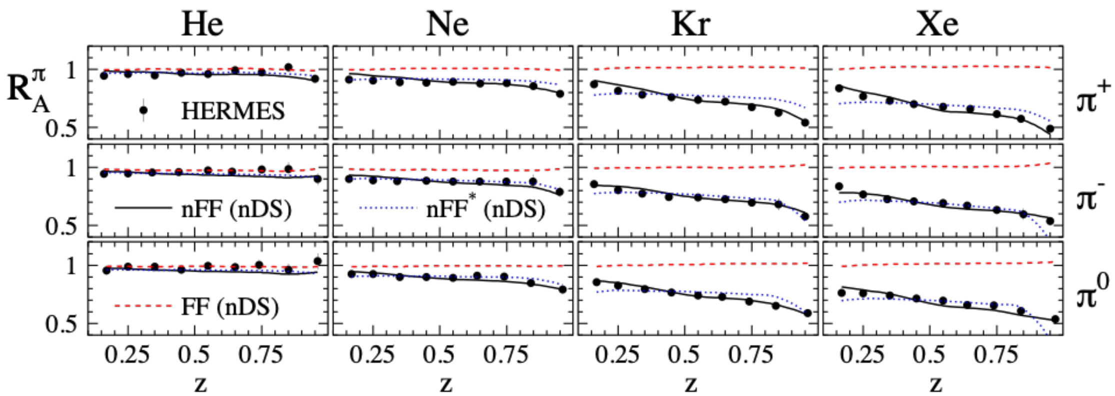

Figure 92: R_{eA} in SIDIS for different nuclei in bins of z as measured by HERMES [213, 215, 263]. The solid lines correspond to the results using effective nuclear FF [220] and the nDS medium modified parton densities [264]. The red dashed lines are estimates assuming the nDS medium modified PDFs but standard DSS vacuum FFs [265, 266] and indicate that nPDFs are insufficient to explain the data

It is critical to see if these hadronization effects in cold nuclear matter persist at the higher $\sqrt{s}$ and Q^2 accessed at RHIC and EIC – both to probe the underlying mechanism, which is not understood currently, and to explore its possible universality. The combination of p+p jet data from RHIC and future SIDIS data from EIC will also provide a much clearer picture of modified gluon hadronization than will be possible with EIC data alone. Using the Run-15 200 GeV p+Au data, STAR will be able to make a first opportunistic measurement of these hadron-jet fragmentation functions in nuclei, but the precision will be limited. Additional p+p and p+Au data will be needed in Run-24 in order to provide a sensitive test for universality, as shown in Fig. 93.

QGP Droplet Substructure

Toroidal Vorticity: In addition to cold QCD effects, a high-statistics measurement of p+Au collisions will be highly valuable to explore novel fluid configurations that have recently been predicted [267]. In particular, the data is needed to discover vortex rings or tubes at midrapidity, included by shear in the asymmetric initial state.

It has been suggested [268] that p+A collisions at RHIC form the "smallest QGP droplets." This claim is often based on anisotropic yields, which resemble those from A+A collisions that are attributed to hydrodynamic collective flow. Indeed, with well-chosen initial conditions and tuned parameters, three-dimensional viscous hydro calculations can reproduce the measured anisotropies from small, asymmetric collisions [269] at RHIC. However, a claim of

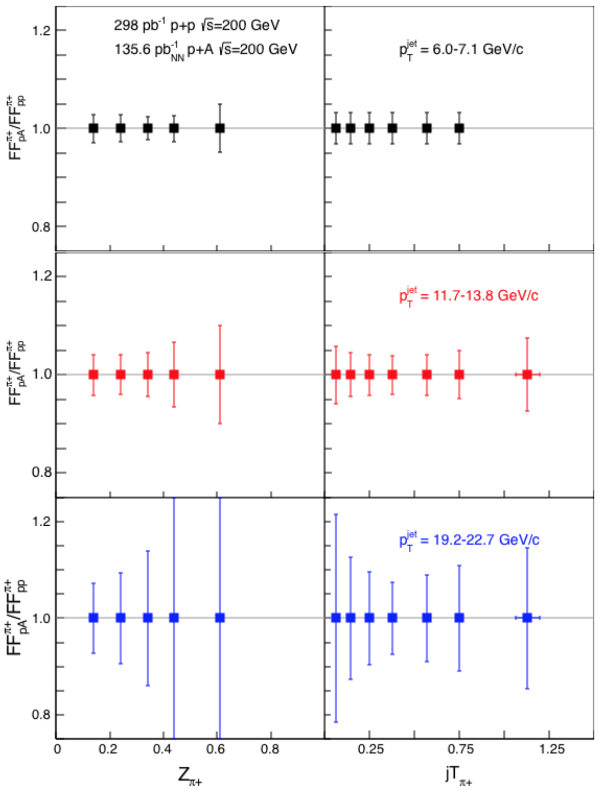

Figure 93: Anticipated precision for measurements of π^+ fragmentation functions in p+A,p+p at $|\eta| < 0.4$ vs. z and j_T in Run-24 for three representative jet p_T bins. Uncertainties for π^- will be similar to those shown here for π^+, while those for kaons and (anti)protons will be a factor of ~ 3 larger. Note that, to be species independent, the nucleon-nucleon equivalent luminosity is specified for p+Au.

QGP formation in such small systems would be much more compelling if it were based on more than one observable, especially since other, non-hydrodynamic mechanisms contribute to v_n in these systems, e.g. [22].

As Helmholtz observed more than 150 years ago [270], vortex rings are ubiquitous in hydrodynamic systems subject to initial conditions characterized by a "push down the middle," such as a smoker blowing a ring. Clear observation of this novel phenomenon would constitute important evidence that the smallest systems at RHIC truly do form a fluid system.

This signature probes aspects of particular and fundamental importance to the RHIC program, as well. The vortex ring structure is sensitive to the degree and timescale of equilibration in these small systems, as well as the extreme shear fields in the initial state [271]. Fluctuations in the vortical fields probe hydrodynamic structures at the smallest possible scales, as they arise directly from rotational derivatives in the "surface" of the flux tube.

The experimental signature of toroidal vortex structure is the so-called "ring parameter" [267]:

$$\overline{\mathcal{R}}^z_\Lambda \equiv \left\langle \frac{\vec{S}'_\Lambda \cdot (\hat{z} \times \vec{p}'_\Lambda)}{|\hat{z} \times \vec{p}'_\Lambda|} \right\rangle, \tag{7}$$

where $+\hat{z}$ is the direction of the proton beam, and the average is taken over all particles and events. This is the average polarization relative to the hyperon production plane. Rings will

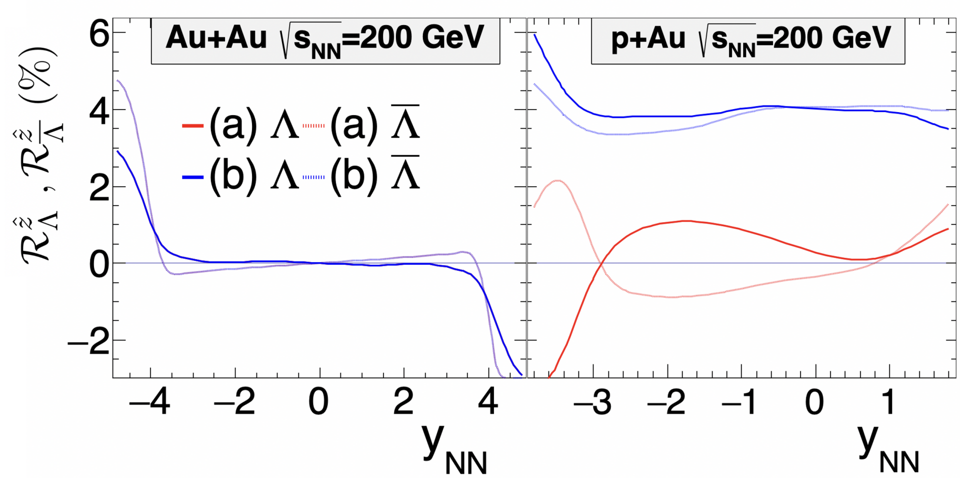

Figure 94: The "ring parameter" $\overline{\mathcal{R}}^z_\Lambda$ for $b = 0$ Au+Au and p+Au collisions at top RHIC energy. Blue (red) curves correspond to a scenario in which a toroidal vortex structure is (is not) generated by shear forces in the initial state. Solid (dashed) curves correspond to Λ ($\overline{\Lambda}$; note that baryon current is locally conserved in these collisions, so small differences between Λ and $\overline{\Lambda}$ are expected at finite baryon density. From [267].

be most clear for central collisions, but the detailed centrality dependence of the effect is currently under investigation [271]. We focus on 0-10% centrality.

Figure 94 shows $\overline{\mathcal{R}}^z_\Lambda$ calculated [267] for completely central Au+Au and p+Au collisions at $\sqrt{s_{NN}} = 200$ GeV. Calculations were done with MUSIC [272], a three-dimensional relativistic viscous hydrodynamics simulation that locally conserves baryon number, and calculation of the thermal vorticity along the freezeout hypersurface.

Initial condition (a) corresponds to the usual Bjorken "boost-invariant" flow profile used in most A+A simulations, whereas condition (b) features strong shear fields generated in the initial condition, leading to observable vortex toroids. Both initial conditions generate identical $dN/d\eta$ distributions, but the latter is argued [267] to be more natural.

The statistical requirement to discover these toroidal vortex structures may be estimated by STAR's previous hyperon polarization measurements. The uncertainty on global polarization measurements $\delta\overline{P}_\Lambda \propto N_\Lambda^{-1/2} \cdot R_{\rm EP}^{-1}$, where N_Λ is the total number of hyperons in the analysis, and $R_{\rm EP}$ is the event plane resolution [7]. Because there is no event plane involved in the production plane polarization, on the other hand, the uncertainty on the ring observable goes as $\delta\overline{\mathcal{R}}^z_\Lambda \propto N_\Lambda^{-1/2}$. For the same-magnitude signal, then, $\overline{\mathcal{R}}^z_\Lambda$ enjoys an effective $R_{\rm EP}^{-2}$ "statistical advantage" over $\overline{P}_\Lambda$. Since STAR measured [102] $\overline{P}_\Lambda \approx 1\%$ at $\sqrt{s_{NN}} = 11$ GeV with 3.5σ significance, with the same number of hyperons in the analysis, we should be able to measure $\overline{\mathcal{R}}^z_\Lambda \sim 1\%$ with 7σ significance. The 11-GeV analysis involved 6M Λs, and we estimate 0.02 Λs per central $(0-10\%)$ p+Au collision at $\sqrt{s_{NN}} = 200$ GeV. Therefore, the 7σ measurement will require $6M/0.02 = 300M$ central p+Au collisions.

Also crucial to this measurement is that data must be collected with both polarities of STAR's magnetic field. This is because of large and highly nontrivial decay-topology-

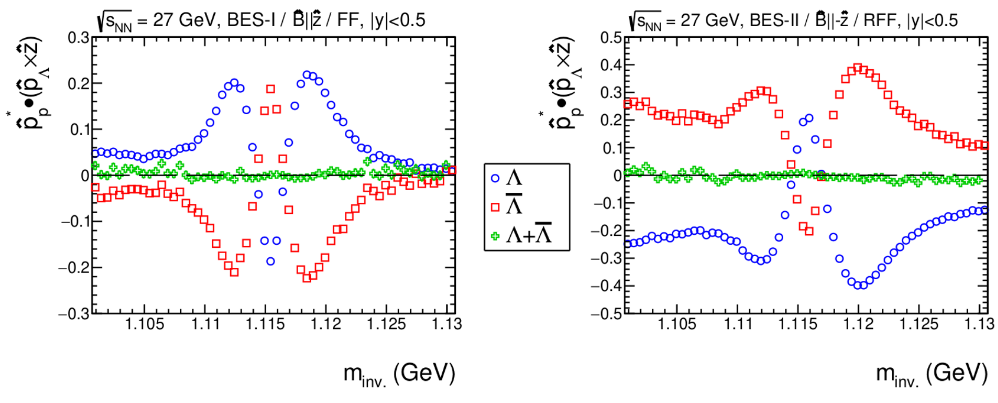

Figure 95: Production-plane polarization (modulo an overall scaling by $\frac{8\pi}{\alpha_\Lambda}$) for Λ (blue) and $\overline{\Lambda}$ (red) candidates, as a function of invariant mass. The data comes from STAR measurements of Au+Au collisions at $\sqrt{s_{NN}}$ in the BES-I (left) and BES-II (right) campaigns. STAR's solenoidal magnetic field was directed to the West and East, respectively, for these two datasets. For the BES-I data, hyperon candidates were identified with "standard" topological cuts, whereas the candidates shown in BES-II were identified using the new KFParticle package.

dependent detector effects, which will give a "false" production plane polarization signal. The magnitude of the artifact is an order of magnitude larger than the physical signal of interest, and it is highly sensitive to momentum, PID, and topological cuts. We could not feel confident applying such large and complex "correction factors" based solely on detector simulations, if we claim a completely novel signature with far-reaching physical implications. Fortunately, the sign of this artifact flips with the magnetic field polarity.

Figure 95 illustrates these points. Au+Au collisions at $\sqrt{s_{NN}} = 27$ GeV were recorded by STAR using opposite polarities of the magnetic field. For Λs, the quantity $\hat{p}_{\rm p} \cdot (\hat{p}_\Lambda \times \hat{z})$, where $\vec{p}_{\rm p}$ is the daughter proton momentum, is proportional to $\overline{\mathcal{R}}^z_\Lambda$. For $\overline{\Lambda}$s, the quantity $\hat{p}_{\overline{\rm p}} \cdot (\hat{p}_{\overline{\Lambda}} \times \hat{z})$, where $\vec{p}_{\rm p}$ is the daughter proton momentum, is proportional to $-\overline{\mathcal{R}}^z_{\overline{\Lambda}}$.

A rapidity cut symmetric about midrapidity ($|y| < 0.5$ was used; for a symmetric system, the physical production plane polarization vanishes by symmetry– any nonvanishing value results purely from topologically-sensitive efficiency effects.

Consider first the Λ curve from BES-I, the blue points in the left panel. Clearly, the effect has a nontrivial dependence on invariant mass; note even the asymmetry about $m_{\rm inv} = m_\Lambda$. Equally clearly, it is large, corresponding to values $\overline{\mathcal{R}}^z_\Lambda = \frac{8}{\pi\alpha_\Lambda}\hat{p}_{\rm p} \cdot (\hat{p}_\Lambda \times \hat{z}) \approx 50\%$, an order of magnitude larger than the predicted value of physical effect of interest.

In terms of topologically-sensitive efficiency effects, substituting $\Lambda \to \overline{\Lambda}$ is equivalent to flipping the sign of the magnetic field. The red datapoints in the left panel are a perfect mirror image to the blue points in that panel, as indicated by the vanishing green points, which are the sum. Further note that naive interpretation of the data in the left panel would suggest that the vortical ring values for the hyperons and antihyperons ($\overline{\mathcal{R}}^z_\Lambda$ and $\overline{\mathcal{R}}^z_{\overline{\Lambda}}$) would be identical in magnitude and sign.

The right panel shows the same colliding system, but measured during the BES-II campaign with the opposite orientation of STAR's magnetic field. As expected from the above discussion, $\overline{\mathcal{R}}^z_{\Lambda} = -\overline{\mathcal{R}}^z_{\overline{\Lambda}}$. The shape and magnitude of the artifact is different from the BES-I case, however, because a different method has been used to identify hyperon candidates. This illustrates the cut-dependence of the artifact.

In short, for reliable extraction of the ring vorticity measure, STAR must measure p+Au collisions with both field orientations, in order to cancel the complex efficiency-driven artifacts. Finally, we point out that this sort of cancellation is not unique to this observable. Indeed, there is an analogous effect for the global polarization, which precludes extracting the *first*-order azimuthal dependence of $\overline{P}_{\Lambda}$; there, the artifact is of order 100%, compared to the physical and measured value of $\sim 2\%$ [273].

For symmetric collisions (e.g. Au+Au), the quantity $\overline{\mathcal{R}}^z_{\Lambda}$ must be antisymmetric about midrapidity. However, at very forward/backward rapidities, circular vorticity has been reported in hydrodynamic [274–278] and transport [279–285]. This effect, also visible in the left panel in figure 94, arises from strong temperature gradients and edge effects in three-dimensional space. It is of very different origin than the ring voriticity of interest here.

Finally, production plane polarization at large x_{F} has been observed (primarily) in p+p and (in some) p+A collisions [286–291] at energies up to $\sqrt{s_{NN}} = 41$ GeV. This effect, which is believed to be completely hadronic in origin but remains incompletely understood, is distinguishable from the hydrodynamically-driven ring vorticity discussed here by its rapidity dependence, which is strongly forward-focused, as well as the fact that $\overline{\Lambda}$s do not display production plane polarization at all. Thus, in addition to double-checking topologically-dependent efficiency artifacts (discussed above), it is important that STAR will measure the effect both for hyperons and antihyperons to distinguish hydrodynamic from hadronic phenomena.

4 Computing Resources

In 2019, STAR submitted the computing resource request for years 2021–2025. Recently, there was a proposal to upgrade the STAR DAQ system that will allow STAR to take data at approximately double the bandwidth in the 2023-2025 runs as compared to the expected 2022 rates for which the previous resource request was prepared. The increased DAQ bandwidth will improve the statistical precision for various observables aimed towards the detail investigation of microscopic structure of QGP. These include the net-proton high order cumulant ratios C_6/C_2, thermal dilepton spectra and low p_T J/ψ v_1, v_2 etc which are unique at STAR compared to sPHENIX at the top RHIC energy. Furthermore, STAR will be able to accommodate the triggers reading out forward and mid-rapidity tracking/calorimeter detectors together which offers a unique chance to characterize the QGP over a wide pseudorapidity coverage.

An updated request on the additional resources due to this upgrade was submitted to SDCC in November 2021. The request was discussed with NPP management at the mini-retreat on "Nuclear Physics Computing from RHIC to EIC" in January 2022. We would like to emphasize that the requested resources are essential for completing the scientific mission of the STAR experiment, by producing and finishing the analyses from the requested datasets taken in 2023–2025 in a timely fashion.

Table 6 and Table 7 list the updated requests on the network capacity needs and the storage/CPU resource needs, respectively.

Network and HPSS capability	2022 capacity	2023-2025 needs
DAQ to SDCC network upload	40 Gbps	40 Gbps
SDCC to DAQ local network	28×1 Gbps	48×1 Gbps
Tape Drive Capacity	20 Gbps	40 Gbps

Table 6: Updated request on network capacity needs

Year	Species	Additional HPSS Space Needed (RAW+DST) (PB)	Total Storage Space Needed (Xrootd) (PB)	Total Storage Space Needed (NFS/Central) (PB)	Required CPU Total [kHS06]
2021	BES-II	0.43	3.06	3.504	203
2022	500 GeV p+p	11.07	3.63	3.854	295
2023	200 GeV Au+Au	55.4	7.0	4.75	626
2024	200 GeV p+p/p+Au	35.5	9.1	4.75	626
2025	200 GeV Au+Au	73.8	13.5	4.75	626

Table 7: Updated request on storage and CPU resources

5 Future Opportunities

Experience from the BES-II has shown us that the excellent performance from RHIC may allow us to take short opportunistic datasets that enable unique physics programs with minimal extra running time. Below we outline two such opportunistic programs, both are of great interest to STAR and the larger nuclear physics community.

5.1 Imaging shape and radial profile of atomic nuclei via collective flow measurements

The success of the hydrodynamic framework of heavy-ion collisions permits us today to perform quantitative extractions of the transport properties of the QGP via the state-of-the-art multi-system Bayesian analysis approaches. [92–94] Such extractions rely largely on a correct description of the initial condition of the QGP prior to the hydrodynamic expansion. Recent experimental data in ^{96}Ru+^{96}Ru and ^{96}Zr+^{96}Zr isobar collisions [292], ^{238}U+^{238}U [29] and ^{129}Xe+^{129}Xe [293–297] collisions, as well as dedicated theoretical studies [30, 33, 36, 37, 298–303], have indicated the importance of nuclear deformation and the nuclear radial profile, i.e. radial distribution of proton and neutrons in the nucleus, on the measured anisotropic flow. However, the impact of these collective nuclear structure effects are not yet considered in these Bayesian approaches. For a reliable extraction of transport properties and initial-state from the collective flow data, we need to ensure that the uncertainty associated with the structure of the colliding ions is under control in the hydrodynamic models, especially since all species at RHIC and the LHC are expected to present some deformations and some uncertainties in the nuclear skin and radius (as indicated in Table 8 for nuclear deformation). These uncertainties can be gauged precisely using pairs of isobar collisions, as demonstrated by the ^{96}Ru+^{96}Ru and ^{96}Zr+^{96}Zr collisions at RHIC, where the ratio of flow observables can be determined with $< 0.4\%$ precision [292]. Note that these ratios are made at the same $N_{\rm ch}$ in each isobar, and therefore are essentially insensitive to final state effects and are precision probes of the initial conditions as we shall discuss below.

	β_2	β_3	β_4
^{238}U	0.286 [304]	0.078 [305]	0.09 [306]
^{208}Pb	0.05 [304]	0.04 [307]	?
^{197}Au	-(0.13-0.16) [306, 308]	?	-0.03 [306]
^{129}Xe	0.16 [306]	?	?
^{96}Ru	0.05-0.16 [304, 306]	?	?
^{96}Zr	0.08 [304]	?	0.06 [306]

Table 8: Some estimates of the deformation values β_2, β_3, and β_4 for the large nuclei collided at RHIC and the LHC with references given, mostly on global analysis of $B(En)$ transition data over a broad range of nuclei. There are also uncertainties in their values for surface diffuseness a_0 and half radius R_0 which are not listed.

It is straightforward to see why the geometry of heavy-ion collisions is sensitive to nuclear deformation and radial profile. We refer to the cartoon in Fig. 96. A nucleus can be modeled through a nucleon density of Woods-Saxon form:

$$\rho(r,\theta,\phi) = \frac{\rho_0}{1+e^{[r-R(\theta,\phi)]/a_0}},\ R(\theta,\phi) = R_0\left(1+\beta_2[\cos\gamma Y_{2,0}+\sin\gamma Y_{2,2}]+\beta_3 Y_{3,0}+\beta_4 Y_{4,0}\right), \tag{8}$$

where the nuclear surface $R(\theta,\phi)$ includes only the most relevant deformation components from nuclear structure physics, quadrupole $n=2$, octupole $n=3$ and hexadecapole $n=4$. The angle $0 \leq \gamma \leq \pi/3$ controls the triaxiality of the quadruple deformation or the three radii R_a, R_b, R_c of the ellipsoid, with $\gamma=0$ corresponds to prolate ($R_a = R_b < R_c$), and $\gamma = \pi/3$ corresponds to oblate ($R_a < R_b = R_c$). The nuclear radial profile is controlled by the surface diffuseness or nuclear skin a_0 and half radius R_0. In heavy-ion collisions, the shape of the deformed ions strongly affects the geometry of overlap. The entire mass distribution is probed simultaneously, and one can use multi-particle correlation observables to infer information of all these parameters. This way of probing nuclear densities is different from the standard techniques of low-energy physics, where β_n, a_0 and R_0 are inferred from the orientation-averaged form factor data from e+A and hadron+A scatterings and multipole transition probabilities, $B(En)$, between low-lying rotational states. Furthermore, the time scales involved in high-energy heavy-ion collisions are much shorter ($< 10^{-24}$s), than the typical timescale of the EM transition involved in the rotational bands (typically on the order of 10^{-20} s [309]). As we shall also argue below, a remarkable question is whether the manifestation of nuclear deformation and nuclear skin– collective features of the nuclear many-body system – is the same across energy scales.

The presence of multipoles, β_n, in the colliding ions modifies non-trivially the corresponding spatial anisotropy, ε_n, of the produced QGP, and consequently the final-state flow harmonic, v_n. Similarly, different values of a_0 and R_0 modify the effective size of the overlap region and therefore the "radial" flow or the event-by-event mean transverse momentum $[p_{\mathrm{T}}]$. [37] Recent studies show that nuclear skin a_0 also impacts the v_2, and simple event activity observables such as multiplicity distributions $p(N_{\mathrm{ch}})$ and participants $p(N_{\mathrm{part}})$. [36,303] Predictions for many other observables and their sensitivities to nuclear deformation and nuclear skin have been made, such as p_{T} fluctuations [32], spectator neutron production [310], mixed-flow harmonics [311], and v_n–p_{T} correlations [297, 300, 312].

Earlier studies of nuclear deformation are mainly focused on the elliptic flow, v_2 in central collisions. They have established a simple relation between quadrupole deformation and ϵ_2 and v_2 [312, 313],

$$\left\langle \epsilon_2^2 \right\rangle = a' + b'\beta_2^2, \qquad \left\langle v_2^2 \right\rangle = a + b\beta_2^2, \tag{9}$$

where the a' and a are mean-squared eccentricity and elliptic flow without deformation, while the b' and b describe the parametric dependence of the deformation-enhanced component of eccentricity and elliptic flow, respectively. The strict quadratic dependence of Eq. 9 leads to a very robust equation relating the β_2 between any pair of collision systems. Applied to RHIC data, it allows one to derive a constraint on the $\beta_{2,\mathrm{U}}$ and $\beta_{2,\mathrm{Au}}$, as shown in the right panel of Fig. 97. This highlights how, at present, the low-energy nuclear structure model calculation

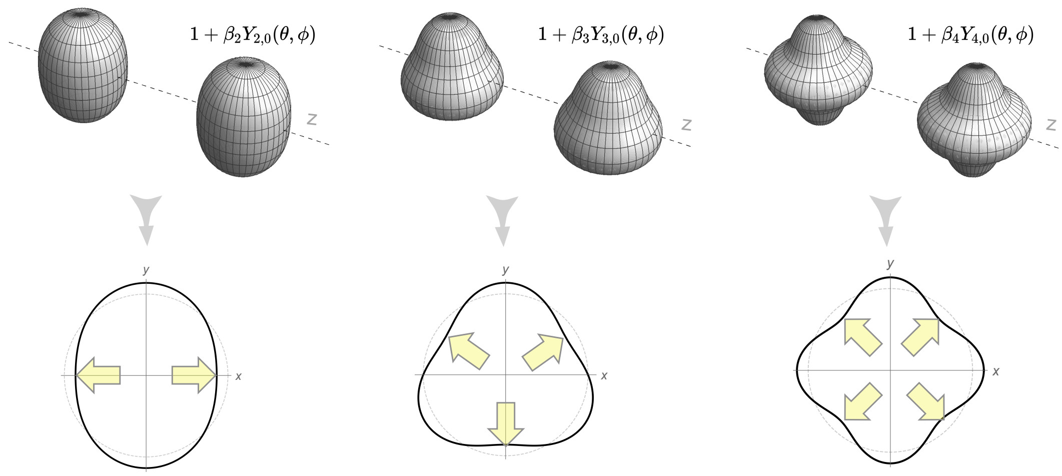

Figure 96: A cartoon of a collision of nuclei with quadruple (left), octupole (middle) and hexadecapole (right) deformations including only the $Y_{n,0}$ mode and with $\beta_n = 0.25$ (we ignore the large Lorentz contraction in the z-direction). The bottom row shows how the initial condition of the medium formed after the collision looks in the transverse plane. The yellow arrows indicate the direction of maximum pressure gradients along which the medium expands with the largest velocity, leading to final state harmonic flow v_n with n-fold symmetry.

and the flow data from high-energy nuclear collisions are fairly inconsistent. Relations similar to Eq. 9 can also be written down for v_3 and v_4, which can be used to potentially constrain octupole and hexadecapole deformations [31].

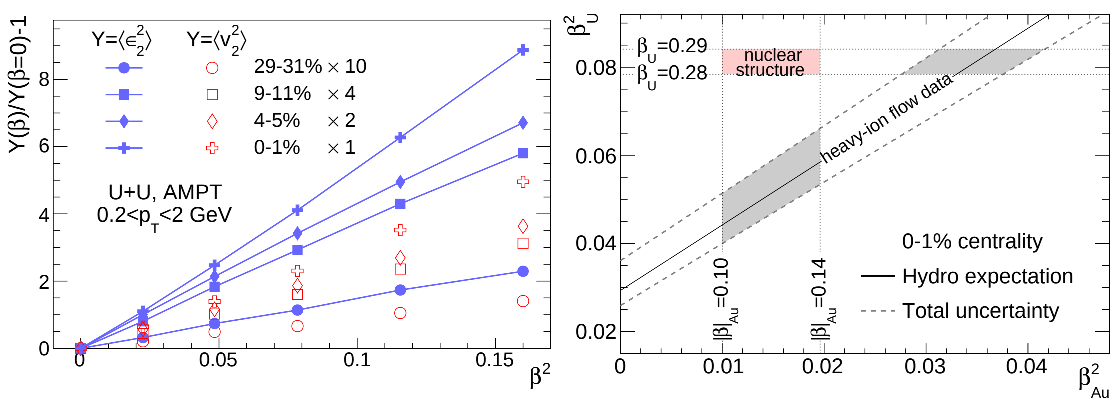

Figure 97: Left panel: $\left\langle v_2^2(\beta)\right\rangle / \left\langle v_2^2(0)\right\rangle - 1 = b/a\ \beta_2^2$ (empty symbols) and $\left\langle \epsilon_2^2(\beta_2)\right\rangle / \left\langle \epsilon_2^2(0)\right\rangle - 1 = b'/a'\ \beta_2^2$ (full symbols) as a function of β_2^2 in U+U collisions from the AMPT model. Different symbols correspond to different centrality classes. Right panel: $\beta_{2,\mathrm{U}}^2$ as a function of $\beta_{2,\mathrm{Au}}^2$. The region between the dashed lines is consistent with the hydrodynamic expectation based on Eq. (9) and STAR v_2 data in 0–1% centrality. Figures taken from Ref. [302].

The most precise tool for structure imaging, however, is provided by collision of isobaric systems, as demonstrated by recent measurements in ^{96}Ru+^{96}Ru and ^{96}Zr+^{96}Zr collisions. [292] The crucial point is that since isobar nuclei have the same mass number, deviations from unity of the ratio of any observable must originate from differences in their structures, which impact the initial state of QGP and its final state observables. Ratios of many observables between ^{96}Ru+^{96}Ru and ^{96}Zr+^{96}Zr, both published and new preliminary results shown in QM2022 [292, 314], show deviations from unity in an observable- and centrality-dependent manner, which must originate from differences in their structures. Model studies show that the isobar ratio for a given observable $\mathcal{O}$ probes only the nuclear structure parameter differences, i.e. $\Delta\beta_n^2 = \beta_{n\mathrm{Ru}}^2 - \beta_{n\mathrm{Zr}}^2$,$\Delta a_0 = a_{0\mathrm{Ru}} - a_{0\mathrm{Zr}}$ and $\Delta R_0 = R_{0\mathrm{Ru}} - R_{0\mathrm{Zr}}$ [34]:

$$R_{\mathcal{O}} \equiv \frac{\mathcal{O}_{\mathrm{Ru}}}{\mathcal{O}_{\mathrm{Zr}}} \approx 1 + c_1\Delta\beta_2^2 + c_2\Delta\beta_3^2 + c_3\Delta a_0 + c_4\Delta R_0 \ , \tag{10}$$

where the coefficients c_1–c_4 describes how the heavy-ion initial state is controlled by the nuclear structure and are weak functions of system size. Figure 98 highlights some recent measurements: ratios of multiplicity distribution $p(N_{\mathrm{ch}})$, v_2, v_3, variance of p_{T} fluctuations $\langle\delta p_T^2\rangle/\langle p_T\rangle^2$, and $\langle p_{\mathrm{T}}\rangle$ between the isobar systems. All of them show non-monotonic centrality dependence similar in shape to the theoretical predictions that include effects of nuclear skin as well as nuclear deformations. [33, 34, 311, 315] In particular, the data imply a larger quadrupole deformation β_2 in ^{96}Ru, a larger octupole deformation β_3 in ^{96}Zr, and a larger a_0 value consistent with a larger neutron skin in ^{96}Zr, Δr_{np}, defined as the rms radius difference between the neutron and proton distributions: $\langle r_n^2\rangle^{1/2} \equiv \langle r_n^2\rangle^{1/2} - \langle r_p^2\rangle^{1/2}$. These detailed measurements over-constrain the WS parameters and can be used to test the initial conditions used in hydrodynamic models. Note that the neutron skin thickness Δr_{np} is directly related to the slope parameter L for the density dependence of the symmetry energy, which is particularly important in astrophysics concerning neutron stars. [316] The preliminary extraction of L from the measured $\langle p_{\mathrm{T}}\rangle$ ratio in the isobar data seems to prefers a value of 47–70 MeV as shown in Fig. 98, quite consistent with low-energy nuclear reaction measurements [317] but systematically lower than the PREXII results [318].

An additional observable showing large sensitivity to the nuclear quadrupole deformation is the Pearson correlation coefficient, $\rho(v_2^2, [p_{\mathrm{T}}])$, between v_2 and the mean transverse momentum, $[p_{\mathrm{T}}]$. This observable probes in particular the full quadrupole structure of the colliding ions, i.e., both β_2 and its triaxiality γ in Eq. 8 [32, 312],

$$\rho(v_2^2, [p_{\mathrm{T}}]) \approx a - b\cos(3\gamma)\beta^3, \ a, b > 0. \tag{11}$$

Therefore prolate deformation in the colliding nuclei is expected to reduce $\rho(v_2^2, [p_{\mathrm{T}}])$, while oblate deformation is expected to increase it. This observable has been measured by the STAR collaboration in U+U and Au+Au collisions, which established unambiguously the large and dominating influence of the nuclear quadruple deformation, see Fig. 99(a). The large prolate deformation of ^{238}U yields a strong negative contribution to the $v_2 - [p_{\mathrm{T}}]$ correlation, enough to make it change sign. A large impact of $\beta_{2\mathrm{U}}$ has further been observed in the fluctuations of $[p_{\mathrm{T}}]$. The same measurement is also performed by the ATLAS and ALICE collaborations in ^{129}Xe+^{129}Xe and ^{208}Pb+^{208}Pb collisions [296, 319], see Fig. 99(b). A comparison with a Trento model calculation based on input from nuclear structure theory [297]

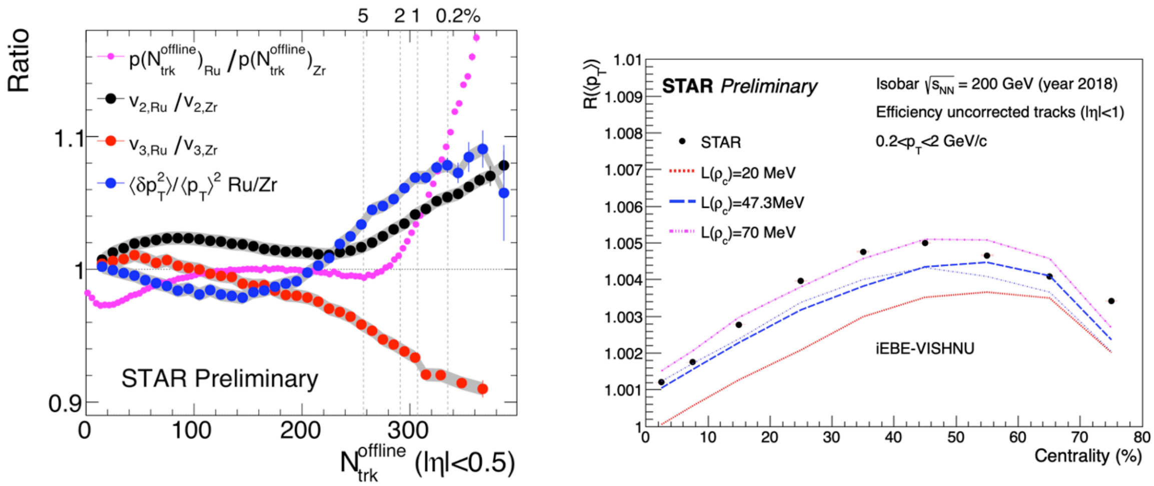

Figure 98: Left panel: STAR preliminary results of isobar ratio of $p(N_{\mathrm{ch}})$, v_2, v_3, and variances $\langle \delta p_{\mathrm{T}}^2 \rangle / \langle p_T \rangle^2$ as a function of N_{ch}. Right panel: The centrality dependence of the Ru+Ru/Zr+Zr ratio of $\langle p_T \rangle$, compared with hydrodynamic model calculations [37].

provide strong evidence that ^{129}Xe is a highly-deformed triaxial ellipsoid with an overall quadrupole deformation of $\beta_{2\mathrm{Xe}} \sim 0.2$ and triaxiality of $\gamma_{\mathrm{Xe}} \sim \pi/6$. Hydrodynamic models based on state-of-the-art initial conditions with deformation values from Table 8 struggle to describe quantitatively all these experimental measurements. [25, 320, 321] The reason could be that the radial flow response of the system to fluctuations induced by the deformation of the colliding ions is not fully captured by the existing models. Collisions of well-deformed ions, and their comparisons with the collisions of more spherical species, provide us with a new way to test the hydrodynamic description.

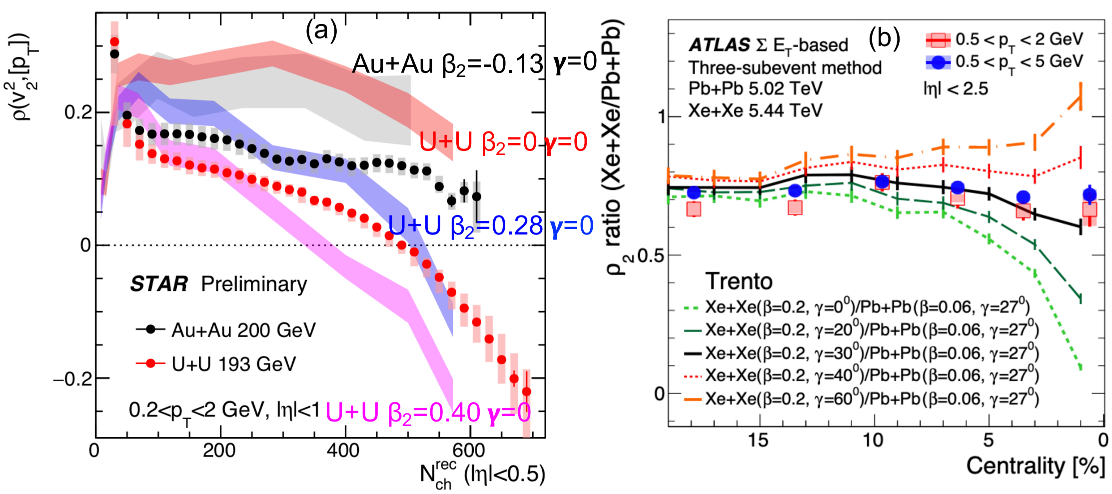

Figure 99: Left panel: STAR preliminary results of Pearson correlation coefficient $\rho(v_2^2, [p_{\mathrm{T}}])$ in U+U and Au+Au collisions, showing a sign-change due to large prolate deformation of ^{238}U. Right panel: ATLAS results of the ratio of $\rho(v_2^2, [p_{\mathrm{T}}])$ between Xe+Xe and Pb+Pb collisions, showing a strong preference for ^{129}Xe being a highly-deformed triaxial ellipsoid.

To summarize, flow measurements in heavy-ion collisions have large potential to provide detailed information on the shape and radial profile of colliding nuclei. By connecting the highest and lowest energy scales, they allow us to answer important questions in heavy ion physics and have broader impact to the larger nuclear physics community. Here are a few of them:

- How distributions of protons and neutrons in atomic nuclei give rise to the complex initial condition of heavy ion collisions? Can we use nuclear shapes and nuclear radial profiles as additional handles to understand particle production and generation of eccentricities, e.g. by comparing flow observables at the same final state multiplicity in isobar systems with different nuclear structures?

- Can we gauge uncertainties in the extraction of the transport properties of the QGP due to uncertainties in the initial condition arising from nuclear structure?

- Are the nuclear shape and radial profile inferred from hydrodynamic response the same as those measured in nuclear structure experiments? Can isobar collisions serve as a precision tool for the extraction of the neutron skin, competitive to the existing measurements? and what are the energy and longitudinal dependence of nuclear structures?

To address these and other related questions, several workshops exploring the intersection between nuclear structure and heavy-ion collisions have been planned, including a month-long INT program in early 2023. Rapid progress is expected in the next two years.

Thus we propose to collide more species to extract their value of deformation parameters β_2, γ, β_3 and β_4, and a_0 and associated neutron skin from flow measurements, with a twofold purpose: 1) provide a new handle on the initial state and hydrodynamic response of the QGP, 2) perform studies of nuclear structure physics at high energy to complement the information coming from lower energies, and so assess the consistency of nuclear phenomena across energy scales. The ground state of almost all stable nuclei is deformed (see for example the interactive chart in Ref. [322]). RHIC, with its flexibility to collide almost any nuclei from p+p to U+U is a unique facility to perform such studies in the foreseeable future. The best example to showcase this capability is the run of isobars performed in 2018, where the two systems, Zr+Zr and Ru+Ru, were alternated on a fill-by-fill basis, leading to extremely small systematic uncertainties on the final observables. [292] This allows one to detect minute differences in the physics observables such as multiplicity, $[p_{\mathrm{T}}]$ and v_n in the comparison of the two systems. Consequently, even small differences in the values of β_n and a_0 of the colliding systems can be precisely mapped. [30] For each species, we need roughly 100 million minimum bias and 50 million 0–5% central events. Assuming the standard 50% RHIC+STAR up time and 1.5 KHz DAQ rate, same as Au+Au running, we will be able to collect 130M minbias events and 64M central events in three days of physics running. This is slightly less than the existing U+U dataset taken in 2011, but with comparable statistical precision due to the increased acceptance from the iTPC. Adding two days of setup time, this leads to about five days of total time for each species.

The system scan we propose can be divided into two steps. Given the tight schedule for the next few years, instead of making an explicit proposal on how much running time are needed to fully explore these topics, we discuss what can be achieved if we are given certain number of days.

- **≈10 days:** In the first step, we would like to scan two nuclei in the vicinity of the most studied species at RHIC, ^{197}Au, to improve the modeling of Au+Au collisions, information which is crucial for the future precision interpretation of high-statistics data expected from Run-23+25. To achieve this, ideal candidates are ^{208}Pb and ^{196}Hg (^{198}Hg could be a substitute). Having ^{208}Pb at $\sqrt{s_{\rm NN}} = 200$ GeV provides a crucial bridge with the ^{208}Pb at LHC energies: comparison between ^{208}Pb measurements at RHIC and the LHC will constrain any possible energy dependence of the initial state effects and pre-equilibrium dynamics. Additionally, ^{208}Pb is nearly spherical, so that Pb+Pb collisions at the same energy will allow us to better understand the impact of the moderate deformation of ^{197}Au in Au+Au collisions, as well as the impact of the difference of a_0 parameter and neutron skin between ^{197}Au and ^{208}Pb. The Hg+Hg collisions would then permit us to understand more deeply the nature of the deformation of ^{197}Au, which, being an odd-mass nucleus, hasn't been determined in low-energy experiments. ^{196}Hg is an oblate nucleus with $|\beta_2| \approx 0.1$, and the observable $\rho(v_2^2, [p_{\rm T}])$ can be used quantify whether ^{197}Au is more or less oblate than ^{196}Hg, an information which will gauge more tightly the initial geometry of Au+Au collisions. Adding Hg+Hg collisions will also provide an independent cross-check on the initial state, for example one can setup three relations like Eq. 9 from Pb+Pb, Hg+Hg and Au+Au to triangulate the consistency of the three deformation values. [31]

- **Additional time:** In the second step, our proposal is to use hydrodynamics and flow measurements to perform precision cross-checks of low-energy nuclear physics by constraining the evolution of the quadrupole deformation and neutron skin along the chain of stable samarium isotopes. It would be useful in particular to collide three isotopes: ^{144}Sm ($\beta_2 = 0.08$, as spherical as ^{208}Pb), ^{148}Sm ($\beta_2 = 0.14$, triaxial much as ^{129}Xe and ^{197}Au), and ^{154}Sm ($\beta_2 = 0.34$ well-deformed like ^{238}U). The evolution of the quadrupole deformation can be mapped precisely at RHIC, thus offering a valuable test of nuclear structure knowledge. If data on ^{154}Sm+^{154}Sm collisions is available, it would be desirable to also have ^{154}Gd+^{154}Gd ($\beta_2 = 0.31$) collisions. The comparison between the two well-deformed isobaric systems could potentially yield the most precise information about the relative deformation and relative neutron skin between two ground state nuclei. Theoretical studies further suggest that ground states in the region $Z \sim 56/N \sim 88$ [323] (including the samarium isotopes) may display enhanced octupole correlations, i.e., β_3 values. These would manifest in high-energy collisions as enhanced v_3, as well as in the correlators $\rho(v_3^2, [p_{\rm T}])$. Such enhancements are already observed in ^{96}Zr+^{96}Zr relative to ^{96}Ru+^{96}Ru collisions (Fig. 98 and Ref. [314]), however nuclear structure modeling for these medium mass nuclei are quite challenging and it is unclear yet whether the observed enhancements are due to octupole correlation or static octupole deformation. The heavier species mentioned above would be a more sensitive choice for identifying static octupole deformation. The study of octupole deformation is also fundamentally interesting because nuclei with large β_3 provides a stringent test of the electric-dipole moment (EDM) [324]. The exact choice of species is still under refinement, presently we have a preference for ^{154}Sm and ^{148}Sm, followed by ^{154}Gd and ^{144}Sm.

Finally, one should note that the STAR DAQ rate for these moderate-sized systems could be significantly larger, possibly reaching 2KHz. This enhanced DAQ rate will compensate partially the smaller number of charged particles expected in these systems compared to larger systems.

5.2 Fixed-target Measurements Using Light Beam and Target Combinations

Although the proposed fixed-target Au+Au energy scan has been completed, if the opportunity exists for further measurements, light beam and target combinations could help to clarify the role and mechanisms of nucleon stopping. Indeed, STAR was recommended to consider installing a beryllium target, that being the lowest Z feasible solid target which could work with the target apparatus. This was not done previously because changing the target requires opening the STAR beampipe and removing the existing target, and that could not be done until the Au+Au energy scan had been completed. Both the collider and STAR have demonstrated that fixed-target runs can be quickly tuned, as the demands on collider operations are modest, and efficiently run, as the collider can control and deliver sufficient intensity to fill the STAR DAQ bandwidth and the experiment can cleanly trigger on these events.

Recently it has come to the attention of the STAR collaboration that fixed-target collisions using light beam and target combinations could also benefit the Space Radiation Protection community. Cosmic rays are a serious concern to astronauts, electronics, and spacecraft. Although 90% of the cosmic ray flux is comprised of energetic protons and another 9% is Helium nuclei, the remaining 1%, which is made up of nuclei from Li to Fe, is not negligible both because the energy loss is proportional to Z^2 and because additional damage is done by the energetic light nuclei (p, d, t, ^3He, and ^4He) produced through the fragmentation of the target and projectile nuclei. The damage done by the light nuclei becomes increasingly important for higher energy cosmic rays. Light ion cross section measurements represent the largest uncertainty in space radiation estimates. The energy spectrum of cosmic rays in the solar system is concentrated at energies below 1 GeV/n. Extensive measurements have been made using the dedicated NSRL facility at the booster, and at other lower energy facilities. However, the Space Radiation Community has recently identified higher energy systems, using beams from 3 to 50 GeV/n on C, Al, and Fe targets as one of the next areas of need. [**?**] This energy range is dominated by Galactic Cosmic Rays (GCR). The requirements would be to measure the cross section for light nucleus (p, d, t, ^3He, and ^4He) production through fragmentation of the target and projectile. STAR has excellent particle identification for all of these particle species using both dE/dx and

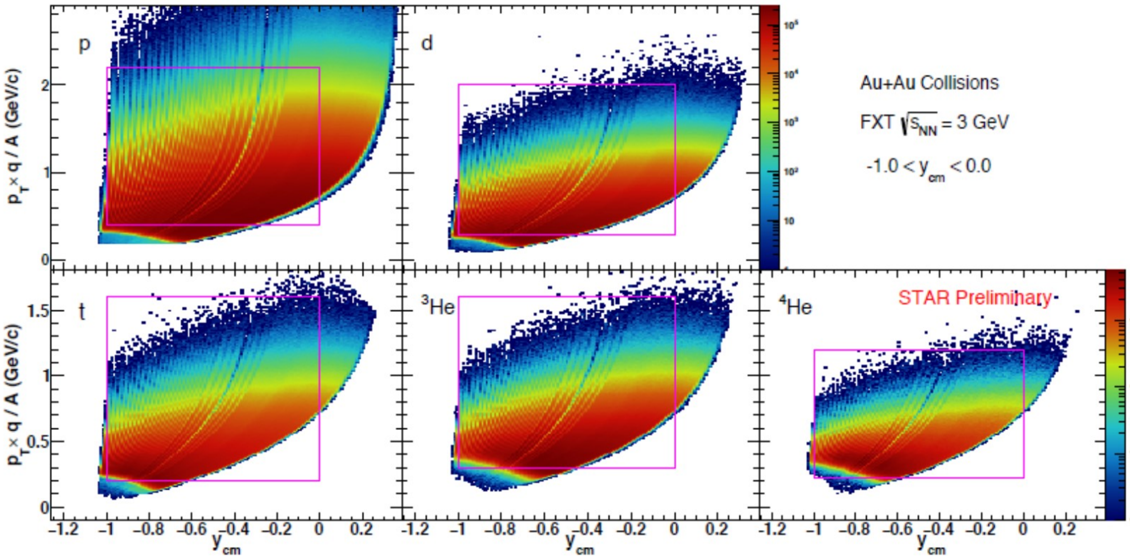

Figure 100: The acceptance for light nuclei (p, d, t, ^3He, and ^4He) achieved in the $\sqrt{s_{\mathrm{NN}}}$= 3 GeV Au+Au system using both dE/dx and ToF.

time-of-flight (capabilities specifically identified as essential in the NASA report [?], however the acceptance is only in the target-side of the rapidity distribution (see Fig. 100. For symmetric systems this is not a problem. This can be seen in Fig. 101 which shows the rapidity densities (dN/dy) for light nuclei. The results are reflected about midrapidity. The figure shows that the light nuclei associated with target fragmentation are seen in the less central collisions. The projectile fragmentation can be inferred by reflection. For asymmetric systems, for which reflection symmetry is not possible, inference of the projectile fragmentation would require both light-on-heavy and heavy-on-light combinations. STAR has reached out to determine if the STAR detector has sufficient acceptance in p_T and y to meet the needs of the Space Radiation Protection community. An overview of the RHIC/STAR capabilities was presented at the Workshop for Applied Nuclear Data Activities (WANDA2022) conference in February of 2022. In the session summary the opportunity to make these measurements at RHIC was characterized as a "unique, time-limited opportunity to obtain critical high-energy data".

NASA had been considering constructing detector systems to make these measurements at the FAIR facility at GSI in Darmstadt, Germany. STAR is an existing detector with the required capabilities and analysis teams that have proven expertise to measure the light nuclei cross sections in fixed-target experiments. The RHIC facility has demonstrated capability to efficiently deliver the required beams. In addition, there is significant uncertainty about when the SIS-100 accelerator will be available as the construction timeline has been disrupted by the war in Ukraine and the cessation of cooperation between Germany and Russia.

As it has been determined that the measurements that could be made at RHIC using the STAR detector will meet the needs of the Space Radiation Protection community, STAR

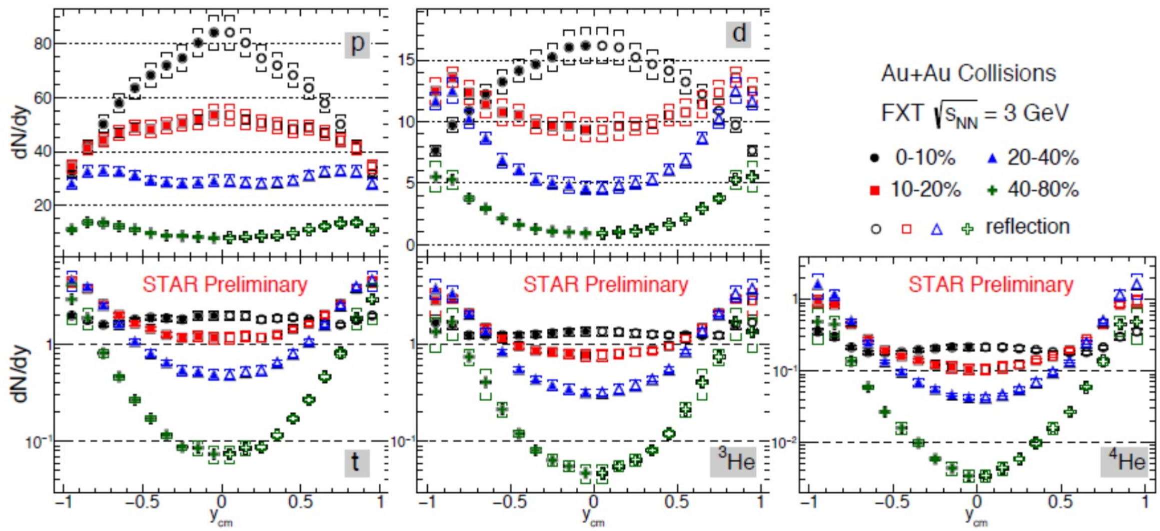

Figure 101: Preliminary dN/dy results for light nuclei (p, d, t, ^{3}He, and ^{4}He) measured in the $\sqrt{s_{\rm NN}}$= 3 GeV Au+Au system using both dE/dx and ToF.

is proposing brief energy scans using C, Si, and Fe beams on light targets (C, Al, and Fe). We propose three energies for each beam (E_{Tot} = 6, 21, and 51 GeV, E_{Kin} = 5, 20, and 50, or $\sqrt{s_{\rm NN}}$ = 3.6, 6.4, and 9.8 GeV respectively). For each beam, the collider would need 12 hours to develop the beam (this was the amount of time needed to develop the individual beams for the Au+Au FXT energy scan). In order to get enough statistics on each of the three targets, 36 hours would be needed for each beam-energy combination. Additionally, it is likely that the collider would need some time to reconfigure to circulate low energy beams (approximately one day). Therefore the request is for three weeks of beam time (one week for each of the three beam species). The STAR collaboration considers the full energy Au+Au, p+Au, and p+p programs to be the highest priority, and this opportunity would only be considered if addition weeks of operations were available.

Beam	Energy	Targets	Time
Machine Setup			1 day
Carbon	5 GeV	C, Al, Fe	2 days
Carbon	20 GeV	C, Al, Fe	2 days
Carbon	50 GeV	C, Al, Fe	2 days
Total			1 week
Machine Setup			1 day
Aluminum	5 GeV	C, Al, Fe	2 days
Aluminum	20 GeV	C, Al, Fe	2 days
Aluminum	50 GeV	C, Al, Fe	2 days
Total			1 week
Machine Setup			1 day
Iron	5 GeV	C, Al, Fe	2 days
Iron	20 GeV	C, Al, Fe	2 days
Iron	50 GeV	C, Al, Fe	2 days
Total			1 week
Grand Total			3 weeks

Table 9: Summary of the FXT beam/target scan request. Assumptions are 12 hours of beam development for each energy and 36 hours of physics running (12 hours for each of the three targets). Additionally one day would be needed to configure RHIC for low energy running.

6 Charge for the 2022 NPP PAC

BNL Nuclear Physics PAC 2022 Charge - March 20, 2022

Charge
STAR: Beam Use Requests for Runs 23-25
sPHENIX: Beam Use Requests for Runs 23-25
CeC: Beam Use Requests

The Beam Use Requests should be submitted in written form to PAC by May 6, 2022

The BURs should be based on the following number of cryo-weeks. The first number is the proposed RHIC run duration for scenario 1 and the second number corresponds to optimal duration (scenario 2) presented to the DOE-ONP in BNL's FY24 Lab Managers' Budget Briefing:

- 2023: 24 (28)
- 2024: 24 (28)
- 2025: 24 (28)

Note the eventual running cryo-weeks for each run will depend on the final budget guidance for that year so it can be lower than 24 weeks.

Presentations: STAR: Report on Run 2022, update on BES-II, small systems and spin physics analyses, and the latest development regarding the Isobar results.

CeC X: Results from Run 2022

PHENIX: Update on ongoing analysis efforts and data archiving efforts

sPHENIX: Installation status and schedule including TPOT status, commissioning, computing plan and readiness for data taking.

Written report from the PAC is expected within two weeks after the meeting.

References

[1] H.-j. Xu *et al.*, Chin. Phys. **C42**, 084103 (2018), 1710.07265.

[2] S. A. Voloshin, Phys. Rev. **C98**, 054911 (2018), 1805.05300.

[3] STAR, M. Abdallah *et al.*, Phys. Rev. Lett. **128**, 092301 (2022), 2106.09243.

[4] Y. Feng, J. Zhao, H. Li, H.-j. Xu, and F. Wang, Phys. Rev. C **105**, 024913 (2022), 2106.15595.

[5] STAR, N. M. Abdelwahab *et al.*, Phys. Lett. **B745**, 40 (2015), 1409.2043.

[6] Y. Feng, Y. Lin, J. Zhao, and F. Wang, Phys. Lett. B **820**, 136549 (2021), 2103.10378.

[7] J. Adams *et al.*, Nucl. Instrum. Meth. A **968**, 163970 (2020), 1912.05243.

[8] Z.-T. Liang and X.-N. Wang, Phys. Rev. Lett. **94**, 102301 (2005), nucl-th/0410079, [Erratum: Phys.Rev.Lett. 96, 039901 (2006)].

[9] S. A. Voloshin, (2004), nucl-th/0410089.

[10] K. Schilling, P. Seyboth, and G. E. Wolf, Nucl. Phys. B **15**, 397 (1970), [Erratum: Nucl.Phys.B 18, 332 (1970)].

[11] X.-L. Sheng, L. Oliva, and Q. Wang, Phys. Rev. D **101**, 096005 (2020), 1910.13684.

[12] STAR, J. Adam *et al.*, Phys. Rev. C **98**, 014910 (2018), 1805.04400.

[13] A. Bilandzic, C. H. Christensen, K. Gulbrandsen, A. Hansen, and Y. Zhou, Phys. Rev. **C89**, 064904 (2014), 1312.3572.

[14] J. Jia, M. Zhou, and A. Trzupek, Phys. Rev. C **96**, 034906 (2017), 1701.03830.

[15] N. Borghini, P. M. Dinh, and J.-Y. Ollitrault, Phys. Rev. C **63**, 054906 (2001), nucl-th/0007063.

[16] ATLAS, M. Aaboud *et al.*, JHEP **01**, 051 (2020), 1904.04808.

[17] A. Behera, M. Nie, and J. Jia, Phys. Rev. Res. **2**, 023362 (2020), 2003.04340.

[18] B. Schenke and S. Schlichting, Phys. Rev. **C94**, 044907 (2016), 1605.07158.

[19] P. Bozek, W. Broniowski, and J. Moreira, Phys. Rev. **C83**, 034911 (2011), 1011.3354.

[20] C. Shen and B. Schenke, Phys. Rev. **C97**, 024907 (2018), 1710.00881.

[21] L.-G. Pang, G.-Y. Qin, V. Roy, X.-N. Wang, and G.-L. Ma, Phys. Rev. C **91**, 044904 (2015), 1410.8690.

[22] G. Giacalone, B. Schenke, and C. Shen, Phys. Rev. Lett. **125**, 192301 (2020), 2006.15721.

[23] P. Bozek, Phys. Rev. C **93**, 044908 (2016), 1601.04513.

[24] P. Bozek and H. Mehrabpour, Phys. Rev. C **101**, 064902 (2020), 2002.08832.

[25] B. Schenke, C. Shen, and D. Teaney, Phys. Rev. C **102**, 034905 (2020), 2004.00690.

[26] G. Giacalone, F. G. Gardim, J. Noronha-Hostler, and J.-Y. Ollitrault, Phys. Rev. C **103**, 024909 (2021), 2004.01765.

[27] S. H. Lim and J. L. Nagle, (2021), 2103.01348.

[28] ALICE, S. Acharya *et al.*, JHEP **07**, 103 (2018), 1804.02944.

[29] STAR, L. Adamczyk *et al.*, Phys. Rev. Lett. **115**, 222301 (2015), 1505.07812.

[30] G. Giacalone, J. Jia, and V. Somà, (2021), 2102.08158.

[31] J. Jia, Phys. Rev. C **105**, 014905 (2022), 2106.08768.

[32] J. Jia, Phys. Rev. C **105**, 044905 (2022), 2109.00604.

[33] C. Zhang and J. Jia, Phys. Rev. Lett. **128**, 022301 (2022), 2109.01631.

[34] J. Jia and C.-J. Zhang, (2021), 2111.15559.

[35] H.-J. Xu *et al.*, Phys. Rev. Lett. **121**, 022301 (2018), 1710.03086.

[36] H. Li *et al.*, Phys. Rev. Lett. **125**, 222301 (2020), 1910.06170.

[37] H.-j. Xu *et al.*, (2021), 2111.14812.

[38] U. Gursoy, D. Kharzeev, and K. Rajagopal, Phys. Rev. C **89**, 054905 (2014), 1401.3805.

[39] STAR, J. Adam *et al.*, Phys. Rev. Lett. **127**, 052302 (2021), 1910.12400.

[40] M. A. *et al.* [STAR], (2022), 2204.01625.

[41] M. A. *et al.* [STAR], Phys. Rev. Lett. **128** (2022).

[42] STAR, M. Abdallah *et al.*, Phys. Lett. B **825**, 136865 (2022), 2110.09666.

[43] STAR, M. Abdallah *et al.*, Phys. Rev. D **105**, 032007 (2022), 2109.13191.

[44] STAR, L. Adamczyk *et al.*, Phys. Lett. B **771**, 13 (2017), 1607.07517.

[45] STAR, J. Adam *et al.*, Phys. Lett. B **797**, 134917 (2019), 1905.13669.

[46] PHENIX, A. Adare *et al.*, Phys. Rev. Lett. **101**, 122301 (2008), 0801.0220.

[47] S. Marzani, G. Soyez, and M. Spannowsky*Looking inside jets: an introduction to jet substructure and boosted-object phenomenology* Vol. 958 (Springer, 2019), 1901.10342.

[48] A. J. Larkoski, S. Marzani, and J. Thaler, Phys. Rev. D **91**, 111501 (2015), 1502.01719.

[49] STAR, M. S. Abdallah *et al.*, Phys. Rev. C **105**, 044906 (2022), 2109.09793.

[50] STAR, M. Abdallah *et al.*, Phys. Rev. D **104**, 052007 (2021), 2103.13286.

[51] STAR, J. Adam *et al.*, Phys. Lett. B **811**, 135846 (2020), 2003.02114.

[52] ALICE, S. Acharya *et al.*, Phys. Lett. B **793**, 420 (2019), 1805.05212.

[53] CMS, A. M. Sirunyan *et al.*, Phys. Rev. Lett. **127**, 102002 (2021), 2103.14089.

[54] S. Wang, W. Dai, B.-W. Zhang, and E. Wang, Eur. Phys. J. C **79**, 789 (2019), 1906.01499.

[55] M. A. *et al.* [STAR], Phys. Lett. B **827** (2022).

[56] STAR, M. S. Abdallah *et al.*, (2021), 2112.00240.

[57] STAR, M. Abdallah *et al.*, (2021), 2110.09513.

[58] STAR, M. S. Abdallah *et al.*, (2021), 2108.00924.

[59] STAR, M. S. Abdallah *et al.*, Longitudinal double-spin asymmetry for inclusive jet and dijet production in polarized proton collisions at $\sqrt{s} = 510$ GeV, 2021, 2110.11020.

[60] STAR, M. Abdallah *et al.*, (2021), 2111.10396.

[61] STAR, L. Adamczyk *et al.*, Phys. Rev. Lett. **115**, 092002 (2015).

[62] STAR, L. Adamczyk *et al.*, Phys. Rev. D **95**, 071103 (2017).

[63] STAR, M. S. Abdallah *et al.*, Phys. Rev. D **103**, L091103 (2021).

[64] STAR, J. Adam *et al.*, Phys. Rev. D **100**, 052005 (2019).

[65] D. de Florian, R. Sassot, M. Stratmann, and W. Vogelsang, Phys. Rev. Lett. **113**, 012001 (2014).

[66] NNPDF, E. R. Nocera, R. D. Ball, S. Forte, G. Ridolfi, and J. Rojo, Nucl. Phys. B **887**, 276 (2014).

[67] STAR, J. Kwasizur, Longitudinal Double-Spin Asymmetries for Dijet Production at Intermediate Pseudorapidity in Polarized Proton-Proton Collisions at $\sqrt{s} = 510$ GeV, in *APS Division of Nuclear Physics Meeting*, 2020.

[68] STAR, J. Kwasizur, Longitudinal Double-Spin Asymmetries for Dijet Production at Intermediate Pseudorapidity in Polarized Proton-Proton Collisions at $\sqrt{s} = 510$ GeV, in *24th International Spin Symposium*, 2021.

[69] J. L. Albacete, G. Giacalone, C. Marquet, and M. Matas, Phys. Rev. D **99**, 014002 (2019), 1805.05711.

[70] D. Kharzeev, E. Levin, and L. McLerran, Nucl. Phys. A **748**, 627 (2005), hep-ph/0403271.

[71] C. Marquet, Nucl. Phys. A **796**, 41 (2007), 0708.0231.

[72] PHENIX, A. Adare *et al.*, Phys. Rev. Lett. **107**, 172301 (2011), 1105.5112.

[73] M. Strikman and W. Vogelsang, Phys. Rev. D **83**, 034029 (2011), 1009.6123.

[74] U. D'Alesio, F. Murgia, and C. Pisano, Physics Letters B **773**, 300 (2017), 1707.00914.

[75] Z.-B. Kang, A. Prokudin, F. Ringer, and F. Yuan, Physics Letters B **774**, 635 (2017), 1707.00913.

[76] A. Aprahamian *et al.*, Reaching for the horizon: The 2015 long range plan for nuclear science, 2015, The 2015 Long Range Plan for Nuclear Science "Reaching for the Horizon" http://science.energy.gov/~/media/np/nsac/pdf/2015LRP/2015_LRPNS_091815.pdf.

[77] RHIC luminosity projection https://www.rhichome.bnl.gov//RHIC/Runs/RhicProjections.pdf.

[78] SN0619 : A Proposal for STAR Inner TPC Sector Upgrade (iTPC) https://drupal.star.bnl.gov/STAR/starnotes/public/sn0619.

[79] STAR, CBM eTOF Group, The CBM Collaboration eTOF Group, (2016), 1609.05102.

[80] The STAR Forward Calorimeter System and Forward Tracking System beyond BES-II https://drupal.star.bnl.gov/STAR/files/Proposal.ForwardUpgrade.Nov_.2018.Review.pdf.

[81] J. Jia and P. Huo, Phys. Rev. **C90**, 034915 (2014), 1403.6077.

[82] L.-G. Pang, H. Petersen, G.-Y. Qin, V. Roy, and X.-N. Wang, Eur. Phys. J. **A52**, 97 (2016), 1511.04131.

[83] W. Li, Nucl. Phys. A **967**, 59 (2017), 1704.03576.

[84] CMS, V. Khachatryan *et al.*, Phys. Rev. C **92**, 034911 (2015), 1503.01692.

[85] ATLAS, M. Aaboud *et al.*, Eur. Phys. J. C **78**, 142 (2018), 1709.02301.

[86] STAR Collaboration, L. Adamczyk *et al.*, Manuscript under preparation (2016).

[87] S. K. Das *et al.*, Phys. Lett. B **768**, 260 (2017), 1608.02231.

[88] S. Chatterjee and P. Bożek, Phys. Rev. Lett. **120**, 192301 (2018), 1712.01189.

[89] B. Chen, M. Hu, H. Zhang, and J. Zhao, Phys. Lett. B **802**, 135271 (2020), 1910.08275.

[90] STAR Collaboration, J. Adam *et al.*, Phys. Rev. Lett. **121**, 132301 (2018).

[91] ATLAS Collaboration, M. Aaboud *et al.*, Phys. Rev. Lett. **121**, 212301 (2018).

[92] J. E. Bernhard, J. S. Moreland, S. A. Bass, J. Liu, and U. Heinz, Phys. Rev. C **94**, 024907 (2016), 1605.03954.

[93] JETSCAPE, D. Everett *et al.*, Phys. Rev. C **103**, 054904 (2021), 2011.01430.

[94] G. Nijs, W. van der Schee, U. Gürsoy, and R. Snellings, (2020), 2010.15130.

[95] G. Denicol, A. Monnai, and B. Schenke, Phys. Rev. Lett. **116**, 212301 (2016), 1512.01538.

[96] H. Niemi, G. S. Denicol, P. Huovinen, E. Molnar, and D. H. Rischke, Phys. Rev. **C86**, 014909 (2012), 1203.2452.

[97] X. Guo, S. Shi, N. Xu, Z. Xu, and P. Zhuang, Phys. Lett. B **751**, 215 (2015), 1502.04407.

[98] B. Chen, X. Du, and R. Rapp, Nucl. Part. Phys. Proc. **289-290**, 475 (2017), 1612.02089.

[99] ALICE, J. Adam *et al.*, JHEP **05**, 179 (2016), 1506.08804.

[100] ATLAS, M. Aaboud *et al.*, Eur. Phys. J. C **78**, 762 (2018), 1805.04077.

[101] CMS, A. M. Sirunyan *et al.*, Phys. Rev. Lett. **118**, 162301 (2017), 1611.01438.

[102] STAR, L. Adamczyk *et al.*, Nature **548**, 62 (2017), 1701.06657.

[103] STAR, J. Adam *et al.*, Phys. Rev. Lett. **126**, 162301 (2021), 2012.13601.

[104] STAR, B. Abelev *et al.*, Phys. Rev. C **76**, 064904 (2007), 0706.0472.

[105] Z.-T. Liang, J. Song, I. Upsal, Q. Wang, and Z.-B. Xu, (2019), 1912.10223.

[106] Y. Xie, D. Wang, and L. P. Csernai, Eur. Phys. J. C **80**, 39 (2020), 1907.00773.

[107] X.-L. Sheng, Q. Wang, and X.-N. Wang, (2020), 2007.05106.

[108] STAR, M. Abdallah *et al.*, (2022), 2204.02302.

[109] V. Voronyuk *et al.*, Phys. Rev. C **83**, 054911 (2011), 1103.4239.

[110] W.-T. Deng and X.-G. Huang, Phys.Rev. **C85**, 044907 (2012), 1201.5108.

[111] X.-L. Zhao, G.-L. Ma, and Y.-G. Ma, Phys. Rev. C **99**, 034903 (2019), 1901.04151.

[112] X.-L. Zhao, Y.-G. Ma, and G.-L. Ma, Phys. Rev. C **97**, 024910 (2018), 1709.05962.

[113] D. E. Kharzeev, L. D. McLerran, and H. J. Warringa, Nucl. Phys. **A803**, 227 (2008), 0711.0950.

[114] U. Gürsoy, D. Kharzeev, E. Marcus, K. Rajagopal, and C. Shen, Phys. Rev. C **98**, 055201 (2018), 1806.05288.

[115] ALICE, S. Acharya *et al.*, Phys. Rev. Lett. **125**, 022301 (2020), 1910.14406.

[116] STAR, J. Adam *et al.*, Phys. Rev. Lett. **123**, 162301 (2019), 1905.02052.

[117] STAR, F. Seck, Nucl. Phys. A **1005**, 122005 (2021).

[118] STAR, L. Adamczyk *et al.*, Phys. Rev. Lett. **113**, 022301 (2014), 1312.7397, [Addendum: Phys.Rev.Lett. 113, 049903 (2014)].

[119] D. Kharzeev and R. D. Pisarski, Phys.Rev. **D61**, 111901 (2000), hep-ph/9906401.

[120] D. Kharzeev, Phys.Lett. **B633**, 260 (2006), hep-ph/0406125.

[121] R. Milton *et al.*, Phys. Rev. C **104**, 064906 (2021).

[122] L. Finch and S. Murray, Phys. Rev. C **96**, 044911 (2017), 1801.06476.

[123] F. Becattini, M. Buzzegoli, A. Palermo, and G. Prokhorov, Phys. Lett. B **822**, 136706 (2021), 2009.13449.

[124] S. Cao, G.-Y. Qin, and S. A. Bass, Phys. Rev. C **92**, 024907 (2015).

[125] JETSCAPE, A. Kumar *et al.*, Nucl. Phys. A **1005**, 122009 (2021), 2002.07124.

[126] Y. Mehtar-Tani and K. Tywoniuk, Phys. Rev. D **98**, 051501 (2018), 1707.07361.

[127] Y. Mehtar-Tani and K. Tywoniuk, Nucl. Phys. A **979**, 165 (2018), 1706.06047.

[128] B. G. Zakharov, Eur. Phys. J. C **81**, 57 (2021), 2003.10182.

[129] L. Chen, G.-Y. Qin, S.-Y. Wei, B.-W. Xiao, and H.-Z. Zhang, Phys. Lett. B **773**, 672 (2017), 1607.01932.

[130] A. H. Mueller, B. Wu, B.-W. Xiao, and F. Yuan, Phys. Lett. B **763**, 208 (2016), 1604.04250.

[131] STAR, J. Adam *et al.*, (2020), 2006.00582.

[132] STAR, N. R. Sahoo, Measurement of γ+jet and π^0+jet in central Au+Au collisions at $\sqrt{s_{\rm NN}} = 200$ GeV with the STAR experiment, 2020, 2008.08789.

[133] F. D'Eramo, K. Rajagopal, and Y. Yin, JHEP **01**, 172 (2019), 1808.03250.

[134] ALICE, J. Adam *et al.*, JHEP **09**, 170 (2015), 1506.03984.

[135] STAR, L. Adamczyk *et al.*, Phys. Rev. C **96**, 024905 (2017), 1702.01108.

[136] A. Bazavov *et al.*, Phys. Rev. D **95**, 054504 (2017), 1701.04325.

[137] S. Borsanyi *et al.*, JHEP **10**, 205 (2018), 1805.04445.

[138] CMS, V. Khachatryan *et al.*, Phys. Lett. B **772**, 489 (2017), 1605.06966.

[139] ALICE, B. Abelev *et al.*, Phys. Lett. B **718**, 1273 (2013), 1209.3715.

[140] STAR, L. Adamczyk *et al.*, Phys. Rev. C **96**, 054904 (2017), 1702.07705.

[141] ALICE, S. Acharya *et al.*, JHEP **06**, 035 (2020), 2002.10897.

[142] ALICE, S. Acharya *et al.*, (2021), 2101.02581.

[143] ALICE, S. Acharya *et al.*, (2021), 2101.04623.

[144] ALICE, S. Acharya *et al.*, (2021), 2101.04577.

[145] LHCb, R. Aaij *et al.*, (2021), 2108.02681.

[146] M. Alvioli, L. Frankfurt, V. Guzey, M. Strikman, and M. Zhalov, CERN Proc. **1**, 151 (2018).

[147] V. Guzey and M. Zhalov, JHEP **10**, 207 (2013), 1307.4526.

[148] V. Guzey, M. Strikman, and M. Zhalov, Phys. Rev. C **99**, 015201 (2019), 1808.00740.

[149] B. Sambasivam, T. Toll, and T. Ullrich, Phys. Lett. B **803**, 135277 (2020), 1910.02899.

[150] V. Guzey, Phys. Part. Nucl. Lett. **16**, 498 (2019).

[151] V. Guzey and M. Klasen, Phys. Rev. D **104**, 114013 (2021), 2012.13277.

[152] V. Guzey and M. Klasen, Inclusive and diffractive dijet photoproduction in ultraperipheral heavy ion collisions at the LHC, in *28th International Workshop on Deep Inelastic Scattering and Related Subjects*, 2021, 2106.16084.

[153] W. Chang *et al.*, (2022), 2204.11998.

[154] V. Guzey, M. Strikman, and M. Zhalov, Eur. Phys. J. C **74**, 2942 (2014), 1312.6486.

[155] H. Xing, C. Zhang, J. Zhou, and Y.-J. Zhou, The $\cos 2\phi$ azimuthal asymmetry in ρ^0 meson production in ultraperipheral heavy ion collisions, 2020, 2006.06206.

[156] STAR, J. the STAR Collaboration, Adam *et al.*, Phys. Rev. Lett. **123**, 132302 (2019), 1904.11658.

[157] W. Zha *et al.*, Phys. Rev. C **97**, 044910 (2018).

[158] M. B. G. Ducati and S. Martins, Phys. Rev. D **97**, 116013 (2018).

[159] W. Shi, W. Zha, and B. Chen, Phys. Lett. B **777**, 399 (2018), 1710.00332.

[160] M. R. Whalley, D. Bourilkov, and R. C. Group, The Les Houches accord PDFs (LHAPDF) and LHAGLUE, in *HERA and the LHC: A Workshop on the Implications of HERA and LHC Physics (Startup Meeting, CERN, 26-27 March 2004; Midterm Meeting, CERN, 11-13 October 2004)*, pp. 575–581, 2005, hep-ph/0508110.

[161] M. Cacciari and G. P. Salam, Phys. Lett. B **641**, 57 (2006), hep-ph/0512210.

[162] X. Ji, F. Yuan, and Y. Zhao, Phys. Rev. Lett. **118**, 192004 (2017), 1612.02438.

[163] Y. Hatta, Y. Nakagawa, F. Yuan, Y. Zhao, and B. Xiao, Phys. Rev. D **95**, 114032 (2017), 1612.02445.

[164] S. Bhattacharya, R. Boussarie, and Y. Hatta, Phys. Rev. Lett. **128**, 182002 (2022), 2201.08709.

[165] Y. Hatta, B.-W. Xiao, and F. Yuan, Phys. Rev. Lett. **116**, 202301 (2016), 1601.01585.

[166] ZEUS, I. Abt *et al.*, JHEP **12**, 102 (2021), 2106.12377.

[167] PHENIX, C. Aidala *et al.*, Nature Phys. **15**, 214 (2019), 1805.02973.

[168] W. Zhao, C. Shen, and B. Schenke, (2022), 2203.06094.

[169] ATLAS, G. Aad *et al.*, (2021), 2101.10771.

[170] STAR, R. A. Lacey, Nucl. Phys. A **1005**, 122041 (2021), 2002.11889.

[171] D. Kharzeev, Phys. Lett. B **378**, 238 (1996), nucl-th/9602027.

[172] BeAGLE: a Tool to Refine Detector Requirements for eA Collisions EIC R&D; Project eRD17 E. Aschenauer, M. Baker, W. Chang, J. Lee, Z. Tu et al. https://wiki.bnl.gov/eic/index.php/BeAGLE.

[173] Z. Tu *et al.*, Phys. Lett. B **811**, 135877 (2020), 2005.14706.

[174] A. Accardi *et al.*, Eur. Phys. J. A **52**, 268 (2016), 1212.1701.

[175] STAR Collaboration, J. Adam *et al.*, Phys. Rev. D **103**, 092009 (2021).

[176] STAR Collaboration, J. Adam *et al.*, Phys. Rev. D **103**, 072005 (2021).

[177] J.-w. Qiu and G. F. Sterman, Phys. Rev. D **59**, 014004 (1999), hep-ph/9806356.

[178] K. Kanazawa, Y. Koike, A. Metz, and D. Pitonyak, Phys. Rev. D **89**, 111501 (2014).

[179] L. Bland *et al.*, Physics Letters B **750**, 660 (2015).

[180] STAR, H. Liu, Measurement of transverse single-spin asymmetries for dijet production in polarized p+p collisions at $\sqrt{s} = 200$ GeV at STAR, in *Nuclear Physics Seminar, Brookhaven National Laboratory*, 2020, https://indico.bnl.gov/event/8633/.

[181] M. Boglione *et al.*, Phys. Lett. B **815**, 136135 (2021), 2101.03955.

[182] L. Gamberg, Z.-B. Kang, and A. Prokudin, Phys. Rev. Lett. **110**, 232301 (2013).

[183] STAR, B. Abelev *et al.*, Phys. Rev. Lett. **99**, 142003 (2007), 0705.4629.

[184] J. Collins and J.-W. Qiu, Phys. Rev. D **75**, 114014 (2007).

[185] T. C. Rogers and P. J. Mulders, Phys. Rev. D **81**, 094006 (2010).

[186] X. Liu, F. Ringer, W. Vogelsang, and F. Yuan, Factorization and its breaking in dijet single transverse spin asymmetries in *pp* collisions, 2020, 2008.03666.

[187] Z.-B. Kang, K. Lee, D. Y. Shao, and J. Terry, The sivers asymmetry in hadronic dijet production, 2020, 2008.05470.

[188] J. P. Ralston and D. E. Soper, Nuclear Physics B **152**, 109 (1979).

[189] R. Jaffe and X.-D. Ji, Nucl. Phys. B **375**, 527 (1992).

[190] P. Mulders and R. Tangerman, Nucl. Phys. B **461**, 197 (1996), hep-ph/9510301, [Erratum: Nucl.Phys.B 484, 538–540 (1997)].

[191] D. Sivers, Nuovo Cim. C **035N2**, 171 (2012), 1109.2521.

[192] C. Alexandrou *et al.*, Phys. Rev. D **98**, 091503 (2018).

[193] R. Jaffe and X.-D. Ji, Phys. Rev. Lett. **67**, 552 (1991).

[194] Z.-B. Kang, X. Liu, F. Ringer, and H. Xing, JHEP **11**, 068 (2017), 1705.08443.

[195] Z.-B. Kang, A. Prokudin, F. Ringer, and F. Yuan, Phys. Lett. B **774**, 635 (2017), 1707.00913.

[196] J. C. Collins, S. F. Heppelmann, and G. A. Ladinsky, Nucl. Phys. B **420**, 565 (1994), hep-ph/9305309.

[197] L. Adamczyk *et al.*, Phys. Lett. B **780**, 332–339 (2018).

[198] M. Radici and A. Bacchetta, Phys. Rev. Lett. **120**, 192001 (2018), 1802.05212.

[199] STAR, J. Adam *et al.*, Phys. Rev. D **98**, 091103(R) (2018), 1808.08000.

[200] STAR, Y. Xu, Longitudinal and Transverse Spin Transfer of Λ and $\overline{\Lambda}$ Hyperons in Polarized p+p Collisions at $\sqrt{s} = 200$ GeV at RHIC-STAR, in *XXVIII International Workshop on Deep-Inelastic Scattering and Related Subjects, Stony Brook University*, 2021, https://indico.bnl.gov/event/9726/contributions/46261/.

[201] F. Yuan, Phys. Rev. Lett. **100**, 032003 (2008).

[202] F. Yuan, Phys. Rev. D **77**, 074019 (2008).

[203] U. D'Alesio, F. Murgia, and C. Pisano, Phys. Lett. B **773**, 300 (2017), 1707.00914.

[204] A. Airapetian *et al.*, Phys. Lett. B **693**, 11–16 (2010).

[205] C. Adolph *et al.*, Phys. Lett. B **744**, 250–259 (2015).

[206] D. Müller, D. Robaschik, B. Geyer, F.-M. Dittes, and J. Hoˇ rejši, Fortsch. Phys. **42**, 101 (1994), hep-ph/9812448.

[207] X.-D. Ji, Phys. Rev. Lett. **78**, 610 (1997), hep-ph/9603249.

[208] A. Radyushkin, Phys. Lett. B **380**, 417 (1996), hep-ph/9604317.

[209] M. Burkardt, Phys. Rev. D **62**, 071503 (2000), hep-ph/0005108, [Erratum: Phys.Rev.D 66, 119903 (2002)].

[210] S. Klein and J. Nystrand, Photoproduction of J / psi and Upsilon in pp and anti-p p collisions, in *5th Workshop on Small x and Diffractive Physics*, 2003, hep-ph/0310223.

[211] S. R. Klein, J. Nystrand, J. Seger, Y. Gorbunov, and J. Butterworth, Comput. Phys. Commun. **212**, 258 (2017), 1607.03838.

[212] J. Lansberg, L. Massacrier, L. Szymanowski, and J. Wagner, Phys. Lett. B **793**, 33 (2019), 1812.04553.

[213] HERMES, A. Airapetian *et al.*, Phys. Lett. B **577**, 37 (2003), hep-ex/0307023.

[214] HERMES, A. Airapetian *et al.*, Nucl. Phys. B **780**, 1 (2007), 0704.3270.

[215] HERMES, A. Airapetian *et al.*, Phys. Lett. B **684**, 114 (2010), 0906.2478.

[216] W. Brooks and H. Hakobyan, Nucl. Phys. A **830**, 361C (2009), 0907.4606.

[217] NuSea, M. Vasilev *et al.*, Phys. Rev. Lett. **83**, 2304 (1999), hep-ex/9906010.

[218] K. J. Eskola, P. Paakkinen, H. Paukkunen, and C. A. Salgado, Epps21: A global qcd analysis of nuclear pdfs, 2021.

[219] PHENIX, S. Adler *et al.*, Phys. Rev. Lett. **98**, 172302 (2007), nucl-ex/0610036.

[220] R. Sassot, M. Stratmann, and P. Zurita, Phys. Rev. D **81**, 054001 (2010), 0912.1311.

[221] E. Aschenauer *et al.*, (2014), 1409.1633.

[222] N. Armesto, H. Paukkunen, J. M. Penín, C. A. Salgado, and P. Zurita, Eur. Phys. J. C **76**, 218 (2016), 1512.01528.

[223] H. Paukkunen, K. J. Eskola, and C. Salgado, Nucl. Phys. A **931**, 331 (2014), 1408.4563.

[224] K. J. Eskola, H. Paukkunen, and C. A. Salgado, JHEP **10**, 213 (2013), 1308.6733.

[225] H. Paukkunen and P. Zurita, JHEP **12**, 100 (2014), 1402.6623.

[226] L. Gribov, E. Levin, and M. Ryskin, Phys. Rept. **100**, 1 (1983).

[227] E. Iancu and R. Venugopalan, The Color glass condensate and high-energy scattering in QCD, in *In *Hwa, R.C. (ed.) et al.: Quark gluon plasma* 249-3363*, 2003, hep-ph/0303204.

[228] H. Weigert, Prog. Part. Nucl. Phys. **55**, 461 (2005), hep-ph/0501087.

[229] J. Jalilian-Marian and Y. V. Kovchegov, Prog. Part. Nucl. Phys. **56**, 104 (2006), hep-ph/0505052.

[230] F. Gelis, E. Iancu, J. Jalilian-Marian, and R. Venugopalan, Ann. Rev. Nucl. Part. Sci. **60**, 463 (2010), 1002.0333.

[231] G. Giuliani, H. Zheng, and A. Bonasera, Prog. Part. Nucl. Phys. **76**, 116 (2014), 1311.1811.

[232] Y. V. Kovchegov and E. Levin*Quantum chromodynamics at high energy* Vol. 33 (Cambridge University Press, 2012).

[233] A. H. Mueller and J.-w. Qiu, Nucl. Phys. B **268**, 427 (1986).

[234] L. McLerran and R. Venugopalan, Phys. Rev. D **49**, 2233 (1994).

[235] L. McLerran and R. Venugopalan, Phys. Rev. D **49**, 3352 (1994).

[236] L. McLerran and R. Venugopalan, Phys. Rev. D **50**, 2225 (1994).

[237] Y. V. Kovchegov, Phys. Rev. D **54**, 5463 (1996).

[238] Y. V. Kovchegov, Phys. Rev. D **55**, 5445 (1997).

[239] J. Jalilian-Marian, A. Kovner, L. McLerran, and H. Weigert, Phys. Rev. D **55**, 5414 (1997).

[240] A. H. Mueller, Nucl. Phys. **B415**, 373 (1994).

[241] A. H. Mueller and B. Patel, Nucl. Phys. B **425**, 471 (1994), hep-ph/9403256.

[242] I. Balitsky, Nucl. Phys. **B463**, 99 (1996), hep-ph/9509348.

[243] I. Balitsky, Phys. Rev. D **60**, 014020 (1999), hep-ph/9812311.

[244] Y. V. Kovchegov, Phys. Rev. **D60**, 034008 (1999), hep-ph/9901281.

[245] Y. V. Kovchegov, Phys. Rev. D **61**, 074018 (2000), hep-ph/9905214.

[246] J. Jalilian-Marian, A. Kovner, and H. Weigert, Phys. Rev. D **59**, 014015 (1998), hep-ph/9709432.

[247] J. Jalilian-Marian, A. Kovner, A. Leonidov, and H. Weigert, Phys. Rev. D **59**, 014014 (1998), hep-ph/9706377.

[248] E. Iancu, A. Leonidov, and L. D. McLerran, Phys. Lett. B **510**, 133 (2001), hep-ph/0102009.

[249] E. Iancu, A. Leonidov, and L. D. McLerran, Nucl. Phys. **A692**, 583 (2001), hep-ph/0011241.

[250] Y. V. Kovchegov and M. D. Sievert, Nucl. Phys. B **903**, 164 (2016), 1505.01176.

[251] CMS, S. Chatrchyan *et al.*, Eur. Phys. J. C **74**, 2951 (2014), 1401.4433.

[252] STAR, E. Braidot, Nucl. Phys. A **854**, 168 (2011), 1008.3989.

[253] J. L. Albacete and C. Marquet, Phys. Rev. Lett. **105**, 162301 (2010), 1005.4065.

[254] Z.-B. Kang, I. Vitev, and H. Xing, Phys. Rev. D **85**, 054024 (2012), 1112.6021.

[255] J. Jalilian-Marian and A. H. Rezaeian, Phys. Rev. D **86**, 034016 (2012), 1204.1319.

[256] J. L. Albacete and C. Marquet, Nucl. Phys. A **854**, 154 (2011), 1009.3215.

[257] K. J. Eskola, H. Paukkunen, and C. A. Salgado, JHEP **07**, 102 (2008), 0802.0139.

[258] A. H. Rezaeian, Phys. Rev. D **86**, 094016 (2012), 1209.0478.

[259] T. Sjostrand, S. Mrenna, and P. Z. Skands, Comput. Phys. Commun. **178**, 852 (2008), 0710.3820.

[260] Di-jet production from pythia8.189 is scaled down due to its overestimation of inclusive π_0 yields compared to those reported by BRAHMS in phys. rev. lett. 98 (2007) 252001 and STAR in phys. rev. lett. 97 (2006) 152302.

[261] T. Kaufmann, A. Mukherjee, and W. Vogelsang, Phys. Rev. D **92**, 054015 (2015), 1506.01415, [Erratum: Phys.Rev.D 101, 079901 (2020)].

[262] D. de Florian, R. Sassot, M. Epele, R. J. Hernández-Pinto, and M. Stratmann, Phys. Rev. D **91**, 014035 (2015), 1410.6027.

[263] A. Khouaja *et al.*, Nucl. Phys. A **780**, 1 (2006).

[264] D. de Florian and R. Sassot, Phys. Rev. D **69**, 074028 (2004), hep-ph/0311227.

[265] D. de Florian, R. Sassot, and M. Stratmann, Phys. Rev. D **75**, 114010 (2007), hep-ph/0703242.

[266] D. de Florian, R. Sassot, and M. Stratmann, Phys. Rev. D **76**, 074033 (2007), 0707.1506.

[267] M. A. Lisa *et al.*, (2021), 2101.10872.

[268] J. L. Nagle and W. A. Zajc, Ann. Rev. Nucl. Part. Sci. **68**, 211 (2018), 1801.03477.

[269] PHENIX, C. Aidala *et al.*, Phys. Rev. C **95**, 034910 (2017), 1609.02894.

[270] H. Helmholtz, The London, Edinburgh, and Dublin Philosophical Magazine and Journal of Science **33**, 485 (1867), https://doi.org/10.1080/14786446708639824.

[271] C. Shen *et al.*, In preparation.

[272] B. Schenke, S. Jeon, and C. Gale, Phys. Rev. **C82**, 014903 (2010), 1004.1408.

[273] I. Upsal, *Global Polarization of the $\Lambda/\overline{\Lambda}$ system in the STAR BES*, Ph.D. thesis, The Ohio State University, 2018.

[274] Y. B. Ivanov and A. Soldatov, Phys. Rev. C **95**, 054915 (2017), 1701.01319.

[275] Y. B. Ivanov and A. Soldatov, Phys. Rev. C **97**, 044915 (2018), 1803.01525.

[276] Y. B. Ivanov, V. Toneev, and A. Soldatov, Phys. Atom. Nucl. **83**, 179 (2020), 1910.01332.

[277] Y. B. Ivanov, V. Toneev, and A. Soldatov, J. Phys. Conf. Ser. **1435**, 012012 (2020).

[278] B. Fu, K. Xu, X.-G. Huang, and H. Song, (2020), 2011.03740.

[279] M. Baznat, K. Gudima, A. Sorin, and O. Teryaev, Phys. Rev. C **88**, 061901 (2013), 1301.7003.

[280] O. Teryaev and R. Usubov, Phys. Rev. C **92**, 014906 (2015).

[281] M. I. Baznat, K. K. Gudima, A. S. Sorin, and O. Teryaev, Phys. Rev. C **93**, 031902 (2016), 1507.04652.

[282] W.-T. Deng and X.-G. Huang, Phys. Rev. C **93**, 064907 (2016), 1603.06117.

[283] D.-X. Wei, W.-T. Deng, and X.-G. Huang, Phys. Rev. C **99**, 014905 (2019), 1810.00151.

[284] X.-L. Xia, H. Li, Z.-B. Tang, and Q. Wang, Phys. Rev. C **98**, 024905 (2018), 1803.00867.

[285] A. Zinchenko, A. Sorin, O. Teryaev, and M. Baznat, J. Phys. Conf. Ser. **1435**, 012030 (2020).

[286] G. Bunce *et al.*, Phys. Rev. Lett. **36**, 1113 (1976).

[287] COSY-TOF, F. Hauenstein *et al.*, Eur. Phys. J. A **52**, 337 (2016), 1607.06305.

[288] F. Abe *et al.*, Phys. Rev. D **34**, 1950 (1986).

[289] B. Lundberg *et al.*, Phys. Rev. D **40**, 3557 (1989).

[290] HERA-B, I. Abt *et al.*, Phys. Lett. B **638**, 415 (2006), hep-ex/0603047.

[291] HADES, G. Agakishiev *et al.*, Eur. Phys. J. A **50**, 81 (2014), 1404.3014.

[292] STAR, M. Abdallah *et al.*, Phys. Rev. C **105**, 014901 (2022), 2109.00131.

[293] ALICE Collaboration, Phys. Lett. B **784**, 82 (2018), 1805.01832.

[294] CMS, A. M. Sirunyan *et al.*, Phys. Rev. C **100**, 044902 (2019), 1901.07997.

[295] ATLAS Collaboration, (2019), 1911.04812.

[296] ATLAS, (2022), 2205.00039.

[297] B. Bally, M. Bender, G. Giacalone, and V. Somà, Phys. Rev. Lett. **128**, 082301 (2022), 2108.09578.

[298] U. W. Heinz and A. Kuhlman, Phys.Rev.Lett. **94**, 132301 (2005), nucl-th/0411054.

[299] Q. Y. Shou *et al.*, Phys. Lett. B **749**, 215 (2015), 1409.8375.

[300] G. Giacalone, Phys. Rev. Lett. **124**, 202301 (2020), 1910.04673.

[301] G. Giacalone, *A matter of shape: seeing the deformation of atomic nuclei at high-energy colliders*, PhD thesis, U. Paris-Saclay, 2020, 2101.00168.

[302] G. Giacalone, J. Jia, and C. Zhang, (2021), 2105.01638.

[303] H.-j. Xu, H. Li, X. Wang, C. Shen, and F. Wang, Phys. Lett. B **819**, 136453 (2021), 2103.05595.

[304] S. Raman, C. W. G. Nestor, Jr, and P. Tikkanen, Atom. Data Nucl. Data Tabl. **78**, 1 (2001).

[305] S. E. Agbemava, A. V. Afanasjev, and P. Ring, Phys. Rev. C **93**, 044304 (2016), 1603.03414.

[306] P. Möller, A. J. Sierk, T. Ichikawa, and H. Sagawa, Atom. Data Nucl. Data Tabl. **109-110**, 1 (2016), 1508.06294.

[307] L. M. Robledo and G. F. Bertsch, Phys. Rev. C **84**, 054302 (2011), 1107.3581.

[308] S. Hilaire and M. Girod, Eur. Phys. J. A **33**, 237 (2007).

[309] T. Nakatsukasa, K. Matsuyanagi, M. Matsuo, and K. Yabana, Rev. Mod. Phys. **88**, 045004 (2016), 1606.04717.

[310] L.-M. Liu *et al.*, (2022), 2203.09924.

[311] S. Zhao, H.-j. Xu, Y.-X. Liu, and H. Song, (2022), 2204.02387.

[312] J. Jia, S. Huang, and C. Zhang, (2021), 2105.05713.

[313] G. Giacalone, Phys. Rev. C **99**, 024910 (2019), 1811.03959.

[314] Haojie Xu talk, Chunjian Zhang poster, (STAR Collabration),Constraints on neutron skin thickness and nuclear deformations using relativistic heavy-ion collisions from STAR, https://indico.cern.ch/event/895086/contributions/4724887/,https://indico.cern.ch/event/895086/contributions/4749420/.

[315] G. Nijs and W. van der Schee, (2021), 2112.13771.

[316] J. M. Lattimer and M. Prakash, Phys. Rept. **442**, 109 (2007), astro-ph/0612440.

[317] B.-A. Li, B.-J. Cai, W.-J. Xie, and N.-B. Zhang, Universe **7**, 182 (2021), 2105.04629.

[318] PREX, D. Adhikari *et al.*, Phys. Rev. Lett. **126**, 172502 (2021), 2102.10767.

[319] ALICE, S. Acharya *et al.*, (2021), 2111.06106.

[320] G. Giacalone, Phys. Rev. C **102**, 024901 (2020), 2004.14463.

[321] G. Giacalone, F. G. Gardim, J. Noronha-Hostler, and J.-Y. Ollitrault, Phys. Rev. C **103**, 024910 (2021), 2004.09799.

[322] Chart of Nuclear Quadrupole Deformations, https://www.nndc.bnl.gov/nudat2/.

[323] P. A. Butler, J. Phys. G **43**, 073002 (2016).

[324] C. J. Lister and J. Butterworth, Nature **497**, 190 (2013).